ROLE OF SURFACE LIGAND CHEMISTRY ON SHAPE EVOLUTION AND OPTOELECTRONIC PROPERTIES OF DIRECT BAND GAP SEMICONDUCTORS

by

Meghan Teunis McLeod

A Dissertation

Submitted to the Faculty of Purdue University

In Partial Fulfillment of the Requirements for the degree of

Doctorate of Philosophy

Department of Chemistry and Chemical Biology

Indianapolis, Indiana

August 2017

THE PURDUE UNIVERSITY GRADUATE SCHOOL
STATEMENT OF COMMITTEE APPROVAL

Dr. Rajesh Sardar, Chair

Department of Chemistry and Chemical Biology

Dr. Partha Basu

Department of Chemistry and Chemical Biology

Dr. Chen Yang

Department of Chemistry

Dr. Chengde Mao

Department of Chemistry

Approved by:

Dr. Eric Long

Head of the Graduate Program

"People often remark that I'm pretty lucky. Luck is only important in so far as getting the chance to sell yourself at the right moment. After that, you've got to have talent and know how to use it."

-Frank Sinatra

ACKNOWLEDGMENTS

I would like to thank the many people who have helped and encouraged me during my graduate career. First I would like to express my gratitude to my advisor Dr. Rajesh Sardar, Thank you for your continued guidance and assistance during my doctoral studies. Without your patience, motivation, enthusiasm, and knowledge my research and writing would never have reached the level they are today.

I would also like to thank the rest of my thesis committee Dr. Partha Basu, Dr. Chen Yang, and Dr. Chengde Mao for their encouragement and comments.

I want to express my thanks to Dr. Barry Muhoberac. Thank you for your insightful comments and discussions not only on this dissertation, but also on numerous projects over the last five years. Also to Dr. Amanda Siegel, thank for your comments and discussions on my work. I truly appreciate you guidance and the knowledge that you have shared with me.

My graduate studies would not be complete without the members of the Sardar lab, both past and present, Dr. Sukanta Dolai, Dr. Gayatri Joshi, thank you for welcoming me into the lab and the world of nanomaterials. My first two years of research would not have been the same without your guidance and training. To Dr. Katie Lawrence, thank you for all the collaborations, comments and edits, and coffee breaks over the last five years. I would also like to thank the current members of the lab, Thakshila Liyanage, Ashur Real, and Yang Yang, for your support and encouragement over the last few months. Finally to my fallow graduate students in the department, thank you for taking the time to listen to my presentations, exchange ideas and offer encouragement.

Finally, I would like to thank my family. To my parents Tim and Pam Teunis thank you for supporting me my entire life and always encouraging me to have big goals and even bigger dreams. To the best role models a little sister could ask for, Jamie Shaw and Jen and Brett Wardrop. Last but not least, I thank my husband Chauncey McLeod for being supportive and understanding over the past five years. Without your love and encouragement I would not have reached this level of success.

TABLE OF CONTENTS

LIST OF TABLES

LIST OF FIGURES

LIST OF ABBREVIATIONS

Br	bromide
Cd	cadmium
CF_3	trifluoromethyl
CH_3	methyl
$CHCl_3$	chloroform
CIE	Commission Internationale de l'Eclairage
Cl	chloride
COO	carboxylate
Cs	cesium
CS_2	carbon disulfide
DA	decylamine
DADD	diaminododecane
DCM	dichloromethane
DDA	dodecylamine
DFT	density functional theory

DMF	N,N-dimethylformamide
DTC	dithiocarbamate
EDS	energy dispersive spectroscopy
EMA	effective mass approximation
E_{og}	optical band gap
eV	electron volt
F	fluoride
FET	field effective transistor
FTIR	fourier transform infrared spectroscopy
fwhm	full width half maxima
H	hydrogen
^{1}H NMR	proton nuclear magnetic resonance
HA	hexylamine
HDA	hexadecylamine
HOMO	highest occupied molecular orbital
HRTEM	high-resolution transmission electron microscopy

HT	hexanethiol
kDa	kiladalton
LDI-TOF-MS	laser desorption ionization-time of flight-mass spectroscopy
LED	light emitting diode
LUMO	lowest unoccupied molecular orbital
MeCN	acetonitrile
N	nitrogen
Nap	naphthalene
NC	nanocrystal
$N(CH_3)_2$	dimethylamine
NH_3	ammonium
NH_4OH	ammonium hydroxide
nm	nanometer
OAMI	octyl ammonium ions
OCF_3	trifluoromethoxy
OCH_3	methoxy

ODE	octadecene
OLA	oleylamine
Pb	lead
PDTC	phenyl dithiocarbamate
Ph	phenyl
PL	photoluminescence
PL-QY	photoluminescence quantum yield
PLE	photoluminescence excitation
Py	pyrene
QC	quantum cube
QD	quantum dot
QPL	quantum platelet
QR	quantum rod
QW	quantum wire
R	radius
S	sulfur

SAXS	small angle x-ray scattering
Se	selenium
SEM	scanning electron microscopy
SH	thiol
TCB	trichlorobenzene
TCSPC	time -correlated single photon counting
Te	tellurium
TEM	transmission electron microscopy
UV-vis	ultra-violet visible
WLE	white-light emission
XPS	x-ray photoelectron spectroscopy
XRD	x-ray diffraction

ABSTRACT

Author: McLeod, Meghan, Teunis. PhD
Institution: Purdue University
Degree Received: August 2017
Title: Role of Surface Ligand Chemistry on Shape Evolution and Optoelectronic Properties of Direct Band Gap Semiconductors
Major Professor: Rajesh Sardar

The expansion of the applications of direct band gap semiconductor nanocrystals (NCs) has been a result of the control colloidal synthetic methods offer on the optoelectronic properties. These properties are readily controlled by the surface chemistry and even a small change in the surface passivating ligand can show profound effects. Furthermore, the choice of surface passivating ligand also impacts the NC shape evolution, which in turn influence the surface area, quantum yield, and charge transport properties that are critical to optimize device fabrication.

In this dissertation, the unique aspects of surface chemistry that control both NC shape evolution and optoelectronic properties are investigated. We began by investigating how surface chemistry controls the shape evolution of methyl ammonium lead bromide ($CH_3NH_3PbBr_3$) perovskite NCs. In addition to the surface passivating ligand, the reaction temperature and solvent system were also examined. Through a series of control experiments, the critical parameter for the formation of quantum wires (QWs) was found to be the presence of a long chain acid, while the quantum platelets (QPLs) required a long chain amine and chlorinated solvent, and quantum cube (QC) formation was kinetically driven. The higher ordered stacking of the QPLs and bundling of the QWs was also found to be controlled by surface ligand chemistry.

Next we further examined how surface chemistry impacts shape evolution, but in the system of metal chalcogenide NCs. We developed a versatile, low temperature, and gram scale synthesis of QWs, QPLs, and quantum rods (QRs) using both cadmium and zinc as metal precursors and sulfur and selenium as chalcogenide precursors. Through systematic investigation of both the surface chemistry and reaction progression, the growth and formation mechanism was also determined. The 1D QW growth required a long chain amine while the QPLs required the presence of both a long and short chain amine to drive 2D growth. Finally, the QRs would found to be a kinetically-controlled process.

Ultrasmall semiconductor NCs are known to possess high surface to volume ratios and therefore even a minute change in surface chemistry will have a significant impact on the optoelectronic properties. Our investigation focused on $(CdSe)_{34}$ NCs, and how exchanging native amine ligands with various chalcogenol based ligands influences these properties. These NCs lie in the strong confinement regime and therefore have a higher probability of undergoing exciton delocalization, resulting in red shifts of the first excitonic peak and reduction of the optical band gap. Additionally, we examined different characteristics of the ligand (level of conjugation, electron withdrawing or donating nature of para-substitution, binding mode and head group) to examine how these parameters impact exciton delocalization. We observed the highest shift in the optical band gap (of 650 meV) after exchanging the native amine ligands with pyrene dithiocarbamate. Through this investigation it was determined that ligand characteristics (specifically conjugation and binding mode) have significant influence in the proposed hole delocalization.

Finally, we continued the investigation of how surface chemistry controls optoelectronic properties of ultrasmall NCs, but expand our work to those of methyl ammonium lead halide. We developed a low temperature and colloidal synthesis of white-light emitting NCs with a diameter of 1.5 nm. Through precise manipulation of the surface halide ions, it was possible to tailor the emission to match that of nearly pure white light.

CHAPTER 1. DIRECT BAND GAP SEMICONDUCTORS (METAL CHALCOGENIDE AND PEROVSKITE) NANOCRYSTALS: FUNDAMENTALS AND OPPORTUNITIES

1.1 Motivation

Through centuries fossil fuels have been the major source of energy. With the increase of global populations, use of carbon related materials has dramatically increased to meet the global energy demand. The excessive use of carbon materials for energy production resulted in uncontrollable release of greenhouse gases into the earth's environment that showed detrimental effects on global weather patterns. Sunlight is the most abundant source of natural energy that can be used to produce solar fuels (e.g. H_2) and convert electricity (e.g., through photovoltaic devices). This renewable energy production requires efficient capture of solar energy. In 1972, Fujishima and coworkers reported the first photovoltaic application of direct band-gap semiconductor materials (TiO_2).[14]

Semiconductor band gaps can exists either as direct or indirect based on the momentum of the valence and conduction band energies. In the case of a direct band gap semiconductor, the top of the valence band and bottom of the conduction band have the same value of momentum (see Figure 1.1). When a direct band gap material absorbs energy from photons, an electron will become excited to the conduction band while the hole remains in the valence band.[15, 16] Since both the electron and hole have the same momentum vector, the rate of radiative recombination is faster than that of indirect band gap materials, where the momentum vector of the electron and hole are not the same. This ability to produce charge carriers (electrons and holes) is the working principle

behind many solid-state applications including photovoltaic and photocatalytic devices. In these devices, the semiconductor materials interact with sunlight to generate the electron/hole pairs. The electrons can be used as electric energy (photovoltaic device) or to reduce H^+ (photocatalytic devices). The efficiency of these devices is affected by charge carrier properties such as charge separation, recombination, transfer, and transport. The charge separation is based largely on the NCs diameter since that dictates the distance between the valence and conduction bands as well as the coulombic interaction energy between the electron hole pair. This separation is not possible in bulk materials where the discrete energy levels do not exist.

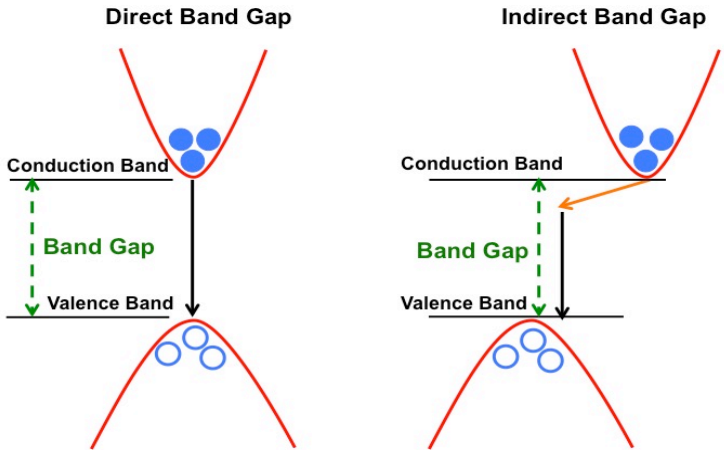

Figure 1.1: The difference between the positions of the valence and conduction bands in direct versus indirect band gap semiconductors. The same momentum vector allows for enhanced radiative recombination in direct band gap materials making them more applicable for solid-state devices.

The idea of renewable energy production took a big step forward in 1993 when Bawendi and coworkers first synthesized spherical colloidal metal chalcogenides semiconductor NCs (SNCs) (e.g., CdSe and CdS SNCs)[17]. These early SNCs displayed far better and efficient optoelectronic properties which made them more suitable for both photocatalytic and photovoltaic applications than bulk and previously synthesized

NCs.[18, 19] In order to promote and sustain the cutting edge research, in 1999 the United States federal government founded “National Nanotechnology Initiative” program. However, the bottleneck of using spherical SNCs maintained the extremely low power conversion efficiency (<1 %) of the fabricated devices. By changing the shape of the NCs from spherical to rod, the efficiency was increased to ~3%.[20] The literature reports suggest that the increase in efficiency of anisotropically-shaped SNC-based photovoltaic devices is because of their ability to transport photogenerated charges over a long distance without multiple hopping. Therefore, our initial hypothesis was ultrathin (<3 nm thickness) anisotropically-shaped SNCs of a few hundred nanometers (nm) in dimension should enhance the charge transport. Moreover, for the successful transformation of laboratory research into technology requires large-scale synthesis of semiconductor NCs.

Semiconductor NCs were first recognized by Peng in 2001.[21] However the NCs were not isolated and characterized until later when they became more heavily stuided. In the past two decades, numerous research groups have focused on various aspects of these NCs including; studying the growth mechanisms of quantum confined metal chalcogenides, producing these NCs in gram scale quantities; exploring their unique size and surface-ligand dependent photophysical and electronic properties; and examining the roll the magic-size NCs play as precursors for the formation of one dimensional (1D) and two dimensional (2D) SNCs.[19, 22-24]

In recent years, the field of direct band gap semiconductors has grown to include the class of materials known as perovskites and their impact on the advancement of solid-state devices. The first report of fabricating photovoltaic devices with this material was

in 2009 and reported efficiencies of 3.8%[25] When the size of the material was reduced to the millimeter scale, efficiencies of 10%[26] were reported. It is expected that employing anisotropically-shaped NCs of perovskite would provide enhanced electronic and charge transport properties. This is especially true in the case of 2D materials since they are known to possess larger lateral dimensions that allows for increased charge transport.

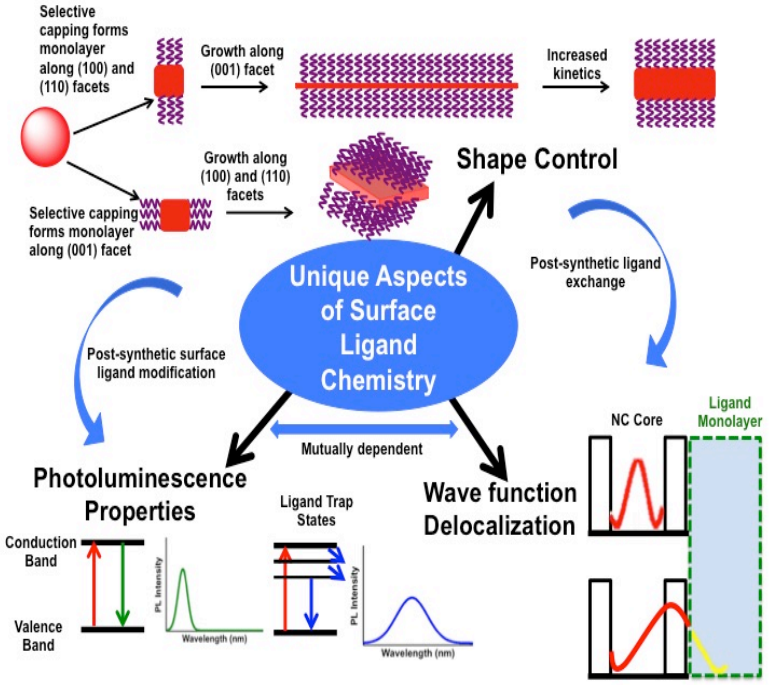

Figure 1.2 An overview of how the unique aspects of surface chemistry influence the shape and optoelectronic properties of semiconductor NCs; (A) surface chemistry impacts shape control by specific adhesion to different crystal facets prohibiting or promoting growth along various axes, (B) surface ligand dependent expansion of the excitonic wave function beyond the NC core boundary into the ligand monolayer, (C) the emission properties of the NC can be tailored by the presence of surface ligand trap states

The scientific scope of this dissertation is to study the important nanoscale structural parameters controlling the formation of anisotropically-shaped, strongly quantum-confined metal chalcogenides and perovskite NCs. Additionally we aim to

further manipulate their unique optoelectronic properties through the systematic selection of surface ligand chemistry**.** As illustrated in Figure 1.2 below

- **Structurally Well-Defined Perovskite NCs Formation.** We examined the applicability of the mesoscale assembly model as the basis to illustrate the formation of QWs and QPLs, and their superstructures formation. We studied the effect of surface ligands on the growth and assembly of these semiconductor NCs.
- **Facile Gram Scale Synthesis of Metal Chalcogenide Anisotropic NCs.** We accomplished a versatile, low temperature, and gram scale synthesis of anisotropically-shaped ME NCs (M= Cd or Zn and E = S or Se) and examined how precursor identity and surface ligands control the shape.
- **Surface Ligand Chemistry Controlled SNC Optoelectronic Properties.** We investigated the effects of nanoscale structural properties of surface ligand chemistry on the optoelectronic properties of strongly quantum confined semiconductor NCs.
- **Surface Controlled White-Light Emission of Perovskite NCs.** We performed the synthesis of ultrasmall perovskite NCs and tailored their white-light emission by tailoring the surface composition and trap states.

This thesis aims at examining how modification of the unique aspects of surface chemistry can control the shape and optoelectronic properties of semiconductor NCs. Shape is a parameter that offers control over the surface area, quantum yield, and charge transport, which are critical to optimized device fabrication. We examine how the identity of the surface passivating ligands and their interactions control NC shape in both perovskite and metal chalcogenide systems. Next we performed post-synthetic ligand

exchange to manipulate surface chemistry to enhance exciton delocalization in metal chalcogenide NCs. Finally, we tailor the compositions of methyl ammonium lead halide NCs for white-light emission in LED applications.

1.2 Surface Chemistry

Due to their small size and large surface area, NCs are not thermodynamically stable in solution without the addition of surface passivating ligands.[27] While surface ligands are critical to enhance stability and solubility, the surface chemistry of the NC also plays a crucial roll in the control of NC shape and the optoelectronic properties.[28] The early investigations of surface chemistry centered on control of the nucleation and growth process and the preservation of colloidal stability. This included both the stability of the nuclei in the reaction, which is required for the growth of larger sizes or additional shapes, and for the isolation of the final NC. Manipulation of surface chemistry, such as in composition, trap states, and surface passivating ligands, leads to control of optoelectronic properties (as further discussed later). Finally, modification of surface chemistry can facilitate more efficient charge transfer and allow for better charge transport. The enhanced charge transfer and transport capabilities of the NC are influenced more by surface chemistry controlled shape and conducting nature of the surface passivating ligand.

1.2.1 Effects of Surface Chemistry on Shape Control

Initial investigations about surface chemistry were focused on how these capping molecules acted as surfactants and stabilizers, keeping the synthesized NCs soluble. It was later established that the identity of the surface passivating ligand can impact the

shape and crystal structure of the NC. This is due to the fact that anisotropic growth is driven by surface energy and the surface energy is controlled by the surfactants used.[29] In the case of surface passivating ligands, these molecules stabilize the surface through selective adhesion. This can block or inhibit certain crystal faces from contributing to the growth process and subsequently leads to shape control. The crystal facet energy is known to be exponentially coordinated to growth and a greater surface energy induces faster growth in specific directions.[30] A specific example of this is shown in the case of wurtzite CdSe quantum rods. The amine ligands bound to the cadmium surface prevent growth along the (100) and (110) planes and enhance growth along the (001)[31, 32]

1.3 Shape

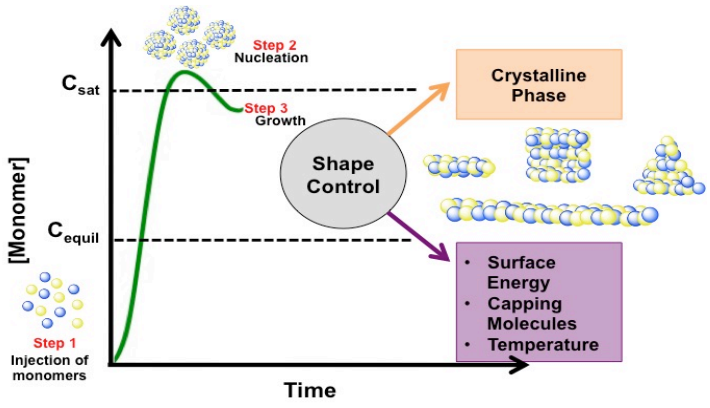

Figure 1.3 The LaMer Model of growth and nucleation. Step 1, injection of the monomers. The monomer concentration continues to increase until it surpasses that of supersaturation (C_{sat}). Once this concentration is obtained, Step 2, the nucleation of the NC seeds, occurs. The nucleation process consumes some of the monomer concentration and the final step of further growth proceeds. The shape of the final NC is dictated by several factors. The crystalline phase impacts which crystal facets are going to be involved in the NC growth. The crystal facets where the growth is occurring will possess a greater surface energy. The capping molecules present also affect this growth with their inhibiting growth (see Figure 2) or promoting enhanced confinement through ligand-ligand interactions.

The starting point of any growth is the nucleation of NCs which act as precursors for anisotropic shapes The LaMer model shown in Figure 3 describes the basis of this process. This begins, in Step 1, with the injection of the monomers until their concentration exceeds the maximum supersaturation (C_{sat}). The growth rate of the monomers decreases as Step 2 proceeds with the formation of nuclei. In the final step, the nuclei continue to grow and the shape is tailored by factors including crystal facets and corresponding surface energy, capping molecules, and temperature (these specific parameters will be discussed in more detail later). For anisotropic shapes, the stability of the monomer itself it also crucial for this type of growth since a high monomer concentration is required to overcome the energy barrier (thermodynamic equilibrium) and allows for the reaction to be under kinetic control.[24, 29]

Shape control is a result of the crystalline nature of the NC surface leading to its faceted nature. Both the zinc blende and wurtzite crystal structures of metal chalcogenide NCs can undergo surface strain effects leading to specific shape engineering. Based on the energetic favorability of the different crystal facets, they interact with the binding head of the surface passivating ligands enabling the shape control.[33, 34] By bonding with the metal sites on the NC surface and subsequently reducing the surface charge, the surface passivating ligand act as stabilizers and reduce the surface energy of the NCs.[35] The interface of the NC surface and the surface ligands is known to be highly dynamic and parameters such as temperature, the binding strength between the metal site and ligand binding moiety, ligand induced steric hindrances, and any ligand solvent interactions. During NC growth, equilibrium exists between the ligands bound to the surface and those remaining free. This equilibrium causes a continuous exchange and the

rate of this exchange is inversely proportional to the ligand's binding strength. Additionally, during NC growth, there is completion between thermodynamic and kinetic forces and this self-exchange process can affect the growth rate of individual crystal facets.[36] Interactions resulting in a strong bond between the surface facet and the ligand will lead to hindered growth in that respective direction.[37] As a consequence of this, different surface passivating ligands are employed in the synthesis to alter the growth kinetics in different axes of the NC.

One of the most significant results of the quantum confinement phenomenon is the shape-dependent optoelectronic properties of semiconductor NCs.[38, 39] Depending on the dimension of the NC, the confining of the exciton (bound electron-hole pair) results in a specific band gap. An additional contribution to the tuning of the band gap is the number of dimensions that the NC can be confined in. This includes three dimensions (NCs), two dimensions (nanoplates and nanorods), and one dimension (nanowires).[40] Typically, as the number of confined dimensions increases, so does the degree of electronic (exciton) confinement and subsequent larger range of band gap tunability.[41] Therefore, NCs, due to having the largest range of tunability, have attracted the most attention and are more commonly utilized for various applications. Even though they do not the greatest range of variability, elongated structures have demonstrated the ability to have a significant energy separation between the absorption and emission maxima, shown by a larger Stokes shift, which results in reduced reabsorption for fluorescence based applications.[42, 43]

Another parameter that impacts the shape of the NCs is the reactivity of the precursors during the synthesis.[35, 44] By increasing the reactivity of the precursors,

and subsequently increasing the monomer concentrations, it is possible to induce anisotropic growth of the NCs. This increase in monomer concentrations allows the thermodynamic energy barrier to be overcome and growth in additional directions off various crystal facets is permitted.

The shape of the NC also influences the number of atoms present on the surface and can dictate the most efficient application for that type of NC. In the case of spherical NCs, given that they possess the smallest number of total surface atoms and are the most thermodynamically stable, are most applicable in bio-imaging since the stability of the NC is crucial. On the other hand, elongated structures, such as quantum wires and platelets, are ideal for applications where the charge carriers interact with their surrounding environment since a larger portion of their atoms reside on the surface. These applications include redox chemistry, energy transfer, and photocatalysis.[45, 46]

The precise control of NC shape allows for an abundance of unique optical and electronic properties, and even now some of these have yet to be fully explored and understood. Additionally, the techniques used for shape control of one type of semiconductor NC do not always translate to another system[37]. This is because not only do ligand-ligand and ligand-solvent interactions play a critical role in these mechanisms, but interactions between the NCs themselves are also important.

1.3.1 Mechanisms of Shape Control

There have been three main mechanisms proposed to explain how NCs transform into anisotropic structures; classical crystal growth, oriental attachment, and mesoscale assembly (shown in Figure 1.4). The process of classical crystal growth occurs through monomer-monomer addition to the template structure through the dissolution of unstable

precursors and the reformation of the more stable, larger structure.[47] This chemical growth involves the precipitation of solid crystals form the solution.[48] A complete understanding of the parameters that control this precipitation, such as solvent and surface passivating ligands, can improve the engineering of specific shapes and sizes. In the case of a given solvent, there will be varying levels of solubility of the individual precursors. For NC growth and formation occur, the solution must be supersaturated with the required precursors, which can require the use to high temperatures. Nucleation of the monomers continues as long as the concentration of the growth species is greater than the minimum concentration for nucleation. Once the concentrations decreases below this level, nucleation stops, but growth still continues.[49] Uniformity and a small size distribution are achieved with a short nucleation period preceding a self-shapening growth step. It is at this time when kinetics can control the size focusing.[48] Smaller particles grow more rapidly due to the fact that they have a lower free energy driving force. Once the nucleation process is stopped, due to the depletion of reactants, either

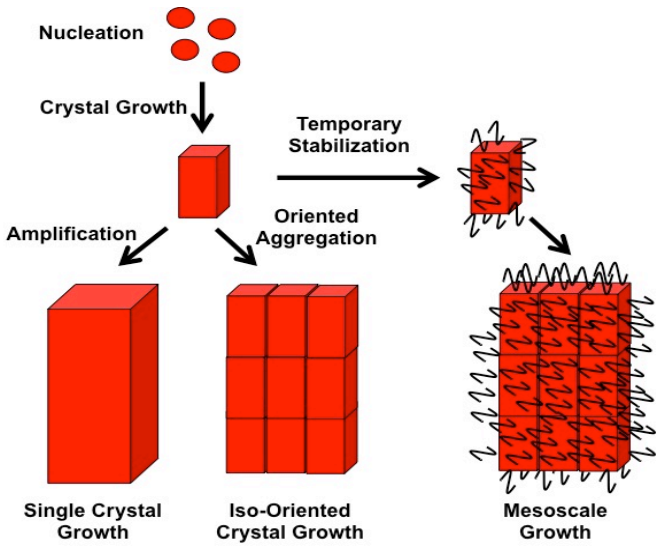

Figure 1.4. The three various mechanisms of shape control; classic crystal growth, oriented attachment, and mesoscale assembly. Based on figure in Colfen et al.[7]

Oswald ripening or defocusing can occur. In this instance, the larger size NCs will continue to grow and may even join together to form two-dimensional structures.[50-52] However, the size distribution at this stage is much broader and more difficult to control, making this not an ideal method for NC shape control.

In the mechanism of oriented attachment, isotropic NCs serve as a precursor to anisotropic growth.[53] The growth of anisotropic NCs from oriented attachment is unique because it results from continued growth along one axis. This unilateral growth is a powerful tool that has been used for the successful synthesis of nanowires and nanorings. It has been proposed that oriented attachment progresses through the reconstruction of the isotropic NC surface in a effort to reduce surface energy. Furthermore, the majority of original NCs have been found to be metal rich, and therefore have intrinsically reduced dipole moments. It is therefore beneficial to explore other growth and formation mechanisms to produce more relevant processes.

Mesoscale assembly is the last growth mechanism discussed for growth and formation of one- and two-dimensional structures. This method accurately permits uniform and controlled growth with ideal conditions such as: low temperatures (70-140°C) and organic solvents. Additionally, magic-sized CdSe NCs act as the nuclei and growth is driven by high monomer concentration in reaction mixture as well as the hydrophobic or van der Waals interaction with the surface passivating ligands.

It is expected that a monomer with a highly uniformed size and shape will translate to a high degree of crystallographic coherence of the final structure as a result of more efficient epitaxial packing and matching.[54] However, these effects are dependent on the degree of balance between attractive van der Waal and repulsive electrostatic

interactions. If one of these forces is more dominant, the initial orientations of the nuclei may be irreversibly fixed.[55] It is also known that both the solvent and surface ligands present can either promote or inhibit growth on distinct crystal facets. One instance of this is in the case of polymers, which are known to induce aggregation through surface binding or interparticle bridging (enthalpic effects).[56] Organic surfactants or surface ligands are known to have steric, van der Waal, or hydrophobic-hydrophilic interactions from the ligand chains can induce shape control during the growth process.[7]

The precursors for this type of assembly are spherical NCs and the assembled structures are either one-, two- or three-dimensions with a tightly packed crystal lattice. In most previously studied systems, the assembly is driven by the hydrophobic interactions between the organic surface-passivating ligands and adjacent and neighboring NCs.[7] The surface of these NCs have low curvature so the hydrophobic forces are strengthened by the collective intermolecular interactions and growth into structures such as rods and platelets, which have reduced curvature, are a more favorable transition. Additionally, a strong driving force exists though the decrease of energy when going from a disordered to ordered system.

In systems where anisotropic structures form through mesoscale assembly, it has been reported that the NCs themselves can become ordered by the interactions of the surface passivating ligands. When the NC structures become so stable that no further growth is favored, but the binding affinity between the organic molecules at the NC interfaces leads to additional arrangement of structures.[7] This is most commonly seen in systems in which the NCs have a high degree of shape anisotropy, and the NCs can

impulsively assemble into complex and higher ordered superstructures.[7] Since this phenomenon was first observed, it has been a key objective of nanotechnology research.

1.4 Effect of Surface Chemistry on Optoelectronic Properties

The optoelectronic properties are often a combination of several contributing factors. For example, as the size of the NC decreases, there is a subsequent increase in the atoms that reside on the NC surface. A larger surface area often results in incomplete surface passivation and a lowering of the PLQY.[45] Another consequence of ultrasmall size is the appearance of two fluorescence emission bands. The first, at a higher energy, is a band edge emission resulting from direct excitation and recombination. The second, at a lower energy, is a broad-band emission and is a result of mid-gap defect sites on the NC surface. In the case of CdSe NCs, these trap sites are a consequence of Se^{2-} facets that do not bind to the ligands commonly used in the synthetic methods and therefore have empty sp^3 orbitals.[57] There has been previous work done demonstrating that these Se sites can be passivated with excess Cd^{2+} ions and subsequent enhancement of emission properties. The cadmium atoms on the surface can also interact with surface passivating ligands through orbital mixing. However, in an instance of insufficient surface passivation, the resulting "dangling orbitals" can trap charge carriers leading to a higher rate of nonradiative recombination and loss of PLQY.[57, 58] Typically, to offset these effects, as well as to enhance solubility and stability, molecules such as amines, phosphines, thiols, and carboxylic acids, which bind strongly with cadmium, are employed as surface passivating ligands. These molecules absorb to the NC surface through metal-ligand interactions.[17]

1.5 Strongly Confined NCs

In ultrasmall NCs have radius that are less than that of their Bohr radius resulting in the phenomenon of quantum confinement.[16, 59] Different radii produce various levels of quantum confinement and different energy levels of the highest occupied molecular orbital (HOMO) and lowest unoccupied molecular orbital (LUMO) of the NCs.[39, 60] Since these are ultrasmall NCs and therefore have fewer atoms on the surface and subsequently fewer orbitals causing the discrete energy levels.[16, 39, 60] The ability of the electronic transition dipoles of the NCs to interact with light, in the same way that molecules can, leads to to the description of "molecule-like" NCs. In 1984, Brus first described how the quantum confinement effect is material dependent. Brus was the first to propose a theoretical calculation that takes into account how both size and material affect the quantum confinement and demonstrate that as the size increases, the band gap will decrease.[39, 61]

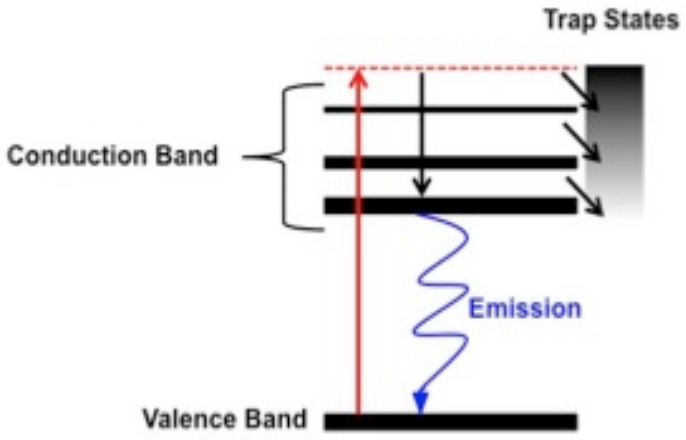

Figure 1.5 The origin of trap state emission. After the absorption of energy, an electron is excited from the valence band to the conduction band. In the case of a partially passivated surface, there exist surface related trap states. Instead of direct radiative recombination (band edge emission), the electron can get stuck in one of these trap states resulting in emission from a variety of lower energy levels, contributing to a broad band emission.

This equation, used to predict the band gap using the wave function to define the spherical volume is found below. In the equation used to calculate the theoretical band gap energy of a semiconductor NC, $E_{g(SNC)}$, ; $E_{g(bulk)}$ is defined as the band gap energy of the bulk matierl, R is defined as the radius of the NC, m_e^* is the effective mass of the excited eletrcon, m_h^* is the effective mass of the excited hole, h is Planck's constant, ε_0 is the permittivity of the vacuum, and ε_r is the relative permittivity .[39, 62] The second term in the equation demonstrates that the radius is inversely proportional to the theoretical band gap of the NC. The subtraction term shows the contribution to the band gap energy from the coulombic interaction forces of the NC. It is also evident that this term is inversely proportional to he radius as well[39].

$$E_{g(SNC)} = E_{bulk} + \frac{\hbar^2}{8R^2}\left(\frac{1}{m_e^*} + \frac{1}{m_h^*}\right) - \frac{1.786e^2}{4\pi\varepsilon_0\varepsilon_r R^2}$$

1.5.1 Wave Functions

The strongly confined nature of the NCs results in their electrons taking on a wave-like nature. These electrons are thought of in terms of a wave function, which is a "mathematical function used in quantum mechanics to propagate a wave associated with a particle using Schrodinger's equation".[63] Assuming a particle in a box model, the wave function can be simplified and solved yielding all of the wave functions have a amplitude of zero at the boundary of confinement. These values correspond to the discrete energy levels of the HOMO and LUMO.[64]

It is the wave function that makes it possible for the electronic applications of semiconductor NCs by allowing the transport of excitons.[65-67] The smaller the NC, the greater the kinetic energy of the exciton and in cases where the kinetic energy is greater

than that of coulombic interaction energy of the electron hole pair, delocalization of the wave function is more probable. Hence, as the diameter of the NC decreases, the wave function of the exciton can easily fill up the core and further extend outside of the boundary into the surrounding monolayer of the surface passivating ligands.[67, 68] In some cases, the wave function can extend past the ligand monolayer and interact with the wave functions of neighboring NCs called excitonic coupling.[66, 69] This delocalization of the wave function is limited to smaller (< 2 nm diameter) NCs. In the case of larger (> 2 nm diameter) NCs, the wave function is confined to the core and cannot extend outside the boundary resulting in no delocalization effects. The extent of the delocalization is also dependent on the nature and identity of the surface passivating ligands.[66, 69]

1.5.2 Exciton Delocalization

As previously stated, the identity of the surface passivating ligand can impact the delocalization of the excitonic wave function. Exciton delocalization is the process of the exciton wave function extending outside the core boundary. During this process, the exciton is temporary "displaced" from the ground state of the core, lowering the band gap energy of the NC and resulting in a red shift of the first excitonic peak in the absorption spectra.[70, 71] Due to its importance in electronic device fabrication, exciton delocalization has been of great interest to many groups such as Weiss, Fenkel, and Wannier.[67, 70, 71] These photoexcited excitons can dissociate into free carriers (electrons and holes) and used in photovoltaic devices or the bound excitons, which emit light, can be used in other applications such as lasers.[16, 72] The determination of whether the excitons are considered bound or free carriers is determined by electron-hole interactions, specifically those of the expansion of the wave function. If the interactions

are considered negligible, then the electron-hole pairs are considered free carriers. However, in a case where the attractive coulombic forces bind the electron-hole pair, they are considered a bound exciton. In the nanoscale, the dimensions of the material have the greatest impact on the delocalization. As previously discussed, in strongly confined NCs, the kinetic energy of the exciton is greater than that of the coulombic interaction of the electron-hole pair. Considering this, strongly confined NCs are an ideal system to investigate how surface chemistry affects the exciton delocalization,

1.6 Applications of Semiconductor NCs

The unique optical and electronic properties of strongly confined NCs have resulted in a great deal of interest in the development of solid-state devices fabricated with these materials. These applications include light emitting diodes (LEDs), phototdetectors, photocatalysts, field-effect transistors (FETs), and photovoltaics. [73] The applications that have received the most attention are the solid-state device applications of LEDs, FETs, and photovoltaics. This is due in part to the narrow emission bands of the SNCs and their enhanced stability over their bulk counterparts.[74] These devices work on the operating principle of the quantum confined NCs interacting with light via the transition dipoles. As opposed to a molecule where the wave function is localized in a smaller area, the NCs wave function is spread out over a number of unit cells. This is an advantage for the solid-state applications since the delocalized wave function has a lower probability density at the NC surface. Therefore, the NCs have the capability to have a near unity quantum yield and are less likely to undergo quenching.[74] One of the most promising examples of using SNCs as white-light emitting LEDs was by Rosenthal in 2010, when the authors demonstrated that ultrasmall

NCs (diameter < 2 nm) could emit pure white light. This showed the ability of these materials to impact the energy market and fueled the fabrication of semiconductor-based LEDs across the entire color spectrum with consistently improving efficiencies. Similarly, in the field of FETs the advancement of semiconductor NCs, specifically PbSe, has been instrumental in allowing for the development of low cost devices.[75]

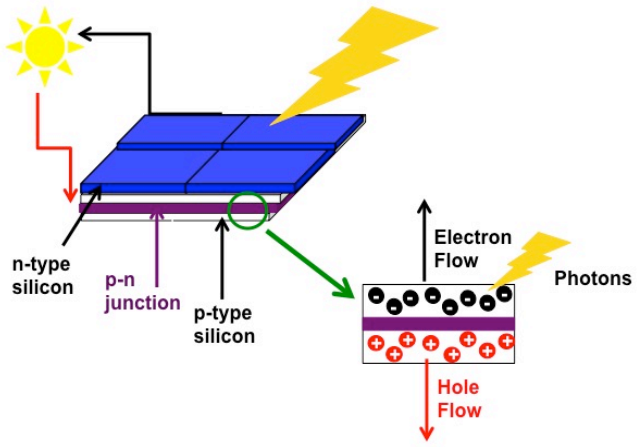

Figure 1.6: The working principle of a solar cell. The photons from the sun generate electron hole pairs in the photoactive material. The charges are separated by the p-n junction and driven to either the cathode (electrons) or anode (holes).

The most studied application for semiconductor NCs however, is in photovoltaic devices. The early research in solar cells began nearly over 150 years ago when the first interactions between semiconductors and solar light were observed.[76] This lead to the basis of what is now considered the photovoltaic effect, or the ability to turn light into electrical power. In a photovoltaic device, photons are absorbed by the semiconductor material which produces electron-hole pairs. These pairs then diffuse to the junction where the charges are separated and transported to either the cathode (electrons) or anode (holes) as shown in Figure 6. By understanding this process, it is possible to engineer semiconductors that have ideal band gap energies to enhance the efficiency of the device.

Currently, the quantum dot-sensitized solar cells have the best reported efficiencies and work by injecting the electrons from the semiconductor NC into a large band gap semiconductor (such as TiO_2) and employs a hole scavenger to complete the redox process.[77] Additionally, metal chalcogenides have been the most common semiconductor used as an intermediate energy level, to generate the electron-hole pairs, in solar cells. This is due to their large Stokes shifts or separation between the absorption and emission maximas, which help to reduce light reabsorption. However, the class of materials known as pervoskites has become a candidate for the next generation of solar cells.

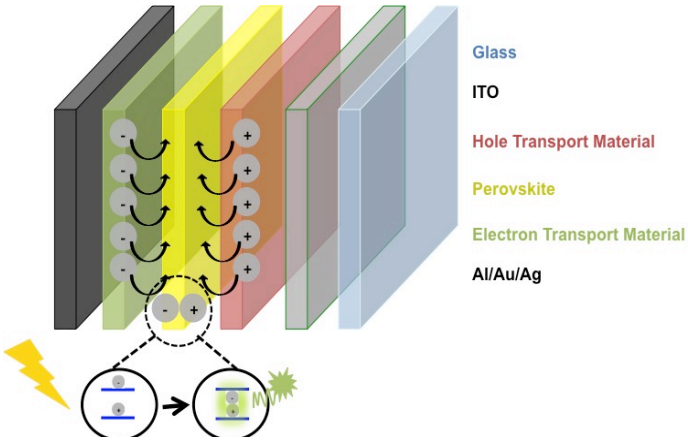

Figure 1.7 The device architecture of a perovskite-based LED device. Carriers (electrons and holes) are injected into the emitter (perovskite) and confined to promote radiative recombination. Based on figure in Veldhues et al[8]

In the 1990's, methyl ammonium lead halide ($CH_3NH_3PbX_3$) materials were investigated for use in FETs[26, 78] and LEDs.[79, 80] The first example of a perovskite-based solar cell was in 2009 and yielded an efficiency of only 3%.[25] In addition to this low efficiency, these first solar cells also presented low stability and as a result, the material received little further attention. This remained until 2012 when the first examples of a solid-state device were reported with efficiencies increasing to near

10%.[81, 82] After that, the field exploded and this increase in research efforts resulted in a reported solar cell efficiency of >21% by 2015. The speed of progress and advancement in this application is extraordinary considering the time frame from the first reported device to where the field is now. This advancement is much greater than any previous generation of solar cell device and can be attributed to factors including the less expensive fabrication cost, ease of manufacturing and processing, and the outstanding optoelectronic properties of the perovskite materials compared to the current silicon and dye-sensitized solar cell devices.[83-86] The first reports of using perovskite materials in LEDs[87, 88] and laser[89] applications were in the early 1990's. This reports used bulk crystals as well as layering various compositions of perovskite. By employing the layered materials, the authors reported enhanced stability in addition to the ability to tune the optical properties as a result of the various halides or organic cations.[90] However, the limitations of the synthetic methods stalled the development of these applications until 2014.[91] This was when the first solution-based synthesis were reported. These procedures, done at room temperature offered a lower-cost alternative to large-scale optoelectric applications. The device architecture of a perovskite-based LED is shown in Figure 7. By tuning the halide composition, the emission can spread over a range of colors and had early efficiencies of about 0.4%[92] and have increased to 8%[93]. There have also been reports employing Cs-based materials[94] and various shaped NCs (nanoparticles, nanoplates, and nanowires)[95-97] rather than thin films of bulk materials.

1.7 Purpose and Specific Aims of This Thesis

The purpose of this work is to develop a better understanding of how the unique aspects of surface chemistry control the shape and optoelectronic properties of direct

band gap semiconductor NCs. This investigation was comprised of four specific aims; (1) the synthesis of structurally well-defined perovskite NCs; (2) the development of a facile gram scale synthesis of metal chalcogenide anisotropic NCs; (3) the investigation of surface ligand chemistry on optoelectronic properties of semiconductor NCs; and (4) the surface controlled white-light emission of perovskite NCs.

In Chapter 2, we investigate a new and up and coming class of materials of $CH_3NH_3PbX_3$ perovskite NCs. The ability to control the shape is a result of surface chemistry modification, reaction temperature, and finally the solvent system. Through this work it was determined that the critical parameters for the formation of quantum platelets were the presence of chlorinated solvent and a long chain amine, where as the formation of the quantum cubes was kinetically driven. Finally, the quantum wires require a long chain acid to drive the mesoscale assembly. The quantum wires and platelets were also found to assemble into bundles and stacks. Through this investigation, it was determined that the long chain amine is responsible for the ordered stacking of the quantum platelets and the long chain acid drives the bundling of the quantum wires.

In Chapter 3, we further investigate how shape controlled the optoelectronic properties of metal chalcogenide semiconductor NCs. This report started by developing a synthetic method to produce quantum wires, quantum rods, and quantum platelets using cadmium and zinc as a metal precursor and selenium and sulfur as a chalcogenide precursor. Additionally, the method developed has the advantages of being phosphine free, low temperature, and can be performed at the gram scale. This project provided a complete understanding of how the growth and formation mechanism is dependent on precursor identity and the surface passivating ligand.

Next in Chapter 4 we examined how various properties of the surface passivating ligands (functional group substitution, level of conjugation, and binding mode and head group) affect the exciton delocalization. It was hypothesized that with our system of strongly confined $(CdSe)_{34}$ NCs we would observe a significant increase in the delocalization effects. We investigated this by first using a known class of ligands, para-substitued phenyldithiocarbamate (X-PDTC), and observed an unpresidented shift of 610 meV in the first excitonic peak. This was compared to previous reports of ~200 meV using the same class of ligands with larger NCs (diameters > 2 nm). We next examined different parameters of the ligand such as level of conjugation, binding mode and head group to examine what effect these had on exciton delocalization. We observed an even greater shift of 650 meV after exchanging the native ligands with pyrene dithiocarbamate (py-DTC). We further hypothesized that the observed delocalization was in fact hole delocalization between the HOMO of the $(CdSe)_{34}$ NCs and the HOMO of the surface passivating ligand. Through this investigation it was also determined that the energy level match between the HOMO of the NC and the HOMO of the surface passivating ligand is not the only parameter to consider, but that the characteristics of the ligand also play a role.

Finally, in Chapter 5 we continue our work with methyl ammonium lead bromide perovskite NCs but tailor the surface chemistry to engineer white-light emission. We developed the first low temperature, colloidal synthesis to prepare ultrasmall (~1.5 nm diameter) $CH_3NH_3PbBr_3$ perovskite NCs, which emit pure white-light. The emission properties of the NCs were improved through precise manipulation of surface halide ions that resulted in large quantum yields of ~12% and radiative lifetime of ~20 ns.

1.8 References

1. Cölfen, H. and S. Mann, *Higher‐order organization by mesoscale self‐assembly and transformation of hybrid nanostructures.* Angewandte Chemie International Edition, 2003. **42**(21): p. 2350-2365.
2. Veldhuis, S.A., et al., *Perovskite Materials for Light‐Emitting Diodes and Lasers.* Advanced Materials, 2016. **28**(32): p. 6804-6834.
3. Fujishima, A., *Electrochemical photolysis of water at a semiconductor electrode.* nature, 1972. **238**: p. 37-38.
4. Park, N.-G., *Organometal perovskite light absorbers toward a 20% efficiency low-cost solid-state mesoscopic solar cell.* The Journal of Physical Chemistry Letters, 2013. **4**(15): p. 2423-2429.
5. Scholes, G.D. and G. Rumbles, *Excitons in nanoscale systems.* Nature materials, 2006. **5**(9): p. 683-696.
6. Murray, C., D.J. Norris, and M.G. Bawendi, *Synthesis and characterization of nearly monodisperse CdE (E= sulfur, selenium, tellurium) semiconductor nanocrystallites.* Journal of the American Chemical Society, 1993. **115**(19): p. 8706-8715.
7. Herron, N., et al., *Crystal structure and optical properties of Cd32S14 (SC6H5) 36. DMF4, a cluster with a 15 Angstrom CdS core.* Science, 1993. **259**(5100): p. 1426-1428.
8. Soloviev, V., et al., *Size-dependent optical spectroscopy of a homologous series of CdSe cluster molecules.* Journal of the American Chemical Society, 2001. **123**(10): p. 2354-2364.
9. Gur, I., et al., *Air-stable all-inorganic nanocrystal solar cells processed from solution.* Science, 2005. **310**(5747): p. 462-465.
10. Qu, L., Z.A. Peng, and X. Peng, *Alternative routes toward high quality CdSe nanocrystals.* Nano Letters, 2001. **1**(6): p. 333-337.
11. Landes, C., et al., *Observation of large changes in the band gap absorption energy of small CdSe nanoparticles induced by the adsorption of a strong hole acceptor.* Nano letters, 2001. **1**(11): p. 667-670.
12. Peng, Z.A. and X. Peng, *Mechanisms of the shape evolution of CdSe nanocrystals.* Journal of the American Chemical Society, 2001. **123**(7): p. 1389-1395.
13. Peng, Z.A. and X. Peng, *Nearly monodisperse and shape-controlled CdSe nanocrystals via alternative routes: nucleation and growth.* Journal of the American Chemical Society, 2002. **124**(13): p. 3343-3353.
14. Kojima, A., et al., *Organometal halide perovskites as visible-light sensitizers for photovoltaic cells.* Journal of the American Chemical Society, 2009. **131**(17): p. 6050-6051.
15. Mitzi, D.B., K. Chondroudis, and C.R. Kagan, *Organic-inorganic electronics.* IBM journal of research and development, 2001. **45**(1): p. 29-45.
16. Buckley, J.J., et al., *Chalcogenol Ligand Toolbox for CdSe Nanocrystals and Their Influence on Exciton Relaxation Pathways.* ACS nano, 2014. **8**(3): p. 2512-2521.

17. Lilly, G.D., et al., *Switchable photoconductivity of quantum dot films using cross-linking ligands with light-sensitive structures.* Journal of Materials Chemistry, 2011. **21**(31): p. 11492-11497.
18. Mullin, J.W., *Crystallization*. 2001: Butterworth-Heinemann.
19. Peng, X., *Mechanisms for the Shape‐Control and Shape‐Evolution of Colloidal Semiconductor Nanocrystals.* Advanced Materials, 2003. **15**(5): p. 459-463.
20. Cho, K.-S., et al., *Designing PbSe nanowires and nanorings through oriented attachment of nanoparticles.* Journal of the American Chemical Society, 2005. **127**(19): p. 7140-7147.
21. Yu, J.H., et al., *Synthesis of quantum-sized cubic ZnS nanorods by the oriented attachment mechanism.* Journal of the American Chemical Society, 2005. **127**(15): p. 5662-5670.
22. Bealing, C.R., et al., *Predicting nanocrystal shape through consideration of surface-ligand interactions.* ACS nano, 2012. **6**(3): p. 2118-2127.
23. Puzder, A., et al., *The effect of organic ligand binding on the growth of CdSe nanoparticles probed by ab initio calculations.* Nano Letters, 2004. **4**(12): p. 2361-2365.
24. Hughes, B.K., J.M. Luther, and M.C. Beard, *The Subtle Chemistry of Colloidal, Quantum-Confined Semiconductor Nanostructures.* ACS Nano, 2012. **6**(6): p. 4573-4579.
25. Adair, J.H. and E. Suvaci, *Morphological control of particles.* Current opinion in colloid & interface science, 2000. **5**(1): p. 160-167.
26. Wise, F.W., *Lead salt quantum dots: the limit of strong quantum confinement.* Accounts of Chemical Research, 2000. **33**(11): p. 773-780.
27. Bawendi, M.G., M.L. Steigerwald, and L.E. Brus, *The quantum mechanics of larger semiconductor clusters (" quantum dots").* Annual Review of Physical Chemistry, 1990. **41**(1): p. 477-496.
28. Brus, L.E., *Electron–electron and electron‐hole interactions in small semiconductor crystallites: The size dependence of the lowest excited electronic state.* The Journal of chemical physics, 1984. **80**(9): p. 4403-4409.
29. Smith, A.M. and S. Nie, *Semiconductor Nanocrystals: Structure, Properties, and Band Gap Engineering.* Accounts of Chemical Research, 2010. **43**(2): p. 190-200.
30. Sun, J., L.-W. Wang, and W.E. Buhro, *Synthesis of cadmium telluride quantum wires and the similarity of their effective band gaps to those of equidiameter cadmium telluride quantum dots.* Journal of the American Chemical Society, 2008. **130**(25): p. 7997-8005.
31. Ithurria, S. and B. Dubertret, *Quasi 2D colloidal CdSe platelets with thicknesses controlled at the atomic level.* Journal of the American Chemical Society, 2008. **130**(49): p. 16504-16505.
32. Scher, E.C., L. Manna, and A.P. Alivisatos, *Shape control and applications of nanocrystals.* Philosophical Transactions of the Royal Society of London A: Mathematical, Physical and Engineering Sciences, 2003. **361**(1803): p. 241-257.

33. Ruberu, T.P.A., et al., *Molecular control of the nanoscale: effect of phosphine–chalcogenide reactivity on CdS–CdSe nanocrystal composition and morphology.* ACS nano, 2012. **6**(6): p. 5348-5359.
34. Amirav, L. and A.P. Alivisatos, *Photocatalytic hydrogen production with tunable nanorod heterostructures.* The Journal of Physical Chemistry Letters, 2010. **1**(7): p. 1051-1054.
35. Huynh, W.U., J.J. Dittmer, and A.P. Alivisatos, *Hybrid nanorod-polymer solar cells.* science, 2002. **295**(5564): p. 2425-2427.
36. Dirksen, J. and T. Ring, *Fundamentals of crystallization: kinetic effects on particle size distributions and morphology.* Chemical Engineering Science, 1991. **46**(10): p. 2389-2427.
37. Zhang, Q., S.-J. Liu, and S.-H. Yu, *Recent advances in oriented attachment growth and synthesis of functional materials: concept, evidence, mechanism, and future.* Journal of Materials Chemistry, 2009. **19**(2): p. 191-207.
38. Cao, G., *Synthesis, properties and applications*. 2004: World Scientific.
39. Oaki, Y. and H. Imai, *The hierarchical architecture of nacre and its mimetic material.* Angewandte Chemie International Edition, 2005. **44**(40): p. 6571-6575.
40. Oaki, Y. and H. Imai, *Nanoengineering in echinoderms: the emergence of morphology from nanobricks.* Small, 2006. **2**(1): p. 66-70.
41. Rousseau, M., et al., *Multiscale structure of sheet nacre.* Biomaterials, 2005. **26**(31): p. 6254-6262.
42. Tang, Z., N.A. Kotov, and M. Giersig, *Spontaneous organization of single CdTe nanoparticles into luminescent nanowires.* Science, 2002. **297**(5579): p. 237-240.
43. Jongen, N., et al., *Precipitation of self-organized copper oxalate polycrystalline particles in the presence of hydroxypropylmethylcellulose (HPMC): control of morphology.* Journal of Colloid and Interface Science, 2000. **226**(2): p. 189-198.
44. Banfield, J.F., et al., *Aggregation-based crystal growth and microstructure development in natural iron oxyhydroxide biomineralization products.* Science, 2000. **289**(5480): p. 751-754.
45. Fleer, G. and C. Stuart, *MA; Scheutjens, JMHM; Cosgrove, T.; Vincent, B.* Polymers at interfaces, 1993. **2**.
46. Underwood, D.F., T. Kippeny, and S.J. Rosenthal, *Ultrafast carrier dynamics in CdSe nanocrystals determined by femtosecond fluorescence upconversion spectroscopy.* The Journal of Physical Chemistry B, 2001. **105**(2): p. 436-443.
47. Pokrant, S. and K.B. Whaley, *Tight-binding studies of surface effects on electronic structure of CdSe nanocrystals: the role of organic ligands, surface reconstruction, and inorganic capping shells.* The European Physical Journal D-Atomic, Molecular, Optical and Plasma Physics, 1999. **6**(2): p. 255-267.
48. C., A.N. 2014: Columbia University.
49. Chamarro, M., et al., *Enhancement of electron-hole exchange interaction in CdSe nanocrystals: A quantum confinement effect.* Physical review B, 1996. **53**(3): p. 1336.

50. Chukwuocha, E.O., M.C. Onyeaju, and T.S. Harry, *Theoretical studies on the effect of confinement on quantum dots using the brus equation.* 2012.
51. Kovalenko, M.V., M. Scheele, and D.V. Talapin, *Colloidal nanocrystals with molecular metal chalcogenide surface ligands.* Science, 2009. **324**(5933): p. 1417-1420.
52. Green, M., *A new approach to the formal classification of covalent compounds of the elements.* Journal of organometallic chemistry, 1995. **500**(1): p. 127-148.
53. Tsybeskov, A.L.E.D.J.L.L., *Semiconductor Nanocrystals*. Nanostructure Science and Technology. 2003: Springer US.
54. Colvin, V., M. Schlamp, and A.P. Alivisatos, *Light-emitting-diodes made from cadmium selenide nanocrystals and a semiconducting polymer.* Nature, 1994. **370**(6488): p. 354-357.
55. Kamat, P.V., et al., *Beyond photovoltaics: semiconductor nanoarchitectures for liquid-junction solar cells.* Chemical reviews, 2010. **110**(11): p. 6664-6688.
56. Knowles, K.E., et al., *Chemical control of the photoluminescence of CdSe quantum dot– organic complexes with a series of para-substituted aniline ligands.* Journal of the American Chemical Society, 2009. **132**(3): p. 1041-1050.
57. Dolai, S., et al., *Isolation of bright blue light-emitting CdSe nanocrystals with 6.5 kDa core in gram scale: high photoluminescence efficiency controlled by surface ligand chemistry.* Chemistry of Materials, 2014. **26**(2): p. 1278-1285.
58. Lee, J.-S., et al., *Band-like transport, high electron mobility and high photoconductivity in all-inorganic nanocrystal arrays.* Nature nanotechnology, 2011. **6**(6): p. 348-352.
59. Frenkel, J., *On the transformation of light into heat in solids. I.* Physical Review, 1931. **37**(1): p. 17.
60. Wannier, G.H., *The structure of electronic excitation levels in insulating crystals.* Physical Review, 1937. **52**(3): p. 191.
61. Gregg, B.A., *Excitonic solar cells.* The Journal of Physical Chemistry B, 2003. **107**(20): p. 4688-4698.
62. Ahn, N., et al., *Highly reproducible perovskite solar cells with average efficiency of 18.3% and best efficiency of 19.7% fabricated via Lewis base adduct of lead (II) iodide.* Journal of the American Chemical Society, 2015. **137**(27): p. 8696-8699.
63. Nirmal, M. and L. Brus, *Luminescence photophysics in semiconductor nanocrystals.* Accounts of Chemical Research, 1999. **32**(5): p. 407-414.
64. Talapin, D.V. and C.B. Murray, *PbSe nanocrystal solids for n-and p-channel thin film field-effect transistors.* Science, 2005. **310**(5745): p. 86-89.
65. Brongersma, M.L., N.J. Halas, and P. Nordlander, *Plasmon-induced hot carrier science and technology.* Nature nanotechnology, 2015. **10**(1): p. 25-34.
66. Bang, J.H. and P.V. Kamat, *Quantum dot sensitized solar cells. A tale of two semiconductor nanocrystals: CdSe and CdTe.* ACS nano, 2009. **3**(6): p. 1467-1476.

67. Chondroudis, K. and D.B. Mitzi, *Electroluminescence from an organic-inorganic perovskite incorporating a quaterthiophene dye within lead halide perovskite layers.* Chemistry of materials, 1999. **11**(11): p. 3028-3030.
68. Mitzi, D.B., *Synthesis, crystal structure, and optical and thermal properties of (C4H9NH3) 2MI4 (M= Ge, Sn, Pb).* Chemistry of materials, 1996. **8**(3): p. 791-800.
69. Mitzi, D.B., M. Prikas, and K. Chondroudis, *Thin film deposition of organic-inorganic hybrid materials using a single source thermal ablation technique.* Chemistry of materials, 1999. **11**(3): p. 542-544.
70. Kim, H.-S., et al., *Lead iodide perovskite sensitized all-solid-state submicron thin film mesoscopic solar cell with efficiency exceeding 9%.* Scientific reports, 2012. **2**: p. 591.
71. Lee, M.M., et al., *Efficient hybrid solar cells based on meso-superstructured organometal halide perovskites.* Science, 2012. **338**(6107): p. 643-647.
72. Gao, P., M. Grätzel, and M.K. Nazeeruddin, *Organohalide lead perovskites for photovoltaic applications.* Energy & Environmental Science, 2014. **7**(8): p. 2448-2463.
73. Green, M.A., A. Ho-Baillie, and H.J. Snaith, *The emergence of perovskite solar cells.* Nature Photonics, 2014. **8**(7): p. 506-514.
74. Stranks, S.D. and H.J. Snaith, *Metal-halide perovskites for photovoltaic and light-emitting devices.* Nature nanotechnology, 2015. **10**(5): p. 391-402.
75. Sum, T.C. and N. Mathews, *Advancements in perovskite solar cells: photophysics behind the photovoltaics.* Energy & Environmental Science, 2014. **7**(8): p. 2518-2534.
76. Era, M., et al., *Organic‐inorganic heterostructure electroluminescent device using a layered perovskite semiconductor (C6H5C2H4NH3) 2PbI4.* Applied physics letters, 1994. **65**(6): p. 676-678.
77. Hattori, T., et al., *Highly efficient electroluminescence from a heterostructure device combined with emissive layered-perovskite and an electron-transporting organic compound.* Chemical physics letters, 1996. **254**(1-2): p. 103-108.
78. Kondo, T., et al., *Biexciton lasing in the layered perovskite-type material (C6H13NH3) 2PbI4.* Solid state communications, 1998. **105**(4): p. 253-255.
79. Chondroudis, K. and D.B. Mitzi, *Electroluminescence from an organic–inorganic perovskite incorporating a quaterthiophene dye within lead halide perovskite layers.* Chemistry of materials, 1999. **11**(11): p. 3028-3030.
80. Kieslich, G., S. Sun, and A.K. Cheetham, *Solid-state principles applied to organic–inorganic perovskites: new tricks for an old dog.* Chemical Science, 2014. **5**(12): p. 4712-4715.
81. McMeekin, D.P., et al., *A mixed-cation lead mixed-halide perovskite absorber for tandem solar cells.* Science, 2016. **351**(6269): p. 151-155.
82. Cho, H., et al., *Overcoming the electroluminescence efficiency limitations of perovskite light-emitting diodes.* Science, 2015. **350**(6265): p. 1222-1225.
83. Yantara, N., et al., *Inorganic halide perovskites for efficient light-emitting diodes.* The journal of physical chemistry letters, 2015. **6**(21): p. 4360-4364.

84. Hassan, Y., et al., *Structure‐Tuned Lead Halide Perovskite Nanocrystals.* Advanced Materials, 2016. **28**(3): p. 566-573.
85. Zhang, D., et al., *Solution-phase synthesis of cesium lead halide perovskite nanowires.* Journal of the American Chemical Society, 2015. **137**(29): p. 9230-9233.
86. Zhang, Q., et al., *Room-temperature near-infrared high-Q perovskite whispering-gallery planar nanolasers.* Nano Lett, 2014. **14**(10): p. 5995-6001.

CHAPTER 2. STRUCTURALLY WELL DEFINED PEROVSKITE NANOCRYSTALS

2.1 Synopsis

The unmatched solar energy conversion efficiencies, reported up to 20%, has facilitated the class of organic-inorganic hybrid materials known as perovskites continued growth over the past five years. These materials have the ability to redefine the field of photovoltaics, however the further development of synthetic methods, specifically a complete understanding of their growth and formation kinetics in the colloidal state is required. Here in we report the synthesis of methyl ammonium lead bromide ($CH_3NH_3PbBr_3$) quantum wires (QWs), quantum platelets (QPLs), and quantum cubes (QCs). The ability to tailor the shape is a through the combination of several factors including surface chemistry, reaction temperature, and the solvent system. The investigation began with the synthesis of the QWs, requiring a long chain acid to drive 1D growth and ordering of the wires into bundles. The investigation moved to the QPLs and determined that the critical parameters for the formation were the presence of chlorinated solvent and a long chain amine and finally to the QCs, where the formation was shown to be kinetically driven.

2.2 Introduction

In the last five to seven years, the field of semiconductors has greatly shifted it focus to pervoskites as an ideal material for the fabrication of next generation solar cells and other solid-state devices[15, 84, 98, 99]. To further the expansion of this field, materials with controllable optoelectronic properties, including absorption, emission, and

charge transport, are required for applications including solar cells, LEDs, and lasers. The class of materials known as perovskites have been labeled an excellent candidate for such applications, but the field is still lacking critical information about how shape control and further complex assemblies can enhance these optoelectronic properties.

This class of material has been known since the 1800's when the crystal structure of $CaTiO_3$ was discovered[99], however it wasn't until the 1990's that the $CH_3NH_3PbX_3$ materials were investigated for use in FETs[26, 78] and LEDs[79, 80]. The first example of a perovskite-based solar cell was in 2009 and yielded an efficiency of only 3%[25]. In addition to this low efficiency, these first solar cells also presented low stability and as a result, the material received little further attention. This remained until 2012 when the first examples of a solid-state device were reported with efficiencies increasing to near 10%[81, 82]. After that, the field exploded and these increase research efforts resulted in a reported solar cell efficiency of >21% by 2015. The speed of progress and advancement in this application is extraordinary considering the time frame from the first reported device to where the field is now. This phenomenon, which is much greater than any previous generation of solar cell device, can be attributed to factors included the less expensive fabrication cost, ease of manufacturing and processing, and the outstanding optoelectronic properties of the perovskite materials compared to the current silicon and DSSC devices[83-86].

The first step in this research was to further explore the outstanding charge transport properties of bulk metal halide perovskite materials. When employed in solar cells, they achieved efficiencies exceeding 20%. After the success of the bulk films, the use of 2D materials of metal halide perovskites was also investigated for fabricate

photovoltaic devices, which resulted in enhanced stability of the device. In addition to the enhance stability, reducing the size and increasing the confinement dimensions of these materials also allowed for the enrichment of their optical and electronic properties.

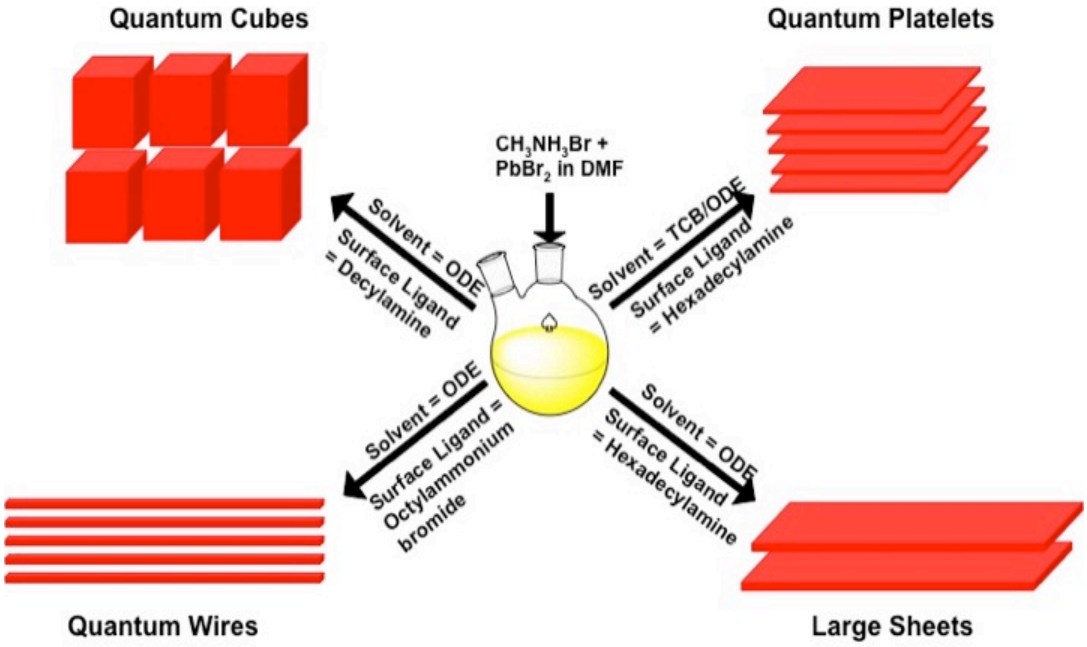

Figure 2.1 Solvent- and surface ligand-dependent shape evolution of $CH_3NH_3PbBr_3$ perovskite nanocrystals. By controlling nucleation and growth parameters through variation of reaction medium, surface ligands, and temperature, the shapes of the nanocrystals are systematically changed yielding a variety of structures: quantum platelets, quantum cubes, spherical nanocrystals, and large sheets

In addition to the enhanced charge transport and quantum yields of these materials, another advantage of this system is the ability to tune their band gap to incorporate different ranges of the solar spectrum. These energies, which vary from 1.5 to 2.3 eV[100, 101], can be tuned by altering the different components of the cation, metal, and halide. By changing the halide, it is possible to tune the absorption and emission properties from the deep ultraviolet to visible region of the spectrum. Currently, the most commonly metal to use in these materials is lead. However, in an effort to make these materials more

environmentally friendly, researchers have examined the possibility of using other metals, such as tin and germanium, that are known to have less toxic effects[102, 103]. The successful synthesis of these lead-free materials have demonstrated no change in the brightness (quantum yield) of these materials, however, the stability of the tin based perovskites requires additional optimization to generate the stability as observed with the lead based materials[104]. It has also been demonstrated that by changing the metal, allows for the tuning of the optical properties into the near IR region.

The tenability of the band gap is not the only quality that has progressed the field of perovskites so quickly. When compared to other current materials used in solar cell fabrication, including Si, CdTe, and CIGS, the optical absorption coefficient of $CH_3NH_3PbI_3$ is larger and therefore the amount of material required to obtain an equivalent efficiency is less and this also lowers the fabrication cost[105, 106]. It has previously stated that these materials have enhanced charge transport properties. This is a consequence of the high carrier (electron and hole) mobility (60 cm^2/Vs) and long lifetimes (~100 ns) which lead to large diffusion lengths (1 um). These factors make it possible for the charge carriers to be transported ~300 nm before electron-hole recombination occurs[107-110].

The majority of the previously discussed devices, using thin film materials of $CH_3NH_3PbX_3$ were fabricated using various deposition methods including both solution- and vapor-based. In this method, the precursor solutions, organic halides (methyl ammonium halide) and lead halides (PbX_2), dissolved in solvents such as DMF or DMSO are spin-coated and then heated to temperatures between 100-150 °C. These single step methods were the first developed and have a highest reported efficiency of 19.7%.

Researchers then investigated how to better control of uniformity and thickness of these films. The leaders in this development were Mitzi and Gretzel, who were able to achieve efficiencies of >15% while the device fabrication was more uniform, reproducible and allowed more control over the grain size. But the trade off for better grain size control is surface smoothness. The larger grain sizes tend to exhibit less surface coverage, which can inhibit the device performance.

Since the first report of a solution based synthesis of colloidal methyl ammonium lead halide perovskite NCs, there has been a critical knowledge gap in the field of how the different properties of surface chemistry can effect shape control. The main driving force to bridge this gap is the fact that anisotriopcially-shaped NCs will provide unique photophysical, electronic, and charge transport properties compared to their bulk counterparts, thus resulting in highly efficient optoelectronic device applications. However, two main questions still need to be addressed; 1) How can we tailor the synthetic conditions to selectively grow anisotropically shaped NCs?, 2) What are their shape-dependent molecular structures and corresponding optoelectronic properties?

Comparing various anisotropic nanostructures such as platelets and rods, nanowires of various materials[111-117] have shown great promise in the fabrication of FETs,[118-120] optoelectronic devices,[116, 117, 121] and sensors[114, 122] because of their unique optical and electronic properties. Nanowires are also able to transport photogenerated charge carriers over a long distance with minimum hopping, which is an ideal electronic property for fabrication of high efficiency solar cells. Over the past two decades, synthetic methods have focused on carbon nanotubes,[123, 124] and metal oxide[116, 125] and semiconductor[126-128] nanowires.

Unlike point-initiated uniaxial growth of metal oxide or semiconductor crystals into nanowire materials,[113, 115, 126, 129] our QW growth was driven by the spontaneous self-organization of spherical perovskite NCs. Our solution-based hybrid organic-inorganic lead bromide QW synthesis is simple and reproducible with remarkable optical and photophysical properties (absorption and emission peaks, quantum yields, and PL lifetimes) that are different from those recently reported for solid-phase crystallization approaches to $CH_3NH_3PbI_3$ nanowire synthesis.[130-132] We suggest that dipole-dipole interactions between spherical NCs and Van der Waals interactions between surface stabilizing ligands drive the mesoscale assembly of spherical NCs into high quality single-crystalline bundles of QWs with high quantum yield and long PL lifetime. Although colloidal synthetic approachs[9, 133] have been attempted for preparation of $CH_3NH_3PbBr_3$ nanowires, control over structure and optical properties, especially as they relate to structural dimensionality, remains key scientific challenges to fully understand the charge transport properties of this new type of nanostructure, specifically for high performance device applications.

After the initial report of the colloidal synthesis, Akkerman et al. synthesized pseudorectangular-shaped, 2D $CsPbX_3$ nanoplatelets.[134]. Similar to other 2D semiconductor QPLs, or quantum belts,[3, 135-141] have gained interest due to their high exciton binding energies and large absorption cross-sections.[142, 143] Furthermore, compared to zero- and one-dimensional NCs, 2D QPLs possess larger lateral dimensions that increase their carrier mean-free path and reduce hopping. 2D QPLs are also expected to increase the photoconversion efficiency of solar cells by minimizing carrier recombination. However, in the literature, few reports are available that demonstrate the

synthesis of large square-shaped $CH_3NH_3PbBr_3$ sheets,[9, 144-146] and those sheets display only poor photoluminescence properties, mainy, low PLQY and high nonradiative rate constants (k_{nr})). Therefore, in order to investigate the structure-property relationships of perovskite QPLs, it is important to design new synthetic methods to prepare NCs of well-defined dimensionality along with enhanced photophysical properties.

Here, we report the formation of ultrathin (<4 unit cell thickness) pseudorectangular-shaped $CH_3NH_3PbBr_3$ QPLs with morphology similar to that reported for CdSe and CdS QPLs,[3, 135, 138, 141] and a colloidal-based, bright-green light emitting, hybrid organic-inorganic $CH_3NH_3PbBr_3$) QWs with aspect ratio as high as 250 and (PL) lifetimes of ~90 ns. Based on our time-dependent microscopy characterization, we hypothesize that both QPL and QW formation is driven by mesoscale-assisted growth of seed NCs that involves cooperative van der Waals interactions between surface passivating ligands. Our small angle X-ray scattering (SAXS) analysis suggests that the stacked QPLs are separated by a layer of ligand on the flat plane (001) of cubic $CH_3NH_3PbBr_3$ perovskite with spacing consistent with a hexadecylamine bilayer, while the bundles of QWs are separated by a layer oleic acid in the bilayer. We have also determined that the presence of a chlorinated cosolvent in the reaction mixture is a prerequisite for the formation of QPLs. Without establishing this experimental condition the result is formation of large sheets of square-shaped $CH_3NH_3PbBr_3$ quantum plates of several hundred nanometers in dimension similar to those reported in the literature.[9, 144, 145] In the case of the QWs, the presence of oleic acid is critical not only to produce the ordered bundled structure of the quantum wires, but the unilateral 1D growth as well.

Finally, by systematically tuning the thermodynamic growth regime we are able to synthesize $CH_3NH_3PbBr_3$ quantum cubes. When steady-states photophysical properties of 2.5 ± 0.5 nm thickness $CH_3NH_3PbBr_3$ QPLs are compared with the 12.1 ± 1.2 nm edge-length quantum cubes we find that the k_{nr} is dominant in the cubes while more radiative exciton recombination takes place in the platelets. Formation of the different shapes of $CH_3NH_3PbBr_3$ perovskite NCs that can be achieved through appropriate manipulation of nucleation and growth conditions is outlined in Figure 2.1. We believe our research will provide simple and reliable but versatile synthetic methods to control the size, shape and assembly of anisotropic perovskite NCs, which still poses one of the more challenging issues in modern nanoscience-based research. The 2D perovskite QPLs, and 1D QWs, with high PLQY could be envisioned as an ideal nanomaterial for molecular ink to use in semiconductor-based solid-state device fabrication.

2.3 Methods and Materials

2.3.1 Materials

Lead (II) bromide ($PbBr_2$, 99.999%), methylamine solution (2M in THF), hydrobromic acid (HBr, 48%), n-octylamine ($CH_3(CH_2)_7NH_2$, 99%), oleic acid (99%), octanoic acid (99%), decylamine (99%), hexadecylamine (90%), 1,2,4-trichlorobenzene (TCB, 99%),1-octadecene (ODE, 90%, technical grade), acetone (ACS reagent, 99.5%), and toluene (99.5%) were purchased from Sigma-Aldrich. N,N-dimethylformamide was purchased from Fischer. All measurements were conducted inside the N_2 filled glovebox. Commercially available ODE was kept under high vacuum overnight and transferred to the N_2 filled glovebox. All sample preparation was conducted inside the glovebox. All solvents were purged with N_2 for 30 min prior to use.

2.3.2 Synthesis of Methylammonium Bromide (CH_3NH_3Br) and Octylammonium Bromide ($CH_3(CH_2)_7NH_3Br$)

The bromide salts were prepared using a modified literature procedure.[147] Briefly, HBr (10.34 mL, 0.2 mol) was added drop-wise to either the methylamine solution (7.2 mL, 0.2 mol) or the octylamine (32.98 mL 0.2 mol) with an additional 20 mL of ethanol and then stirred at 0 ^oC for 3 hrs. The ethanol was removed by rotary evaporator and the remaining solid was redissolved in a minimal amount of ethanol. Recrystallization by the addition of ether resulted in a snow-white crystalline solid, which was dried under vacuum and stored in the glove box.

2.3.3 Synthesis of $CH_3NH_3PbBr_3$ QWs

In a two neck round bottom flask, 0.38 mmol of oleic acid was dissolved in 6 mL of 1-octadecene under N_2 and the reaction mixture was stirred at 95 ^oC for 45 min. At this point 0.06 mmol of solid $CH_3(CH_2)_6CH_2NH_3Br$ was added to the reaction mixture and stirred for another 30 min. Separately, 0.032 mmol of CH_3NH_3Br and 0.037 mmol of $PbBr_2$ were dissolved in 100 and 200 mL DMF, respectively. The CH_3NH_3Br solution was added first to the round bottom flask and then allowed to react for 60 sec. Then $PbBr_2$ solution was added resulting in a light yellow solution. At 240 sec, 0.5 mL of the reaction mixture was injected into 5-mL acetone to quench the reaction. The solid was collected by centrifugation at 5000 rpm for 5 min, dissolved in toluene, and centrifuged at 7000 rpm for 5 min. Finally the clear yellow supernatant was collected for further characterization.

2.3.4 Synthesis of $CH_3NH_3PbBr_3$ QPLs

In a typical $CH_3NH_3PbBr_3$ QPL synthesis, 1.5 mL of ODE, 0.5 mL TCB, and 115 μL (0.36 mmol) of oleic acid were stirred together at room temperature for 45 min. Separately, 3.4 mg (0.016 mmol) of $CH_3(CH_2)_7NH_3Br$ and 17 mg (0.07 mmol) of hexadecylamine were dissolved in 250 μL of ODE and then added to oleic acid. The reaction mixture was stirred for 30 min at 60 ^oC. Then 3.5 mg (0.0315 mmol) of CH_3NH_3Br and 18.7 mg (0.05 mmol) of $PbBr_2$ were dissolved in 100 and 200 μL DMF, respectively. The CH_3NH_3Br solution and $PbBr_2$ solution were injected simultaneously into the above mentioned reaction mixture. The solution color turned light yellow almost instantaneously. Then 15 sec after the addition of $PbBr_2$ solution, a 200 μL aliquot was removed and injected into 2 mL of acetone to quench the growth. The solution was centrifuged at 5000 rpm for 2 min and the resulting solid was then dissolved in toluene and centrifuged again at 5000 rpm for 2 min. The clear yellow supernatant was collected. The solution was dried under high vacuum and stored in a 3 mL vial capped under nitrogen.

2.3.5 Synthesis of $CH_3NH_3PbBr_3$ Quantum Cubes

$CH_3NH_3PbBr_3$ quantum cubes were synthesized as follows: In a round bottom flask, 2.0 mL of ODE and 60 μL (0.19 mmol) of oleic acid were mixed and stirred at 110 ^oC for 45 min, and then 10 μL (0.05 mmol) of decylamine were added. The reaction mixture was stirred for an additional 30 min. Separately, 3.5 mg (0.0315 mmol) of CH_3NH_3Br and 18.7 mg (0.05 mmol) of $PbBr_2$ were dissolved in 100 and 200 μL DMF, respectively. The CH_3NH_3Br solution and $PbBr_2$ solution were injected simultaneously. The solution color turned light yellow almost instantaneously and at 30 sec 200 μL of the

reaction mixture was injected into 2 mL of acetone to quench the reaction. The purification steps were identical as described for $CH_3NH_3PbBr_3$ QPL synthesis.

2.3.6 UV-vis Absorbance, Photoluminescence, Photoluminescence Lifetime, and Absolute Quantum Yield Measurements

The absorption spectra were collected using a Varian-Cary 50 Scan UV-visible spectrophotometer with 1 cm quartz cuvettes over a range of 300-800 nm. All spectra were recorded in toluene, and toluene was used as a background for all measurements. The photoluminescence emission (PL) spectra were collected using a Cary Eclipse fluorescence spectrophotometer from Varian Instruments with 1 cm quartz cuvettes. The lifetime measurements were recorded using a time-correlated single photon counting (TCSPC) experimental set up. The data acquisition card was from Edinburgh Instrument (TCC900). The laser was a 405 nm pulsed laser from PICQUANT (LDH-D-C-405M. CW-80MHz) with pulse width < 100 ps. The detector was a photomultiplier tube from HAMAMATSU (HT422-40). The following stretched-exponential equation was used to determine the excited state lifetime.

$$g(t) = \frac{\beta}{t}(\Gamma_{str}t)^{\beta}\, exp\left[-(\Gamma_{str}t)^{\beta}\right]$$

Absolute quantum yield was measured using the Hamamatsu absolute PL spectrophotometer C11347 with a 150 W Xenon light source and an integrating sphere (from Spectralon).

2.3.7 Elemental Analysis

A field emission scanning electron microscopy system (Hitachi S-4700), equipped with an energy dispersive X-ray (EDS) analyzer, was used to determine the Pb:Br ratio.

2.3.8 Transmission Electron Microscopy (TEM) Characterization

The samples for TEM analysis were prepared inside a glove box by placing 10 μL of the sample dissolved in toluene onto a formver-coated copper grid (Electron Microscopy Science). The sample was allowed to set for 30 seconds and any excess solution was removed by wicking with a Kimwipe in order to avoid particle aggregation. Images were acquired using a JEOL-3200FS-JEM instrument operating at 200 kV. At least 300 QPLs were analyzed for width, length, and thickness averaging, and 300 quantum cubes were counted for edge-to-edge distance measurement.

2.3.9 Powder X-ray Diffraction (XRD) and Small Angle X-ray Scattering (SAXS) analyses

Wide-angle XRD was recorded on a Rigaku MiniFlexTM II (Cu Kα) instrument. Samples were prepared by dropcasting the purified PQWs on piranha cleaned glass coverslips. SAXS measurements were conducted on the beamline 12-1D-C at Argone's advanced photon source. The pinhole setup at 12-ID-C used a photon energy of 18 keV, with a flux of approximately 5×10^{12} photons/second. The sample to detector distance was ~2200 mm, where a 4-quadrant mosaic X-ray CCD camera Platinum detector, built in house (1024 × 1024 pixel), was used. The samples on glass coverslips were mounted vertically such that the glass was perpendicular to the beam. They were then rotated using a motor at a frequency ranging from 3-5 Hz. Two-dimensional scattering data was taken, which was averaged and integrated of the χ angle to obtain *Intensity* versus $q\ (\mathring{A}^{-1})$. (*Warning:* piranha solution is highly reactive and must be handled with extreme caution. It reacts violently with organic materials and may not be stored in tightly closed vessels).

2.4 Results and Discussion

2.4.1 Colloidal Synthesis of $CH_3NH_3PbBr_3$ QWs

Our approach is based on general colloidal synthetic methods that included use of organic ligands as stabilizers to control the size, morphology, and organization of the resulting nanostructures.[148, 149] Figure 2.2 A illustrates the transmission electron microscopy (TEM) image of the resulting $CH_3NH_3PbBr_3$ QWs with lengths from 300-900 nm and 3.8 ± 0.4 nm diameter. X-ray diffraction (XRD) characterization was performed to analyze the phase structure of the QWs and then compared with single crystal $CH_3NH_3PbBr_3$ bulk perovskite that was synthesized according to the literature[2]. Their XRD characterization is shown in Figure 2.2B. The diffraction peaks in QWs were broadened compared to bulk perovskite, which suggest their nanometer-size structure, while the positions of the diffraction peaks correspond to cubic phase. The broad XRD pattern of our $CH_3NH_3PbBr_3$ QWs is similar to the literature report of 3.3 nm diameter $CH_3NH_3PbBr_3$ NCs[150] but markedly different from $CH_3NH_3PbBr_3$ nanowires where extremely sharp peaks were detected.[9] The high-resolution TEM analysis of our $CH_3NH_3PbBr_3$ is shown in Figure 2.2C giving an interplanar distance fringe separation of ~5.9 Å, which is characteristic of (001) planes in the cubic phase structure of $CH_3NH_3PbBr_3$ perovskite. The formation of these $CH_3NH_3PbBr_3$ QWs took place within the 240 sec interval after the injection of $PbBr_2$ in *N,N*-dimethylformamide (DMF) into the reaction mixture containing oleic acid, octylammonium bromide, and methylammonium bromide, which were all dissolved in 1-octadecene at 95 °C.

In order to investigate the mechanism of QW formation, we characterized the time-dependence of both the optical spectroscopic and TEM analyses of the reaction mixture under synthesis conditions. Figures 2.3A and B show UV-visible and PL spectra, respectively, of the resulting perovskite material after quenching and purification at different time points. The 30 sec reaction sample displayed its absorption peak at 426 nm and band-edge PL maximum at 428 nm along with a long tail covering the visible region of the spectrum. These optical properties are markedly different from bulk $CH_3NH_3PbBr_3$

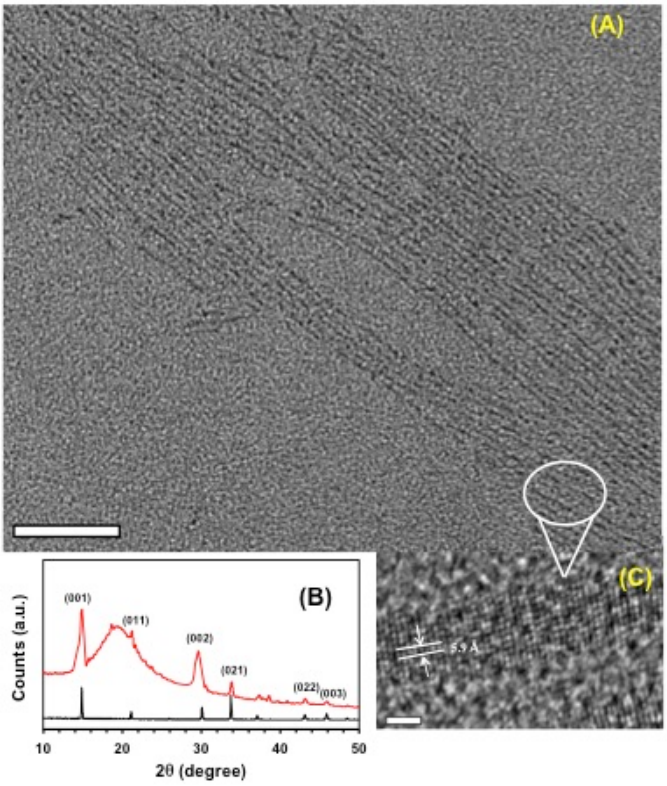

Figure 2.2 (A) TEM image of $CH_3NH_3PbBr_3$ QWs. Scale bar is 100 nm. (B) Experimental XRD pattern corresponding to the cubic-phase of the perovskite QWs (red) and bulk $CH_3NH_3PbBr_3$ perovskite (black). The broad peak (red) centered near 20^o is due to glass coverslip. (C) High-resolution TEM image of a portion of a quantum wire showing cubic-phase lattice spcing. Scale bar is 2 nm.

materials[2] and likely indicate the formation of NCs in the solution.[144, 145] Furthermore, the long tail suggests that the surface of the NCs was not fully passivated and this optical feature most likely originates from surface-related nonradiative trap states rather than a large size distribution of the NCs in solution, as was previously reported for ultrasmall CdSe NCs of similar size.[151-154] The 60 sec reaction sample displayed a well-defined absorption peak at 495 nm and its band-edge PL peak at 514 nm with a 93 meV Stokes shift. As the reaction progressed to 240 sec, both the absorption and band-edge PL peaks red-shifted to 522 nm and 524 nm, respectively. These red shifts are expected in the case of formation of 1-D nanostructures (Figure 2.2A) and Table 2.1. We believe that the progressive red-shift of these peaks was due to the transformation of ultrasmall NCs into 1D nanostructures[53] and the resulting reduction in quantum confinement. The negligible Stokes shift (10 meV) (Figure 2.4) of the QWs is an indication that their surface was nicely passivated with ligands with a low population of

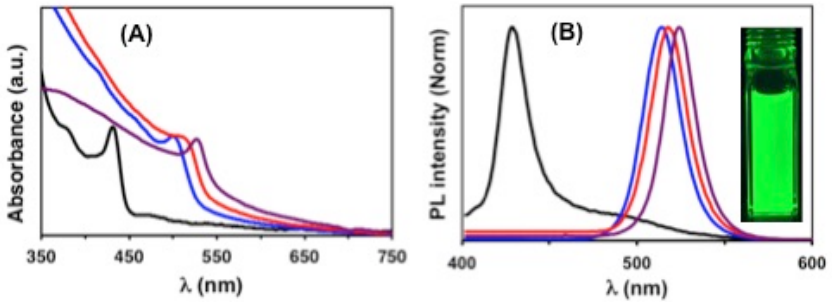

Figure 2.3 Time-dependent (A) absorption and (B) normalized emission spectra of perovskite $CH_3NH_3PbBr_3$ QWs reaction at 30 (black), 60(blue) 120 (red) and 240 (purple) seconds.. Insert: Solution color of $CH_3NH_3PbBr_3$ quantum wires dissolved in toluene under illumination at 350 nm..

trap states, which is important in the context of longer charger carrier lifetimes and transport of photogenerated carriers.

2.4.2 Structural Characterization of $CH_3NH_3PbBr_3$ QWs

The formation of $CH_3NH_3PbBr_3$ QWs was also investigated by time-dependent TEM analysis. The 30 sec reaction sample displayed nearly monodispersed, ultrasmall spherical $CH_3NH_3PbBr_3$ NCs with 1.5 ± 0.1 nm diameter (Figure 2.5A). A narrow size distribution should provide a sharp band-edge emission peak in the PL spectrum rather than a combination of band-edge and broad-band PL peaks. We believe that the broad PL peak measured with the 30 sec reaction sample is related to the surface structure of our 1.5 nm diameter NCs and not their size distribution. In the ultrasmall size range, a large percentage of atoms occupy surface NC sites. Any unpassivated surface sites would result in formation of surface midgap trap states[153, 154] where photogenerated holes could be trapped, and perhaps recombine with photoexcited electrons far from the band-edge. Such recombination could display a broad tail in the PL spectra as previously observed for ultrasmall CdSe NCs (1.6 nm diameter).[152] After another 30 sec, the diameter increased to 2.4 ± 0.2 nm. These data are in agreement with the absorption and PL peak shifts from 426 to 495 nm and 428 to 514 nm, respectively, in accordance with the known relationship between size and optical peak wavelength of perovskite NCs.[145, 155] These results strongly support our expectation that at the early stages of synthesis, ultrasmall NCs are formed in the reaction mixture. In the 60 sec sample "pearl-necklace" assemblies consisting of spherical NCs were observed (Figure 2.5B). Similar pearl-necklace assemblies were observed previously with the growth of CdTe nanowires from spherical quantum dots.[53] Therefore, we believe $CH_3NH_3PbBr_3$ QWs were formed neither through "oriented attachment" of spherical $CH_3NH_3PbBr_3$ NCs directly to the ends of the QWs, nor through point-initiated vectorial growth. In the case of oriented

attachment, the diameter of the $CH_3NH_3PbBr_3$ QWs should be smaller than the diameter of the spherical NCs. The oriented attachment-driven growth involves direct crystal-to-crystal interactions causing crystalline fusion to form a single crystal lattice.[156, 157] Under this growth condition, the width and/or diameter of the anisotropic nanostructures (nanorods, nanoplatelets, nanowires) should be identical or lower in width/diameter to the spherical NCs.[156, 158, 159] However instead we observed a second intermediate stage where QWs were formed having diameter of 3.2 ± 0.2 nm in the same sample that the spherical NCs (Figure 2.5C) were observed. The increased diameter of $CH_3NH_3PbBr_3$ QWs nicely corroborated the red shifts in both the absorbance and emission spectra found with spherical NCs of diameter 2.4 nm. Thus, because we found (i) the same crystallographic structure (cubic) for $CH_3NH_3PbBr_3$ spherical NCs (Figure 2.6) and QWs, (ii) appearance of pearl-necklace assemblies, and (iii) an increase in diameter during the

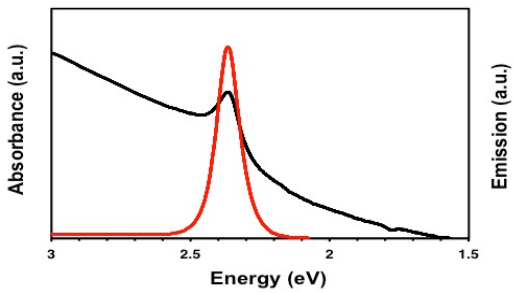

Figure 2.4. The absorption (black, 2.38 eV) and emission (red, 2.37) spectra of $CH_3NH_3PbBr_3$ QWs showing no detectable stokes shift.

growth of QWs, we propose $CH_3NH_3PbBr_3$ QWs were formed through cooperative interactions between the spherical NCs causing "mesoscale growth and assembly."[10, 160] It is important to note that the $CH_3NH_3PbBr_3$ QWs were extremely stable under prolonged exposure to the electron beam during the TEM analysis (Figure 2.7). Our observation is markedly different from recent studies on $CH_3NH_3PbBr_3$ nanoplates, where

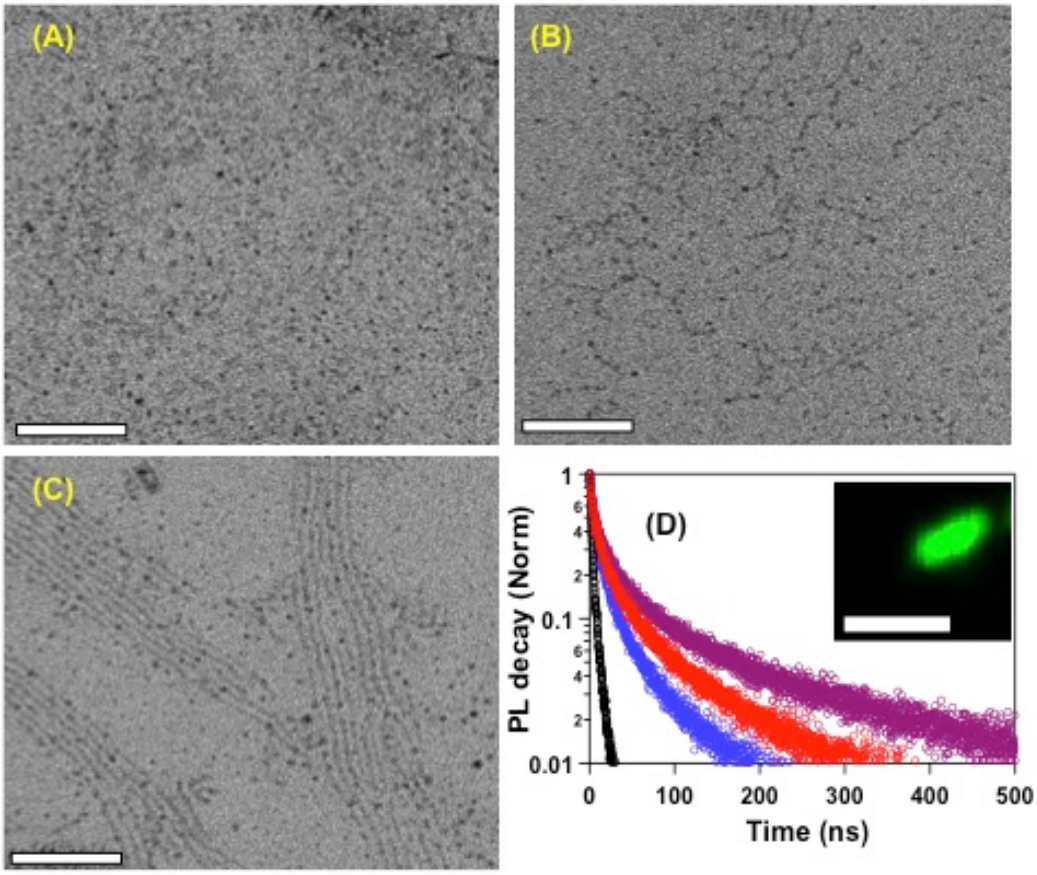

Figure 2.5 Time-dependent TEM images of $CH_3NH_3PbBr_3$ QWs at 30 (A), 60 (B), and 120 (C seconds. Scale bars are 50 nm. (D) Normalized photoluminescence decay measurements at the highest emission maxima. Insert: Confocal microscopy image of a bundle of $CH_3NH_3PbBr_3$ quantum wires. Scale bar is 1 mm. The black, blue, red, and purple lines in Fig. D represent synthesis progression at 30, 60, 120, 240 sec, respectively.

crystalline spherical NCs were formed from nanoplates during the TEM analysis.[9, 145]

Based on our structural characterizations, we hypothesize that both octylammonium ions (OAMIs) and oleic acid are prerequisite to control the formation of spherical NCs as well as the mesoscale growth and assembly to $CH_3NH_3PbBr_3$ QWs. During the preparation of this article, colloidal synthesis of $CsPbBr_3$ nanowires was reported.[161] However, their synthetic procedure (150 ^{0}C), nanowire structural

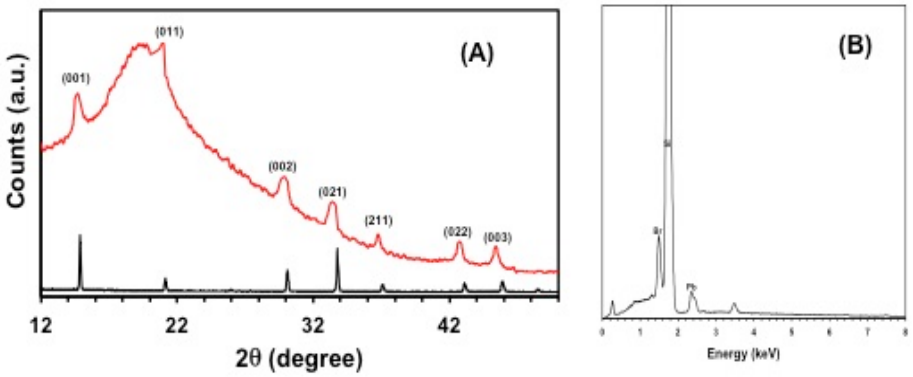

Figure 2.6 XRD pattern (A) and EDS spectra (B) corresponding to the cubic-phase $CH_3NH_3PbBr_3$ 2.4 nm NCs

properties (orthorhombic phase), and 1D morphology (~10 nm in diameter) were completely different than our organic-inorganic hybrid $CH_3NH_3PbBr_3$ QWs as discussed above.

2.4.3 Electronic Properties of $CH_3NH_3PbBr_3$ QWs

We compared the optical band-gap of our NCs obtained at different time point during the QWs synthesis (spherical NCs, QWs, and the mixture of both) with effective mass approximation (EMA) theory,[162] with the consideration that all the NCs maintained quantum well properties. However, our experimental data do not agree with the EMA calculation (Figure 2.8). This could be due to reduction in the dimension of the NCs, as well as the role of surface passivating ligands in modulating confinement energy. Recently, a similar disagreement was found for $CH_3NH_3PbBr_3$ nanoplates with different thickness, and the authors suggested that the exciton wave functions could escape from the inorganic core boundary of the plates and hybridize with neighboring nanoplates.[145] This exciton delocalization mechanism and deviation of optical properties from theoretical calculations are further supported by a recent investigation of $CsPbBr_3$ nanoplates.[134] In this context, we have reported that the smallest size CdSe

NCs (ranging from 1.6 to 2.5 nm in diameter) displayed the highest delocalization and hybridization of electron and/or hole wave functions with adjacent NCs, resulting in the largest shift in the optical band-gap.[163] Therefore, we believe that the change in optical band-gap of 0.42 eV for a difference in diameter of 0.9 nm between the spherical NCs of $CH_3NH_3PbBr_3$ at the early stages of the synthesis could be caused by a combination of both NC size and identity of surface passivating ligands affecting quantum confinement. Nevertheless, such deviation of the optical band-gap from a simple EMA calculation was also observed for $CsPbBr_3$ nanocubes in the strong confinement regime (<5 nm in edge-length).[155] Therefore, modeling the complex photophysical properties of our $CH_3NH_3PbBr_3$ NCs and QWs requires a sophisticated mathematical model with a variety of possible spacial organization (e.g., pearl-necklace, bundle-type), which is not within the scope of this work.

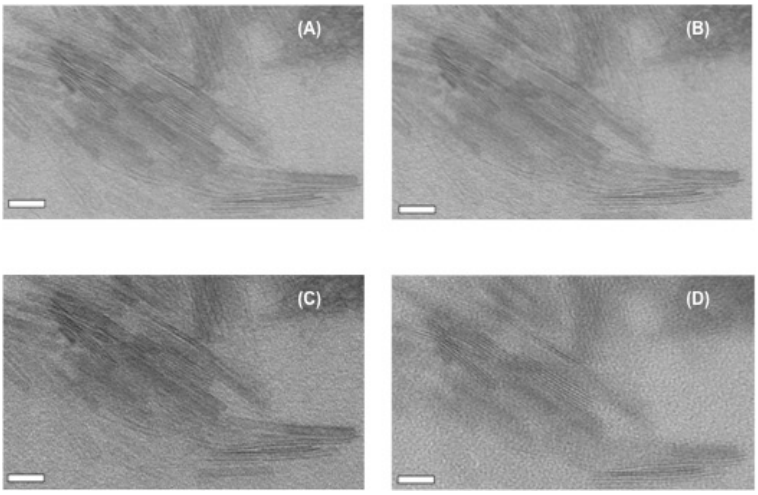

Figure 2.7 Low magnification TEM images of the $CH_3NH_3PbBr_3$ quantum wires at different point of the analysis under the exposure of 200 kV beam energy. (A) 0 min, (B) 10 min, (C) 20 min, and (E) 30 min. Scale bar is 100 nm

The $CH_3NH_3PbBr_3$ QWs displayed bight green color under illumination with 350 nm light and an absolute PL quantum yield (ϕ) of 59 ±7 % (Table 2.1). The increase in ϕ from spherical NCs to QWs is because of their more crystalline character (Figure 2.2B), dimensionality, and surface passivation, which would together cause an increase in the PL lifetime (Figure 2.5D) as was observed from the biexponential fits with t_{fast} = 11 ns and t_{slow} = 89 ns (Figure 2,9). Perhaps, among all these parameters, we believe that

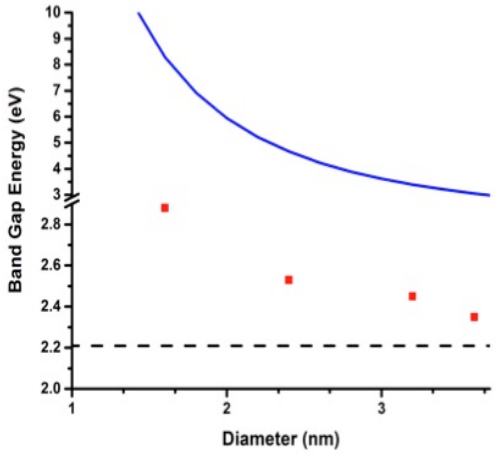

Figure 2.8 Experimental band-gap energy of the $CH_3NH_3PbBr_3$ nanocrystals measured by UV-vis spectroscopy versus diameter of the spherical nanocrystals (red squares, 1.5 and 2.4 nm) and diameter of the quantum wires (red squares, 3.2 and 3.8 nm). Theoretical band-gap calculation is shown by the blue line using the effective mass approximation (EMA)

surface ligand chemistry played a major role in producing the high ϕ and PL lifetime of our QWs as discussed below. Importantly, the PL lifetime of $CH_3NH_3PbBr_3$ QWs was at least 25 times greater than $CH_3NH_3PbI_3$ nanowires grown on a solid surface.[133] The ϕ of our QWs was higher than those found with direct band-gap CdSe (diameter = 2.0 nm, ϕ = 15%)[164] and CdTe (diameter = 3.5 nm, ϕ = 16.2%)[53] semiconductor nanowires, $CH_3NH_3PbBr_3$ nanowires with larger diameter than ours (diameter = 47 nm, ϕ = 13%),[9]

and $CH_3NH_3PbBr_3$ spherical NCs (diameter = 6.0 nm, ϕ = 17%).[165] Furthermore, $CH_3NH_3PbI_3$ nanowires (diameter = 10-200 nm) prepared via the solid-phase crystallization approach displayed ϕ of 0.012% and PL lifetime of <10 ns,[130, 131] which are markedly different than our $CH_3NH_3PbBr_3$ QWs. The $CH_3NH_3PbBr_3$ QWs were imaged via confocal microscopy (Figure 2.5D, insert) and emitted bright green color throughout their entire length. By comparison with Figure 2.2A, we believe the image displays a bundle of individual QWs.

The sharp band-edge PL peak, high quantum yield, and long PL lifetime (Table 2.1) of the $CH_3NH_3PbBr_3$ QWs together suggest that the surface of the QWs was nicely passivated with OAMIs (Figure 2.10), which eliminated the surface defects and nonradiative trap states, and the PL decay occurred through radiative recombination. We believe that the OAMIs are directly attached to the QWs via electrostatic interactions with surface bromide ions. Furthermore, oleic acid likely interacts with the ammonium head groups of OAMIs as part of an OAMI bilayer-type structures, as discussed later. As shown in Table 2.1 for $CH_3NH_3PbBr_3$ perovskite, ϕ and PL lifetime increased dramatically from our 1.5 nm diameter spherical NCs to the 3.8 nm diameter QWs. It is known that as the size decrease, the surface-to-volume ratio increase, which results in a larger percentage of atoms residing on the surface. Any unpassivated surface atoms create nonpassivated trap states, which reduce radiative (k_r) and enhance nonradiative (k_{nr}) decay rates. Under our experimental conditions, the k_{nr} value was found to be ~80 times higher than k_r for ultrasmall 1.5 nm diameter spherical NCs, whereas k_r was the dominating factor for $CH_3NH_3PbBr_3$ QWs. These experimental data are in agreement with the proposed surface chemistry and surface structure of spherical NCs and QWs in

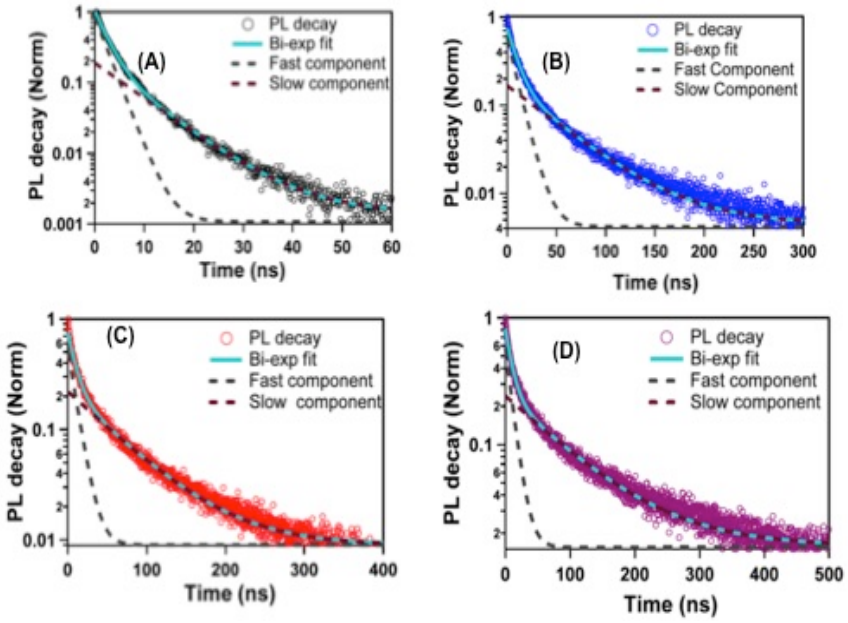

Figure 2.9 Normalized, biexponential fit of TCSPC spectra of reaction mixture at 30 (A), 60 (B), 120 (C), and 240 (D) sec The time constant of the slow component (t_{slow}) is 9, 50, 63, and 89 ns at the four incubation time points.

which better surface passivation reduces surface defects and nonradiative trap states, resulting in higher ϕ, PL lifetime, and k_r (Table 2.1).

2.4.4 Surface Ligand Chemistry of $CH_3NH_3PbBr_3$ QWs

We characterized the $CH_3NH_3PbBr_3$ QW surface ligand chemistry, which is generally known to directly influence the nucleation and growth processes of nanostructures, as well as long-term colloidal stability. The X-ray photoelectron spectroscopic (XPS) analysis (Figure 2.11A-C) of five randomly selected areas of two different preparations showed an average Pb-to-Br atomic ratio of 1:3.4 with higher bromide ion concentration at the surface of 3.8 nm diameter $CH_3NH_3PbBr_3$ QWs. Our experimental data are in agreement with the previously reported XPS results on 3.3 nm diameter $CH_3NH_3PbBr_3$ NCs in which the Pb-to-Br atomic ratio was found to be 1:3.5.[150] For $CH_3NH_3PbBr_3$ bulk material the ratio is 1:3.[166-169] Because

$CH_3NH_3PbBr_3$ perovskite consist of $[PbBr_6]^{4-}$ octahedral unit cells, the excess bromide ions in the QWs were assigned to bromide ions residing on the surface. The appearance of two sharp Pb 4f peaks (binding energies: 138 and 148 eV) without any shoulder suggests the nano-sized structure of the synthesized materials.[150] The broad Br 3d peak was fitted to two peaks (binding energies: 67.8 and 68.9 eV) with the higher intensity peak at 68.9 eV indicating a bromide rich surface and the peak at 67.8 eV corresponding to core bromide ions.[150] In the N 1s spectrum, two peaks were observed with binding energies at 399.1 and 401.7 eV, which correspond to the nitrogen from OAMI and $CH_3NH_3^+$, respectively.[150] Taken together, the appearance of two sharp peaks in our $CH_3NH_3PbBr_3$ QWs in Pb 4f region, the broad Br 3d peak, and the two N 1s peaks are all in agreement with the literature of nano-sized $CH_3NH_3PbBr_3$ NCs.[150] Our energy dispersive X-ray analysis (EDS) of the same samples confirmed that the average stoichiometric composition of Pb-to-Br was 1:3.3 (Figure 2.11D). The atomic ratio Pb-to-

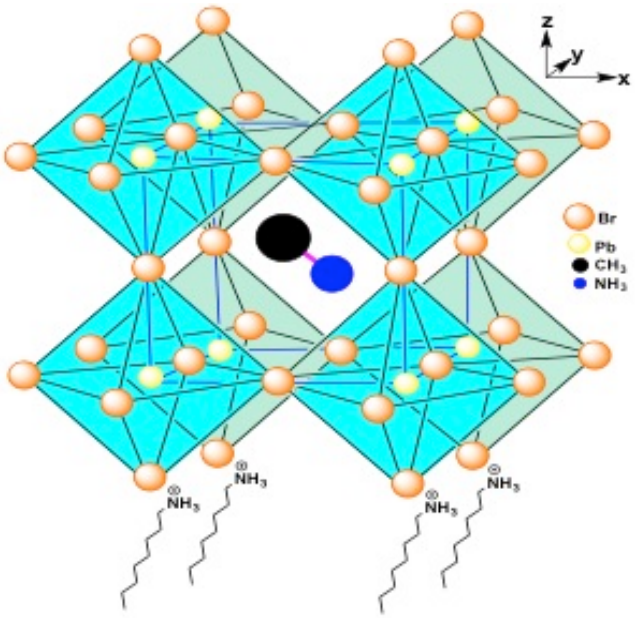

Figure 2.10 Three-dimensional schematic representation of cubic phase lead bromide perovskite with chemical formula $CH_3NH_3PbBr_3$.[1, 2]

Br was found to be 1:3.3. This ratio is higher than the ideal 1:3 ratio for either $CH_3NH_3PbBr_3$ bulk perovskite material[2] or $CsPbBr_3$ NCs and nanocubes.[155] However, the 1:3.3 EDS ratio is in agreement with the XPS analysis where the Pb-to-Br was found to be 1:3.4.The bromide rich surface and presence of OAMI, which has a cationic head group, suggest that the OAMI acted as a surface passivating ligand coordinating with surface bromide ions through electrostatic interaction.[145, 150] These data are consistent with our proposed structure.

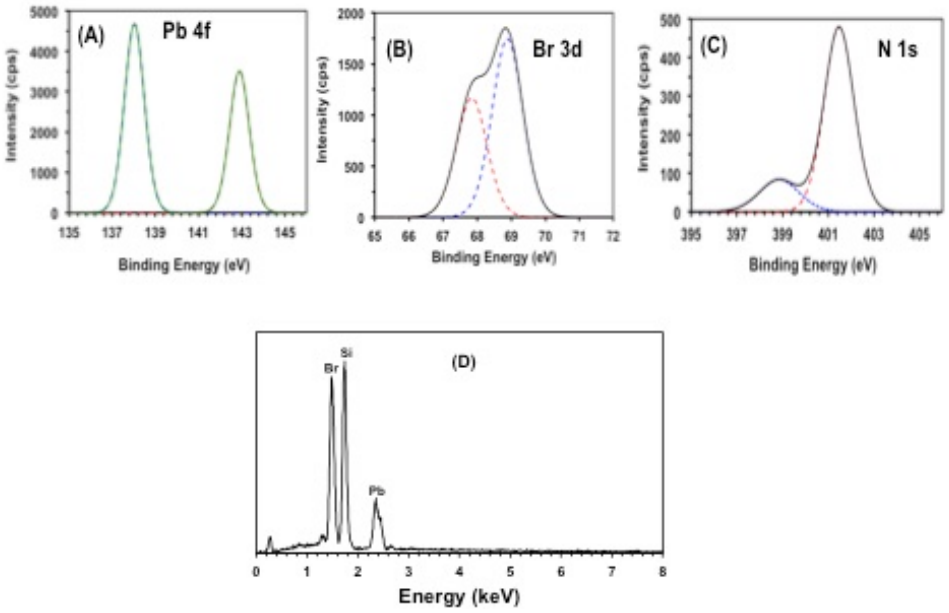

Figure 2.11 X-ray photoelectron spectroscopic (XPS) analysis of CH_3NH_3PbBr QWs. The Pb 4f (A), Br 3d (B), and N 1s (C) spectral profile of the $CH_3NH_3PbBr_3$ QWs. The solid lines are the experimental data and dotted lines are the fits. (D) A representative energy dispersive X-ray (EDS) spectroscopy analysis of $CH_3NH_3PbBr_3$ QWs.

As illustrated in Figure 2.12A, we observed a broad proton signal from the carboxylic acid group at 11.87 ppm in the ^1H NMR spectrum. Pure oleic acid showed proton signals associated with both the double bond and the carboxylic acid resonances at 5.34 and 11.87 ppm, respectively. The peaks corresponding to the same resonances in the

$CH_3NH_3PbBr_3$ QWs sample were much broader. Such peak broadening is generally observed when organic ligands are attached onto the surface of inorganic nanostructures.[152, 170, 171] The broadening of the resonance peaks is likely due to a combination of spin-spin relaxation broadening and dipole broadening, as well as a distribution of chemical shifts.[172, 173] Sharp resonances at 1-3 ppm are from alkane hydrogens and perhaps from residual solvents.

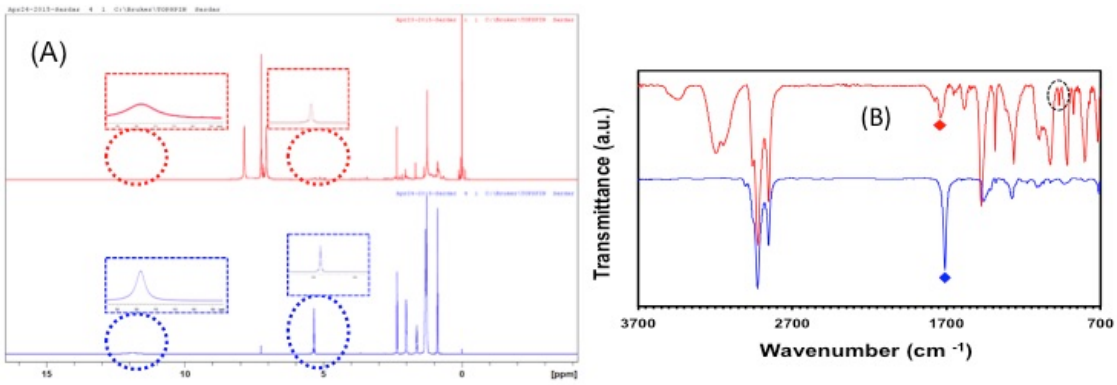

Figure 2.12 1H NMR (A) and FTIR (B) characterization of pure oleic acid (blue) and $CH_3NH_3PbBr_3$ QWs (red).

FTIR spectroscopy was used to confirm the existence of oleic acid and n-octylammonium cations as surface passivating ligands of our QWs as shown in Figure 2.12B. The peak at 1735 cm^{-1} in the QW spectrum (red diamond), which was assigned to the C=O stretching band of a carboxylic acid group, was 26 cm^{-1} higher than 1709 cm^{-1} found in the pure oleic acid (blue diamond),[11] indicating the acid group is involved in an electronic interaction but not negatively charged oleate ion. The presence of oleic acid bound to the surface of the QWs as passivating ligands was also confirmed by the appearance of the O-H stretch at 970 cm^{-1} (dotted circle).[11] Pure oleic acid showed asymmetric and symmetric C-H stretching bands at 2925 and 2853 cm^{-1}, respectively,

which were also present in QWs. The new broad intense peaks appearing at 3143 and 3196 cm^{-1} were assigned to the NH_3^+ symmetric stretching bands from OAMI.[12, 13] The peaks at 1653 and 1584 cm^{-1} were attributed to the asymmetric and symmetric NH_3^+ deformations, respectively, from OAMI.[12, 13] The peak 3419 cm^{-1} could be assigned to the effects of hydrogen bonding between the -COOH group of oleic acid and $–NH_3^+$ of OAMI, which will be discussed later.

In order to fabricate efficient solid-state devices in the future, it will be important to investigate in detail the stability of our $CH_3NH_3PbBr_3$ QWs. The QWs (Figure 2.13) were stored under normal laboratory conditions in the dark. We did not observe any noticeable change in the absorption and PL peak positions and shapes over the course of

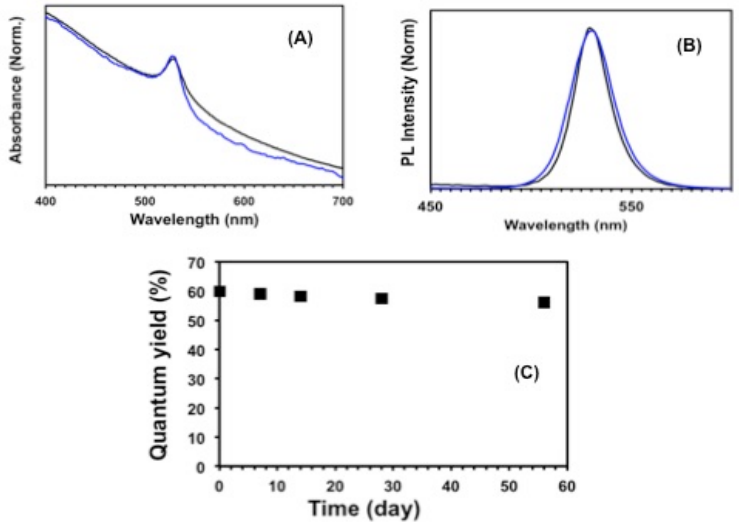

Figure 2.13 The absorbance (A) and emission (B) spectra of freshly QWs (black) and after 56 days (blue). The absolute quantum yield of the $CH_3NH_3PbBr_3$ QWs was also calculated at each time point (Figure C) to quantitatively determine the stability of the nanomaterials and showed an ~4% decrease in quantum yield over **the 56**

nearly two months. Moreover, during this time period, only a 4% decrease in ϕ was observed. We believe this excellent long-term stability of our organolead bromide perovskite QWs is likely due to suitable surface passivation that inhibited degradation by

moisture. However, complete degradation of the PL and ϕ of $CH_3NH_3PbBr_3$ QWs was observed within a week when the colloidal solution (in toluene) was kept in air and light (data not shown). Perhaps, a more comprehensive and systematic study, e.g., varying humidity,[174] light exposure, and solvent is required to properly address the stability of these QWs

2.4.5 Proposed Growth Mechanism of $CH_3NH_3PbBr_3$ QWs

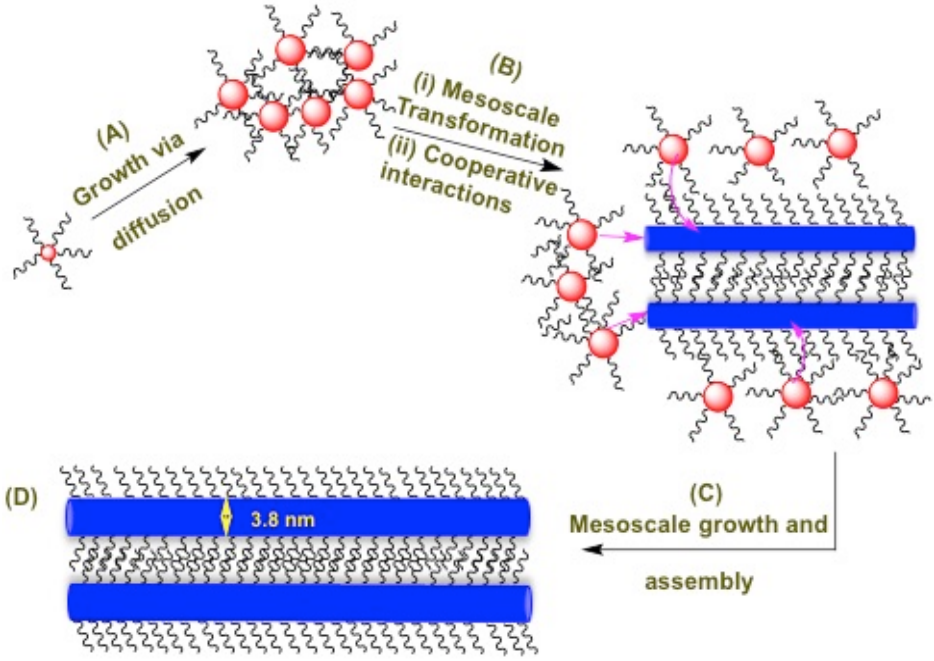

Figure 2.14 Proposed pathway of mesoscale self-assembly of $CH_3NH_3PbBr_3$ QWs.[10] (A) Approximately 1.5 nm $CH_3NH_3PbBr_3$ NCs are formed by 30 sec which grow into ~2.4 nm NCs that undergo pearl-necklace assembly via dipolar interaction. (B) QWa (~ 3.2 nm diameter) are formed via cooperative interaction of the 2.4 nm NCs that undergo a mesoscale transformation. (C) The QWs continue to grow both in diameter and length via mesoscale growth while maintaining their spatial organization through surface ligand chemistry. (D) Formation of bundle-like superstructures made with perovskite QWs. Throughout the growth process, the presence of passivating ligands attached onto the surface of the NCs is extremely important for the cooperative interactions between NCs caused by van der Waals interactions and chain interdigitation.

The appearance of two-distinct intermediate steps in the $CH_3NH_3PbBr_3$ QW formation, i.e., (1) the pearl-necklace assemblies and (2) the mixed aggregates of QWs and spherical NCs, suggests that cooperative interactions between NCs at the early stage of QW formation are very critical. Previously, formation of 1D CdTe nanowires from spherical quantum dots was described as: (1) The detachment of surface passivating ligands during solvent precipitation creates unpassivated quantum dots inducing the dipole-dipole interaction and reducing electrostatic repulsion between them. These interactions between quantum dots are strong and long range as opposed to hydrogen bonding or weak van der Waals interactions, resulting in the appearance of pearl-necklace assemblies.[53] (2) Naked, multiple quantum dots in the assembly fuse together to form single crystal CdTe nanowires. Thus, the last step in CdTe growth is dominated by an aggregation process. We believe our $CH_3NH_3PbBr_3$ QW formation involves (1) dipole-dipole interactions between NCs that results in pearl-necklace assemblies and (2) surface ligand-controlled cooperative interactions causing mesoscale transformation of $CH_3NH_3PbBr_3$ NCs to QWs. In both cases, the presence of pearl-necklace assemblies is critical, however, our transformation of spherical NCs to QWs (mesoscale growth) is substantially different than with CdTe nanowire growth from spherical quantum dots, which can be considered as recrystallization of multiple quantum dots in linear aggregates.[51] Moreover, mesoscale-driven growth does not require detachment of ligands from the surface of the NCs as demonstrated for CdTe nanowire growth. The entropically-controlled mesoscale growth is governed by the cooperative interactions between NCs caused by van der Waals interactions and chain interdigitation of surface passivating ligands. Therefore, the presence of passivating ligands attached onto the

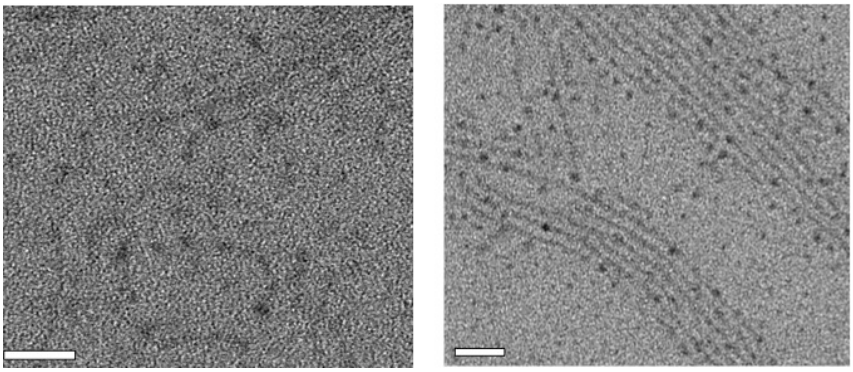

Figure 2.15 TEM images of the pearl-necklace (A) and wire-type assemblies as intermediates $CH_3NH_3PbBr_3$ nanostructures to the final QWs. The scale bars are 20 nm

surface of the NCs throughout the growth process is extremely important.

To determine structural parameters that may cause dipole-dipole interactions between our 2.4 nm diameter spherical perovskite $CH_3NH_3PbBr_3$ NCs, we performed EDS analysis (Figure 2.6B), which showed them to be highly bromide rich (Pb-to-Br was 1:3.8). This excess in bromide could have induced a dipole moment even though the crystal lattice was symmetric[175] because the cationic OAMI would be strongly adsorbed onto the inorganic QW surface. Therefore, pearl-necklace assemblies (Figure 2.3B, 2.14B, and 2.15A) of perovskite NCs would be formed due to polarization in the crystal structure. The high surface charge can induce cooperative interactions between inorganic spherical NCs and surface passivating ligands, e.g., OAMIs and oleic acid, which together would lead into mesoscale transformation to wire-type structures (Figure 2.3C, 2.14C, and 2.15B), as demonstrated previously for the formation of $BaSO_4$ nanofilaments.[176] The driving force for the cooperative mesoscale transformation of spherical NCs to QWs could be reduction of curvature that allows van der Waals contacts between the aligned surface ligands. The last stage of QW formation is continuous attachment of spherical NCs to QW via mesoscale growth by the influence of cooperative

interaction, where van der Waals attractive forces and interdigitation of surface ligands resulted in mesoscale assembly of QW bundles (Figure 2.2A and 2.5D).

We investigated the key role of surface passivating ligands in the formation of $CH_3NH_3PbBr_3$ QWs. We hypothesize that the presence of both oleic acid and OAMIs in the reaction mixture is prerequisite for the formation of $CH_3NH_3PbBr_3$ QWs in that they play stabilizing and formative roles. Our two control experiments were confirmatory. First, the presence of oleic acid and absence of OAMI in the reaction mixture resulted in

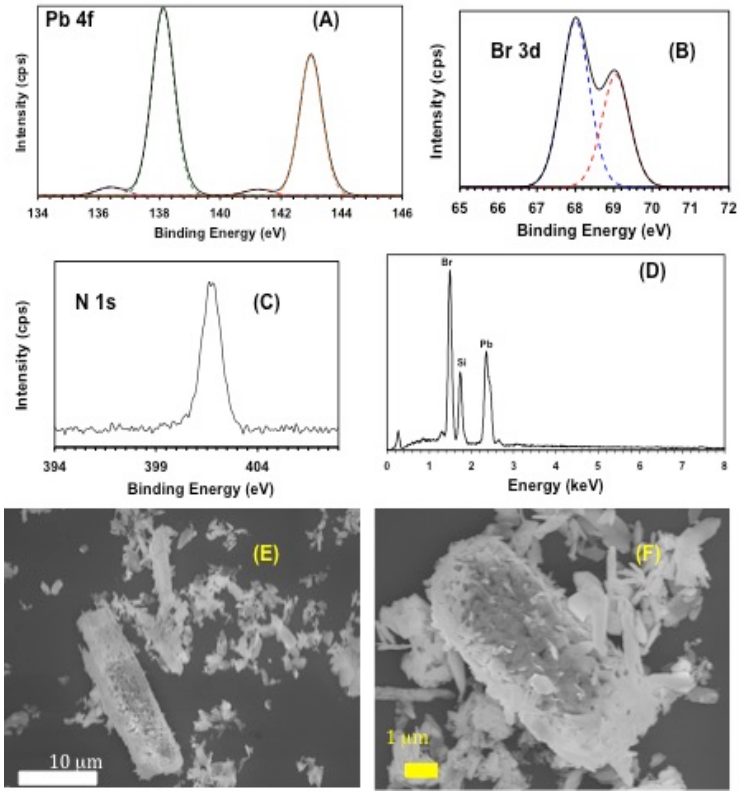

Figure 2.16 The XPS spectra (A-C) confirm the formation of $CH_3NH_3PbBr_3$ bulk material as determined from the appearance of shoulders in the Pb 4f spectrum. The Br 3d peak at 69.1 eV is lower in intensity than the peak at 68.0 eV, and together with the appearance of one nitrogen peak at 401.8 eV confirms the formation of $CH_3NH_3PbBr_3$ bulk material. The sample was also analyzed by EDX (D) and the atomic ratio of Pb-to-Br was found to be 1:2.9, whereas the ideal ratio of bulk $CH_3NH_3PbBr_3$ material should be 1:3. The SEM characterization (E-F) of the bulk $CH_3NH_3PbBr_3$ material showed the appearance of flake-type structure, which is aggregated.

formation of bulk perovskite $CH_3NH_3PbBr_3$ materials with Pb-to-Br ratio of 1:3 in EDS analysis (Figure 2.16D. Thus, OAMI acts as a stabilizing ligand providing stability to spherical $CH_3NH_3PbBr_3$ NCs, and oleic acid alone is not sufficient to retain the colloidal properties of the spherical NCs that formed at the early stage in the reaction mixture. Second, the reaction mixture containing OAMI but no oleic acid showed formation of $CH_3NH_3PbBr_3$ QPLs ($\phi \sim 45\%$) without any spherical NCs or QWs either at 60 or 240 sec after the addition of $PbBr_2$ (Figure 2.17). Thus both OAMI and oleic acid participate directly in the cooperative interaction and mesoscale growth.

We performed another control synthesis experiment by using octanoic acid instead of oleic acid while keeping the other experimental condition identical. Our working hypothesis of QW formation is based on the cooperative interaction and interdigitation of surface passivating ligands. Therefore, reducing the alkyl chain length (from $(CH_2)_{17}$ in oleic acid to $(CH_2)_7$ in octanoic acid) should reduce the van der Waals attractive forces and interdigitation of surface passivating ligands, resulting in disruption in the cooperative interaction. Using octanoic acid, a purified sample from the 4 min reaction mixture was characterized by optical spectroscopy and displayed absorption and emission peaks centered at 505 and 515 nm, respectively (Figure 2.17E). Both these peaks were blue-shifted in comparison to $CH_3NH_3PbBr_3$ QW. TEM analysis of this sample showed formation of polydispersed spherical $CH_3NH_3PbBr_3$ NCs of 7.4 ± 2.8 nm diameter without appearance of any QWs (Figure 2.17F). These data are in agreement with the colloidal synthesis of NCs in which aggregation of NCs would be observed during the growth process if shorter chain surface passivating ligands were present.[149, 177] This aggregation is likely caused by the low diffusion barrier of the shorter chain

ligand (octanoic acid). This result supports that the mixed surface ligation of OAMI and oleic acid is the key to the synthesis of $CH_3NH_3PbBr_3$ QWs through the occurrence of the two crucial intermediate steps of cooperativity and chain interdigitation. Taken together, the appropriate selection of surface ligand chemistry enables the control of van der Waals attractive forces between coated anisotropic nanostructures, which will result in the formation of new hybrid nanomaterials with unique electronic properties.

2.4.6 Mesoscale Assembly of $CH_3NH_3PbBr_3$ QW to Superstructure

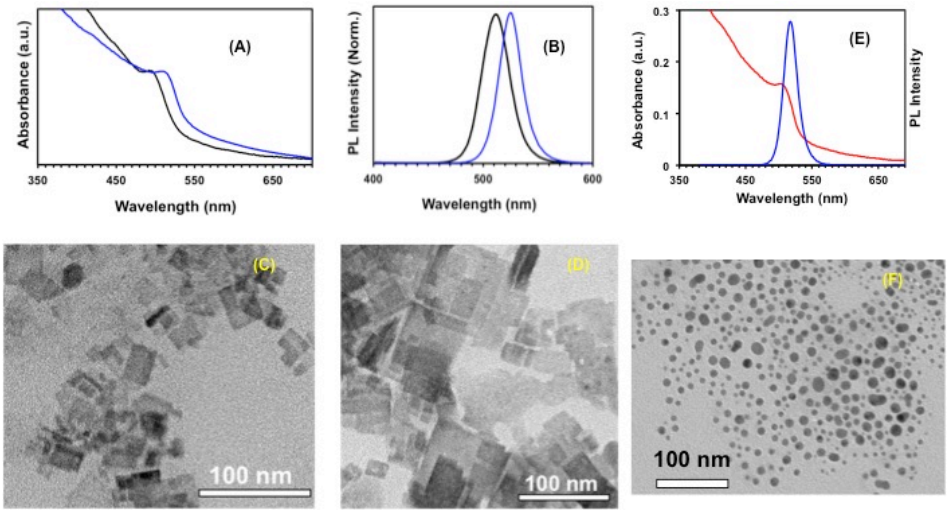

Figure 2.17 UV-vis (A) and PL (B) spectra, and TEM images (D and E) of the $CH_3NH_3PbBr_3$ QPLs synthesized in the absence of oleic acid. UV-vis and PL spectra (C), and TEM images (F) of the spherical $CH_3NH_3PbBr_3$ nanocrystals synthesized in the presence of octanoic acid.

We performed grazing incidence small angle X-ray scattering (GISAXS) of $CH_3NH_3PbBr_3$ QWs (Figure 2.18A) to investigate the bundle-type assemblies observed in Figure 2.2A. The center of the peak (blue curve) was determined by subtracting the blank sample and then fitting with a Gaussian function (dotted red), and was found to be 0.206 $Å^{-1}$. Interestingly, the GISAXS scattering pattern corroborated the parallel alignment of

$CH_3NH_3PbBr_3$ QWs shown in Figure 2.2A, and gave a 3.2 nm separation with the possibility that OAMI and oleic acid are present in between the wires in a bilayer-type structure in the bundle of individual QWs. n-Alkylammonium bromides are known to be shape-directing surfactants, which form a bilayer on the surface of the gold nanorods.[178] We believe our mesoscale growth is one dimensional along the (011)

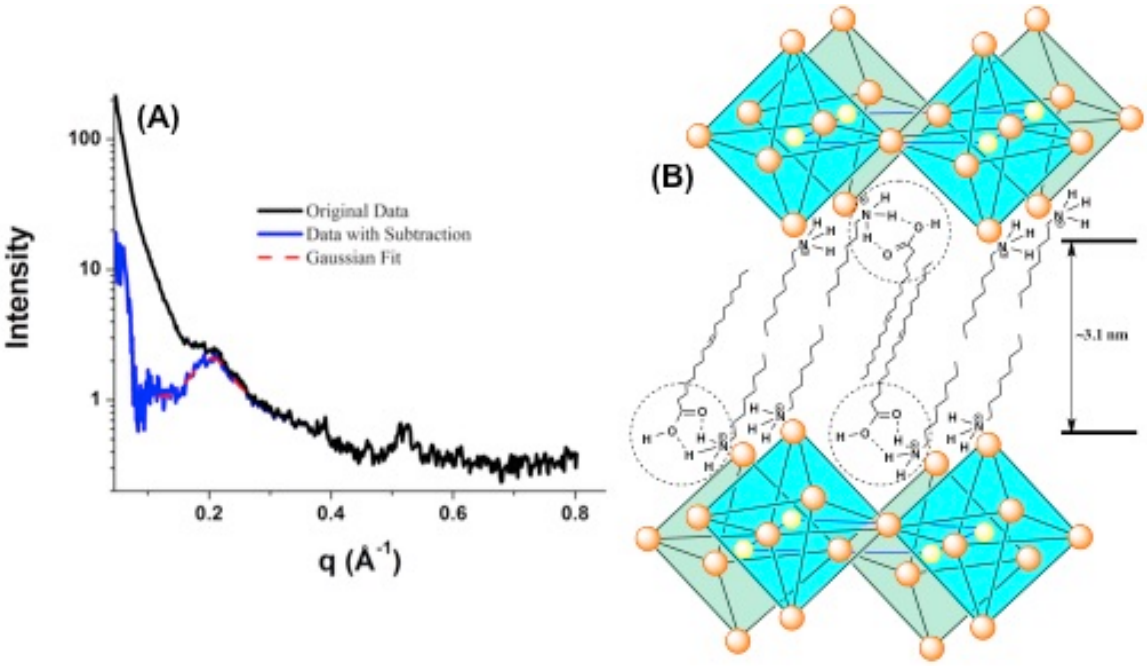

Figure 2.18 (A) GISAXS pattern of perovskite $CH_3NH_3PbBr_3$ QWs showing 3.2 nm wire separation. (B) Proposed surface ligand attachment and interdigitation of $CH_3NH_3PbBr_3$ QWs.

direction rather than forming three-dimensional nanostructures, because OAMI forms an ordered monolayer on the flat (001) wire surface.[159, 161] Our average inter-QW separation was calculated from the TEM image to be 3.1 nm, which is in agreement with the GISAXS value and is greater than two times the fully extended hydrocarbon chain length of OAMI (2.18 nm). This separation suggests participation of oleic acid in the

bilayer-type structure, which would increase the separation of the QWs. The OAMI monolayer has positively-charged ammonium groups that could interact through hydrogen bonding with the carboxylic acid groups of oleic acid. This addition of oleic acid would lead to bilayer-type structure of mixed composition of oleic acid and OAMIs between the $CH_3NH_3PbBr_3$ QWs (Figure 2.18B) and perhaps expand the bilayer thickness. The formation of a bilayer-type structure by oleic acid is known to occur even when it is attached to the surface of nanostructures.[137, 159] An electrostatic interaction between bromide ions and OAMI amine groups would allow substantial adsorption of surface passivating ligands onto the surface of the nanostructures, which is thermodynamically favorable due to release of adsorption enthalpy, and Van der Waals interaction would help drive hydrocarbon tail association, partial interdigitation, and bilayer-type structure formation.

2.4.7 Synthesis and Structural Characterization of $CH_3NH_3PbBr_3$ QPLs

We preformed the synthesis of $CH_3NH_3PbBr_3$ QPLs using a mixture of trichlorobenzene (TCB) and 1-octadecene (ODE) as cosolvents in which long-chain surface passivating ligands were dissolved (see Figure 2,1). Injection of soluble organic cation and metal salt precursors (themselves prepared in “good” solvents) into the cosolvents resulted in formation of colloidal QPLs. In this unique QPL synthesis, the nonpolar cosolvents act as a “poor” solvent that induces controlled crystallization of the precursors due to their lower solubility in nonpolar solvents. Briefly, oleic acid, hexadecylamine and octylammonium bromide were dissolved in TCB-ODE cosolvents at 60 ºC. Separately, CH_3NH_3Br and $PbBr_2$ precursors were prepared in N-dimethylformamide (good solvent) and injected into the cosolvent solution, resulting in

an immediate change of the solution from colorless to light yellow and indicating formation of NCs. The growth was quenched with acetone, and NCs were isolated by centrifugation. The detailed synthetic approach is available in the Experimental Section.

Figure 2.19A and 2.19B illustrate the low and high-resolution transmission electron microscopy (TEM) images of the $CH_3NH_3PbBr_3$ QPLs. The platelets appeared to be pseudorectangular in shape with average length and width of 55.8 ± 4.0 and 8.7 ± 1.2 nm, respectively. In some, cases the QPLs were aligned perpendicular to the carbon support film of the TEM grid. We used this orientation to determine the thickness which was 2.5 ± 0.5 nm corresponding to 3 monolayers of $CH_3NH_3PbBr_3$.[179] Figure 2.19D-F provides histograms of each dimension. From the HRTEM image (Figure 18C), an

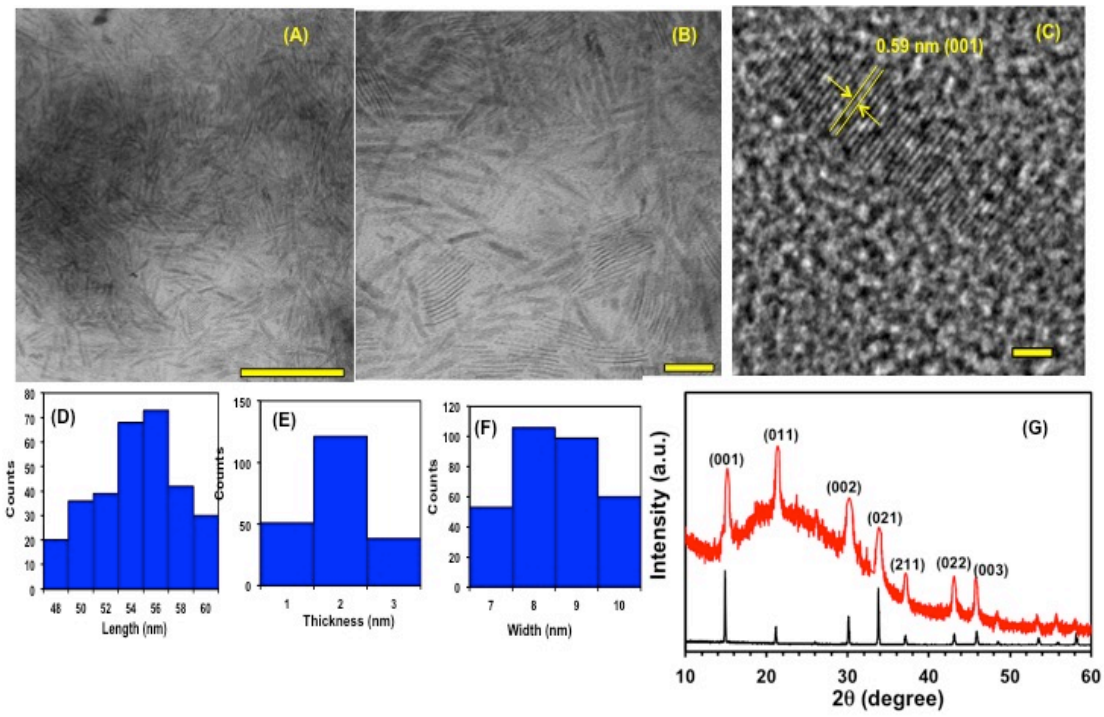

Figure 2.19 Low (A and B) and high (C) resolution TEM images of $CH_3NH_3PbBr_3$ QPLs. Scale bars are 100 nm, 50 nm, and 5 nm respectively. Histograms of dimension analysis of $CH_3NH_3PbBr_3$ QPLs (D-F). XRD pattern of the QPLs (red) and bulk (black) compared (G).

interplanar distance of 5.9 Å corresponding to the (001) crystal plane was also identified. Figure 18G shows an X-ray diffraction (XRD) pattern (red line) of the $CH_3NH_3PbBr_3$ QPLs in which peaks (2θ) at 14.9, 21.6, 30.2, 33.8, 37.0, 43.1, and 45.6º correspond to diffractions from (001), (011), (002), (021), (211), (022), and (003) planes, respectively, of cubic $CH_3NH_3PbBr_3$. The pattern is in agreement with that of single crystal bulk $CH_3NH_3PbBr_3$ perovskite (black line) with cubic crystal structure.[2] Importantly, the XRD peaks of our $CH_3NH_3PbBr_3$ QPLs are much broader than those of the large sheets reported in the literature[9, 145, 146] suggesting our structure has smaller dimensions. Energy dispersive spectroscopy (EDS) characterization (Figure 2.20) of our QPLs displayed a Pb:Br ratio of 1:3.1 that is in agreement with the $CH_3NH_3PbBr_3$ crystal structure in which Pb is present in the center of an octahedron formed by six bromide ions and CH_3NH_3 is present between two octahedra. Because the octylammonium ion is much larger than $CH_3NH_3^+$, it cannot incorporate into the perovskite structure. We should mention that prolong exposure of $CH_3NH_3PbBr_3$ QPLs to the electron beam in the TEM analysis resulted in formation of spherical NCs (Figure 2.20) and particles that were possibly metallic lead. This observation is in agreement with literature reports for square-shaped $CH_3NH_3PbBr_3$ sheets.[9, 145]

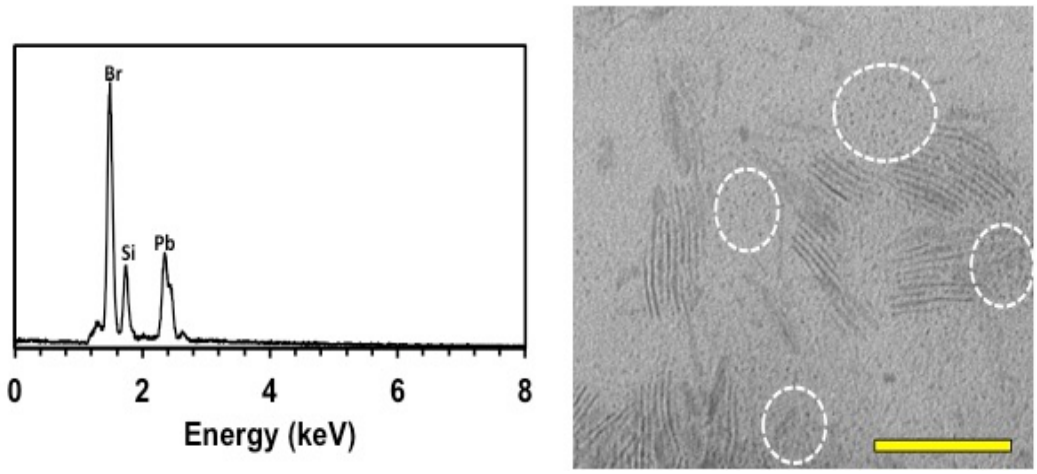

Figure 2.20 EDS analysis (A) showing 1:3 ratio of Pb:Br of $CH_3NH_3PbBr_3$ QPLs. TEM image (B) stability of the $CH_3NH_3PbBr_3$ QPLs under exposure to the 200 kV beam for 5 min

2.4.8 Steady-State Photophysical Properties $CH_3NH_3PbBr_3$ QPLs

The colloidal solution of $CH_3NH_3PbBr_3$ QPLs in toluene was characterized by UV-visible, PL, and time-correlated single photon counting (TCSPC) spectroscopy. As shown in Figure 2.21A, the QPLs display an absorption peak at 526 nm (2.34 eV) and PL peak at 528 nm (2.35 eV), thus having a very small Stokes shift (10 meV). Absorption and PL peaks of QPLs are blue-shifted 19 (90 meV) and 39 (190 meV) nm compared to those of single-crystal $CH_3NH_3PbBr_3$ bulk perovskite,[2] and blue-shfted 40 meV in comparison to square-shaped $CH_3NH_3PbBr_3$ sheets (150 nm in length and 30 nm in width) reported by Zhu et al.[9] The thin dimension of our QPLs as compared to the excitonic Bohr radius of $CH_3NH_3PbBr_3$ (estimated to be 1.4 nm)[145] suggests that the observed blue-shifts are attributable to quantum confinement effects. It is also important to mention that Tisdale and coworkers[144] have suggested $CH_3NH_3PbBr_3$ NCs that are >5.0 nm in diameter should not display quantum confinement effects. Therefore, the

observed absorption and PL peaks at 525 and 531 nm, respectively, reported by Schmidt et al.[165] for 6.0 nm diameter spherical $CH_3NH_3PbBr_3$ NCs are likely characteristic of square-shaped $CH_3NH_3PbBr_3$ large sheets that have undergone decomposition under exposure to the electron beam during TEM analysis and formed spherical NCs. Moreover, TEM images of 6.0 nm diameter spherical $CH_3NH_3PbBr_3$ NCs are identical to those reported by Zhu et al.[9] and Sichert et al.,[145] and the authors inferred formation of metallic Pb particles. Based on the literature, we conclude that the optical band-gap observed in our $CH_3NH_3PbBr_3$ QPLs is due to quantum confinement in thickness rather than length or width, as suggested for CdSe quantum plateles.[138, 141, 180]

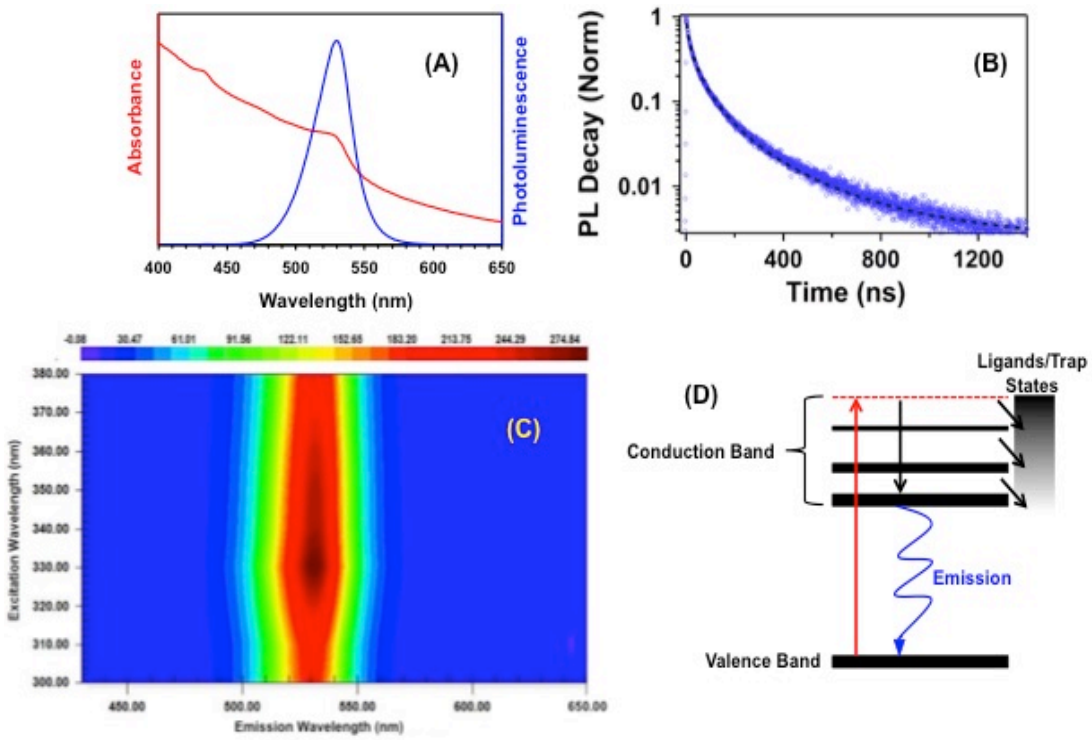

Figure 2.21 (A) UV-visible absorption (red line) and PL (blue line) spectra of $CH_3NH_3PbBr_3$ QPLs in toluene. (B) Time-resolved emission decay (blue circles) of QPLs and stretched exponential fit (black dashed line). (C) Pseudo colored emission intensity measured as a function of excitation wavelength (D) Schematic of recombination channels that reduce emission peak intensity as a function of excitation wavelength.

The time-resolved PL decay curve of the QPLs (Figure 2.21B) was fitted with a stretched exponential function (see Materials and Methods) to determine the average PL lifetime, which was 85 ns. This lifetime is much shorter than single-crystal $CH_3NH_3PbBr_3$ bulk perovskite (~500 ns).[2] Taken together, the small Stokes shifts and large lifetime are attributed to the good crystalline character of our QPLs in which large single-crystal facets allow PL decay through radiative recombination of photoexcited excitons. These data are also in agreement with the high PLQY of 52% for our $CH_3NH_3PbBr_3$ QPLs. To the best of our knowledge, this is the highest PLQY reported for 2D NCs of $CH_3NH_3PbBr_3$ perovskites.[9, 145, 146] Importantly, the PLQY of our three-four monolayer thick $CH_3NH_3PbBr_3$ platelets is slightly higher than that reported for four monolayer thick $CsPbBr_3$ platelets.[181] Using PL-QY and PL lifetime, we calculated the radiative lifetime (k_r) and k_{nr} of our $CH_3NH_3PbBr_3$ QPLs of 6.1 $X10^6$ s^{-1} and 5.6 $X10^6$ s^{-1}, respectively, which are also in agreement with the presence of few trap states in QPLs and most exciton recombination takeing place radiatively. We believe, this is due to the combination of good crystalline character and that the surface of the QPLs was nicely passivated with ligands, which mostly eliminated the surface defects and nonradiative trap states. In this context, the PL intensity of our QPLs as a function of excitation wavelength showed a constant emission wavelength maximum at 528 nm (see pseudo-colored representation in Figure 2.21C). However, the PL intensity decreased as the excitation wavelength decreased (excitation energy increased) suggesting that excited electrons were transferred to the higher energy states of surface passivating ligands. This excitonic recombination would take place through a separate channel, possibly through

the ligand monolayer[182] instead of through direct recombination at the edge of the valence band of $CH_3NH_3PbBr_3$ QPLs (see Figure 2.21D).

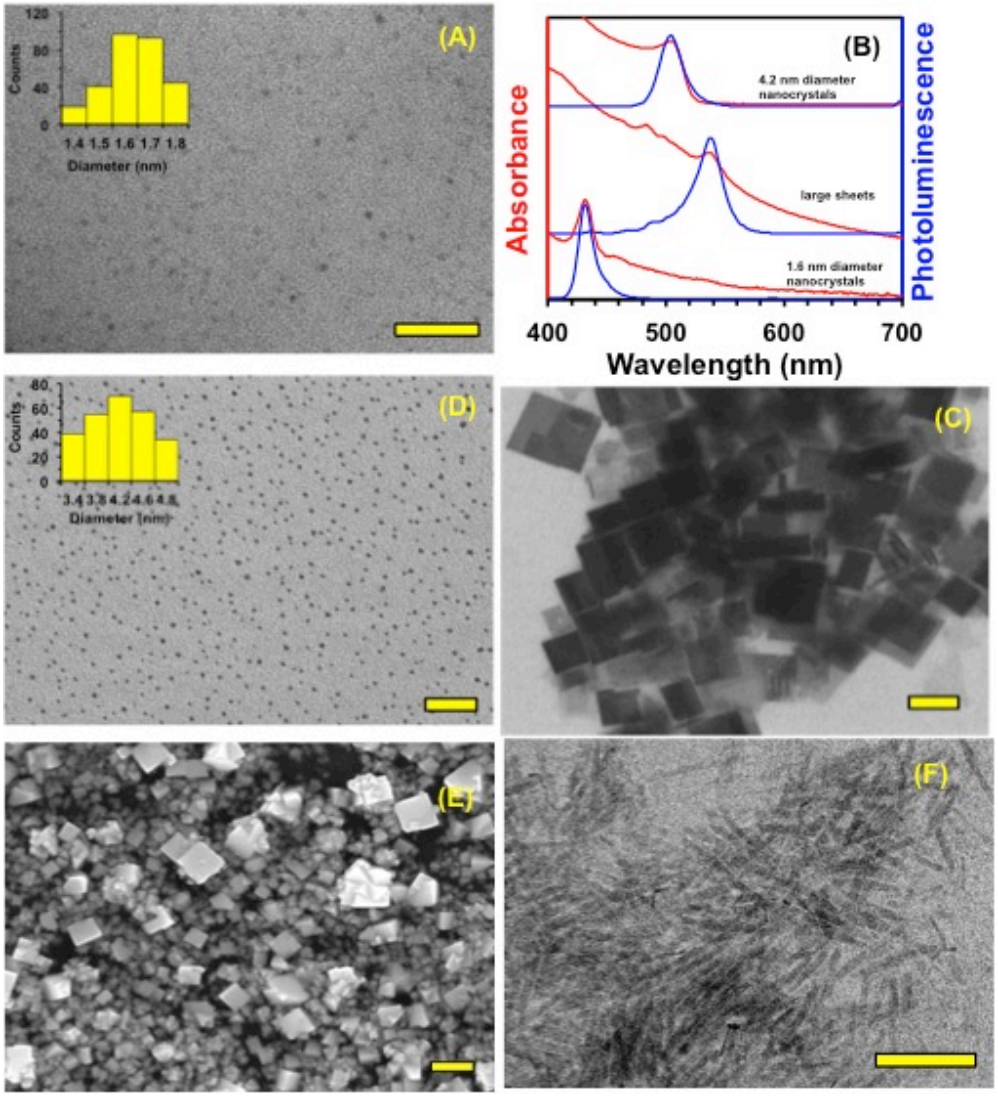

Figure 2.22 (A) TEM image of 1.6 ± 0.2 nm diameter spherical $CH_3NH_3PbBr_3$ NCs isolated at 5 sec reaction time in the quantum platelet synthesis. These NCs act as precursor "seeds" for the formation of QPLs. Scale bar is 50 nm. (B) UV-visible absorption (red) and PL (blue) spectra of NCs shown in (A), (C) and (D). (C) TEM image of purified $CH_3NH_3PbBr_3$ multilayer structures containing an infinite layer of unit cells (Figure 1, bottom right). Scale bar is 100 nm. (D) TEM image of 4.2 ± 0.4 nm diameter spherical $CH_3NH_3PbBr_3$ NCs synthesized under the same experimental conditions as QPLs except using octylammonium bromide (Figure 2.1, bottom left). Scale bar is 50 nm. (E) SEM image of bulk $CH_3NH_3PbBr_3$ perovskite synthesized in the absence of hexadecylamine. Scale bar is 1 mm. (F) TEM image of $CH_3NH_3PbBr_3$ QPLs synthesized using decylamine instead of hexadecylamine. The scale bar is 100 nm

Comparison of the optical band-gap between $CH_3NH_3PbBr_3$ QPLs and literature reports of theoretical calculations on square-shaped sheets of similar perovskite[145] reveals that our QPLs displayed a comparable band-gap. From their calculations using the Kronig-Penny model, Sichert et al.[145] suggested that in stacked NCs, as are found in our case, excitonic wave functions (electron and/or hole) could extend outside of the NC inorganic core boundary, become entangled with the wave functions of neighboring NCs, and result in the formation of minbands.[183, 184] Under such a state of exciton wave function delocalization, the experimental optical band-gap of $CH_3NH_3PbBr_3$ NCs will be smaller than the infinite quantum well calculation, which has also been reported for rectangular-shaped $CsPbBr_3$ QPLs by Akkerman et al.[134]

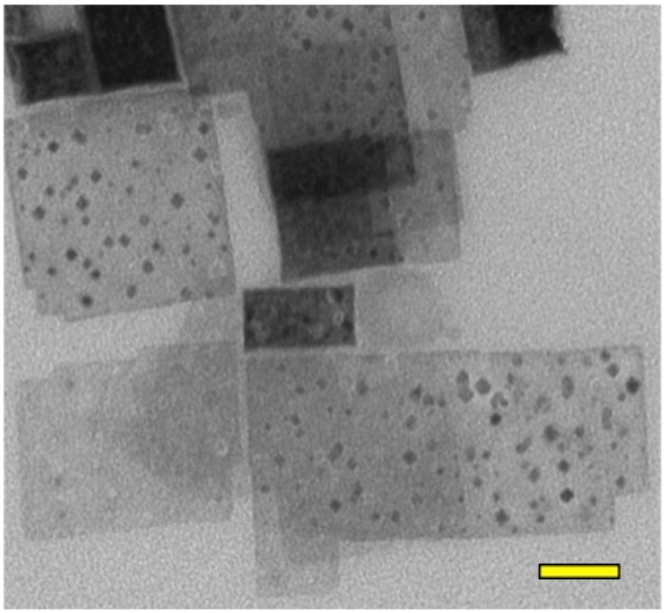

Figure 2.23 Stability of the $CH_3NH_3PbBr_3$ large sheets under exposure to the 200 kV TEM beam energy for 5 min. Scale bar is 50 nm

2.4.9 Formation Mechanism of $CH_3NH_3PbBr_3$ QPLs and their Hierarchical Structure

Unraveling the growth mechanisms responsible for anisotropic NCs is important for preparation of various shapes and to study their structure-property relationships. According to the literature, growth mechanisms fall into two catagories: (1) Growth by monomer attachment onto the growing NC as described by the classical LaMer model[185, 186] and (2) growth by attachment of NC commonly known as oriented attachment.[156, 157, 187] As shown in Figure 2.22A, our QPL formation begins by nucleation of 1.6 ± 0.2 nm diameter spherical NCs, which displayed both absorption and PL emission peaks at 430 nm (Figure 2.22B) and resemble two unit cells of $CH_3NH_3PbBr_3$ perovskite.[144] Therefore, we believe that $CH_3NH_3PbBr_3$ QPL formation is driven by mesoscale-assisted growth of seed NCs ("building blocks"), which is part of mechanism (1) described above. Perhaps our growth follows 2D self-organization and *in situ* recrystallization of seeds as shown for ceria nanosheets[188] or 2D template lameller structure as demonstrated with CdSe QPLs,[141, 180] or even follows oriented assembly of seeds into ultrathin 2D PbS sheets.[159] In the case of ultrathin PbS sheets,[159] the authors observed sheet discontinuity. However, our TEM analysis did not show such morphology, but rather QPLs are quite uniform in dimension with continuous crystalline character.

In QPL growth, choice of solvents and surface ligands plays a critical role. We have found that presence of the chlorinated solvent TCB in the reaction mixture is absolutely necessary in order to obtain QPLs. In the absence of TCB, formation of square-shaped, stacked $CH_3NH_3PbBr_3$ nanosheets was observed (see Figure 2.22C) similar to those reported for $CH_3NH_3PbBr_3$,[9, 144-146] and $CsPbBr_3$ sheets.[181] As shown in Figure 2.22B, the photophysical properties of our sheets closely resemble those

reported in the literature[144, 145] and indicate formation of multilayer structures containing an infinite layer of unit cells. The stability of these large $CH_3NH_3PbBr_3$ sheets under exposure to the electron beam was examined and the sheets were found to be unstable leading to the formation of 7-10 nm diameter spherical NCs, possibly of metallic Pb, as reported earlier (Figure 2.23).[9, 145, 179] In an additional experiment serving as a control, formation of nearly monodispersed spherical $CH_3NH_3PbBr_3$ NCs of 4.2 ± 0.4 nm diameter was observed when the synthesis was conducted under the same experimental conditions as QPLs except using octylammonium bromide (Figure 2.22D). A synthesis

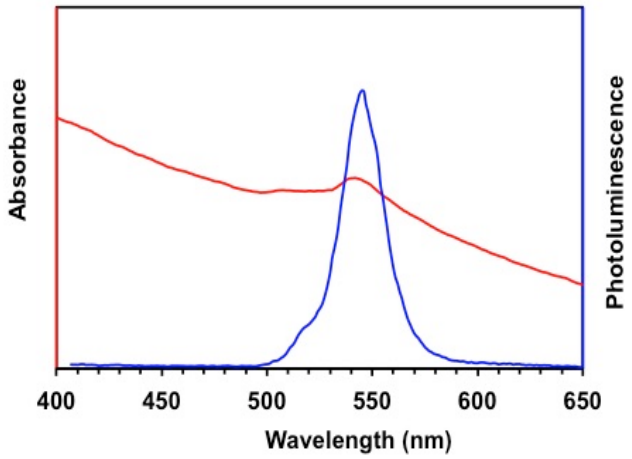

Figure 2.24 UV-visible absorption (red, 540 nm) and PL (blue, 545 nm) spectra of bulk $CH_3NH_3PbBr_3$ perovskites synthesized in the absence of hexadecylamine.

without hexadecylamine produced organically insoluble bulk $CH_3NH_3PbBr_3$ material , which displayed an absorption peak at 540 nm (2.3 eV) and PL peak at 545 nm (2.28 eV) (see Figure 2.24). Importantly, the energy-gaps are much closer than those previously

assigned as bulk $CH_3NH_3PbBr_3$ materials in the literature.[2] Thus, the optical band-gaps of square-shaped $CH_3NH_3PbBr_3$ sheets that are assigned as bulk band-gaps in the literature[144, 145] may not reflect this photophysical property exactly. Perhaps some degree of quantum confinement still exists in $CH_3NH_3PbBr_3$ sheets because in bulk material the band-gap is expected to be >540 nm. Finally, we were able to synthesize

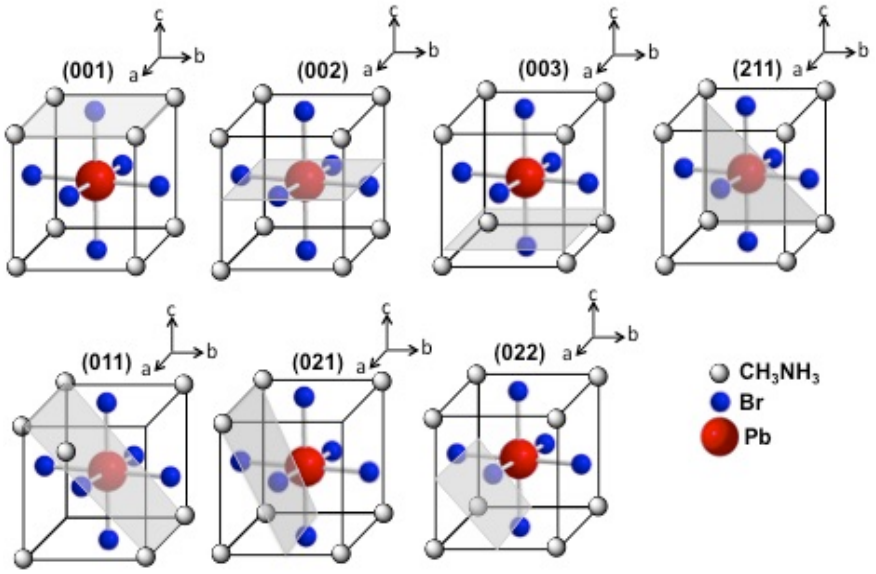

Figure 2.25 Principal crystallographic planes of cubic $CH_3NH_3PbBr_3$ perovskite.[9]

$CH_3NH_3PbBr_3$ QPLs using decylamine instead of hexadecylamine but the ordered hierarchical stacking of the platelets was not observed (see Figure 2.22F). Thus, appropriate chemical structure of surface passivating ligands is required to control various interactions and to achieve higher order assemblies of the NCs as discuss below.

Based on our systematic control experiments, we hypothesize that $CH_3NH_3PbBr_3$ QPL growth is controlled by TCB and the octylammonium ion. At the beginning of the growth process, 1.6 nm diameter seeds are formed in which the planner (001) plane is passivated by octylammonium ions and hexadecylamine through chemisorption.

Importantly, the presence of a long-chain amine (e.g., hexadecylamine) in the reaction mixture is critical to keeping the seeds soluble and allowing further 2D growth. Such growth can be categorized as mesoscale growth resulting from cooperative interactions and entropically-driven processes governed by van der Waals interactions between surface ligands and electrostatic interactions between ions.[10] Furthermore, a small amount of octylammonium bromide initiated the chemisorption of the cationic head group octylamine and inhibited the faster Oswald ripening-driven growth along the (001) plane. Moreover, this plane has lower surface energy in comparison to other high index planes such as (011), and (022).[189] Figure 2.26 illustrates the different crystallographic planes of $CH_3NH_3PbBr_3$ perovskite with cubic crystal structure. Taken together, the long hydrophobic chains of hexadecylamine and octylammonium ions keep the QPLs thinner by allowing only an additional 1-2 unit cells to attach onto the (001) plane. ^{1}H NMR analysis showed absence of oleic acid in the seeds (Figure 2.26). Therefore, growth of seeds to QPLs occurs through continuous attachment of monomers predominantly along the (002), (003), (011), and (022) planes. Our hypothesis is supported by the XRD pattern of QPLs in which a significant increase in intensity of these planes is observed (Figure 2.18C, red trace) in comparison to the standard XRD pattern of bulk $CH_3NH_3PbBr_3$ perovskite (Figure 2.19G black trace). In addition, ability of the chlorinated solvent TCB to associate with Pb allows it to adsorb onto the reactive (002) and (003) planes and control the width.[159] This control is supported by the formation of square-shaped nanosheets (Figure 2.22C) with comparable dimension along their length as the QPLs when synthesis was carried out without using TCB. Finally, the increase in length of $CH_3NH_3PbBr_3$ QPLs occurs along the (011) and (022) planes. When all the monomers

are consumed, oleic acid physisorbs on these planes and provides the lateral structural stabilization of 2D assembles. ^{1}H NMR and FTIR analyses confirm the presence of oleic acid and amines on the surface of our QPLs (see Figure 2.26 and 2.27).

As shown in Figure 2.19A, $CH_3NH_3PbBr_3$ QPLs appear to self-assemble into a hierarchical structure (stacked). In order to acquire further structural information on QPLs, specifically inter-platelets distance, we performed the small angle X-ray scattering (SAXS) analysis with a coplanar sample position and determined an effective distance of 3.5 ± 0.01 nm between QPLs (Figure 2.29). This value is comparable to the spacing

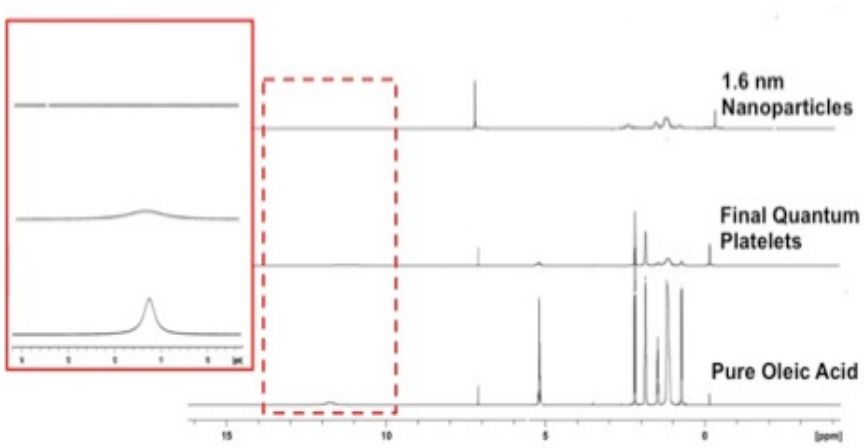

Figure 2.26 ^{1}H NMR analysis was performed on both the 1.6 nm diameter nanocrystals obtained at 5 s (top) and the final quantum platelets (middle). Pure oleic acid (bottom) was used as a reference for the peak positions

between stacked QPLs of 4.0 ± 0.2 nm as calculated from our TEM analysis (Figure 2.19C). Additionally, the 34.9 Å peak was accompanied by an additional higher order peak (2q = 17.45 Å), which would indicate a well ordered stacked QPLs. This spacing is important in the context of attachment of ligands onto the surface of our QPLs, specifically indicating that oleic acid is not passivating the (001) planes of $CH_3NH_3PbBr_3$ perovskite. Under such circumstances, the effective distance between the stacked QPLs would be expected to be <3.0 nm, as reported by Bekenstein et al. for $CsPbBr_3$

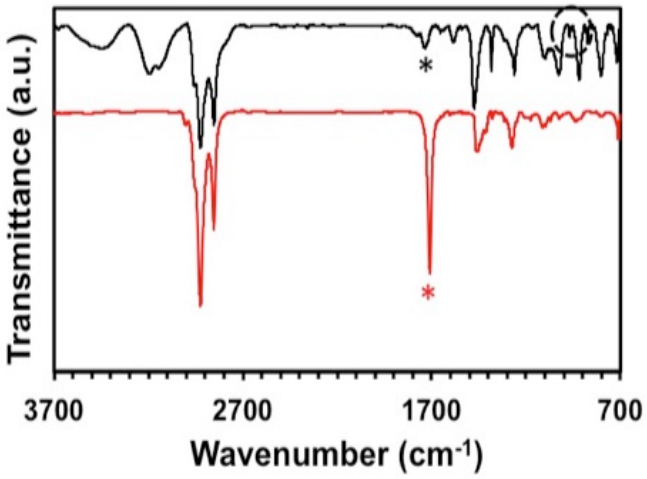

Figure 2.27 The FTIR analysis was used to characterize the surface ligand chemistry of $CH_3NH_3PbBr_3$ quantum platelets (black) through comparison with pure oleic acid (red). The characteristic carbonyl peak (C=O) stretch is observed at 1705 cm^{-1} (red asterisk) in pure oleic acid and 1730 cm^{-1}(black asterisk) in the quantum platelets. This red-shift suggests an electrostatic interaction of this group with the platelet surface. The presence of oleic acid can be further confirmed by the appearance of the O-H stretch at 970 cm^{-1} (dotted circle).[11] In the quantum platelet spectra, broad intense peaks appearing at 3143 and 3196 cm^{-1} are assigned to the $–NH_2$ symmetric stretching bands from the long chain amines.[12] The peaks at 1655 and 1586 cm^{-1} can be attributed to the asymmetric and symmetric $-NH_3^+$ deformations from octylammonium ions and hexadecylamine.[13] The peak 3417 cm^{-1} can be assigned to the effects of hydrogen bonding between the -COOH group from oleic acid and $–NH_3^+$ of either

nanoplates.[181] Therefore, TEM and SAXS analyses strengthen our proposed growth model (Figure 2.28) and support the idea that hexadecylamine and octylammonium attach onto the planner (001) surface of the QPL. A slight reduction of inter-platelet spacing in comparison to the theoretical value of 5.04 nm, which is twice the length of the longest ligand hexadecylamine (ChemBioDraw 14.0), can be explained by partial ligand chain interdigitation. Cooperative interactions between surface passivating ligands are involved in ligand alkyl chain alignment and ligand chain interdigitation leading to mesoscale

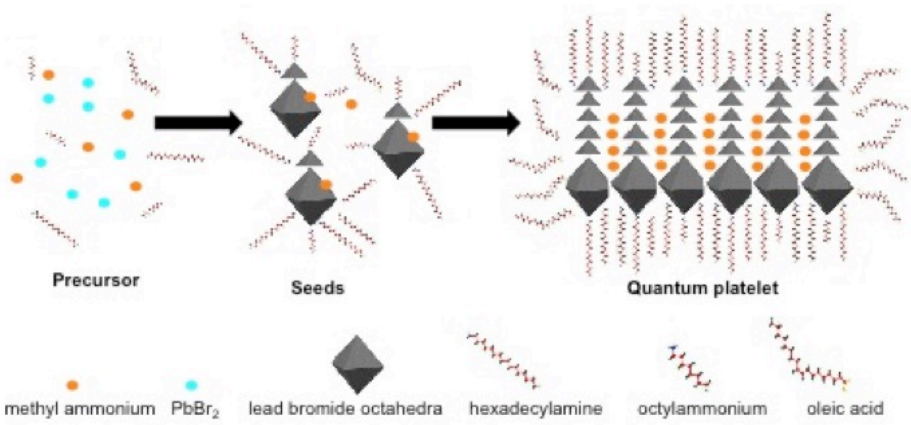

Figure 2.28 Schematic diagram of entropically-controlled mesoscale-assisted growth of 1.6 nm diameter $CH_3NH_3PbBr_3$ seed nanocrystals into quantum platelets. The quantum platelet growth is preferential along the length and width axes, while ligand-mediated interactions maintain the formation of 2D hierarchical structure

assembly. In this context, appearance of randomly oriented QPLs in the TEM analysis was observed when decylamine was used instead of hexadecylamine (Figure 2.22E) in the synthesis. Thus, the presence of long-chain ligands in the reaction medium is essential for higher order assembly. Importantly, ligand-mediated interactions and formation of complex hierarchical structures through self-assembly of 2D NCs have been documented

for metal chalocogenides (e.g., CdTe, CdSe, and PbS)[138, 141, 159, 180, 190] and $CsPbX_3$ nanoplates.[134, 181]

2.4.10 Synthesis and Characterization of $CH_3NH_3PbBr_3$ Quantum Cubes

By systematically controlling the growth conditions, i.e., the reaction temperature and surface ligand chemistry, we obtained nearly monodispersed $CH_3NH_3PbBr_3$ quantum cubes. Figure 2.30A; illustrate the TEM images of quantum cubes having 12.1 ± 1.2 nm edge-lengths. Figure 2.30B shows the XRD pattern of quantum cubes that matches with the cubic crystal structure of bulk $CH_3NH_3PbBr_3$ perovskite.[2] The structure of our $CH_3NH_3PbBr_3$ quantum cubes resembles $CH_3NH_3PbI_3$[146] or $CsPbX_3$[155, 191, 192] quantum cubes reported in the literature. As shown in Figure 2.30C, the quantum cubes display an absorption peak at 516 nm (2.40 eV) and PL peak at 525 nm (2.36 eV) giving a Stokes shift of 9 nm (40 meV). The absorption and PL peaks of our quantum cubes are blue-shifted 29 nm (130 meV) when compared to that of single-crystal $CH_3NH_3PbBr_3$ bulk perovskite[2] because of quantum confinement. The PL-QY of our $CH_3NH_3PbBr_3$ quantum cubes was determined to be 28%. This value is comparable to $CH_3NH_3PbI_3$[146] quantum cubes but is nearly three-fold lower than $CsPbX_3$ quantum cubes.[155, 192] The lower PL-QY of our quantum cubes could be due to relatively poorer crystalline character because of the low temperature used during synthesis (110 ^oC) in comparison with $CsPbX_3$ quantum cubes, which are commonly prepared at higher temperature (>160 ^oC). Moreover, the presence of surface-related mid-gap trap states could also influence the PL-QY. The average PL lifetime of our $CH_3NH_3PbBr_3$ quantum cubes was found to be 39 ns, as determined from the time-resolved PL decay curve (Figure 2.30D). Thus the k_r and k_{nr} values for the quantum cubes were calculated to be

7.2 X10^6 s^{-1} and 18.4 X10^6 s^{-1}, respectively, which suggests the presence of nonradiative trap states. Finally, examination of PL intensity as a function of excitation wavelength gave an increase in intensity up to a particular wavelength and then a decrease as excitation energy continued to be increased, suggesting variable excitonic recombination channels that could also include surface passivating ligands.

2.4.11 Growth Mechanism of $CH_3NH_3PbBr_3$ Quantum Cubes

We hypothesize that the formation of $CH_3NH_3PbBr_3$ quantum cubes is controlled by a kinetically-driven growth process. It is known that kinetic growth requires high flux of monomers, which can be achieved by adequate supply of thermal energy (*kT*).[193] In our investigation, we achieved a high flux of monomers by using a higher reaction temperature (110 ^oC) than is commonly used for $CH_3NH_3PbBr_3$ NC synthesis.[144-146, 159, 165, 194] Moreover, the kinetic energy barrier for transformation of monomers to NCs depends on the surface energy of the crystal facets, which can be controlled by the concentration of surface passivating ligands present in the reaction mixture. Specifically, the structure and number of NC-bound surface passivating ligands control the kinetic

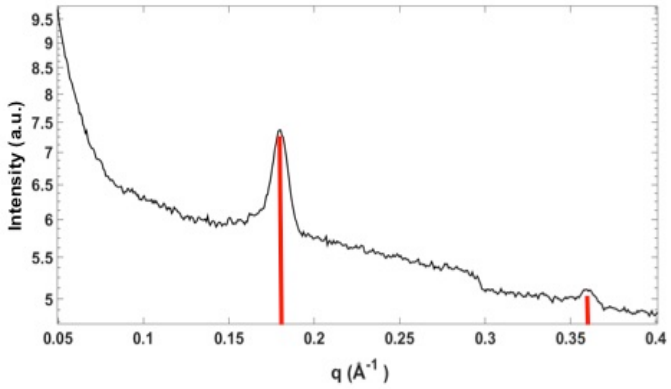

Figure 2.29 Small angle-X-ray scattering (SAXS) pattern of perovskite $CH_3NH_3PbBr_3$ quantum platelets showing 3.5 nm platelet separation. The inset shows long-range order of stacked platelets.

energy barrier. In comparison to $CH_3NH_3PbBr_3$ QPLs, QCs were synthesized in the presence of a lower concentration of passivating ligands. Since oleic acid could form a self-assembled monolayer attached onto the planar (001) surface[159] of a cubic crystal, growth presumably takes place along the (022) and (003) planes (see Figure 2.25). Moreover, in the XRD pattern of quantum cubes, a slight increase in intensity of these two planes was observed (Figure 2.30B, red trace) in comparison to the standard XRD pattern of bulk $CH_3NH_3PbBr_3$ perovskite (Figure 2.30B, black trace) supporting our suggestion. Nevertheless, the roles of reaction temperature and surface ligand chemistry in the formation of anisotropically-shaped perovskite NCs can be more precisely determined by characterizing the seed particles, as demonstrated for metal,[195, 196]

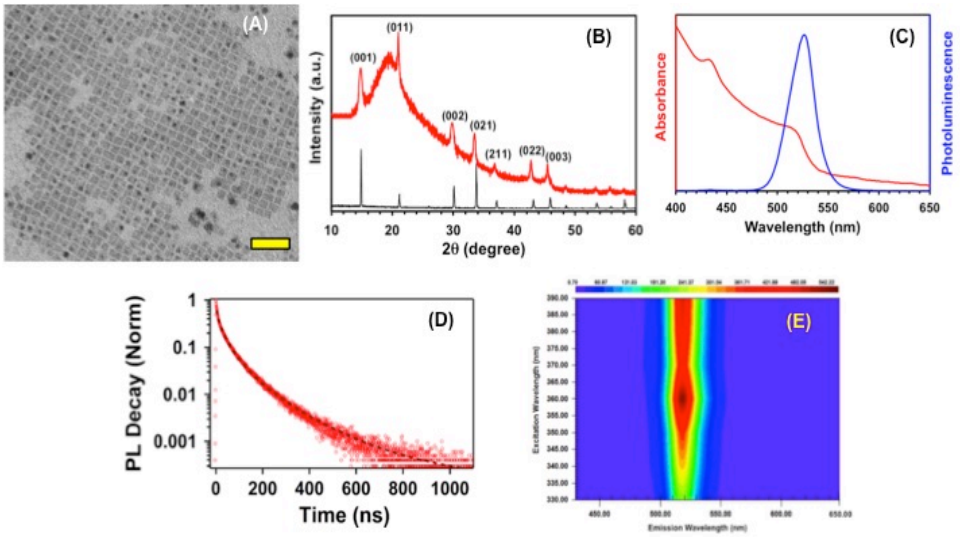

Figure 2.30 (A) TEM images of $CH_3NH_3PbBr_3$ quantum cubes with 50 nm scale bar. (B) XRD pattern of quantum cubes (red) compared with the bulk, single-crystal $CH_3NH_3PbBr_3$ perovskite (black), which was prepared according to the literature.[2] The broad peak covering 15-30° is from the glass coverslip. (C) UV-visible absorption (red line) and PL (blue line) spectra of $CH_3NH_3PbBr_3$ quantum cubes in toluene. (D) Time-resolved emission decay (red circles) of quantum cubes and stretched exponential fit (black dashed line). (E) Pseudo-colored emission intensity measured as a function of excitation wavelength.

metal oxide,[197] and metal chalocogenide semiconductor[198] NCs. Unfortunately, the low stability of organic-inorganic hybrid perovskite NCs under electron beam exposure in TEM analysis makes such determination extremely challenging.

2.5 Conclusions

In summary, we have determined that a combination of experimental parameters control the shape of NCs and their interactions to assemble into complex superstructures. In this investigation, we present simple, versatile, and programmable colloidal synthetic method for preparation of anisotropically-shaped $CH_3NH_3PbBr_3$ perovskite NCs (wires, platelets, and cubes) and the experimental data presented has established the mechanism of their formation. These NCs exhibit unprecedented quantum yield and PL lifetimes, and we believe, our demonstration of ligand controlled growth and assembly will inspire rational design of colloidal synthetic methods allowing preparation of diverse ionic, anisotropic semiconductor perovskite nanostructures. Future studies of these anisotropically-shaped perovskite NCs will focus on preparation of ordered superlattices through solvent-induced self-assembly processes and will enhance their performance in solid-state devices leading to a variety of potential future applications.

2.6 Appendix

Table 2.1. A comparison of absorption, photoluminescence, and excited state properties of $CH_3NH_3PbBr_3$ perovskite nanostructures at various time points during the synthesis.

Reaction time (sec)	Abs max (nm)	PL max (nm)	PL peak FWHM (nm)	PL-QY (%)	PL Lifetime (ns)	Radiative rate constant $(s^{-1})^2$	Non-radiative rate constant $(s^{-1})^2$
30	426	429	20	~1.3	τ_{fast} = 4 ± 1 $\tau_{slow=}$ = 9 ± 2	1.4×10^6	109.6×10^6
60	495	514	22	16 ± 2	$\tau_{fast=}$ = 9 ± 2 $\tau_{slow=}$ = 50 ± 5	3.2×10^6	16.8×10^6
120	511	517	22	44 ± 3	τ_{fast} = 10 ± 1 τ_{slow} = 63 ± 8	6.8×10^6	8.9×10^6
240	522	524	25	59 ± 7	τ_{fast} = 11 ± 1 τ_{slow} = 89 ± 11	6.6×10^6	4.6×10^6

Table 2.2. Comparison of photophysical properties of differently-shaped $CH_3NH_3PbBr_3$ nanocrystals.

Morphology	Reaction temp. (°C)	Absorption peak in nm	Absorption peak in eV	Emission peak in nm	Emission peak in eV	Quantum yield (%)
Quantum platelets	60	526	2.34	528	2.35	52
Large sheets	60	530	2.40	532	3.33	43
Spherical nanocrystals	60	501	2.48	503	2.47	6
Quantum cubes	110	516	2.40	525	2.36	28

2.7 References

1. Green, M.A., A. Ho-Baillie, and H.J. Snaith, *The emergence of perovskite solar cells.* Nature Photonics, 2014. **8**(7): p. 506-514.
2. Park, N.-G., *Organometal perovskite light absorbers toward a 20% efficiency low-cost solid-state mesoscopic solar cell.* The Journal of Physical Chemistry Letters, 2013. **4**(15): p. 2423-2429.
3. Service, R., *Energy technology. Perovskite solar cells keep on surging.* Science (New York, NY), 2014. **344**(6183): p. 458.
4. Snaith, H.J., *Perovskites: the emergence of a new era for low-cost, high-efficiency solar cells.* The Journal of Physical Chemistry Letters, 2013. **4**(21): p. 3623-3630.
5. Chondroudis, K. and D.B. Mitzi, *Electroluminescence from an organic-inorganic perovskite incorporating a quaterthiophene dye within lead halide perovskite layers.* Chemistry of materials, 1999. **11**(11): p. 3028-3030.
6. Mitzi, D.B., K. Chondroudis, and C.R. Kagan, *Organic-inorganic electronics.* IBM journal of research and development, 2001. **45**(1): p. 29-45.
7. Mitzi, D.B., *Synthesis, crystal structure, and optical and thermal properties of (C4H9NH3) 2MI4 (M= Ge, Sn, Pb).* Chemistry of materials, 1996. **8**(3): p. 791-800.
8. Mitzi, D.B., M. Prikas, and K. Chondroudis, *Thin film deposition of organic-inorganic hybrid materials using a single source thermal ablation technique.* Chemistry of materials, 1999. **11**(3): p. 542-544.
9. Kojima, A., et al., *Organometal halide perovskites as visible-light sensitizers for photovoltaic cells.* Journal of the American Chemical Society, 2009. **131**(17): p. 6050-6051.
10. Kim, H.-S., et al., *Lead iodide perovskite sensitized all-solid-state submicron thin film mesoscopic solar cell with efficiency exceeding 9%.* Scientific reports, 2012. **2**: p. 591.
11. Lee, M.M., et al., *Efficient hybrid solar cells based on meso-superstructured organometal halide perovskites.* Science, 2012. **338**(6107): p. 643-647.
12. Gao, P., M. Grätzel, and M.K. Nazeeruddin, *Organohalide lead perovskites for photovoltaic applications.* Energy & Environmental Science, 2014. **7**(8): p. 2448-2463.
13. Stranks, S.D. and H.J. Snaith, *Metal-halide perovskites for photovoltaic and light-emitting devices.* Nature nanotechnology, 2015. **10**(5): p. 391-402.
14. Sum, T.C. and N. Mathews, *Advancements in perovskite solar cells: photophysics behind the photovoltaics.* Energy & Environmental Science, 2014. **7**(8): p. 2518-2534.
15. Eperon, G.E., et al., *Formamidinium lead trihalide: a broadly tunable perovskite for efficient planar heterojunction solar cells.* Energy & Environmental Science, 2014. **7**(3): p. 982-988.
16. Noh, J.H., et al., *Chemical management for colorful, efficient, and stable inorganic–organic hybrid nanostructured solar cells.* Nano letters, 2013. **13**(4): p. 1764-1769.

17. Hao, F., et al., *Lead-free solid-state organic-inorganic halide perovskite solar cells.* Nature Photonics, 2014. **8**(6): p. 489-494.
18. Noel, N.K., et al., *Lead-free organic–inorganic tin halide perovskites for photovoltaic applications.* Energy & Environmental Science, 2014. **7**(9): p. 3061-3068.
19. Hao, F., et al., *Solvent-mediated crystallization of CH3NH3SnI3 films for heterojunction depleted perovskite solar cells.* Journal of the American Chemical Society, 2015. **137**(35): p. 11445-11452.
20. De Wolf, S., et al., *Organometallic halide perovskites: sharp optical absorption edge and its relation to photovoltaic performance.* The journal of physical chemistry letters, 2014. **5**(6): p. 1035-1039.
21. Yin, W.J., T. Shi, and Y. Yan, *Unique properties of halide perovskites as possible origins of the superior solar cell performance.* Advanced Materials, 2014. **26**(27): p. 4653-4658.
22. Leijtens, T., et al., *Electronic properties of meso-superstructured and planar organometal halide perovskite films: charge trapping, photodoping, and carrier mobility.* ACS nano, 2014. **8**(7): p. 7147-7155.
23. Stranks, S.D., et al., *Electron-hole diffusion lengths exceeding 1 micrometer in an organometal trihalide perovskite absorber.* Science, 2013. **342**(6156): p. 341-344.
24. Wehrenfennig, C., et al., *High charge carrier mobilities and lifetimes in organolead trihalide perovskites.* Advanced materials, 2014. **26**(10): p. 1584-1589.
25. Xing, G., et al., *Long-range balanced electron-and hole-transport lengths in organic-inorganic CH3NH3PbI3.* Science, 2013. **342**(6156): p. 344-347.
26. Garnett, E. and P. Yang, *Light Trapping in Silicon Nanowire Solar Cells.* Nano Lett., 2010. **10**(3): p. 1082-1087.
27. Huo, Z., et al., *Sub-Two Nanometer Single Crystal Au Nanowires.* Nano Lett., 2008. **8**(7): p. 2041-2044.
28. Duan, X., et al., *Indium phosphide nanowires as building blocks for nanoscale electronic and optoelectronic devices.* Nature, 2001. **409**(6816): p. 66-69.
29. Cui, Y., et al., *Nanowire Nanosensors for Highly Sensitive and Selective Detection of Biological and Chemical Species.* Science, 2001. **293**(5533): p. 1289-1292.
30. Holmes, J.D., et al., *Control of Thickness and Orientation of Solution-Grown Silicon Nanowires.* Science, 2000. **287**(5457): p. 1471-1473.
31. Huang, M.H., et al., *Room-Temperature Ultraviolet Nanowire Nanolasers.* Science, 2001. **292**(5523): p. 1897-1899.
32. Wang, J., et al., *Highly Polarized Photoluminescence and Photodetection from Single Indium Phosphide Nanowires.* Science, 2001. **293**(5534): p. 1455-1457.
33. Cui, Y., et al., *High Performance Silicon Nanowire Field Effect Transistors.* Nano Lett., 2003. **3**(2): p. 149-152.
34. Goldberger, J., et al., *Silicon Vertically Integrated Nanowire Field Effect Transistors.* Nano Lett., 2006. **6**(5): p. 973-977.
35. Huang, Y., et al., *Logic Gates and Computation from Assembled Nanowire Building Blocks.* Science, 2001. **294**(5545): p. 1313-1317.

36. Duan, X., et al., *Single-nanowire electrically driven lasers.* Nature, 2003. **421**(6920): p. 241-245.
37. Hahm, J.-i. and C.M. Lieber, *Direct Ultrasensitive Electrical Detection of DNA and DNA Sequence Variations Using Nanowire Nanosensors.* Nano Lett., 2004. **4**(1): p. 51-54.
38. Ebbesen, T.W. and P.M. Ajayan, *Large-scale synthesis of carbon nanotubes.* Nature, 1992. **358**(6383): p. 220-222.
39. Iijima, S., *Helical microtubules of graphitic carbon.* Nature, 1991. **354**(6348): p. 56-58.
40. Gargas, D.J., et al., *High Quantum Efficiency of Band-Edge Emission from ZnO Nanowires.* Nano Lett., 2011. **11**(9): p. 3792-3796.
41. Barrelet, C.J., et al., *Synthesis of CdS and ZnS Nanowires Using Single-Source Molecular Precursors.* J. Am. Chem. Soc., 2003. **125**(38): p. 11498-11499.
42. Dong, A., et al., *Colloidal GaAs Quantum Wires: Solution–Liquid–Solid Synthesis and Quantum-Confinement Studies.* J. Am. Chem. Soc., 2008. **130**(18): p. 5954-5961.
43. Cho, K.-S., et al., *Designing PbSe Nanowires and Nanorings through Oriented Attachment of Nanoparticles.* J. Am. Chem. Soc., 2005. **127**(19): p. 7140-7147.
44. Huang, Y., et al., *Directed Assembly of One-Dimensional Nanostructures into Functional Networks.* Science, 2001. **291**(5504): p. 630-633.
45. Horváth, E., et al., *Nanowires of Methylammonium Lead Iodide (CH3NH3PbI3) Prepared by Low Temperature Solution-Mediated Crystallization.* Nano Lett., 2014. **14**(12): p. 6761-6766.
46. Im, J.-H., et al., *Nanowire Perovskite Solar Cell.* Nano Lett., 2015. **15**(3): p. 2120-2126.
47. Zhu, P., et al., *Direct Conversion of Perovskite Thin Films into Nanowires with Kinetic Control for Flexible Optoelectronic Devices.* Nano Lett., 2016. **16**(2): p. 871-876.
48. Zhu, F., et al., *Shape Evolution and Single Particle Luminescence of Organometal Halide Perovskite Nanocrystals.* ACS Nano, 2015. **9**(3): p. 2948-2959.
49. Fu, Y., et al., *Solution Growth of Single Crystal Methylammonium Lead Halide Perovskite Nanostructures for Optoelectronic and Photovoltaic Applications.* J. Am. Chem. Soc., 2015. **137**(17): p. 5810-5818.
50. Akkerman, Q.A., et al., *Solution Synthesis Approach to Colloidal Cesium Lead Halide Perovskite Nanoplatelets with Monolayer-Level Thickness Control.* J. Am. Chem. Soc., 2016. **138**(3): p. 1010-1016.
51. Lhuillier, E., et al., *Two-Dimensional Colloidal Metal Chalcogenides Semiconductors: Synthesis, Spectroscopy, and Applications.* Acc. Chem. Res., 2015. **48**(1): p. 22-30.
52. Rossi, D., et al., *Orientational Control of Colloidal 2D-Layered Transition Metal Dichalcogenide Nanodiscs via Unusual Electrokinetic Response.* ACS Nano, 2015. **9**(8): p. 8037-8043.
53. Son, J.S., et al., *Large-Scale Soft Colloidal Template Synthesis of 1.4 nm Thick CdSe Nanosheets.* Angew. Chem. Int. Ed., 2009. **48**(37): p. 6861-6864.

54. Wang, Y., et al., *The Magic-Size NC (CdSe)34 as a Low-Temperature Nucleant for Cadmium Selenide Nanocrystals; Room-Temperature Growth of Crystalline Quantum Platelets.* Chem. Mater., 2014. **26**(7): p. 2233-2243.
55. Ithurria, S., G. Bousquet, and B. Dubertret, *Continuous Transition from 3D to 1D Confinement Observed during the Formation of CdSe Nanoplatelets.* J. Am. Chem. Soc., 2011. **133**(9): p. 3070-3077.
56. Jung, W., et al., *Colloidal Synthesis of Single-Layer MSe2 (M = Mo, W) Nanosheets via Anisotropic Solution-Phase Growth Approach.* J. Am. Chem. Soc., 2015. **137**(23): p. 7266-7269.
57. Yoo, D., et al., *Chemical Synthetic Strategy for Single-Layer Transition-Metal Chalcogenides.* J. Am. Chem. Soc., 2014. **136**(42): p. 14670-14673.
58. Liu, Y.-H., et al., *Lamellar Assembly of Cadmium Selenide NCs into Quantum Belts.* J. Am. Chem. Soc., 2011. **133**(42): p. 17005-17013.
59. Ithurria, S., et al., *Colloidal nanoplatelets with two-dimensional electronic structure.* Nat. Mater., 2011. **10**(12): p. 936-941.
60. Grim, J.Q., et al., *Continuous-wave biexciton lasing at room temperature using solution-processed quantum wells.* Nat. Nanotech., 2014. **9**(11): p. 891-895.
61. Tyagi, P., S.M. Arveson, and W.A. Tisdale, *Colloidal Organohalide Perovskite Nanoplatelets Exhibiting Quantum Confinement.* J. Phys. Chem. Lett., 2015. **6**(10): p. 1911-1916.
62. Sichert, J.A., et al., *Quantum Size Effect in Organometal Halide Perovskite Nanoplatelets.* Nano Lett., 2015. **15**(10): p. 6521-6527.
63. Vybornyi, O., S. Yakunin, and M.V. Kovalenko, *Polar-solvent-free colloidal synthesis of highly luminescent alkylammonium lead halide perovskite nanocrystals.* Nanoscale, 2016. **8**(12): p. 6278-6283.
64. Tan, Z.-K., et al., *Bright light-emitting diodes based on organometal halide perovskite.* Nat. Nano., 2014. **9**(9): p. 687-692.
65. Talapin, D.V., et al., *Prospects of Colloidal Nanocrystals for Electronic and Optoelectronic Applications.* Chem. Rev., 2009. **110**(1): p. 389-458.
66. Peng, X., et al., *Shape control of CdSe nanocrystals.* Nature, 2000. **404**(6773): p. 59-61.
67. Shi, D., et al., *Low trap-state density and long carrier diffusion in organolead trihalide perovskite single crystals.* Science 2015. **347**(6221): p. 519-522.
68. Zhang, F., et al., *Brightly Luminescent and Color-Tunable Colloidal CH3NH3PbX3 (X = Br, I, Cl) Quantum Dots: Potential Alternatives for Display Technology.* ACS Nano, 2015. **9**(4): p. 4533-4542.
69. Dolai, S., et al., *Mechanistic Study of the Formation of Bright White Light-Emitting Ultrasmall CdSe Nanocrystals: Role of Phosphine Free Selenium Precursors.* Chem. Mater., 2015. **27**(3): p. 1057-1070.
70. Dolai, S., et al., *Isolation of Bright Blue Light-Emitting CdSe Nanocrystals with 6.5 kDa Core in Gram Scale: High Photoluminescence Efficiency Controlled by Surface Ligand Chemistry.* Chem. Mater., 2014. **26**(2): p. 1278-1285.
71. Bowers Ii, M.J., et al., *Structure and Ultrafast Dynamics of White-Light-Emitting CdSe Nanocrystals.* J. Am. Chem. Soc., 2009. **131**(16): p. 5730-5731.

72. Bowers, M.J., J.R. McBride, and S.J. Rosenthal, *White-Light Emission from Magic-Sized Cadmium Selenide Nanocrystals.* J. Am. Chem. Soc., 2005. **127**(44): p. 15378-15379.
73. Tang, Z., N.A. Kotov, and M. Giersig, *Spontaneous Organization of Single CdTe Nanoparticles into Luminescent Nanowires.* Science, 2002. **297**(5579): p. 237-240.
74. Protesescu, L., et al., *Nanocrystals of Cesium Lead Halide Perovskites (CsPbX3, X = Cl, Br, and I): Novel Optoelectronic Materials Showing Bright Emission with Wide Color Gamut.* Nano Lett., 2015. **15**(6): p. 3692-3696.
75. Pacholski, C., A. Kornowski, and H. Weller, *Self-Assembly of ZnO: From Nanodots to Nanorods.* Angew. Chem. Inter. Ed., 2002. **41**(7): p. 1188-1191.
76. Li, D., et al., *Direction-Specific Interactions Control Crystal Growth by Oriented Attachment.* Science, 2012. **336**(6084): p. 1014-1018.
77. Liao, H.-G., et al., *Real-Time Imaging of Pt3Fe Nanorod Growth in Solution.* Science, 2012. **336**(6084): p. 1011-1014.
78. Schliehe, C., et al., *Ultrathin PbS Sheets by Two-Dimensional Oriented Attachment.* Science, 2010. **329**(5991): p. 550-553.
79. Cölfen, H. and S. Mann, *Higher-Order Organization by Mesoscale Self-Assembly and Transformation of Hybrid Nanostructures.* Angew. Chem. Int. Ed., 2003. **42**(21): p. 2350-2365.
80. Li, M., H. Schnablegger, and S. Mann, *Coupled synthesis and self-assembly of nanoparticles to give structures with controlled organization.* Nature, 1999. **402**(6760): p. 393-395.
81. Zhang, D., et al., *Solution-Phase Synthesis of Cesium Lead Halide Perovskite Nanowires.* J. Am. Chem. Soc., 2015. **137**: p. 9230-9233.
82. Brus, L.E., *Electron--electron and electron-hole interactions in small semiconductor crystallites: The size dependence of the lowest excited electronic state.* J. Chem. Phys., 1984. **80**(9): p. 4403-4409.
83. Lawrence, K.N., et al., *Solvent-like ligand-coated ultrasmall cadmium selenide nanocrystals: strong electronic coupling in a self-organized assembly.* Nanoscale, 2015. **7**(27): p. 11667-11677.
84. Liu, Y.-H., et al., *Origin of High Photoluminescence Efficiencies in CdSe Quantum Belts.* Nano Lett., 2009. **10**(1): p. 352-357.
85. Schmidt, L.C., et al., *Nontemplate Synthesis of CH3NH3PbBr3 Perovskite Nanoparticles.* J. Am. Chem. Soc., 2014. **136**(3): p. 850-853.
86. Burschka, J., et al., *Sequential deposition as a route to high-performance perovskite-sensitized solar cells.* Nature 2013. **499**(7458): p. 316-319.
87. Jeon, N.J., et al., *Compositional engineering of perovskite materials for high-performance solar cells.* Nature, 2015. **517**(7535): p. 476-480.
88. Liu, M., M.B. Johnston, and H.J. Snaith, *Efficient planar heterojunction perovskite solar cells by vapour deposition.* Nature, 2013. **501**(7467): p. 395-398.
89. Mitzi, D.B., et al., *Conducting tin halides with a layered organic-based perovskite structure.* Nature 1994. **369**(6480): p. 467-469.

90. Fritzinger, B., et al., *Utilizing Self-Exchange To Address the Binding of Carboxylic Acid Ligands to CdSe Quantum Dots.* J. Am. Chem. Soc., 2010. **132**(29): p. 10195-10201.
91. Owen, J.S., et al., *Reaction Chemistry and Ligand Exchange at Cadmium-Selenide Nanocrystal Surfaces.* J. Am. Chem. Soc., 2008. **130**(37): p. 12279-12281.
92. Badia, A., et al., *Gold-Sulfur Interactions in Alkylthiol Self-Assembled Monolayers Formed on Gold Nanoparticles Studied by Solid-State NMR.* J. Am. Chem. Soc., 1997. **119**(45): p. 11104-11105.
93. Hostetler, M.J., et al., *Alkanethiolate Gold Cluster Molecules with Core Diameters from 1.5 to 5.2 nm: Core and Monolayer Properties as a Function of Core Size.* Langmuir, 1998. **14**(1): p. 17-30.
94. Jasieniak, J., M. Califano, and S.E. Watkins, *Size-Dependent Valence and Conduction Band-Edge Energies of Semiconductor Nanocrystals.* ACS Nano, 2011. **5**(7): p. 5888-5902.
95. Sardar, R., J.W. Park, and J.S. Shumaker-Parry, *Polymer-induced synthesis of stable gold and silver nanoparticles and subsequent ligand exchange in water.* Langmuir, 2007. **23**(23): p. 11883-9.
96. Sardar, R., N.S. Bjorge, and J.S. Shumaker-Parry, *pH-Controlled Assemblies of Polymeric Amine-Stabilized Gold Nanoparticles.* Macromolecules, 2008. **41**(12): p. 4347-4352.
97. Christians, J.A., P.A. Miranda Herrera, and P.V. Kamat, *Transformation of the Excited State and Photovoltaic Efficiency of CH3NH3PbI3 Perovskite upon Controlled Exposure to Humidified Air.* J. Am. Chem. Soc., 2015. **137**(4): p. 1530-1538.
98. Frost, J.M., et al., *Atomistic Origins of High-Performance in Hybrid Halide Perovskite Solar Cells.* Nano Lett., 2014. **14**(5): p. 2584-2590.
99. Li, M. and S. Mann, *Emergence of Morphological Complexity in BaSO4 Fibers Synthesized in AOT Microemulsions.* Langmuir, 2000. **16**(17): p. 7088-7094.
100. Puntes, V.F., K.M. Krishnan, and A.P. Alivisatos, *Colloidal Nanocrystal Shape and Size Control: The Case of Cobalt.* Science, 2001. **291**(5511): p. 2115-2117.
101. Nikoobakht, B. and M.A. El-Sayed, *Evidence for Bilayer Assembly of Cationic Surfactants on the Surface of Gold Nanorods.* Langmuir, 2001. **17**(20): p. 6368-6374.
102. Dou, L., et al., *Atomically thin two-dimensional organic-inorganic hybrid perovskites.* Science, 2015. **349**(6255): p. 1518-1521.
103. Son, J.S., et al., *Large-Scale Soft Colloidal Template Synthesis of 1.4 nm Thick CdSe Nanosheets.* Angew. Chem. Inter. Ed., 2009. **48**(37): p. 6861-6864.
104. Bekenstein, Y., et al., *Highly Luminescent Colloidal Nanoplates of Perovskite Cesium Lead Halide and Their Oriented Assemblies.* J. Am. Chem. Soc., 2015. **137**(51): p. 16008-16011.
105. Hoy, J., et al., *Excitation Energy Dependence of the Photoluminescence Quantum Yields of Core and Core/Shell Quantum Dots.* J. Phys. Chem. Lett., 2013. **4**(12): p. 2053-2060.

106. Micic, O.I., S.P. Ahrenkiel, and A.J. Nozik, *Synthesis of extremely small InP quantum dots and electronic coupling in their disordered solid films.* Appl. Phys. Lett., 2001. **78**(25): p. 4022-4024.
107. Bayer, M., et al., *Coupling and Entangling of Quantum States in Quantum Dot Molecules.* Science, 2001. **291**(5503): p. 451-453.
108. Sugimoto, T., *Preparation of monodispersed colloidal particles.* Adv. Coll. Inter. Sci., 1987. **28**(0): p. 65-108.
109. LaMer, V.K. and R.H. Dinegar, *Theory, Production and Mechanism of Formation of Monodispersed Hydrosols.* J. Am. Chem. Soc., 1950. **72**(11): p. 4847-4854.
110. Shevchenko, E.V., et al., *Structural diversity in binary nanoparticle superlattices.* Nature, 2006. **439**(7072): p. 55-59.
111. Yu, T., B. Lim, and Y. Xia, *Aqueous-Phase Synthesis of Single-Crystal Ceria Nanosheets.* Angew. Chem. Inter. Ed., 2010. **49**(26): p. 4484-4487.
112. Ghezelbash, A. and B.A. Korgel, *Nickel Sulfide and Copper Sulfide Nanocrystal Synthesis and Polymorphism.* Langmuir, 2005. **21**(21): p. 9451-9456.
113. Tang, Z., et al., *Self-Assembly of CdTe Nanocrystals into Free-Floating Sheets.* Science, 2006. **314**(5797): p. 274-278.
114. Sun, S., et al., *Ligand-Mediated Synthesis of Shape-Controlled Cesium Lead Halide Perovskite Nanocrystals via Reprecipitation Process at Room Temperature.* ACS Nano, 2016. **10**(3): p. 3648-3657.
115. Akkerman, Q.A., et al., *Tuning the Optical Properties of Cesium Lead Halide Perovskite Nanocrystals by Anion Exchange Reactions.* J. Am. Chem. Soc., 2015. **137**(32): p. 10276-10281.
116. Lee, S.-M., et al., *Single-Crystalline Star-Shaped Nanocrystals and Their Evolution: Programming the Geometry of Nano-Building Blocks.* J. Am. Chem. Soc., 2002. **124**(38): p. 11244-11245.
117. Aharon, S. and L. Etgar, *Two Dimensional Organometal Halide Perovskite Nanorods with Tunable Optical Properties.* Nano Lett., 2016. **16**(5): p. 3230-3235.
118. Xia, Y., X. Xia, and H.-C. Peng, *Shape-Controlled Synthesis of Colloidal Metal Nanocrystals: Thermodynamic versus Kinetic Products.* J. Am. Chem. Soc., 2015. **137**(25): p. 7947-7966.
119. Tao, A.R., S. Habas, and P. Yang, *Shape Control of Colloidal Metal Nanocrystals.* Small, 2008. **4**(3): p. 310-325.
120. Jun, Y.-w., J.-s. Choi, and J. Cheon, *Shape Control of Semiconductor and Metal Oxide Nanocrystals through Nonhydrolytic Colloidal Routes.* Angew. Chem. Int. Ed., 2006. **45**(21): p. 3414-3439.
121. Peng, X., *Mechanisms for the Shape-Control and Shape-Evolution of Colloidal Semiconductor Nanocrystals.* Adv. Mater., 2003. **15**(5): p. 459-463.

CHAPTER 3. LOW TEMPERATURE COLLODIAL SYNTHESIS OF II-VI QUANTUM -WIRES, -PLATELETS, AND –RODS IN GRAM SCALE MESOSCALE ASSEMBLY VERSUS KINETICALLY –CONTROLLED GROWTH

3.1 Synopsis

1D and 2D semiconductor nanostructures have various alluring and fascinating properties but their use in large-scale applications such as solid-state photovoltaic devices have been limited by current synthetic methods. These current methods require either high temperature or the use of phosphines, both of which are not preferred when developing an easily applicable synthesis. In the case of 1D and 2D structures such as quantum wires, quantum platelets and quantum rods, colloidal NCs often serve as a precursor for anisotropic structure formations. Moreover, the enhanced properties of these anisotropic structures, such as charge transport, have made them an even more desirable product for applications such as photovoltaic devices and photodiodes. Herein we present the gram scale synthesis, driven by mesoscale assembly, of various metal chalcogenide anisotropic NCs using cadmium and zinc as metal precursors and sulfur and selenium as chalcogenol precursors.

3.2 Introduction

Anisotropically shaped semiconductor NCs such as, quantum wires (QWs), quantum platelets (QPLs), and quantum rods (QRs) have shown promise in developing solid-state optoelectronic devices.[46, 199-203] The success of these NCs in modern technology has prompted the nanoscience research to design effective colloidal synthetic methods for gram-scale production of high quality NCs. Commonly used hot injection

methods produces high quality NCs, however, the yield is small.[21, 204-206] This can be overcome by synthesizing NCs at low temperature, in lower reactor volume and using highly reactive precursors.[68, 207-209] Furthermore, a quantitative understanding of the growth mechanism will allow the preparation of NCs with desired shapes (e.g., QWs versus QPLs) and amount without substantial modification of the synthetic conditions. Herein, we report the formation pathways of metal (Cd and Zn) chalcogenide (E = S and Se) QWs, QPLs, and QRs through a solution growth processes. Our time-dependent spectroscopic and microscopic analyses have shown that the reaction between CdX_2 (X = acetate and chloride) and $E_m(amine)_n$ precursor at temperature <70 ^{0}C resulted in the formation of ultrasmall magic-sized NCs as intermediates, which undergo mesoscale-assembly process to form QWs and QPLs. Our investigation shows that the growth environment for QWs and QPLs can be reestablished from the isolated magic-sized NCs, thus providing a critical mechanistic understanding of how anisotropic nanostructures grow from molecular building blocks.

After the first colloidal synthesis of CdSe nanoribbons,[210, 211] which display one-dimensional (1-D) quantum confinement due to their small thickness, Li et al.,[212, 213] Buhro and coworkers,[214-217] and Ithurria and Dubertret[42, 218] independently reported synthesis of flat, pseudo-two-dimension NCs also known as QPLs, quantum disks, or nanoplatelets. The synthesized zinc blende structure of CdSe quantum disks required high reaction temperature (>150 ^{O}C) and presence of fatty acid to suppress 1-D growth.[219] The zinc blende CdE nanoplatelets synthesis of Dubertret group requires either high reaction temperature (>200 ^{O}C) or use of toxic trioctylphosphine-Se as chalcogenide precursor.[42, 220] In contrast, Buhro's work demonstrates low

temperature (<100 ^{O}C) synthesis of CdSe QPLs with Wurtzite structure using selenourea as chalcogenide precursor.[217] The authors mentioned magic-sized NCs as intermediates for the formation of CdSe QPLs at room temperature.[217, 221, 222] The literature reports summarized above are reminiscent of highly specific reaction condition in terms of selection of chalcogenide precursors that only produce 2-D NCs. In this chapter we address several important questions in the process of synthesizing gram-scale II-VI NCs at low temperature, see Figure 3.1: (1) Which parameters (e.g., surface ligand, thermodynamic, and kinetic) control the formation of CdSe QWs, QPLs, and QRs using an identical Se-precursor, $E_m(amine)_n$? (2) Does the reactivity of chalcogenide precursors ($Se_m(amine)_n$ *versus* $S_m(amine)_n$) influence the formation of CdE QWs, QPLs, and QRs? (3) Does the reactivity of the metal precursor (Zn versus Cd) play a role in the formation of ZnE QWs, QPLs, and QRs? (4) What is the chemical identity of the magic-size NC intermediate?

The transformation of spherical NCs as *"building blocks"* to 1-D and 2-D NCs can be explained as one of three commonly described growth process: oriented attachment.[212, 223, 224] self-organization of molecular templates,[53, 190, 225] and mesoscale assembly.[7] Unlike the growth mechanisms involving oriented attachment for PbSe nanowires[31] and PbS nanoplateles[224] that are kinetically-driven processes, our CdE QW and QPL formation was controlled by the chemical nature of the surface passivating ligands. Thus, a combination pf inter-NC, and hydrophobic and/or van der Waals interaction between surface passivating ligands in organic solvent at low temperature is in agreement with our proposed mesoscale assembly. In contrast, our identical chalcogenide precursor ($E_m(amine)_n$) was used for CdE QWs synthesis, resulted

in the formation of CdE QRs at slightly elevated temperature. Thus, we hypothesize that the CdE QRs are formed under a kinetically driven growth condition, which is established with a high flux of monomers in the reaction environments through an increase in the reaction temperature.

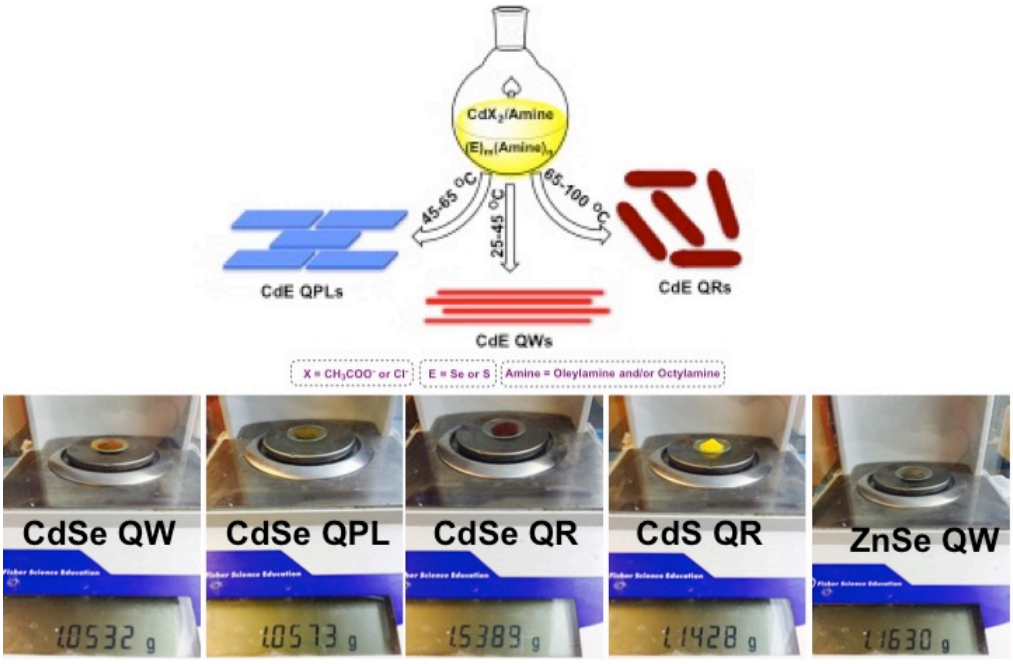

Figure 3.1. Dpicts the synthetic route to produce metal chalcogenide QW, QPL, and QRs by varying surface ligand and temperatures and the gram scale yields of the for mentioned materials.

Our use of CdE as a model system to study the formation mechanisms of QRs, QPLs, and QRs further allowed us to develop shape-controlled synthetic methods to prepare ZnE QRs, QPLs, and QRs. Thus, underscoring the generality of the synthetic methods that could be applicable for shape-directed growth of other metal chalcogenide NCs. Taken together, our mechanistic study allowed for the synthesis of differently-shaped CdE and ZnE NCs in gram scale quantity, and importantly environmentally

friendly ZnE NCs. This will further aid in their widespread application in optoelectronic device fabrications and preparation of eco-friendly photocatalysts.[226, 227]

3.3 Methods and Materials

3.3.1 Materials.

Cadmium acetate dihydrate $(CdOAc)_2$ (99.9%), selenium (pellets, 99.9%), oleylamine (OLA) (98%), 1-hexanethiol (HT) (95%), zinc acetate dihydrate $(Zn(OAc)_2$ (99%), sulfur power (99.98%), cadmium chloride ($CdCl_2$ (99%), zinc chloride ($ZnCl_2$ (99%), octylamine (OA) (98%), toluene (HPLC grade), acetonitrile (MeCN, HPLC grade), and chloroform (HPLC grade), were purchased from Sigma Aldrich and Fisher and used without further purification. Organic solvents were purged with N_2 for 30 minutes prior to use.

3.3.2 Gram Scale Synthesis of CdSe QWs and QR.

In a typical procedure, 3.00 g of $Cd(OAc)_2$ was put in a 500 mL 2 neck round bottom flask with 200 mL of OLA. The mixture was degassed for a period of 15 minutes then returned to N_2 and heated to the appropriate temperature (45 °C for QWs, 100°C for QRs). The selenium precursor was prepared by adding 2.78 g of ground selenium with 36.5 mL of OLA in a 100 mL 2 neck round bottom flask and put under vacuum for 15 minutes. The flask was returned to N_2 and degassed again and 8.5 mL of HT was added. The solution was stirred for 30 minutes then degassed again for an additional 30 minutes. Once the Cd precursor had reached the desired internal temperature, 46 mL of Se precursor was added and the reaction was allowed to run for 1440 minutes. Once the reaction was complete, 100 mL of toluene was added and the reaction was then

precipitated by acetonitrile and centrifuged at 7000 rpm for 5 minutes. The solid was dissolved in toluene for further characterization.

3.3.3 Gram Scale Synthesis of CdS QW and QR

In a typical procedure, 3.00 g of $Cd(OAc)_2$ was put in a 500 mL 2 neck round bottom flask with 200 mL of OLA. The mixture was degassed for a period of 15 minutes then returned to N_2 and heated to the appropriate temperature (25 °C for QW 45°C for QR). The sulfur precursor was prepared by adding 1.12 g of sulfur powder with 36.5 mL of OLA in a 100 mL 2 neck round bottom flask and put under vacuum for 15 minutes. The flask was returned to nitrogen and degassed again and 8.5 mL of HT was added. The solution was stirred for 30 minutes then degassed again for an additional 30 minutes. Once the Cd precursor had reached the desired internal temperature, 46 mL of S precursor was added. When the reaction was complete, the same purification method as in CdSe QWs and QRs synthesis was used.

3.3.4 Gram Scale Synthesis of ZnSe and ZnS QWs

In a typical procedure, 2.40 g of $Zn(OAc)_2$ was put in a 500 mL 2 neck round bottom flask with 200 mL of OLA. The mixture was degassed for a period of 15 minutes then returned to N_2 and heated to the 130 °C . The selenium (sulfur) precursor was prepared by adding 3.6 g of selenium (1.12 g of sulfur) powder with 36.5 mL of OLA in a 100 mL 2 neck round bottom flask and put under vacuum for 15 minutes. The flask was returned to nitrogen and degassed again and 8.5 mL of HT was added. The solution was stirred for 30 minutes then degassed again for an additional 30 minutes. Once the Cd precursor had reached the desired internal temperature, 46 mL of Se (S) precursor was

added.. When the reaction was complete, the same purification method as above was used.

3.3.5 Gram Scale Synthesis of ZnS QRs

In a typical procedure, 2.40 g of $Zn(OAc)_2$ was put in a 500 mL 2 neck round bottom flask with 200 mL of OLA. The mixture was degassed for a period of 15 minutes then returned to N_2 and heated to the 130 °C. The sulfur precursor was prepared by adding 1.33 g of sulfur powder with 36.5 mL of OLA in a 100 mL 2 neck round bottom flask and put under vacuum for 15 minutes. The flask was returned to nitrogen and degassed again and 8.5 mL of HT was added. The solution was stirred for 30 minutes then degassed again for an additional 30 minutes. Once the Cd precursor had reached the desired internal temperature, 25 mL of S precursor was added. When the reaction was complete, the same purification method as above was used.

3.3.6 Gram Scale Synthesis of CdSe QPLs

In a typical synthesis, 2.5 g of $CdCl_2$ was put in a 550 mL 2 neck round bottom flask with 100 mL OLA and 100 mL OA. The mixture was head to 120 °C and held under vacuum for 2 hours. The mixture was returned under N_2 and allowed to cool to 65 °C. The selenium precursor was prepared by adding 4.3 g of selenium powder with 28.15 mL of OLA and 28.15. mL of OA in a 100 mL 2 neck round bottom flask and put under vacuum for 15 minutes. The flask was returned to nitrogen and degassed again and 15.4 mL of HT was added. The solution was stirred for 30 minutes then degassed again for an additional 30 minutes. Once the Cd precursor had reached 65 °C, 71.7 mL of the Se precursor was injected and the reaction allowed to continue for 24 hr. When the reaction was complete, the same purification method as above was used.

3.3.7 Gram Scale Synthesis of CdS QPLs

In a typical synthesis, 2.5 g of $CdCl_2$ was put in a 500 mL 2 neck round bottom flask with 100 mL OLA and 100 mL OA. The mixture was head to 120 °C and held under vacuum for 2 hours. The mixture was returned under N_2 and allowed to cool to 45 °C. The sulfur precursor was prepared by adding 1.74 g of sulfur powder with 28.15 mL of OLA and 28.15. mL of OA in a 100 mL 2 neck round bottom flask and put under vacuum for 15 minutes. The flask was returned to nitrogen and degassed again and 15.4 mL of HT was added. The solution was stirred for 30 minutes then degassed again for an additional 30 minutes. Once the Cd precursor had reached 45 °C, 71.7 mL of the S precursor was injected and the reaction allowed to continue for 24 hr. When the reaction was complete, the same purification method as above was used.

3.3.8 Gram Scale Synthesis of ZnSe QPLs

In a typical synthesis, 1.85 g of $ZnCl_2$ was put in a 500 mL 2 neck round bottom flask with 100 mL OLA and 100 mL OA. The mixture was head to 120 °C and held under vacuum for 2 hours. The mixture was returned under N_2 but kept at the same temperature. The selenium precursor was prepared by adding 4.3 g of selenium powder with 28.15 mL of OLA and 28.15 mL of OA in a 100 mL 2 neck round bottom flask and put under vacuum for 15 minutes. The flask was returned to nitrogen and degassed again and 15.4 mL of HT was added. The solution was stirred for 30 minutes then degassed again for an additional 30 minutes before 71.7 mL of the Se precursor was injected and the reaction allowed to continue for 48 hr. When the reaction was complete, the same purification method as above was used.

3.3.9 Gram Scale Synthesis of ZnS QPLs

In a typical synthesis, 1.85g of $ZnCl_2$ was put in a 500 mL 2 neck round bottom flask with 100 mL OLA and 100 mL OA. The mixture was head to 120 °C and held under vacuum for 2 hours. The mixture was returned under N_2 but kept at the same temperature. The selenium precursor was prepared by adding 1.74 g of sulfur powder with 28.15 mL of OLA and 28.15 mL of OA in a 100 mL 2 neck round bottom flask and put under vacuum for 15 minutes. The flask was returned to nitrogen and degassed again and 15.4 mL of HT was added. The solution was stirred for 30 minutes then degassed again for an additional 30 minutes before 71.7 mL of the S precursor was injected and the reaction allowed to continue for 48 hr. When the reaction was complete, the same purification method as above was used.

3.3.10 Optical Spectroscopic Characterization

UV−vis absorption spectra were collected using a Varian Cary 50 UV−vis spectrophotometer scanning through the range 800−300 nm. Prior to the sample measurements, the baseline was corrected with pure solvent. The photoluminescence emission (PL) spectra were acquired using a Cary Eclipse fluorescence spectrophotometer from Varian Instruments.

3.3.11 NMR Analysis.

The 1H NMR spectra were obtained with a Bruker AVANCE III 500 instrument at 500 MHz working frequency. Typically, ~10−20 mg of purified sample was dissolved in 0.6 mL of chloroform-d (CDCl3) at room temperature. A minimum of 512 scans were collected with a 30° pulse angle with 3.17 s of acquisition and 3 s of relaxation time. All acquired data were plotted via TOPSPIN 2.1 software.

3.3.12 High Resolution TEM Analysis

For high-resolution TEM analysis, samples were prepared inside a glovebox by placing 10 μL of dissolved purified sample in toluene onto a lacey carbon-coated copper grid (Electron Microscopy Science). The sample was allowed to set for 30 second and any excess solution was removed by wicking with a Kimwipe to avoid particle aggregation. Images were obtained using a JEOL-3200FS-JEM instrument at 200 kV beam energy.

3.3.13 Powder X-ray diffraction (XRD) analysis.

Wide-angle XRD was recorded on a Rigaku MiniFlexTM II (Cu Kα) instrument. Sample was prepared by dropcasting the purified sample on a piranha cleaned glass coverslips.

3.3.14 Thermo Gravimetric Analysis (TGA)

TGA analysis was performed on a NETZSCH STA 449F3 Jupiter instrument. The sample was heated at a rate of 10°C per minute and a protective gas (N_2) flow rate of 25 mL per minute. The results from TGA were also used to calculate the percent yield for each structure. Based on the amount of sample used for TGA analysis (10 mg), the weight percent of ligand of the sample, and the ratio of CdSe determined to be 1:1, the percent yield was calculated based on the grams of Cd.

3.4 Results and Discussion

3.4.1 Gram Scale Synthesis and Characterization of CdSe QWs, QPLs, and QRs.

We begin our discussion with the synthesis of CdSe QWs. Briefly, cadmium acetate was mixed with OLA and heated to 45 ^{O}C before injecting the Se-precursor

(prepared by mixing elemental Se, OLA, and HT at room temperature,[68, 228] and the reaction was allowed to continue for 1440 min. The steady state photophysical properties of the purified sample were analyzed by UV-visible and photoluminescence (PL) spectroscopy. As illustrated in Figure 3.2A, toluene solution of the NCs display two sharp absorption peaks at 426 nm (2.91 eV) and 451 nm (2.75 eV), and an extremely sharp emission peak at 450 nm (2.76 eV) with full-width at half-maximum of 12 nm. The photophysical properties of the final QW closely resemble the CdSe nanoribbons reported by Hyeon and coworkers.[229] The low-magnification transmission electron microscopy (TEM) image shows formation of CdSe QWs with micrometer lengths, see Figure 3.2B. From the high-resolution TEM (HRTEM) image (Figure 3.2C), the diameter of the QWs is a uniform 1.6 ± 0.1 nm and they have an average length of 131 ± 10 nm. Therefore, two sharp absorption peaks of CdSe QWs that are much blue-shifted from the band-gap energy (1.7 eV) of bulk CdSe is due to uniform, extremely narrow diameter-dependent strong quantum confinement effects, as similar to the electronic properties of quantum wells.[210] Importantly, the ensemble PL quantum yield (PLQY) of our CdSe QWs is ~10% which is much higher than previously reported in ultrathin 1-D NCs (0.1-2%.)[230] This difference suggests the presence of low amount of trap sites. The X-ray diffraction (XRD) pattern of the CdSe QWs (Figure 3.2D) demonstrates wurtzite structure[217], and the broad peaks are consistent with their nanosize diameters.[217, 231] As compared to bulk wurtzite CdSe, the diffraction peaks of CdSe QWs are slightly red-shifted, indicating the presence of lattice contraction resulting from the high surface tension of the ultrasmall diameter, as previously reported for CdSe nanoribbons[210] and nanobelts. [213, 230] Appearance of two weak peaks at 2θ 27 and 30 associated with

(002) and (101) planes, respectively, of the CdSe QWs reflect their parallel orientation along with elongated structure.[23] The HRTEM image (Figure 3.2C) supports the XRD data of parallel orientation. More importantly, the average spacing between QWs was 0.6 nm shorter than two times the hydrocarbon chain length of surface passivating ligands OLA of 4.2 nm (determined from ChemBioDraw-3D 14.0) indicating that ligand hydrocarbon chain interdigitation is present.

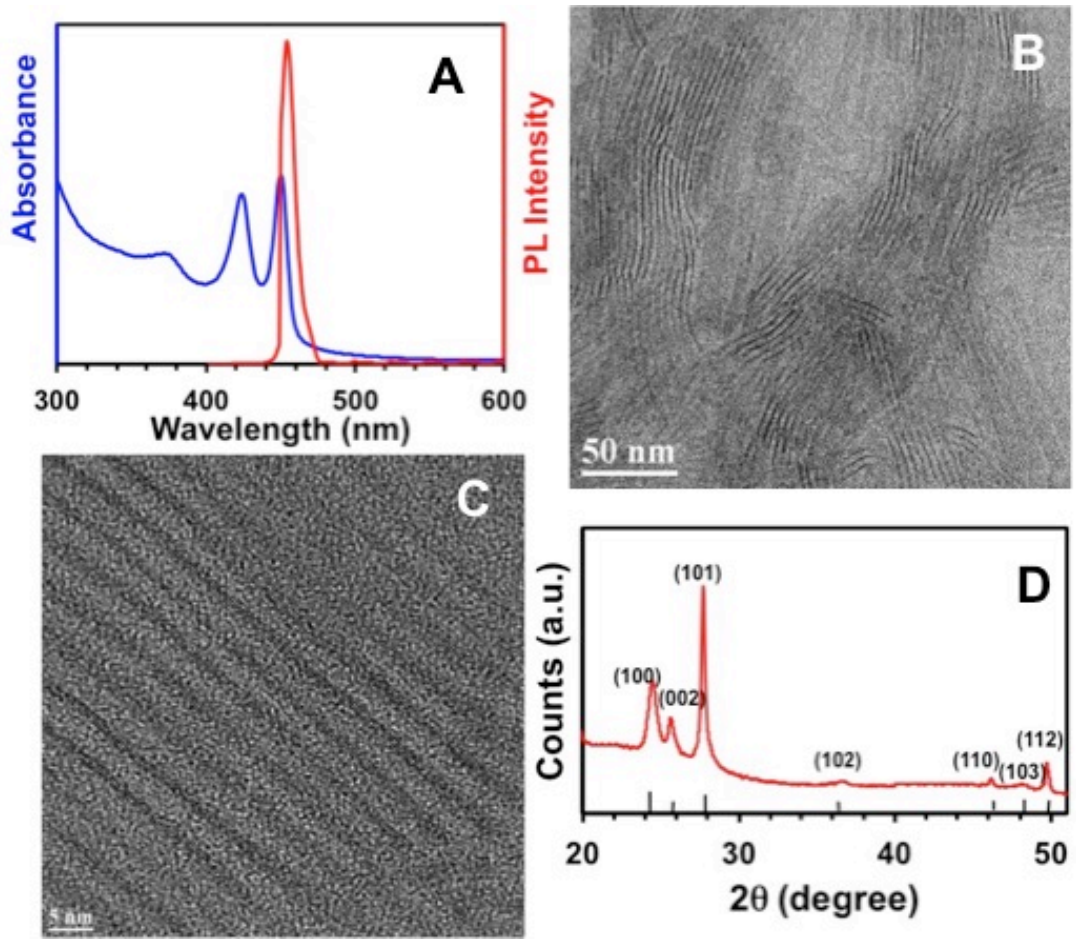

Figure 3.2. The optical and structural characterization of the final CdSe QW. A) absorption (blue) and emission (red) spectra, B) low resolution TEM image, C) high resolution TEM image, and D) powder XRD pattern.

We used a co-solvent system, a mixture of OLA and OA, to synthesize gram scale CdSe QPLs. Briefly, cadmium chloride was added to a 1:1 mixture of OLA and OA, heated to 120 ^{O}C and held under vacuum for 120 min and then the solution was brought

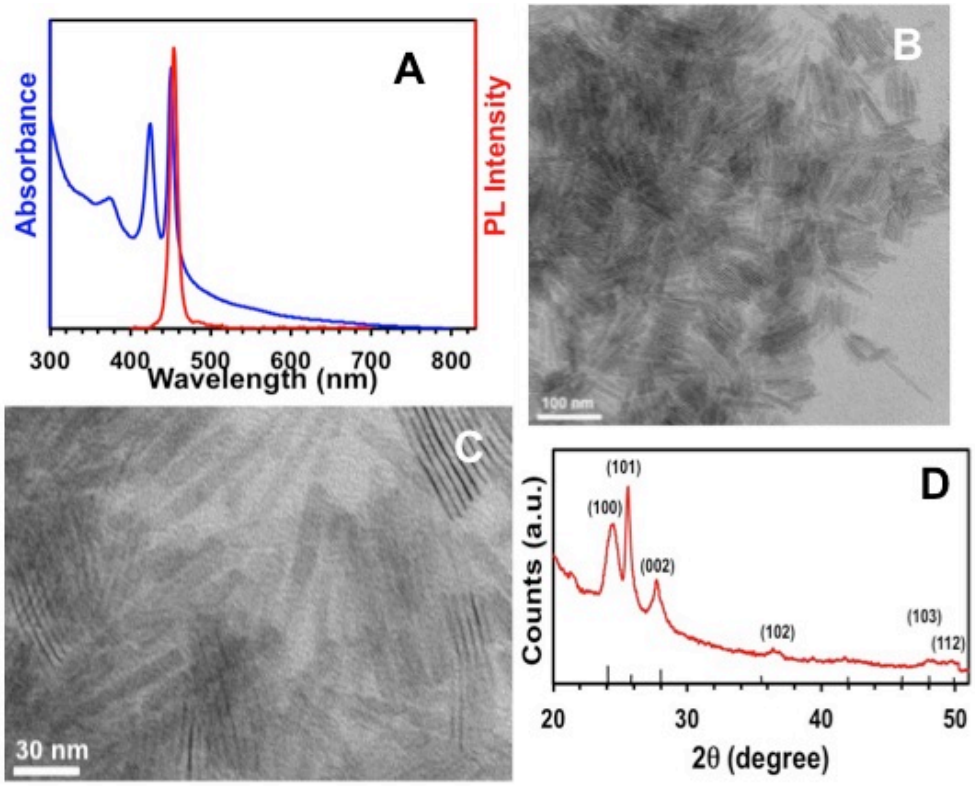

Figure 3.3 The optical and structural characterization of the final CdSe QPLs. A) absorption (blue) and emission (red) spectra, B) low resolution TEM image, C) high resolution TEM image, and D) powder XRD pattern.

down to 65 ^{O}C before injecting the Se precursor and the reaction was continued for 1440 min. The final absorption and emission spectra of the QPL are found in Figure 3.3A. The CdSe QPL display absorption peaks at 448, 424, and 375 nm. The CdSe QPL also display an emission peak at 453 nm and a relatively high quantum yield of ~25%. The XRD pattern (Figure 3.3D) of the purified CdSe QPL matches that of the wurtzite structure. Similar to the XRD patterns of the CdSe QW, this pattern also contains

broader peaks corresponding to the thiiner dimensions of the wurtzite structure. The TEM image of the CdSe QPL can be found in Figure 3.3B. From the high-resolution TEM (HRTEM) image (Figure 3.3C), the width of the QPLs is determined to be uniformed of 2.7 ± 0.2 nm with an average length of 78 ± 6 nm.

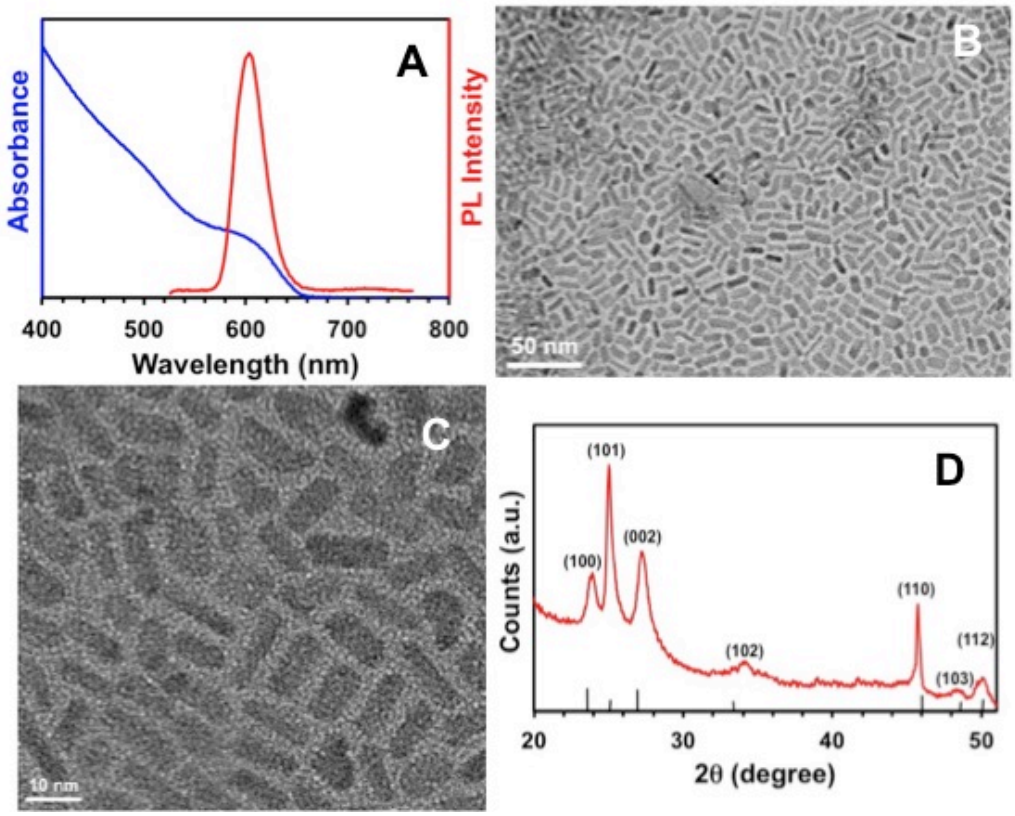

Figure 3.4 The optical and structural characterization of the final CdSe QRs. A) absorption (blue) and emission (red) spectra, B) low resolution TEM image, C) high resolution TEM image, and D) powder XRD pattern.

The formation of CdSe QR was achieved by further increasing the reaction kinetics by changing the temperature to 100 ^{O}C. Previously it has been reported that the conversion from cadmium chalcogenide QW to QR is a thermodynamically driven process.[232, 233] An increase in reaction temperature is required to overcome the

activation barrier for the conversion from QW to QR. The absorption peak for the final structure, found in Figure 3.4A, is present around 605 nm. The TEM images of the final QRs, Figures 3.4B and C, show an average length of 13 ± 2 nm and a diameter of 2.3 ±0.2 nm. The XRD pattern of the CdSe QR, found on Figure 3.4D, is similar to that of both the CdSe QW and QPL confirming a wurtzite structure. These peaks are more defined than those of the QW and QPL as a result of the higher reaction temperature and increase in crystalinity of the material.

3.4.2 Gram Scale Synthesis and Characterization of CdS QWs, QPLs, and QRs.

Our gram scale synthesis of CdSe QWs, QPLs, and QRs inspired us to prepare these anisotropic nanostructures made with CdS. Briefy, for the CdS QWs and QRs, cadmium acetate was mixed with OLA and degassed for 15 min. Once the cadmium precursor was at the appropriate temperature (25°C for the QWs and 45°C for the QRs) the sulfur precursor was injected. For the CdS QPLs, cadmium chloride was added to a 1:1 mixture of OLA and OA, heated to 120°C and held under vacuum for 120 min. The solution was returned to N_2 and cooled to 45 °C before the injection of the S precursor. (See experimental section for full synthesis.) It is known that sulfur is a more reactive precursor than selenium, which explains the lower reaction temperatures for the synthesis of CdS nanostructures, even though the metal to chalcogenide ratio is the same. Figure 3.5A displays the final absorption and emission peaks for CdS QWs at 373 and 385 nm and emission at 387 nm respectively. Figure 3.6A and D illustrate the TEM image of the final CdS QWs with an average length of 132 ± 7 nm and diameter of 1.5 ±0.1 nm. The XRD pattern of the final CdS QWs (Figure 3.5D) agrees with that of previously reported

wurtzite structure, and the broadened peaks consistent with the thin dimensions of theQWs.

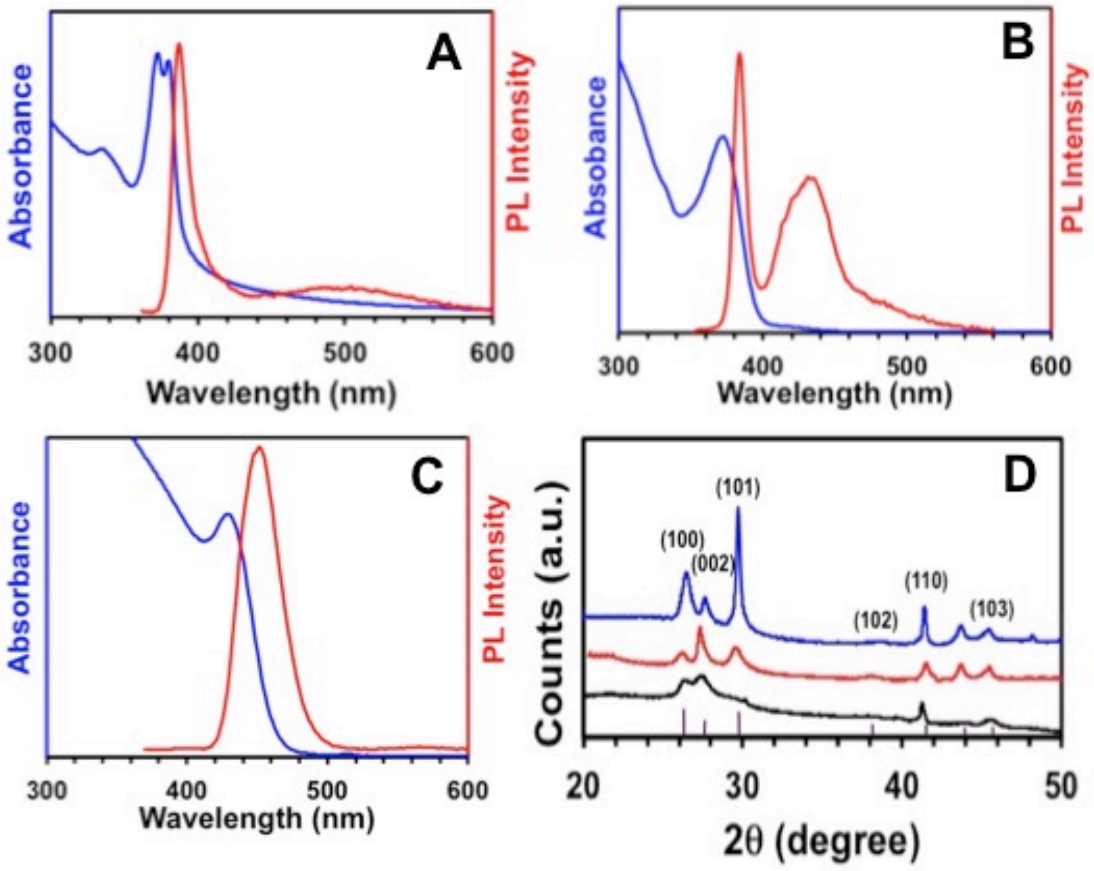

Figure 3.5. Absorption (blue) and emission (red) spectra of CdS QWs (A), QPLs (B), and QRs (C), and D) the powder XRD pattern of the QWs (black), QPL (red), QRs (blue) and the known bulk wurtzite pattern (purple).

There are two absorption peaks present at 375 and 337 nm have been assigned to the I_h-I_e and 2_h-2_e transitions respectively.[214] The absorption spectrum of the CdS QPLs (Figure 3.5A) matches previously reported CdS QPLs that were synthesized using a higher temperature.[234] The CdS QPLs also possess a band edge emission peak at 380 nm and a quantum yield of ~10%. It has already been established that due to the difference in reactivities of the Se and S precursors, this reaction is conducted at a lower

temperature than its selenium counterpart. The XRD pattern (Figure 3.5D), again containing the broad peaks characteristic of the thin dimensions, corresponds to the wurtzite crystal structure. The TEM image of the CdS QPLs can be found in Figure 3.6B. From the HR-TEM image (Figure 3.5E), the average width of the QPLs was determined to be 3.3 ± 0.5 nm and the average length 34 ± 6 nm.

Figure 3.5C shows the final absorption of the CdS QRs. The first energetic absorbance peak at 435 nm with a corresponding emission peak at 446 nm.. From the TEM images in Figure 3.6C and F, it is evident that the rods have an average length and width of 15 ± 2 nm and 2.9 ± 0.3 nm respectively, and are well dispersed in the sample. The XRD pattern (Figure 3.5D) corresponds to the wurtzite crystal structure. However, slightly sharper peaks, compared to the other CdS nanostructures, are observed and can be attributed to the thicker nature of the material.

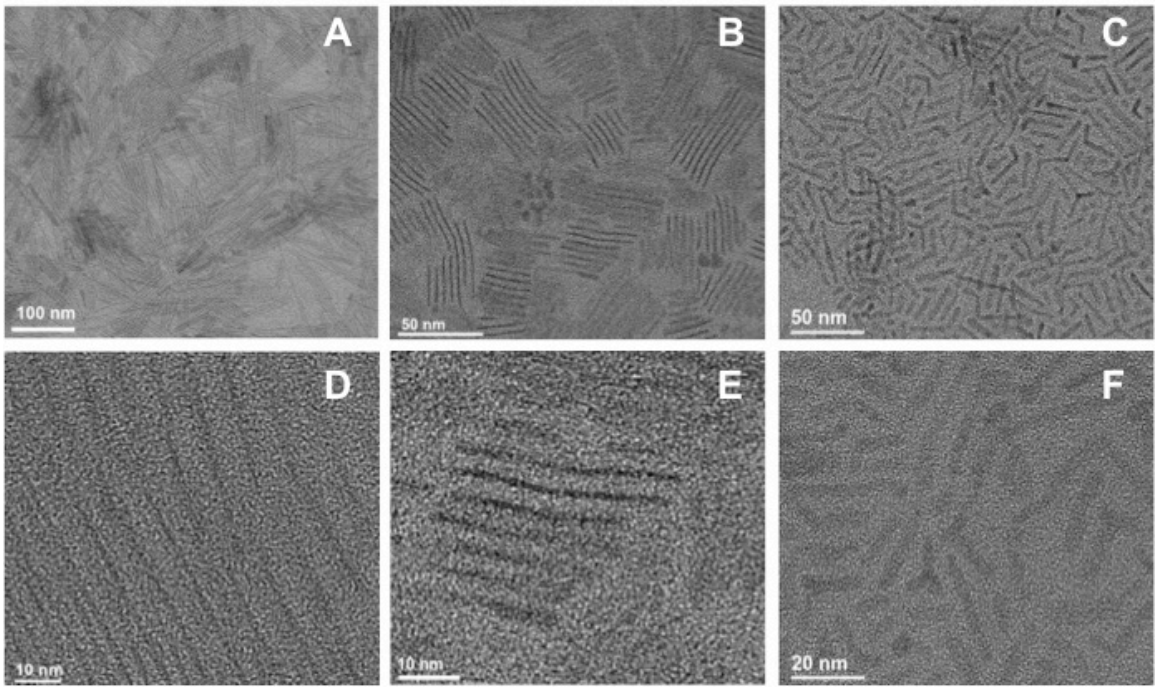

Figure 3.6. The low resolution TEM images of CdS QWs (A), QPLs (B), and QRs (C), and high resolution TEM images of CdS QWs (D), QPLs (E), and QRs (F).

3.4.3 Gram Scale Synthesis and Characterization of ZnS QWs, QRs, and QPLs

The synthesis of the ZnS QWs was performed as follows; zinc acetate was dissolved in OLA and degassed for 15 min. The reaction mixture was returned to N_2 and the temperature raised to 120°C before the injection of the sulfur precursor. Figure 3.7A above depicts the energetic absorbance peaks for the ZnS QWs at 255 nm and 275 nm respectively. Figures 3.8A and D illustrate the final TEM images of the ZnS QWs.. The image of show well defined nanowires with average length and diameter of 153 ± 6 nm ad 1.8 v 0.2 nm respectively. As seen from Table 3.2, the reaction conditions for the ZnS QWs have the same metal to chalcogenide ratio as the cadmium chalcogenide. This

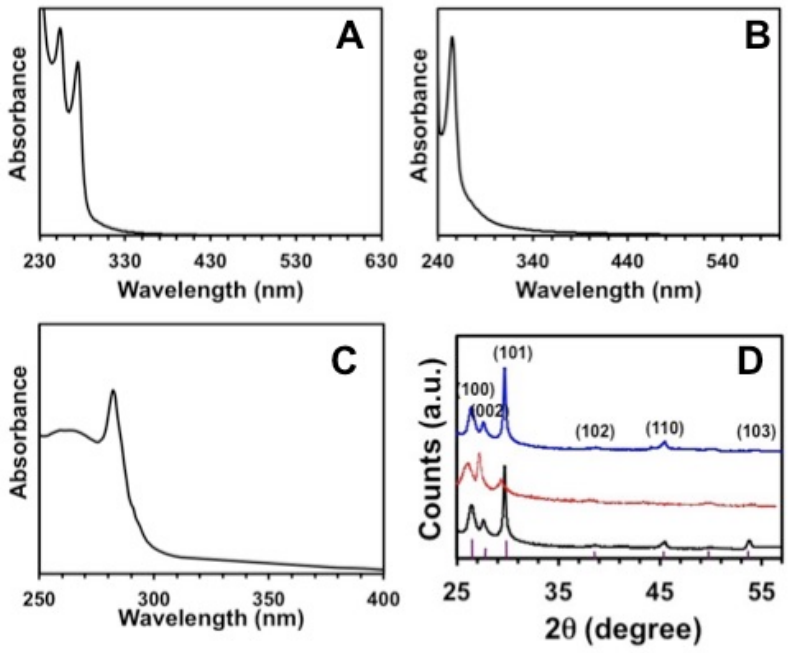

Figure 3.7. Absorption spectra of ZnS QWs (A), QPLs (B), and QRs (C), and D) the powder XRD pattern of the QWs (black), QPL (red), QRs (blue) and the known bulk wurtzite pattern (purple).

could be due to the fact that sulfur is a more reactive chalcogenide and therefore the increase in reaction temperature is enough to drive the QW formation. The XRD pattern

for the material, Figure 3.7D, depicts the wurtzite crystal structure, however, the peaks are much sharper than those of the cadmium chalcogenides. These sharper peaks can be attributed to the higher reaction temperature of he zinc based materials and the subsequent enhanced crystalinity.

Similarly to the cadmium based QPLs, zinc chloride was added to a 1:1 mixture of OLA and OA and heated to 120 °C and held under vacuum for 120 min. The solution was returned to N_2 before the injection of the Se precursor. The absorption spectrum of the final structure synthesized, the ZnS QPLs (Figure 3.7B), display absorbance maximums at 347 and 329 nm corresponding to the I_B-I_e and I_A-I_e transitions respectively.[235] The TEM images of the ZnSe QPLs, found in Figure 3.8B and E, were

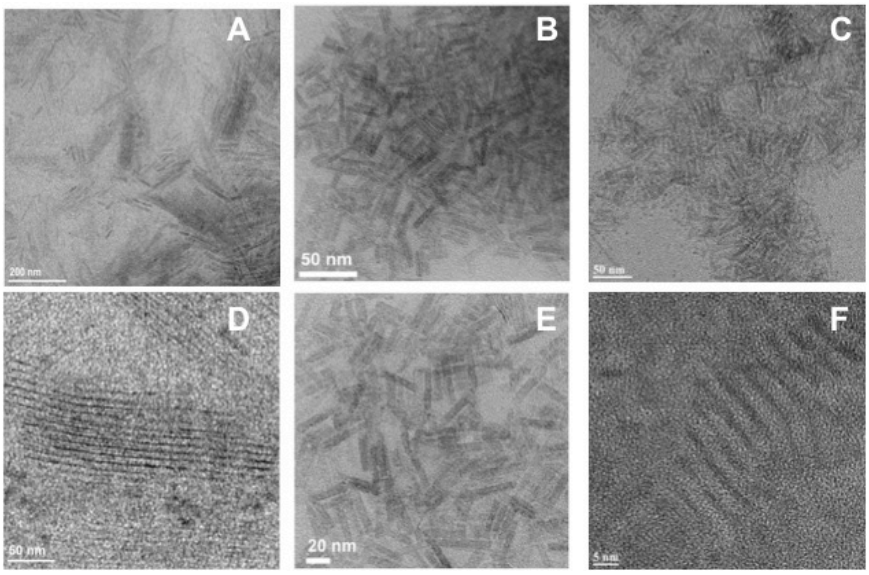

Figure 3.8. The low resolution TEM images of ZnS QWs (A), QPLs (B), and QRs (C), and high resolution TEM images of ZnS QWs (D), QPLs (E), and QRs (F).

used to determine the average length and width of 44 ± 4 nm and 8.9 ± 1 nm respectively. This spectrum matches that of previously reported wurtzite ZnSe QPLs synthesized at high temperatures. The XRD pattern (Figure 3.7D) confirms the wurtzite crystal

structure and again has sharper peaks than either CdSe or CdS QPLs. The relatively sharper peak for ZnSe QPLs could be due to the higher synthetic temperature, resulting in a better crystalinity character. As seen from Table 3.2, there is no change in ratio of the metal to chalcogenide precursors in the QPL reactions, just an increase in the temperature to 120°C. We hypothesize that is due to the fact that the surface chemistry plays a more critical role in the QPL formation.

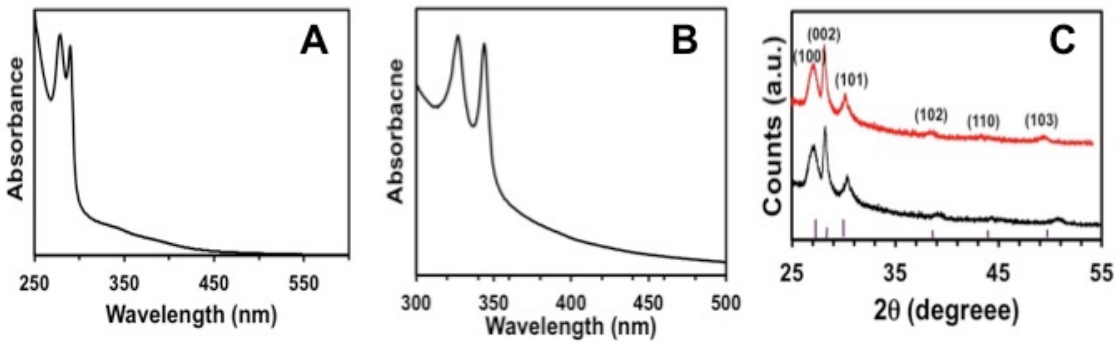

Figure 3.9. Absorption spectra of ZnSe QWs (A), QPLs (B), and (C) the powder XRD pattern of the QWs (black), QPL (red), and the known bulk wurtzite pattern (purple).

The synthesis of ZnS QRs was achieved under the same conditions as the ZnS QWs with the adjustment of an increase in the ratio of sulfur added. The absorption spectrum last of the ZnS structures, the QRs is found in Figure 3.7C. The final QRs display a first excitonic peak at 258 nm. The corresponding TEM images can be found in Figure 3.8C and F, showed average length and width of 31 ± 2 nm and 4.5 ± 0.4 nm. The XRD pattern for the ZnS QRs, Figure 3.7D, similar to the previous ZnS nanostructures, displays the wurtzite structure with sharper, more defined peaks signifying a more crystalline material. This has been known to occur in synthesis at higher temperatures, like these ZnS nanomaterials.[234]

3.4.4 Gram Scale Synthesis and Characterization of ZnSs QWs, and QPLs.

In the case of ZnSe, only two nanostructures, QWs and QPLs were successfully synthesized In the synthesis of ZnSe QWs, zinc acetate was dissolved in OLA and degassed for 15 min The reaction mixture was returned to N_2 and the temperature raised

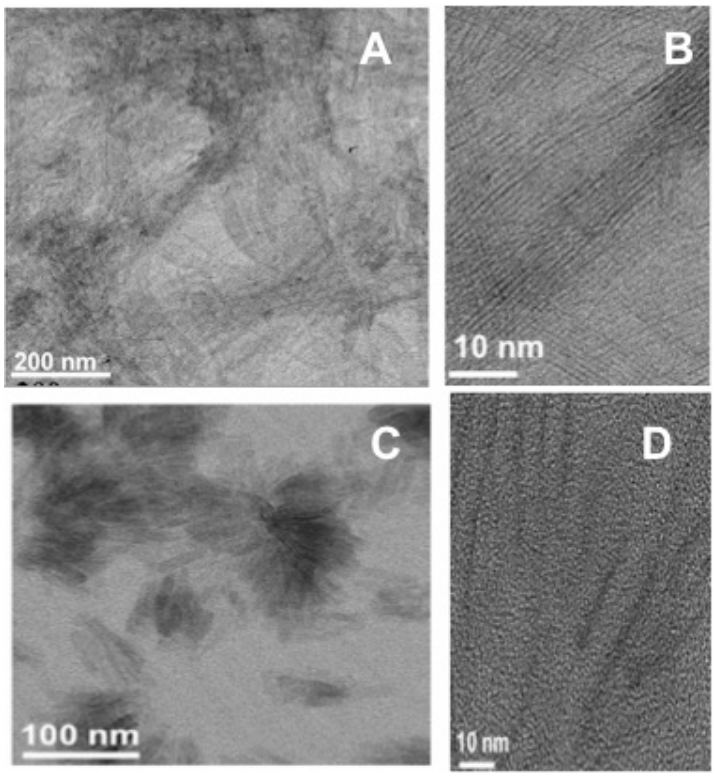

Figure 3.10 The low resolution TEM images of ZnSe QWs (A) and QPLs (B). High resolution TEM images of ZnSe QWs (C) and QPLs (D).

to 120°C before the injection of the selenium precursor. The amount of selenium added was greater than that of both the ZnS, CdSe, and CdS QWs. This can be explained by the lower reactivity of selenium. Figure 3.9A displays the finally absorption spectra for the ZnSe QWs with excitonic peaks at 292 and 280 nm. Figure 3.10 A and B show the final TEM images of the ZnSe QWs with an average length and diameter of 280 ± 14 nm and 2.0 ± 0.1 nm respectively. Like the previous XRD obtained for ZnS structures, the

pattern of ZnSe QWs (Figure 3.9C) display a wurtzite crystal structure and sharper more defined peaks as a result of the higher reaction temperature.

The last structure synthesized was ZnSe QPLs. Briefly, zinc chloride was added to a 1:1 mixture of OLA and OA and heated to 120°C and held under vacuum for 120 min. The solution was returned to N_2 before the injection of the selenium precursor. See experimental section for full synthesis. The absorption spectrum of the final structure synthesized, the ZnSe QPLs (Figure 3.9B), display absorbance maximums at 347 and 329 nm corresponding to the I_B-I_e and I_A-I_e transitions respectively.[235] This spectrum

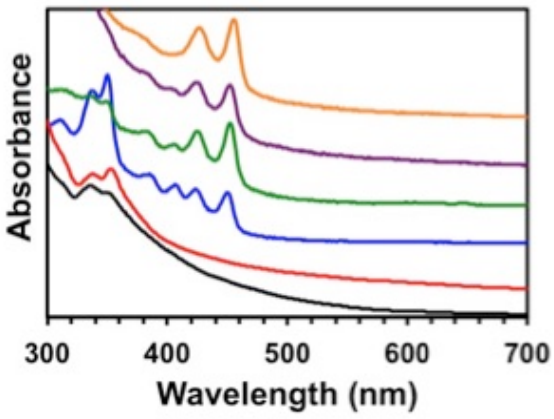

Figure 3.11 Time dependent absorption spectra during the CdSe QW synthesis at 2 minutes (back), 5 minutes (red), 10 minutes (blue), 20 minutes (green), 30 minutes (purple), and 60 minutes (orange).

matches that of previously reported wurtzite ZnSe QPLs synthesized at high temperatures. The XRD pattern (Figure 3.9C) confirms the wurtzite crystal structure and again has sharper peaks than the CdSe QPLs. This peak sharpness is again likely due to the higher synthetic temperature employed in this reaction. The TEM images of the ZnSe QPLs can be found in Figure 3.10C and D. From the HR TEM image, the average length and width of the QPLs were determined to be 66 ± 5 nm and 3.0 ± 0.1 nm . As seen from Table 3.2,

there is no change in ratio of the metal to chalcogenide precursors in the QPL reactions, just in increase in the temperature to 120°C.

It should be noted that the synthesis of ZnSe QRs was not successfully accomplished. We attribute this to both the kinetic required for the formation of QRs from the NC intermediate as well as the lower reactivity of the selenium and zinc precursors. Our attempts to synthesis the ZnSe QRs but increasing the metal chalcogenide ratio to 1:4 was unsuccessful, so we hypothesis that an increase in temperature to above 150°C may allow for the formation of the QRs.

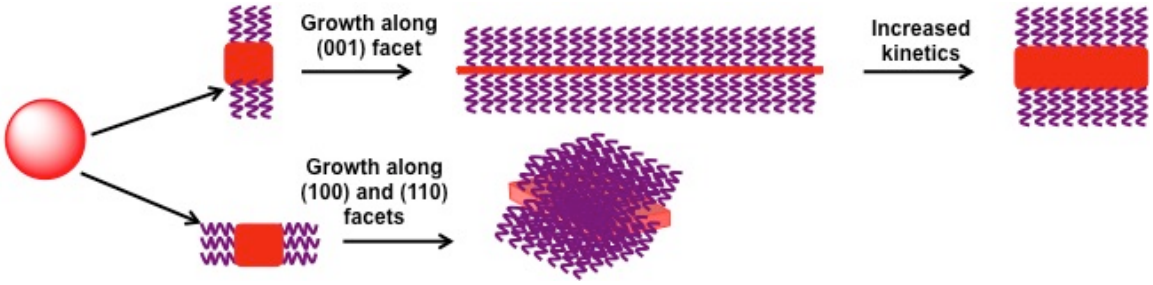

Figure 3.12. Depicts the surface chemistry promoted and mesoscale assembly of QWs and QPLs and the kinetically-controlled growth of QRs.

3.4.5 Proposed Mesoscale-Driven Growth of CdE (Se and S) QWs and QPLs.

In order to successfully develop a large-scale synthesis method, a precise understanding of the NCs growth mechanism is critical. Buhro and coworkers have reported that the magic-sized $(CdSe)_{34}$ and $(CdSe)_{34}$ NCs serve as the precursor for the formation of anisotropically-shaped nanostructures such as QWs and QPLs.[217] We used time dependent UV-vis absorption spectroscopy (Figure 3.11) to monitor the formation and growth of the CdSe QWs, as shown in Figure 3.11 At 5 min there are two distinct peaks present at 339 nm and 350 nm. These peaks are characteristics of magic-sized $(CdSe)_{13}$ NCs.[221]. Over the time, new absorption peaks at 426 and 451 nm

appeared and grew in intensity while intensity of the peaks, which are associated to $(CdSe)_{13}$ NCs slowly diminished. Absorption peaks at 426 and 451 nm were reported to

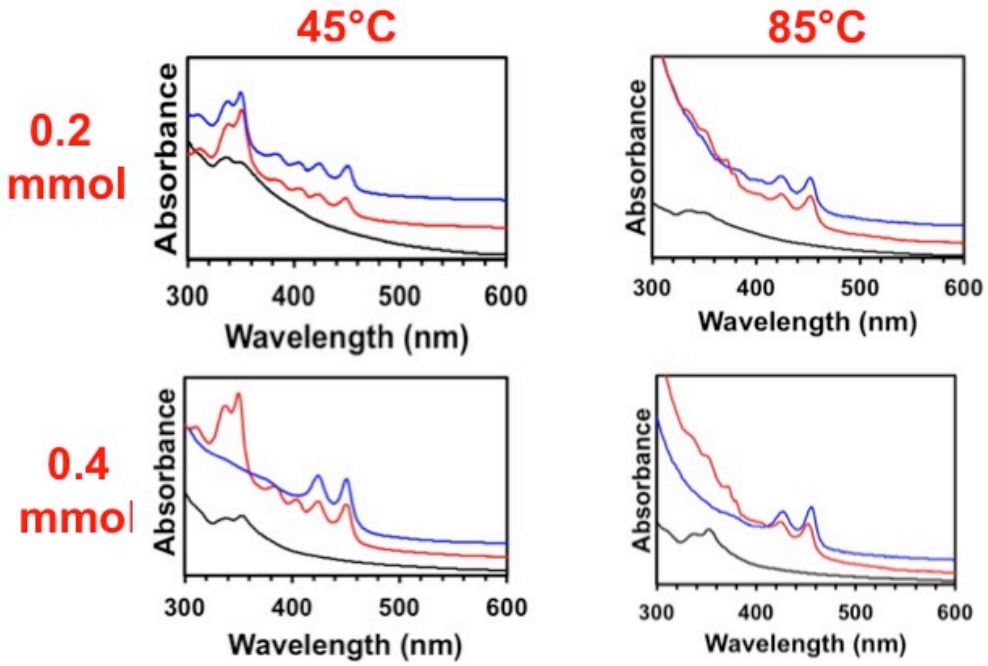

Figure 3.13.Ttime dependent absorption spectra during the ex situ growth of CdSe QW synthesis at 0 minutes (back), 1440 minutes (red), 2880 minutes (blue)

be electronic transitions of CdSe QW. Overtime, these peaks grow in intensity and become more defined until the reaction is complete at 1440 min. Through the cooperative attachment of the magic-size CdSe NCs along the c-axis, the length of the nanowires continues to grow, while the width remains the same as that of the original OLA-coated NCs. This synthesis was based on our published procedure for the synthesis of magic-sized $(CdSe)_{34}$ NCs[228, 236]. The growth of QWs from NCs requires an increase in the reaction kinetics.[206]. To drive the reaction towards QW formation, not only did we increase the temperature to 45 °C, but the ratio of Cd:Se was also increased from 1:1 to 1:2.7.

The XRD data of CdSe QWs in Figure 3.2D show the reflections of (100), (002), and 101 planes. It is known that in the case or oriented attachment, the growth is driven by the highly reactive 110 plane.[224] This plane is not present in our QW, and therefore we can conclude that the growth did not occur via orientated attachment. The proposed mesoscale assembly is driven by the long chain length of the OLA ligand that results in a large lateral diffusion barrier for the cooperative interactions between the CdSe NCs This large lateral barrier promotes growth of the QW along the c-axis.

Accordingly, in the co solvent system of the QPL synthesis, in addition to the long chain of the OLA, a short chain is present in the form of octylamine (OA). This shorter chain length would posses a lower lateral diffusion barrier and subsequent growth in that direction. We propose a mesoscale assembly process for the transition o f the NCs to the other structures. The scheme of this proposed mechanism is depicted in Figure 3.12 In a mesoscale assembly, it is the hydrophobic interaction and chain interdigitation of the surface ligands that promote the formation of different nanostructures from the NC building blocks.

In order to prove our proposed mechanism of mesoscale assembly driven transformation of $(CdSe)_{13}$ NCs to QWs, we isolated the $(CdSe)_{13}$ NCs and used this monomer as a precursor for the CdSe QW formation. We took 0.4 mmol of the monomer and injected it into 5 mL of OLA at 85 °C and monitored the growth with UV spectroscopy, found in Figure 3.13A. At 60 min, peaks corresponding to the $(CdSe)_{13}$ monomer as well as the CdSe QWs were observed in the spectrum. In addition, a peak at 406 nm is also present. We believe that this peak is representative of a larger size CdSe NC that may be an intermediate between the $(CdSe)_{13}$ NCs and the QWs. As time

progresses, the peaks at 335 and 350 nm, corresponding to the $(CdSe)_{13}$ NCs as well at the intermediate peak at 406 nm disappear and the peaks at 426 and 451 nm, corresponding to the CdSe QWs, growth in both sharpness and intensity.

It should also be noted that we performed this experiment with two different concentrations of $(CdSe)_{13}$ monomer (0.2 mmol and 0.4 mmol) at both 65°C and 85°C. It was found that both monomer concentration and temperature were important parameters to consider for QW growth. It has been demonstrated in previous studies that 1 or 2 dimensional growth only occurs if the chemical potential of the monomers present in solution is greater than that of the NC surface atoms.[237] Both concentrations at the higher temperature, 85°C, resulted in QW growth as well as the disappearance of the monomer absorption peaks. However, at the higher monomer concentration, the intensity and sharpness of the final absorption peaks was improved. These results are reinforcing the key role that the higher monomer concentration, and subsequent chemical potential, has on the QW growth. In the case of the higher monomer concentration and subsequent high chemical potential of the solution, the 1D growth was achieved even at the lower temperature It should also be noted that under conditions of the lower temperature and lower monomer concentration, no growth or transformation was observed. Accordingly, under conditions of higher monomer concentration and lower temperature, QW growth was observed, but monomer was still present in the solution even after 48 hours.

A control experiment was also performed using the same reaction conditions that result in NW formation, but using OA in place of OLA. Without the presence of long chain length, the growth along the c-axis was prohibited and no QW formation was

observed. Interestingly, even after 48 hours, the only peaks observed in the UV spectrum were those at 338 and 350 nm corresponding to $(CdSe)_{13}$ NCs (data not shown).

3.4.6 Growth of CdE (Se and S) QRs.

The CdSe QRs have the highest synthetic temperature of any of the cadmium-based nanostructures. This is due to the fact that the formation of QRs requires a greater amount of kinetic energy for the two dimensional growth process.[238] Also, it should be noted that the cadmium to selenium ratio of this reaction, 1:2.7, was greater than that of the CdSe QWs. These increases in reaction temperature and selenium concentration

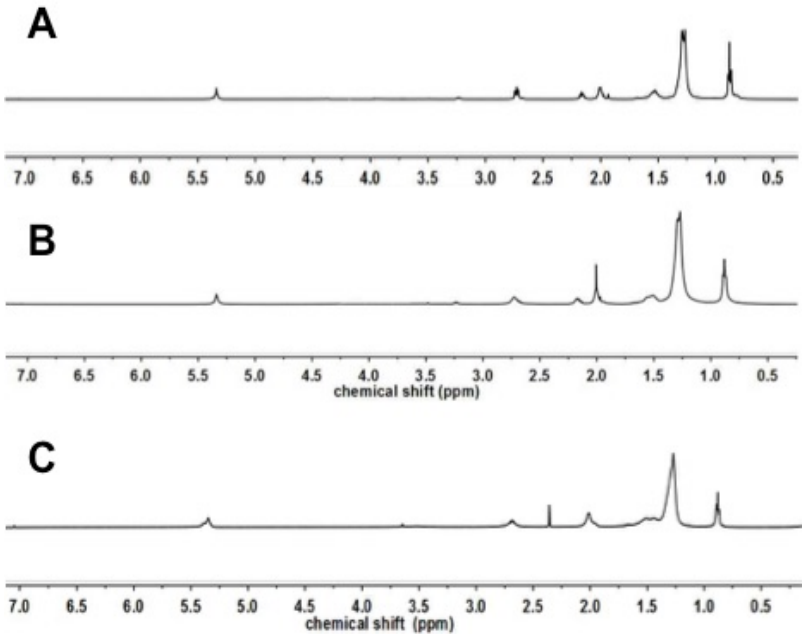

Figure 3.14. ^{1}H NMR characterization of CdSe QWs (A), QPLs (B), and QRs (C).

both aid to increase the kinetics and promote the formation of two-dimensional QRs. Similarly, the CdS QRs also require a higher reaction temperature than the CdS QWs and QPLs and a cadmium to sulfur ratio of 1:2.7. This corroborates the mechanism that was

proposed for the CdSe QRs, where an increase in kinetics is critical to two dimensional growth of the QRs.

3.4.7 Growth of ZnE (Se and S) QWs, QPL, and QRs.

It is known that unlike cadmium chalcogenide reactions, the formation of zinc chalcogenide NCs is controlled by thermodynamics than kinetics parameters.[239, 240] As a result, these zinc based reactions requires higher temperatures, above 100°C., than the cadmium chalcogenide nanostructures (QWs, QPLs, and QRs). Also, due to the difference in the reactivity of the cadmium and zinc precursors, the ratios of metal to chalcogenide were also varied from the cadmium to zinc reactions (see Table 3.2). We

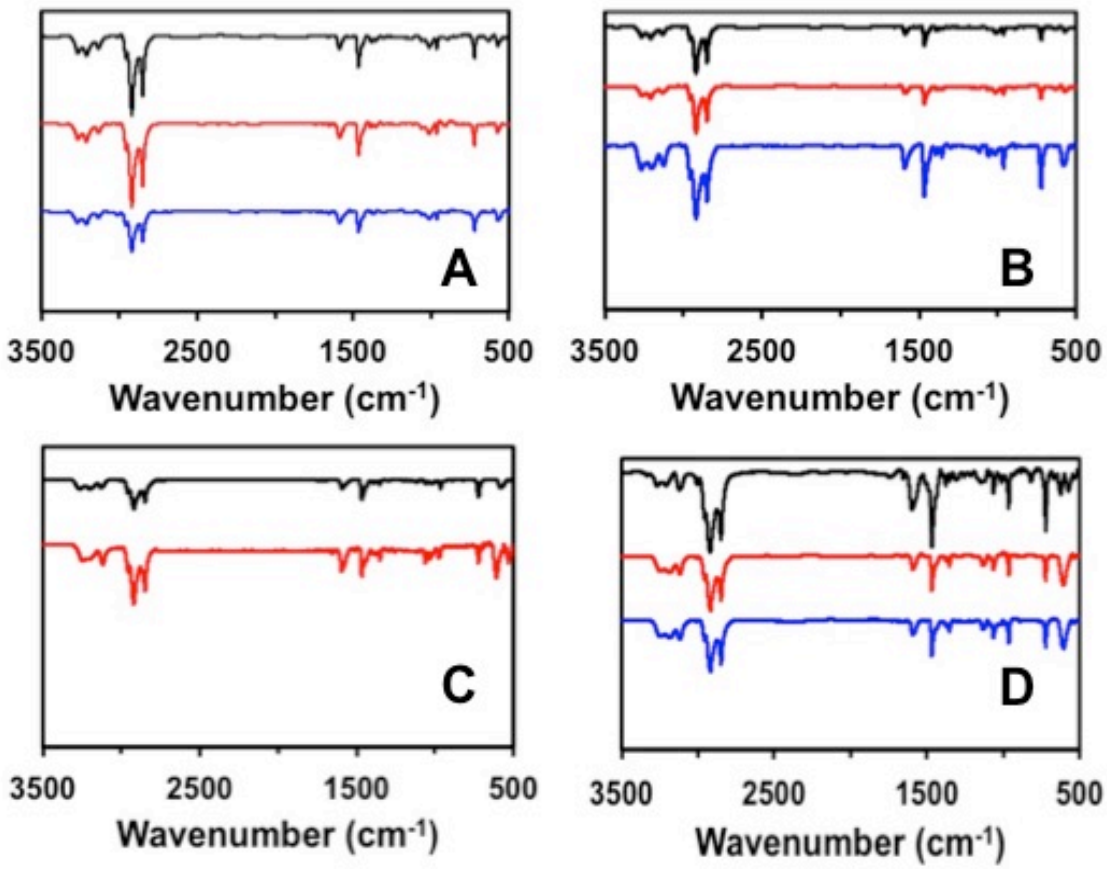

Figure 3.15. FTIR characterization of CdSe (A), CdS (B), ZnSe (C), and ZnS (D) QWs (black), QPLs (Rad), and QRs (blue).

believe that the formation and growth process for the zinc-based materials follow a similar mesoscale growth mechanism to that of their cadmium counterparts.

3.4.8 3urface Characterization of Anisotropic ME NCs

A combination of NMR, FTIR, and TGA analysis was used to characterize the surface of the anisotropic NCs. The NMR spectra of all QWs, QPLs and QRs showed the presence of OLA on the surface (^{1}H NMR of CdSe based materials shown in Figure 3.14). Additionally, the vinyl peak (-CH=CH-) at 5.35 ppm and peak of the methylene adjacent to the amine (-NH_2-CH_3) at 1.5 ppm of OLA were broad, confirming that no free ligand remained. The NMR peak broadening observed in the purified sample is a result of spin-spin relaxation and dipole broadening from the presence of only bound ligand. In the case of the QPL, the same peaks were observed. Due to the overlap of resonances in OA and OLA, it was impossible to distinguish their characteristic ligand,

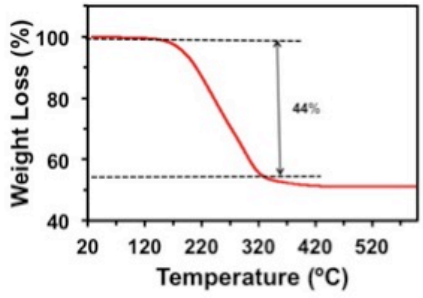

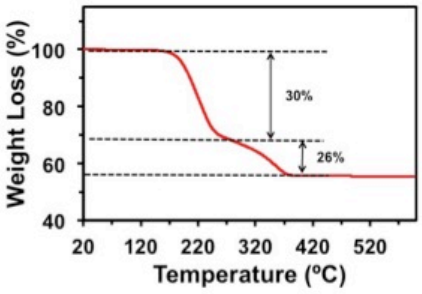

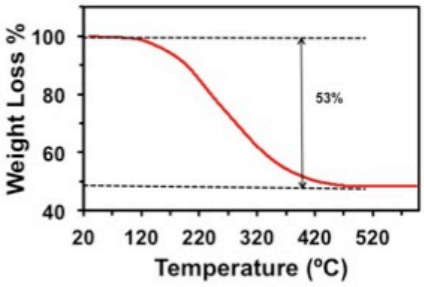

Sample	% OLA	% OctA	% Yield
CdSe QPL	26%	30%	54%
CdSe QW	44%	-	74%
CdSe QR	53%	-	75%
CdS QPL	23%	31%	53%
CdS QW	42%	-	65%
CdS QR	47%	-	65%
ZnS QPL	22%	36%	59%
ZnS QW	51%	-	70%
ZnS QR	57%	-	66%
ZnSe QPL	24%	33%	57%
ZnSe QW	58%	-	64%

Figure 3.16. TGA characterization of CdSe QW (A), QPLs (B), and QRs (C). Table 3 shows the results from all TGA analysis and the subsequent percent yield of each metal chalcogenide nanostructure

Similarly, FTIR analysis of all 11 structures, shown in Figure 3.15, illustrate the surface passivation with primary amines in which the characteristic amine (N-H) bending at 1575 cm^{-1} and stretching in the range of 3400-3000 cm^{-1} respectively are present. The FTIR also displays the characteristic CH_2 bending at 1462 cm^{-1} and symmetric and asymmetric C-H stretching at 2855 cm^{-1} and 2915 cm^{-1} respectively. However, similarly to the limitations of the ^1H NMR analysis, the peaks observed are characteristic of both OLA and OA.

TGA analysis was used to overcome this limitation since OLA and OA have different boiling point. In the case of QWs and QRs, only one type of weight loss (see Table 3.3 and Figure 3.16) was observed indicated a single ligand passivating the surface. The temperature of the weight loss also corresponded to the boiling point of OLA. Interestingly, the percentage of passivated surface was greater for the QRs and than QWs. This can be attributed to the increase in kinetics and thermal energy employed in the QR synthesis. The weight loss curve for the QPLs was significantly different showing a dually passivated surface of both OLA and OA. The TGA also showed a greater percentage of the surface was passivated with OA on all QPL samples. This can be attributed to the increase of the absorption coefficient of shorter ligands.

3.5 Conclusion

Colloidal semiconductor nanoparticles have been the focus of much research in the last two decades, specifically investigating the effects of size, shape and composition on optoelectronic properties. In this context, 1D and 2D structures have shown tremendous promise in solar cell fabrication. However, the potential applications of these nanomaterials have been hindered by a lack of large-scale production methods.

Here we will present low temperature (<150 ^{0}C) syntheses of anisotropically-shaped metal chalcogenide nanostructures including using Cd and Zn as metal precursors and S and Se as chalcogenol precursors in the gram scale. It was determined that a long chain amine was critical to control unilateral growth of QWs while a dually passivated surface containing both a long and short chain amine lead to QPL growth. The QRs were found to be more dependent on the reaction kinetics and required higher temperatures. Finally, it was confirmed that the growth process occurred via mesoscale assembly, with building blocks of ultrasmall NCs.

3.6 Appendix

Table 3.1. Summary of the reaction conditions to prepare all of the anisotropically shaped metal chalcogenide NCs presented in this study.

Entry	Metal Precursor	Chalcogenide Precursor	Metal to Chalcogenide Ratio	Growth and Injection Temp. (°°C)	Reaction Time (hr)	Structure
1	Cd(OAc)-OLA	Se-OLA-HT	1:2.7	45	24	NW
2	Cd(OAc)-OLA	Se-OLA-HT	1:2.7	100	24	NR
3	Cd(OAc)-OLA	S-OLA-HT	1:2.7	25	24	NW
4	Cd(OAc)-OLA	S-OLA-HT	1:2.7	45	24	NR
5	Zn(OAc)-OLA	Se-OLA-HT	1:3.5	120	30	NW
6	Zn(OAc)-OLA	S-OLA-HT	1:2.7	120	30	NW
7	Zn(OAc)-OLA	S-OLA-HT	1:3.2	120	24	NR
8	$CdCl_2$-OLA/OA	Se-OLA/OA-HT	1:4	65	48	NPL
9	$CdCl_2$-OLA/OA	S-OLA/OA-HT	1:4	45	48	NPL
10	$ZnCl_2$-OLA/OA	Se-OLA/OA-HT	1:4	120	48	NPL
11	$ZnCl_2$-OLA/OA	S-OLA/OA-HT	1:4	120	48	NPL

Table 3.2. Summarizes the absorption and emission peaks for all of the anisotropically shaped metal chalcogenide NCs presented in this study.

Entry	Material	Absorption (nm)			Emission (nm)
		First Absorption	Second Absorption	Third Absorption	
1	CdSe NW	451	426	380	453
2	CdSe NPL	448	424	375	450
3	CdSe NR	603			
4	CdS NW	385	373		387
5	CdS NR	435			446
6	CdS NPL	375	337		380
7	ZnS NW	275	255		
8	ZnS NPL	382			
9	ZnS NR	258			
10	ZnSe NW	292	280		
11	ZnSe NPL	347	329		

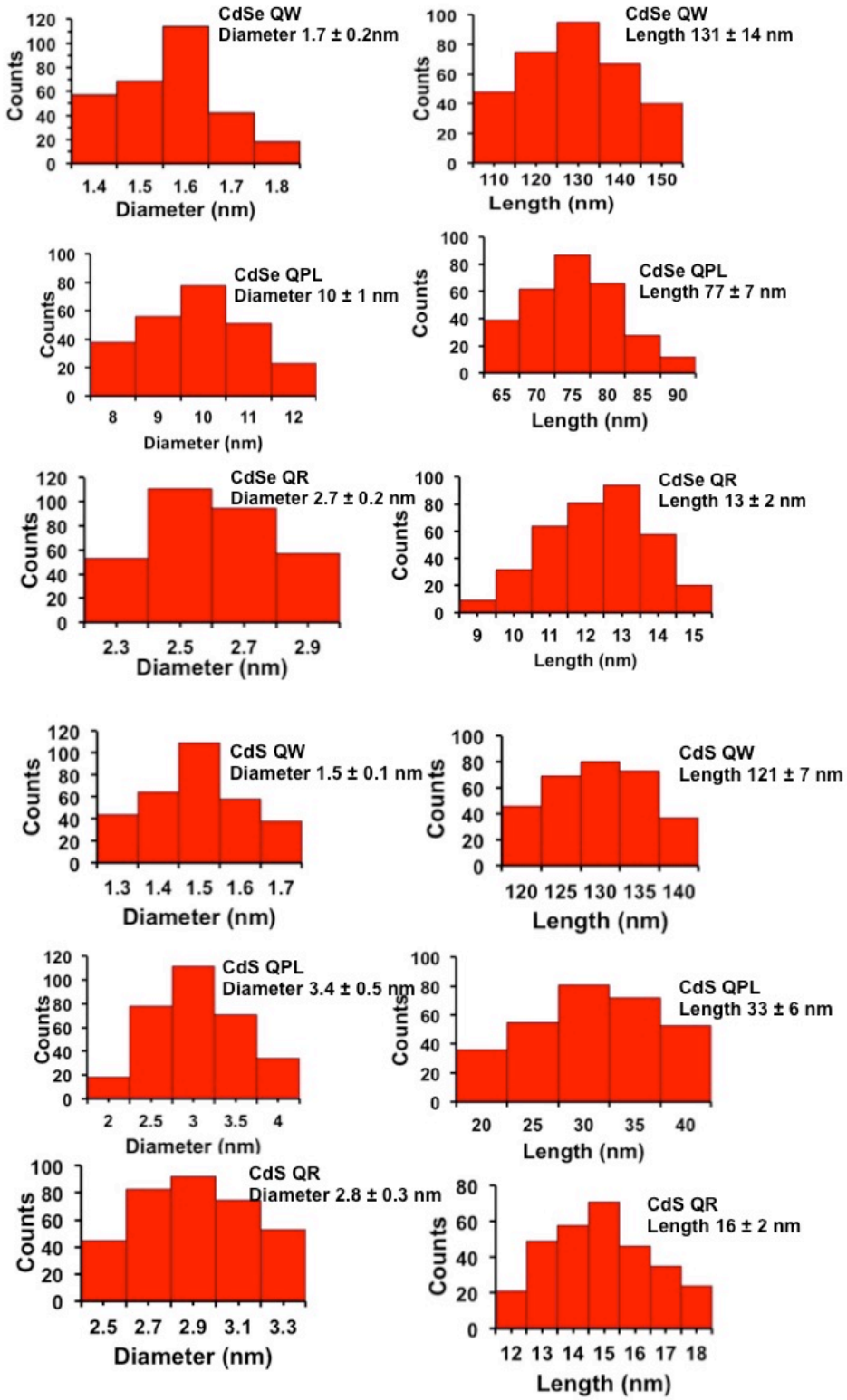

Figure 3.17. Histograms of diameter and length distributions of CdSe and CdSe QWs, QPL, and QRs.

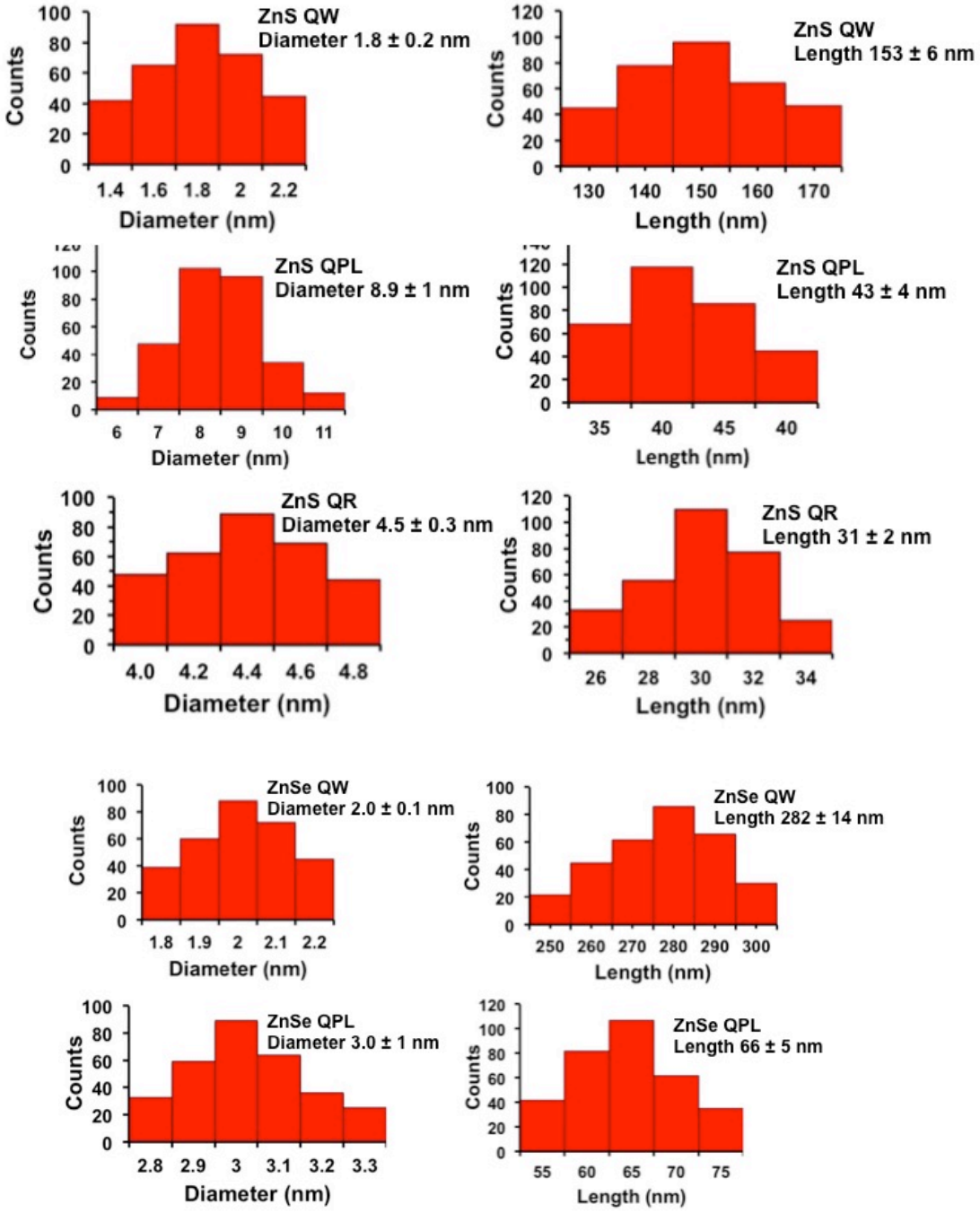

Figure 3.18. Histograms of diameter and length distributions of ZnS QWs, QPLs, and QRs, and ZnSe Qws and QPLs.

3.7 References

1. Huynh, W.U., J.J. Dittmer, and A.P. Alivisatos, *Hybrid nanorod-polymer solar cells.* science, 2002. **295**(5564): p. 2425-2427.
2. Kelzenberg, M.D., et al., *Enhanced absorption and carrier collection in Si wire arrays for photovoltaic applications.* Nature materials, 2010. **9**(3): p. 239-244.
3. Law, M., et al., *Nanowire dye-sensitized solar cells.* Nature materials, 2005. **4**(6): p. 455-459.
4. Liu, Y.-H., et al., *Origin of high photoluminescence efficiencies in CdSe quantum belts.* Nano letters, 2009. **10**(1): p. 352-357.
5. Salant, A., et al., *Quantum rod-sensitized solar cell: nanocrystal shape effect on the photovoltaic properties.* Nano letters, 2012. **12**(4): p. 2095-2100.
6. Tang, J., et al., *Solution-processed core-shell nanowires for efficient photovoltaic cells.* Nature nanotechnology, 2011. **6**(9): p. 568-572.
7. de Mello Donegá, C., P. Liljeroth, and D. Vanmaekelbergh, *Physicochemical Evaluation of the Hot‐Injection Method, a Synthesis Route for Monodisperse Nanocrystals.* Small, 2005. **1**(12): p. 1152-1162.
8. Peng, Z.A. and X. Peng, *Formation of high-quality CdTe, CdSe, and CdS nanocrystals using CdO as precursor.* JOURNAL-AMERICAN CHEMICAL SOCIETY, 2001. **123**(1): p. 183-184.
9. Peng, Z.A. and X. Peng, *Nearly Monodisperse and Shape-Controlled CdSe Nanocrystals via Alternative Routes: Nucleation and Growth.* Journal of the American Chemical Society, 2002. **124**(13): p. 3343-3353.
10. Qu, L., Z.A. Peng, and X. Peng, *Alternative routes toward high quality CdSe nanocrystals.* Nano Letters, 2001. **1**(6): p. 333-337.
11. Chen, Y., et al., *Side reactions in controlling the quality, yield, and stability of high quality colloidal nanocrystals.* Journal of the American Chemical Society, 2005. **127**(38): p. 13331-13337.
12. Dolai, S., et al., *Isolation of bright blue light-emitting CdSe nanocrystals with 6.5 kDa core in gram scale: high photoluminescence efficiency controlled by surface ligand chemistry.* Chemistry of Materials, 2014. **26**(2): p. 1278-1285.
13. Smith, D.K., et al., *Tuning the synthesis of ternary lead chalcogenide quantum dots by balancing precursor reactivity.* ACS nano, 2010. **5**(1): p. 183-190.
14. Xie, R., M. Rutherford, and X. Peng, *Formation of high-quality I– III– VI semiconductor nanocrystals by tuning relative reactivity of cationic precursors.* Journal of the American Chemical Society, 2009. **131**(15): p. 5691-5697.
15. Joo, J., et al., *Low-Temperature Solution-Phase Synthesis of Quantum Well Structured CdSe Nanoribbons.* Journal of the American Chemical Society, 2006. **128**(17): p. 5632-5633.
16. Wang, G., et al., *Synthesis and characterization of one-dimensional CdSe nanostructures.* Applied physics letters, 2006. **88**(19): p. 193115.
17. Li, D., et al., *Direction-specific interactions control crystal growth by oriented attachment.* Science, 2012. **336**(6084): p. 1014-1018.
18. Liu, Y.-H., et al., *Lamellar Assembly of Cadmium Selenide NCs into Quantum Belts.* Journal of the American Chemical Society, 2011. **133**(42): p. 17005-17013.

19. Wang, F., et al., *Two-Dimensional Semiconductor Nanocrystals: Properties, Templated Formation, and Magic-Size NC Intermediates.* Accounts of Chemical Research, 2015. **48**(1): p. 13-21.
20. Wang, Y., et al., *Preparation of Primary Amine Derivatives of the Magic-Size NC (CdSe)13.* Inorganic Chemistry, 2013. **52**(6): p. 2933-2938.
21. Wayman, V.L., et al., *Bound 1D Excitons in Single CdSe Quantum Wires.* The Journal of Physical Chemistry Letters, 2012. **3**(18): p. 2627-2632.
22. Wang, Y., et al., *Magic-Size II–VI NCs as Synthons for Flat Colloidal Nanocrystals.* Inorganic Chemistry, 2015. **54**(3): p. 1165-1177.
23. Ithurria, S., G. Bousquet, and B. Dubertret, *Continuous Transition from 3D to 1D Confinement Observed during the Formation of CdSe Nanoplatelets.* Journal of the American Chemical Society, 2011. **133**(9): p. 3070-3077.
24. Ithurria, S. and B. Dubertret, *Quasi 2D Colloidal CdSe Platelets with Thicknesses Controlled at the Atomic Level.* Journal of the American Chemical Society, 2008. **130**(49): p. 16504-16505.
25. Li, Z. and X. Peng, *Size/shape-controlled synthesis of colloidal CdSe quantum disks: ligand and temperature effects.* Journal of the American Chemical Society, 2011. **133**(17): p. 6578-6586.
26. Mahler, B., et al., *Core/shell colloidal semiconductor nanoplatelets.* Journal of the American Chemical Society, 2012. **134**(45): p. 18591-18598.
27. Wang, Y., et al., *Isolation of the Magic-Size CdSe NCs [(CdSe)13(n-octylamine)13] and [(CdSe)13(oleylamine)13].* Angewandte Chemie International Edition, 2012. **51**(25): p. 6154-6157.
28. Wang, Y., et al., *The Magic-Size NC (CdSe)34 as a Low-Temperature Nucleant for Cadmium Selenide Nanocrystals; Room-Temperature Growth of Crystalline Quantum Platelets.* Chemistry of Materials, 2014. **26**(7): p. 2233-2243.
29. Lee, E.J., et al., *Oriented attachment: An effective mechanism in the formation of anisotropic nanocrystals.* The Journal of Physical Chemistry B, 2005. **109**(44): p. 20842-20846.
30. Schliehe, C., et al., *Ultrathin PbS sheets by two-dimensional oriented attachment.* Science, 2010. **329**(5991): p. 550-553.
31. Srivastava, S., et al., *Light-controlled self-assembly of semiconductor nanoparticles into twisted ribbons.* Science, 2010. **327**(5971): p. 1355-1359.
32. Tang, Z., N.A. Kotov, and M. Giersig, *Spontaneous organization of single CdTe nanoparticles into luminescent nanowires.* Science, 2002. **297**(5579): p. 237-240.
33. Tang, Z., et al., *Self-assembly of CdTe nanocrystals into free-floating sheets.* Science, 2006. **314**(5797): p. 274-278.
34. Cölfen, H. and S. Mann, *Higher‐order organization by mesoscale self‐assembly and transformation of hybrid nanostructures.* Angewandte Chemie International Edition, 2003. **42**(21): p. 2350-2365.
35. Cho, K.-S., et al., *Designing PbSe nanowires and nanorings through oriented attachment of nanoparticles.* Journal of the American Chemical Society, 2005. **127**(19): p. 7140-7147.

36. Chen, Y.-C., T.-C. Liu, and Y.-J. Hsu, *ZnSe·0.5N2H4 Hybrid Nanostructures: A Promising Alternative Photocatalyst for Solar Conversion.* ACS Applied Materials & Interfaces, 2015. **7**(3): p. 1616-1623.
37. Muruganandham, M. and Y. Kusumoto, *Synthesis of N, C Codoped Hierarchical Porous Microsphere ZnS As a Visible Light-Responsive Photocatalyst.* The Journal of Physical Chemistry C, 2009. **113**(36): p. 16144-16150.
38. Teunis, M.B., S. Dolai, and R. Sardar, *Effects of Surface-Passivating Ligands and Ultrasmall CdSe Nanocrystal Size on the Delocalization of Exciton Confinement.* Langmuir, 2014. **30**(26): p. 7851-7858.
39. Yu, J.H., et al., *Giant Zeeman splitting in nucleation-controlled doped CdSe: Mn2+ quantum nanoribbons.* Nature materials, 2010. **9**(1): p. 47-53.
40. Liu, Y.-H., et al., *Origin of High Photoluminescence Efficiencies in CdSe Quantum Belts.* Nano Letters, 2010. **10**(1): p. 352-357.
41. Teunis, M.B., et al., *Mesoscale Growth and Assembly of Bright Luminescent Organolead Halide Perovskite Quantum Wires.* Chemistry of Materials, 2016. **28**(14): p. 5043-5054.
42. Peng, Z.A. and X. Peng, *Mechanisms of the Shape Evolution of CdSe Nanocrystals.* Journal of the American Chemical Society, 2001. **123**(7): p. 1389-1395.
43. Jiang, Z.-J. and D.F. Kelley, *Role of Magic-Sized Clusters in the Synthesis of CdSe Nanorods.* ACS Nano, 2010. **4**(3): p. 1561-1572.
44. Yu, H., et al., *Cadmium Selenide Quantum Wires and the Transition from 3D to 2D Confinement.* Journal of the American Chemical Society, 2003. **125**(52): p. 16168-16169.
45. *Semiconductor Data*, ed. O.L. Madelung. 1996, Berlin: Springer.
46. Dolai, S., et al., *Isolation of Bright Blue Light-Emitting CdSe Nanocrystals with 6.5 kDa Core in Gram Scale: High Photoluminescence Efficiency Controlled by Surface Ligand Chemistry.* Chemistry of Materials, 2013. **26**(2): p. 1278-1285.
47. Li, J.J., et al., *Large-scale synthesis of nearly monodisperse CdSe/CdS core/shell nanocrystals using air-stable reagents via successive ion layer adsorption and reaction.* Journal of the American Chemical Society, 2003. **125**(41): p. 12567-12575.
48. Kazes, M., et al., *Temperature Dependence of Optical Gain in CdSe/ZnS Quantum Rods.* The Journal of Physical Chemistry C, 2007. **111**(22): p. 7898-7905.
49. Kan, S., et al., *Synthesis and size-dependent properties of zinc-blende semiconductor quantum rods.* Nature materials, 2003. **2**(3): p. 155-158.
50. Mokari, T. and U. Banin, *Synthesis and properties of CdSe/ZnS core/shell nanorods.* Chemistry of materials, 2003. **15**(20): p. 3955-3960.

CHAPTER 4. SURFACE CHEMISTRY CONTROLLED OPTOELECTRONIC PROPERTIES OF SEMICONDUCTOR NANOCRYSTALS

4.1 Synopsis

Atomically precise, ultrasmall nanocrystals are an ideal system to study these mechanisms due to the large surface-to-volume ratio, in which surface atoms control the overall photophysical properties. This chapter describes the study of how exchanging the native L-type long chain amine ligands with various chalcogenol ligands with different levels of conjugation, para-substitutions, binding mode, and binding head group affects the photophysical properties of ultrasmall CdSe nanocrystals. We first demonstrate how the electron donating or withdrawing nature of the para-substitution of the surface ligands control the extent of excitonic hole delocalization Based on these results we expanded the investigation to include how other characterisitcs of the surface ligands (level of conjugation, binding mode, and binding head group) impact delocalization. It was determined that the presence of large pi-conjugation (e.g., pyrene vs. phenyl) and bidentate binding head group (e,g., dithiocarbamate vs. thiol) of surface passivating ligands are crucial to promote the highest delocalization of excitonic hole wave functions and the largest red-shift (up to 650 meV) in the absorption peak of the nanocrystals.

4.2 Introduction

Despite the tremendous interest in using ultrasmall semiconductor NCs to provide fundamentally new electronic and electrochemical[241] properties on the molecular level, little is known about shifting the energy levels of these NCs to appropriately match, for

example, the solar spectrum without changing the core size or composition. During the last 20 years, the energy of the quantum dots (QDs) containing a long hydrocarbon ligand (“innsulating”) coating has been controlled through modification of the core size, shape, and composition[242-245] However, the efficiency of solid-state devices[246-252] relies heavily on the effective charge transport between NCs and their surroundings, including the chemical nature of their surface-passivating ligands. In this context, coating with innsulating ligands hinders the charge-transport efficiency. Moreover, the stabilization of excitons (NC-bound electron–hole pairs) through delocalization into the ligand monolayer is fundamentally important to enhance the charge-transfer process from or to NCs[248-252] and increase the electrical conductivity in optoelectronic and photovoltaic devices.[246-248, 253-256] Studying the exciton delocalization of ultrasmall NCs (<2.0 nm in diameter) could also be important since they are in the strong confinement regime and strongly confined excitons are easily susceptible to delocalization onto suitable surface-passivating ligands.[253, 257, 258] Therefore, one would expect a substantial difference in the delocalization of charge carriers at the NC surface–ligand interface in comparison to QDs, which are in the weak to intermediate confinement regime.[242, 259] The extension of the wave function outside the NC boundary is an important aspect of preparing artificial solids, which could result in future applications such as quantum computing.[260-262]

Ultrasmall NCs display discrete energy levels with molecule-like highest occupied molecular orbitals (HOMOs) and lowest unoccupied molecular orbitals (LUMOs)[263-265] as demonstrated through the appearance of distinct oxidation and reduction waves in electrochemical measurements.[241, 266-268] The presence of

distinct orbitals result in an increase in the probability of substantial orbital mixing with the molecular orbitals of the ligands that have appropriate energy and symmetry, a limitation we commonly encounter with QDs. Furthermore, electronic coupling between NCs and surface-passivating ligand should be carefully controlled not only to obtain the desired energy level of the nanomaterials but also to achieve fast charge separation and slow recombination, as observed for ultrasmall NCs.[258, 269, 270] These ultrasmall NCs are fundamentally important because they bridge the gap between small molecules and QDs. Therefore, a precise understanding of underlying electronic, electrochemical, and photophysical properties on the molecular level could become a reality by studying ultrasmall NCs rather than traditionally studied QDs. However, ultrasmall NCs have their band gap only in the blue region of the solar spectrum and therefore are not suitable for photovoltaic or photocatalysis applications. This drawback can be overcome by finding suitable surface ligands that allow band gap manipulation in the region of the solar spectrum through the delocalization of excitons. Even though exciton delocalization in a multilayer film of QDs has been studied by increasing the electronic coupling between QDs,[271-274] scientific knowledge of exciton delocalization in dissolved QDs has been very limited until recently Weiss and coworkers have demonstrated the effective band gap modulation of dissolved innocent ligand-coated CdSe QDs (2.2–3.8 nm diameter) through a postsynthesis ligand-exchange reaction with phenydithiocarbamate (PDTC) lignads.[275]

Herein we report an unprecedentedly large 610 meV decrease in the optical band gap (ΔE_{og}) of 1.6-nm-diameter CdSe NCs due to the coordination of CF_3-substituted PDTC ligands via the ligand-exchange reaction on dodecylamine (DDA)-capped NCs.

This is the largest value reported for CdSe NCs or QDs so far. To our knowledge, this is the smallest-diameter NCs of any type used to study the surface-ligand-induced exciton delocalization process[275-277]. The decrease in the band gap upon CF_3–PDTC treatment is nearly 3-fold higher than the maximum change recently reported for CdSe QDs[275, 278, 279] via the ligand-exchange reaction and at least 10 times higher than the value obtained due to electronic coupling between QDs dissolved in solution or a dried film[273, 277, 280]. We also show that the variation of the band gap depends strongly on both the size of the NCs and the functional group X (X = CF_3, OCF_3, $N(CH_3)_2$, CH_3, OCH_3, H, Br, and F) present in X-PDTC, where the CdSe NC passivated with PDTC ligands containing the most strongly electron-withdrawing functional group ($-CF_3$) or the smallest-diameter NCs induced the largest red shift in band-edge absorption ($\Delta\lambda$, i.e., the lowest-energy absorption band) and the greatest ΔE_{og}. We hypothesize that such a large change is produced because of the delocalization of the wave function of strongly confined excitonic holes of the NC onto the X-PDTC surface ligands, which was initially proposed by Frederick et al. through density functional theory calculations (DFT) on CdSe QDs.[275, 279] We also believe that there could be a contribution from electron delocalization. Finally, we demonstrate that the effects are not due to changes in the NC core size or composition through using laser desorption ionization time-of-flight mass spectrometry (LDI-TOF-MS).

After our investigation of the known class of PDTC ligands with our unique, strongly confined NCs yielded unprecedented delocalization effects, we aimed to examine additional types of ligands and their impact on exciton delocalization. Most previous reports have centered on ligands that have a similar structure (PDTC), however,

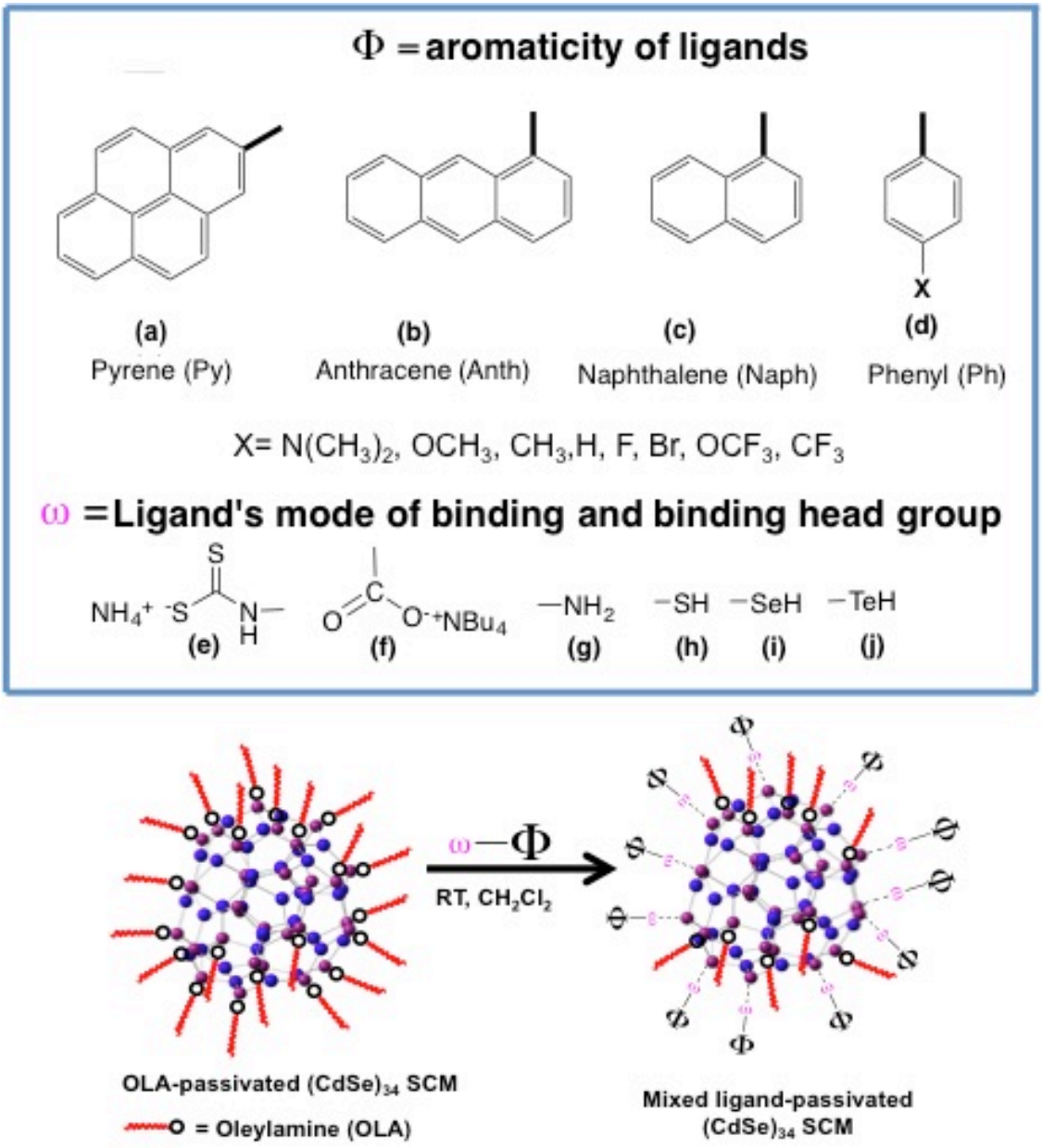

Figure 4.1 Schematic diagram depicting post-synthetic ligand exchange of OLA-passivated $(CdSe)_{34}$ NCs with a generic representation (ω-Φ) of the various ligands shown in Figure 1. The L-type ligand OLA preferentially binds with Cd sites. Purple and blue spheres represent Cd and Se atoms, respectively, of the $(CdSe)_{34}$ NC. The three-dimensional structure of the $(CdSe)_{34}$ NC does not correspond to the proposed core-cage structure reported in the literature.[5, 6] Red wavy lines are the aliphatic chain of OLA with the amine binding head group represented by black circles.

limited studies have examined how different characteristics of the ligand chosen and

influences the delocalization effects. The binding mode, binding head group and level of

conjugation all can impact the exciton delocalization. There have been a limited amount of studies investigating these parameters, but none have been accomplished using an ultrasmall size of semiconductor NCs, which due to their molecule-like character and energy levels as well as large surface to volume ratio, allow for enhancement of the delocalization of the exciton wave function. The large surface to volume ratio results in a majority of the atoms residing on the NC surface, so even a minute change in the surface ligand chemistry can have substantial effects on their optpelectric properties, compared to larger sizes.

Our experimental results as well a theoretical calculations of the molecular orbital (MO) energy levels provide evidence that the delocalization of the hole is influenced by more than just the positions of the NC valence band and surface passivating ligand HOMO. We observe the largest reported shift in the first excitonic peak, of 650 meV, after exchanging the native oleylamine ligands with pyrene dithiocarbamate (py-DTC). We believe that the conjugation of the ligand along with the energy levels of the ligand allow for the improved delocalization.

4.3 Materials and Methods

4.3.1 Materials

Cadmium chloride ($CdCl_2$) (99.9%), selenium (pellets, 99.9%), dodecylamine (DDA) (98%), 1-hexanethiol (HT) (95%), toluene (HPLC grade), acetonitrile (MeCN) HPLC grade), chloroform (HPLC grade), sure seal dichloromethance (DCM) (>99%), carbon disulfide (CS_2) (99.9%), concentrated ammonium hydroxide (NH_4OH) (ACS grade), fluoroanilines (99%), 4-bromoaniline (99%), aniline (99%), 4-trifluoromethylaniline (99%), 4-trifluoromethoxyaniline (99%), *p*-toludine (99%), and *p*-

anisidine (99%) Cadmium acetate dihydrate (Cd $(OAc)_2$•$2H_2O$) (98%),, oleylamine (OLA) (70%), hexanes (95), diphenyl disulfide (99%), diphenyl diselenide (99%), diphenyl ditelluride (99%), diphenyl phosphine (98%), 1- aminopyrene (99%), 1-naphthtmethylamine (97%), and pyrene carboxylate (99%) were purchased from Aldrich and used without further purification. Methanol (99.98%) was purchased from Fisher Scientific**.** Organic solvents were purged with N_2 for 30 min prior to use.

4.3.2 Optical Spectroscopy and Mass Spectrometry Characterization

UV–vis absorption spectra were collected over a range of 800–300 nm using a Varian Cary 50 UV–vis spectrophotometer. Prior to the sample measurements, the baseline was corrected with pure solvent. LDI-TOF MS measurements were performed using a Bruker Autoflex equipped with a nitrogen laser. The samples were prepared by drop-casting the CdSe NCs onto the sample holder and air drying at room temperature.

4.3.3 Surface Characterization

NMR was recorded on a Bruker AVANCE III 500 instrument at 500 MHz frequency. Approximately ~10 mg of NCs were dissolved in 0.6 mL of CD2Cl2 at room temperature and a minimum of 1000 scans were collected. FTIR spectra were acquired using a Thermo Nicolet IS10 FTIR spectrometer. For FTIR analysis, 10 mg was NCs were dissolved in 0.2 mL of $CHCl_3$ or DCM and 20 μL of the solution was drop casted onto s KBr salt plate. The salt plate was placed in a 45°C for 5 minutes. The sample was removed from the oven and allowed to cool to room temperature before analysis. A minimum of 500 scans were collected and all data was processed using Omnic FTIR software.

4.3.4 Synthesis of DDA-coated $(CdSe)_{34}$ NCs

Different sizes (1.6, 1.8, and 2.0 nm in diameter) of CdSe NCs were synthesized using our published procedure with a slight modification.[281] Briefly, in a 100 mL two-necked round-bottomed flask, 0.140 g of $CdCl_2$ was mixed with 5 mL of DDA at 30 °C until all solid dissolved. The optically clear solution was cooled to room temperature, and 10 mL of purged toluene was added before the addition of the selenium precursor. The selenium precursor was prepared separately by dissolving 0.06 g of freshly ground selenium powder in a mixture of 785 μL of DDA and 215 μL of HT at 30 °C under N_2. After the addition of the selenium precursor, the reaction was stirred under N_2 at 40 °C for 2 h. After 2 h, a stable absorption peak was observed, and the NCs were precipitated by the dropwise addition of purged MeCN. The yellow solid was collected by centrifugation. The precipitation step was repeated two more times. Finally, the solid was dried with N_2 and stored in the glovebox for further optical characterization and surface modification.

4.3.5 Synthesis of OLA-Coated $(CdSe)_{34}$ NCs

OLA-passivated (CdSe)34 NCs were synthesized using our published procedure. Briefly, 0.2 g of $Cd(OAc)_2•2H_2O$ was dissolved in 5 mL of OLA in a 100 mL two-neck round bottom flask and placed under vacuum for 15 minutes. while stirring. Once a clear solution was obtained, the solution was put under N_2 and 5 mL of toluene was added. The Cd precursor was allowed to stir for an additional 15 minutes. The Se precursor stock solution was prepared by adding 0.12 g of freshly ground selenium powder to a 25 mL round bottom flask with 1.57 mL OLA and 0.430 mL of HT under N2 atmosphere and stirring until all the Se was dissolved. Next, 1 mL of the Se stock

solution was injected into the Cd precursor and the reaction allowed to stir for 24 hours. The reaction was quenched by diluting with 20 mL of hexanes and adding a 1:1 (v:v) mixture of methanol and acetonitrile drop wise until the solution became cloudy. The solution was centrifuged at 7000 rpm for 5 minutes and a yielded a yellow solid. This precipitation was repeated two additional times to removes excess ligand.

4.3.6 Synthesis of Dithiocarbamate Ligands

Various dithiocarbamate (X-DTC) ligands were prepared according to a literature procedure[282] Briefly, 82.0 mmol of CS_2 was added dropwise over 30 min to 41.0 mmol of the appropriate aniline derivative dispersed in 30 mL of concentrated NH_4OH at 0 °C. The solution was stirred under N_2 overnight. The resulting products for each aniline derivative appeared as a suspended solid that ranged in color from yellow to white to gray. These products were washed with cold chloroform and dried under vacuum overnight. The 4-trifluoromethyl derivative (F_3C-PDTC) did not precipitate at 0 °C. In order to obtain the solid, the reaction mixture was placed in a freezer overnight until the product crystallized. The X-PDTC ligands were stored in the dark before use. The products were characterized by ^1H NMR spectroscopy and electrospray ionization mass spectrometry.

4.3.7 Ligand-Exchange Reaction

All samples were prepared inside a nitrogen-filled glovebox, and reactions were carried out on a Schlenk line. OLA or DDA-coated CdSe NC (0.19 mmol) were dissolved in 10 mL solution of 9:1 DCM:$CHCl_3$ in a 25 mL two-necked round-bottomed flask followed by the addition of 0.39 mmol of X-DTC ligand. The biphasic reaction mixture was vigorously stirred at room temperature from 4 to 48 h depending on the ligand used for the exchange reaction. The exchange reaction was monitored by removing 200 μL of the reaction mixture and then centrifuging to remove insoluble solid. The colored solution (100 μL) was then diluted in 3 mL of DCM for UV–vis spectroscopic characterization. After the reaction mixture displayed its stable lowest-energy absorption maximum, it was centrifuged, dried under reduced pressure, and stored inside a glovebox. The X-DTC-coated samples were stable for at least a month inside the glovebox. The X-DTC-coated CdSe NCs were completely soluble in DCM.

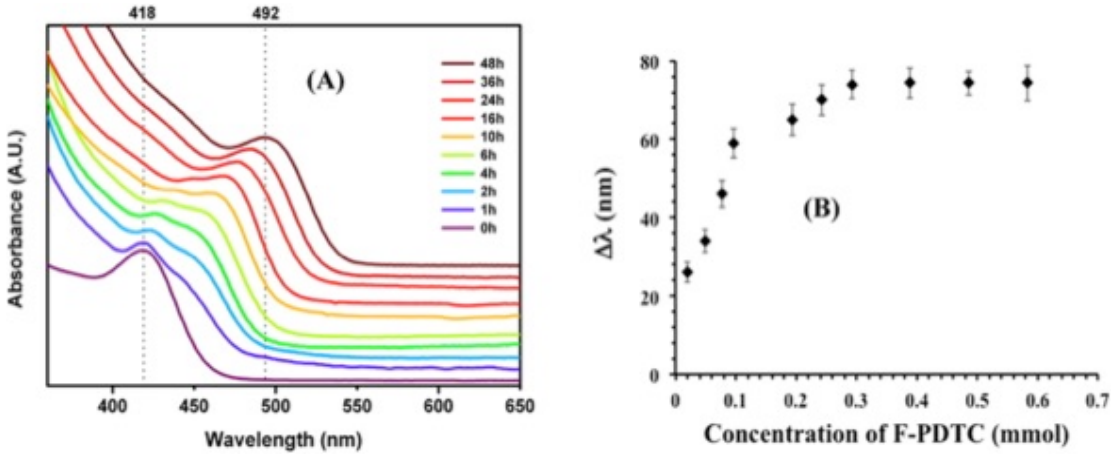

Figure 4.2 (A) Time-dependent absorption spectra of NCs during the ligand exchange reaction of 1.6 nm CdSe NCs upon treatment with 0.39 mmol of F-PDTC at room temperature. The purple curve represents DDA-passivated CdSe NCs. (B) Plot of change of the lowest-energy absorption band of CdSe NCs upon treatment with different concentrations of F-PDTC.

4.4 Results and Discussion

4.4.1 Initial Investigation with F-PDTC

The ligand-exchange reaction was performed according to Figure 4.1. The Materials and Methods section contains details of the synthesis of different sizes of CdSe NCs and the X-PDTC ligands as well as the procedure for the biphasic ligand-exchange reaction. Figure 4.2A shows the time-dependent absorption spectra of CdSe NCs during the ligand-exchange reaction with F-PDTC ligands. The band-edge absorption maxima of DDA-passivated 1.6 nm CdSe NCs was found at 418 nm (2.97 eV), and after nearly 48 h of F-PDTC ligand treatment, the band-edge peak red shifted to 492 nm (2.52 eV), which resulted in a ΔE_{og} of 450 meV. To ensure that the NC surface was adequately passivated with F-PDTC available in the reaction mixture and to observe the highest shift in absorption spectra, an additional 12 h of stirring was performed, resulting in no

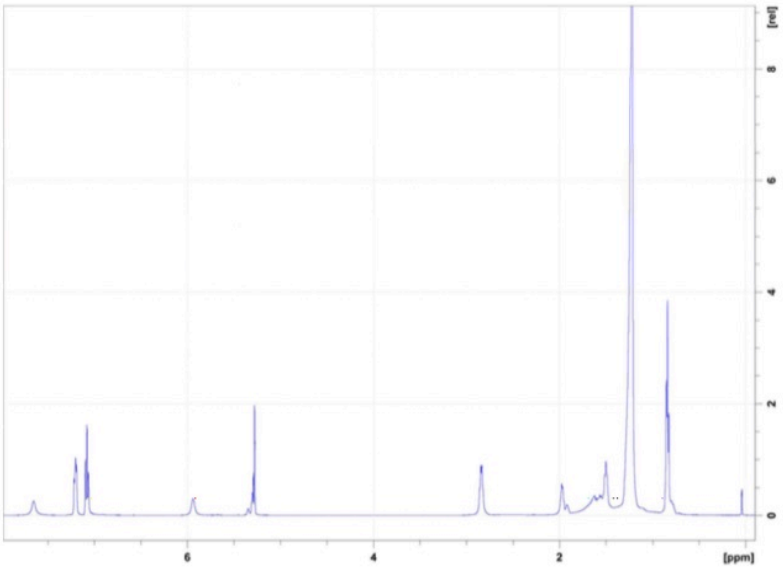

Figure 4.3. 1H NMR spectra of F-PDTC coated 1.6 nm CdSe NCs. The ratio between the methyl protons of DDA and aromatic protons of F-PDTC were used to determine the percent of ligands exchanged.

detectable shift. Furthermore, three different batches of DDA-coated 1.6 nm CdSe NCs were used for this study to confirm that the initial NCs had very similar chemical structure and response.

Importantly, Figure 4.2A also illustrates that at the beginning of the F-PDTC exchange reaction the absorption peak was broad but became sharper as the exchange reaction reached saturation. The initial broadness of the peak can be rationalized as a large variation in the ratio of the number of DDA and F-PDTC ligands on the CdSe NC surface between different NCs in solution. However, the final absorption peak after 48 h of the ligand-exchange reaction is only slightly broader than that of the original DDA-coated CdSe NCs. It is mentioned in the literature that the delocalization of excitons from NCs to their surrounding environment broadens the absorption peak[273, 283] as discussed later in our system.

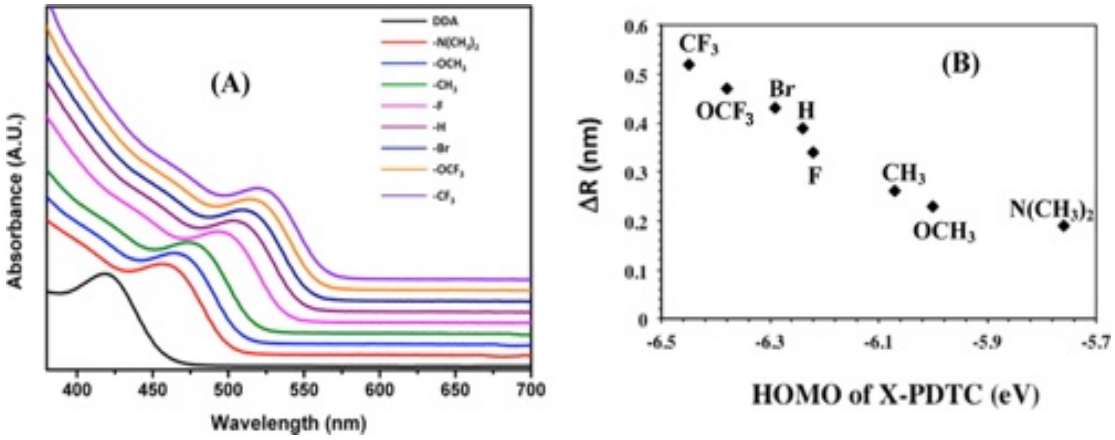

Figure 4.4. (A) Absorption spectra of various PDTC ligand-passivated 1.6 nm CdSe NCs. The spectra were taken at room temperature, and the NCs were dissolved in dichloromethane. (B) Plot of apparent increase in the excitonic radius (ΔR) with respect to the HOMO energy of the PDTC ligand following[39] (see Table 4.1)

Figure 4.2B illustrates the concentration dependence of the lowest-energy NC absorption band under F-PDTC exposure. Evidently, a minimum 2:1 molar ratios of F-PDTC to NCs was required to achieve the maximal change in the band gap. The ratio is much lower than that required for >2.4-nm-diameter CdSe QDs for a similar type of exchange reaction (nearly 5000:1).[275] We believe that the large radius of curvature of ultrasmall CdSe NC created a loosely packed ligand layer that allowed faster penetration of F-PDTC ligands through the coating of DDA ligands, resulting in a rapid exchange reaction. Such exchange is slower for QDs because ligands are tightly packed on the surface, and to perform an exchange reaction, a large amount of reactant is required because such an exchange reaction is controlled by mass transport processes. Furthermore, CdSe QDs previously used for the ligand exchange reaction with PDTC ligands might have taken a longer time because such QDs might be passivated with phophonate groups present as impurities in trioctylphosphine and trioctylphosphine oxide

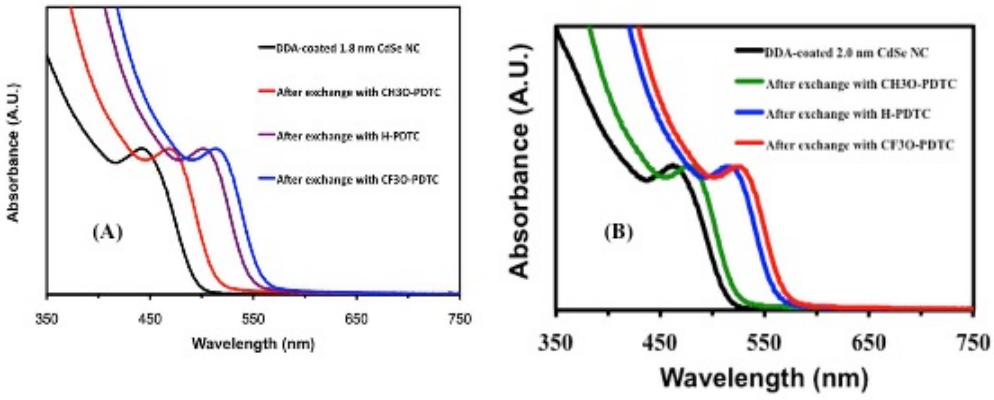

Figure 4.5. Absorption spectra of 1.8 nm (A) and 2.0 nm (B) CdSe NCs passivated with various PDTC ligands. The place exchange reactions were performed on DDA passivated CdSe NCs, which displayed absorption peaks at 440 and 460 nm (black lines) respectively.

used in the synthesis.[284-286] The bidentate phosphonate headgroups would have a stronger interaction with Cd atoms as compared to primary amines, which are capable of only a soft coordination interaction through their lone pairs. Therefore, a shorter reaction time would be required for PDTC ligands to break the bond and displace DDA from the CdSe NCs surface as opposed to QDs. Nevertheless, our experimental results suggest that primary amine-coated NCs/QDs might be suitable materials for performing fast ligand-exchange reactions with bidentate, PDTC-type ligands.

4.4.2 Determination of Percent Exchange using ^{1}H NMR

On the basis of DFT calculations, it was predicted that 1.6 nm CdSe NCs contain a core-cage structure containing 34 Cd and 34 Se atoms in the core, commonly represented by $(CdSe)_{34}$, "magic-sized" NCs.[287, 288] Recently through high-resolution mass spectrometry, we and others have independently demonstrated the existence of $(CdSe)_{34}$ NCs.[281, 289] On the basis of geometry and DFT calculations, 28 Cd and Se atoms are present on the surface; therefore, a maximum of 28 amine ligand could attach to the surface because amines can bind only to Cd sites. Recent experimental work has shown that a maximum of 18 amines are attached to the surface of the $(CdSe)_{34}$ NCs.[289] We performed ^{1}H NMR analysis to determine the number of F-PDTC ligands attached to the $(CdSe)_{34}$ NCs surface resulting from the ligand exchange reaction (Figure 4.3). The analysis showed that on the average 73% of original surface-bound DDA ligands were replaced by PDTC ligands. Therefore, we believe that the surface of the $(CdSe)_{34}$ NCs contained mixed ligands of DDA and PDTC as shown in Figure 4.1.

4.4.3 Investigation of Delocalization Mechanism Using Various Para Substitutions

There is controversy in the literature concerning the mechanism causing the decrease in ΔE_{og} of QDs such as (i) an increase in the NC radius by further growth[290, 291], (ii) an increase in the surrounding dielectric constant[292, 293], and (iii) exciton delocalization into the ligand monolayer after the ligand exchange reaction. We hypothesize that in our NCs such a large ΔE_{og} is due to exciton delocalization, particularly photoexcited holes and perhaps a contribution from electron delocalization, to the HOMO and LUMO of the PDTC ligands, respectively. In such a case, the energetic alignments of CdSe NC orbitals and the orbitals of the PDTC ligand are critical.[279]To test our hypothesis, we investigated different para-substituted PDTCs ranging from electron withdrawing to electron donating, which alter the ligand HOMO and LUMO orbital energies (Figure 4.4A). Table 4.1 summarizes the ΔE_{og} and calculated values that represent the apparent increase in the excitonic radius or "delocalization radius" (ΔR) of CdSe NCs for X-PDTCs bound to NCs. The largest and smallest changes in the ΔE_{og} and

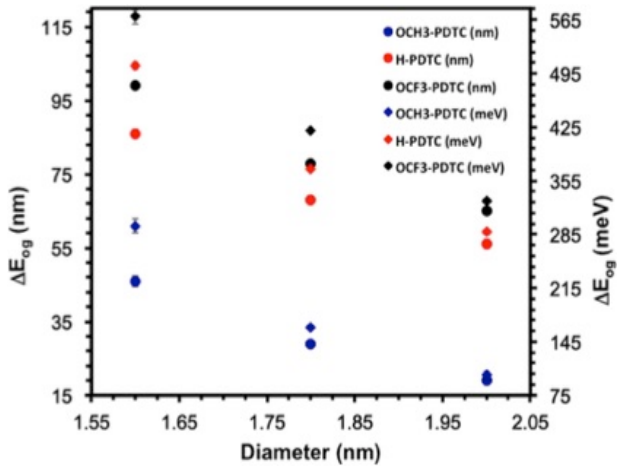

Figure 4.6. Comparison of change in the optical band gap and excitonic radius of various sized CdSe NCs passivated with CF_3O–, H–, and CH_3O–PDTC ligands.

ΔR were obtained for PDTCs containing strongly electron-withdrawing ($-CF_3$) and electron-donating ($-N(CH_3)_2$) functional groups, respectively. Figure 4.4B illustrates the effect of the HOMO energy of X-PDTC ligands on ΔR.[279] The trend in ΔE_{og} parallels the experimental data of CdSe QDs;[279] however, our ΔE_{og}values are nearly a factor of 3 larger than the previous report. Interestingly, our ΔR value for CF_3–PDTC-coated 1.6 CdSe NCs (0.52 nm) is greater than the value reported for 2.8-nm-diameter CdSe QDs (~0.39 nm) coated with the same ligand. Therefore, it is evident that surface ligand chemistry has a more profound effect on ultrasmall NCs than on QDs.

We observed that PDTC containing the strongly electron-withdrawing functional group $-CF_3$provided the largest increase in ΔR, which we hypothesized as being caused by the extent of hole delocalization in our series. However, such a process is energetically unfavorable, and in order for facile hole transfer, the electronic interaction between the NC HOMO and ligand HOMO should be strong along with destabilized hybrid orbitals. Previous DFT calculations[275, 279] predicted that the HOMO of the PDTC ligand containing electron-withdrawing substituents interacted more strongly electronically with the HOMO of the QDs due to the spatial overlap and symmetry matching. The authors also mentioned that due to the energetic alignment between the HOMO of CF_3–PDTC and the HOMO of the QD, these orbitals are more resonantly coupled. These two electronic effects should increase the electron density on the surface Se sites and therefore should reduce the potential energy barrier for photogenerated holes to undergo delocalization into the ligand shell through the conjugated dithiocarbamate linkage, resulting in a decrease in the band gap. In addition, the delocalization of excitons in the bulk CdSe–dithiocarbamate surface ligand interface has been reported

before.[294] Nevertheless, the ΔE_{og} we achieved for CdSe NCs was in the range of 3 to 20 times higher than previously reported with mechanisms ii and iii. Therefore, we believe that the delocalization of strongly confined excitonic holes of ultrasmall CdSe NC into the PDTC ligand shell provides an unprecedentedly large change in the ΔE_{og} of CdSe material due to better energetic alignment of the orbitals. The HOMO energy of our 1.6 nm CdSe NCs is −6.16 eV relative to the vacuum, as determined from the effective mass approximation,[295] and is also close to the value determined by electrochemical techniques,[267, 268, 296, 297] and the Cd^{2+} chelated H-PDTC ligand has a HOMO energy of −6.24 eV[275]. Therefore, the HOMO energy of both NC and PDTC is close in value (<0.1 eV). According to a previous report, both NC and the PDTC ligands have correct orbital symmetry, where NC and PDTC behave as a π acceptor and π donor, respectively.[275] This energy alignment and perfect orbital symmetry matching should allow efficient interfacial orbital mixing, which would facilitate the expansion of the hole wave function into the PDTC ligand shell. Our experimental results are very important in the context of energy modulation of NCs and suggest that the excition delocalization mechanism is not only applicable to our molecule-like ultrasmall NCs but also has a more profound effect than on QDs because of surface-to-volume ratio effects.

4.4.4 Effect of Using Strongly-Confined CdSe NCs

To further explore our hypothesis that the surface ligand effect (mechanism iii) is responsible for the red-shift of λ and the reduction of ΔE_{og} upon PDTC binding, we investigated electron-withdrawing (CF_3O-), electron-donating (CH_3O-), and hydrogen (−H) group effects on two additional sizes of CdSe NCs. One would expect that the ΔE_{og} value would decrease as the size of the NCs increase because of the decrease in confinement energy of the excitons. Figure 4.5 shows the band-edge absorption spectra of 1.8 and 2.0 nm CdSe NCs that were coated with three different PDTC ligands. Figure 4.6 illustrates the comparison of ΔE_{og} values for the three differently sized CdSe NCs Table 4.2 shows the Δλ and ΔE_{og} values for the three differently sized NCs coated with three different types of PDTC ligands. Clearly, for a particular ligand (e.g., CF_3O-PDTC), the band-edge absorption peak was less red shifted for 2.0 nm CdSe NCs than for 1.8 or 1.6 nm.

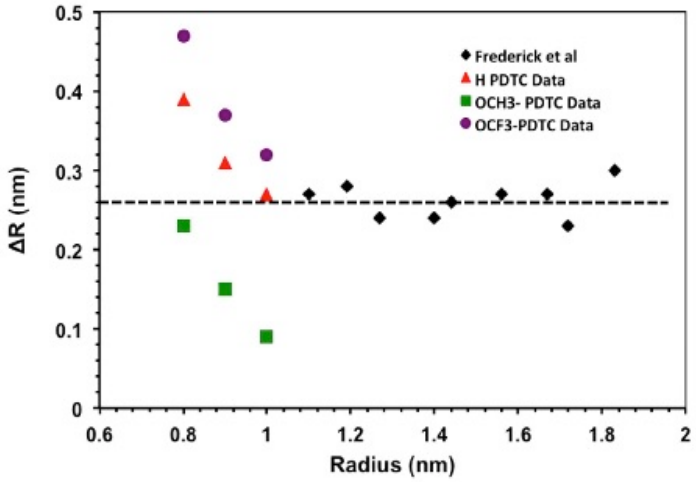

Figure 4.7. Plot of apparent increase in excitonic radius (ΔR) of CdSe NCs after attachment of various PDTC ligands vs original radius ().5,).9, and 1.0 nm). The black diamond data points were taken from reported values of different sizes of CdSe NCs (reprinted and adapted with permission from Frederick, M.T. and Weiss, E. A. ACS Nano 2010, 6. 3195-3200. Copyright 2010 American Chemical Society).

It was shown previously that for mechanism iii the plot of Δ*R* for CdSe QDs with respect to the original radius was nearly constant for a specific ligand.[275] In this current investigation, we characterized a similar trend for our 1.6-, 1.8-, and 2.0-nm-diameter CdSe NC-coated H-PDTC ligands, and the Δ*R* values were found to be 0.27, 0.31, and 0.39 nm, respectively (Figure 4.5 and Table 4.2). Importantly, the Δ*R* values for H-PDTC-coated 2.0-nm-diameter CdSe NCs are in agreement with the work shown by Frederick et at.[275] for 2.2–3.8-nm-diameter CdSe QDs. This Δ*R* value for H-PDTC ligands is comparable to the Cd–S bond length in solution.[298, 299] However, a significant difference in the Δ*R* value (0.39 nm) was observed for similar ligand-coated 1.6 nm CdSe NCs. Therefore, we believe the Δ*R* value is not constant for QDs and ultrasmall NCs, and perhaps the exciton confinement energy plays a critical role, where strongly confined holes[278] could increase the Δ*R* more than just the Cd–S bond length. Apparently, the Δ*R* values also depend on the chemical properties of the surface-passivating ligands (Figure 4.7), which has also been observed before.[279] Our data suggest that the electronic structure of the NCs can be probed by surface ligands, and even smaller NCs than 1.6 nm would offer unprecedented fine tuning of ΔE_{og} and Δ*R*.

As described above, a slight variation in CdSe NC size in the ultrasmall regime has a dramatic influence on the Δ*R* value. For example, 1.6 and 2.0 nm CdSe NCs had Δ*R* values of 0.39 and 0.27 nm, respectively, when H-PDTC was used to passivate the surface. As is mentioned in the literature, the reduction of the band gap of QDs requires electronic resonance between NC and ligand orbitals, which results in the formation of interfacial states. According to the pseudopotential calculation, the HOMO orbital energies for 1.6 and 2.0 nm CdSe NCs are ~−6.16 and ~−5.83 eV, respectively, whereas

the HOMO energy of the H-PDTC ligand is −6.24 eV.[295] Therefore, the HOMO of the H-PDTC ligand will have better energetic alignment with the HOMO of 1.6 nm CdSe NCs than with 2.0 nm CdSe NCs. Presumably, other HOMOs of 1.6 nm NCs could also have close energy matching, thus a large number of NC HOMOs could be in resonance with the HOMO of PDTC ligands. It is also known that the kinetic energy of the hole is larger than the Columbic interaction energy of the electron-hole pair in the 1.6- versus 2.0 -nm-diameter CdSe NCs.[278] Therefore, for the smaller NC, the hole wave function could fill the entire NC core volume and delocalize to the ligand monolayer. Taken together, both the extent of energetic alignment of orbitals and the variable kinetic energy of the hole could provide much stronger delocalization of photogenerated holes in 1.6 nm NCs than in 2.0 nm NCs. The actual interaction between NC and its surface ligands is very complexed, and a detailed theoretical calculation is required to determine such an interaction precisely and support our prediction, which is under investigation. Since our 1.6 nm CdSe NCs are of stable magic-sized geometry and known theoretical structure, they could provide a better scientific understanding of the effects of ligand interaction through a computational study than is possible with traditionally studied QDs.[275, 279]

As we mentioned earlier, mechanism (i) could contribute to the decrease in E_{og} of CdSe NCs for a ligand exchange reaction. According to quantum confinement effects, a decrease in the band gap can be caused by an increase in the actual (not effective as in ΔR) NC size,[265] which could be through further growth of existing NCs by Ostwald ripening or by inorganic core reconstruction to larger size.[267, 268] However, Ostwald ripening of thermodynamically stable ultrasmall NCs takes place either at temperatures >150 °C or requires the addition of Cd and Se precursors to the NCs solution, and neither

criterion is met in our system because the place exchange reaction was performed at room temperature without the addition of extra Cd and Se. Moreover, magic-sized $(CdSe)_{34}$ NCs are thermodynamically very stable and most likely will undergo no further growth during the ligand exchange reaction. Still, inorganic core reconstruction could occur due to steric strain induced by ligands during the ligand exchange reaction. Previous literature reports on CdSe QDs that investigated ligand-induced exciton delocalization used transmission electron microscopy (TEM) to determine the size before and after a ligand exchange reaction.[275, 276] The TEM technique was not sensitive enough to differentiate a size difference of less than 0.3 nm; in addition, QDs were not stable and were susceptible to melting during analysis due to heating by the electron beam and high vacuum[275]. Thus, previous studies on ligand-induced exciton delocalization did not provide conclusive evidence that could completely exclude mechanism (i).

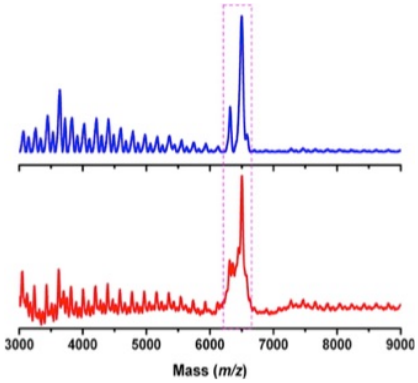

Figure 4.8. Positive mode LDI-TOF-MS spectra of DDA-passivated (blue) CdSe NCs and after the ligand exchange reaction with F-PDTC (red)

4.4.5 LDI-TOF-MS Characterization to Show No Change in Core Size

Recently we have shown that LDI-TOF-MS can be used to determine quantitatively the molecular mass of the inorganic core of ultrasmall CdSe

NCs,[281] which is not possible with traditional TEM analysis. We used LDI-TOF-MS in the present investigation to determine the core mass of DDA- and F-PDTC-passivated CdSe NCs. Figure 4.8 illustrates the LDI-TOF-MS spectra of NCs before DDA passivation (6.5 kDa core mass) and after the F-PDTC ligand exchange reaction (6.5 kDa core mass), and no noticeable difference in the CdSe molecular mass was observed. This experimental result is significant and suggested that mechanism i is not valid for explaining the observed decrease in E_{og} of DDA-coated CdSe NCs upon the ligand exchange reaction with X-PDTC ligands.

4.4.6 Investigating Effect of Dielectric Environment

One would expect that exchanging the DDA ligands with PDTC on the surface of NCs would change their local dielectric environment and thus their E_{og} value. Furthermore, the ground-state absorption spectra of DDA- and X-PDTC-passivated CdSe NCs were recorded in $CHCl_3$ and CH_2Cl_2, respectively, with differing dielectric constants (4.81 and 8.93). Therefore, a combination of changing the surface-passivating ligands and solvent physicochemical properties may have contributed to the E_{og} change and influenced the spectra (mechanism ii). We investigated this by preparing a dry film of F-PDTC-passivated CdSe NCs on a glass coverslip substrate and then collecting the absorption spectrum. As shown in Figure 4.9, no noticeable change in the absorption peak position was observed for the NCs either dissolved in CH_2Cl_2 or in the dried film, which indicated that mechanism (ii) did not play a role in the observed ΔE_{og} upon the place exchange reaction. It is beyond the scope of this study to calculate the precise dielectric constant of the CdSe NCs before (DDA-coated) and after (X-PDTC-coated) ligand exchange to neglect mechanism (ii) completely.

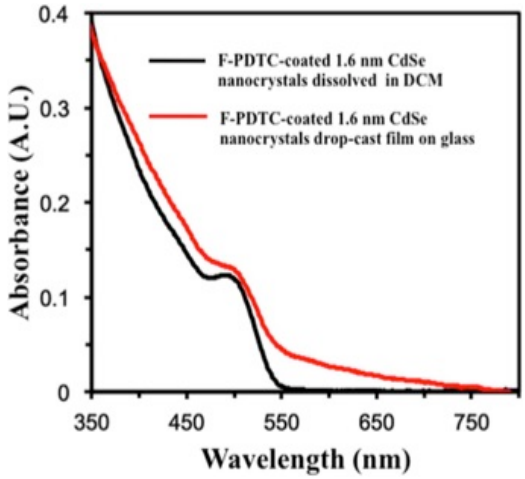

Figure 4.9. Comparison of absorption spectra of F-PDTC-passivated CdSe NCs in two different dielectric environments (DCM vs air). The band-edge peaks at ~490 nm under the two substantially different measurement conditions indicated that the increase in the surrounding dielectric constant did not contribute to the change in energy gap of newly formed F-PDTC-passivated NCs.

Beside the three possibilities mentioned above that could reduce the excitonic band-edge transition, another electronic effect that could change the band gap is the dipole–dipole interaction between the neighboring NCs.[273, 277, 300] Since the band-edge absorption peak positions for dispersed CdSe NCs in solution and NCs relatively closely packed on the film were same (Figure 4.9), we can most likely neglect such a possibility. However, it was brought to our attention that "incoherent hole transfer" would create surface dipoles, which could possibly change the band gap of the NCs in a size-dependent manner.(61) Figure 4.10 illustrates the extinction coefficients for three different sizes of CdSe NCs before and after H-PDTC exchange. It is important to notice that the variation in extinction coefficients before H-PDTC exchange is negligible, but a significant change was observed after the exchange reaction. This information is important and suggests that indeed there is an exciton transfer, possibly by the photogenerated hole from the NC to the surface ligand monolayer.

Finally, we suggest but do not prove that the surface structure of ultrasmall NCs may affect the ligand coordination chemistry and exciton delocalization. Previously it was shown theoretically for ultrasmall semiconductor NCs that differences in crystal facet sizes control the exciton relaxation dynamics.[301] Moreover, ligand binding completely depends on the crystal facets, and some of them do not allow ligands to bind because such electronic interactions are energetically unfavorable. Without the known crystallographic structures for 1.8 and 2.0 nm CdSe NCs, it would be difficult to predict such NC–surface ligand interaction for all three different sizes of CdSe NCs studied here, although DFT calculations of assumed $(CdSe)_{34}$ structures have shown that all surface Cd sites are available for bonding with strongly interacting ligands such as amines, phosphine, and thiols[258, 287, 302, 303] The delocalization of the excitonic hole depending on the strong electronic interaction between NC and surface-passivating ligands may play a minor role, but the crystal facet could contribute some effects to steady-state absorption characteristic.

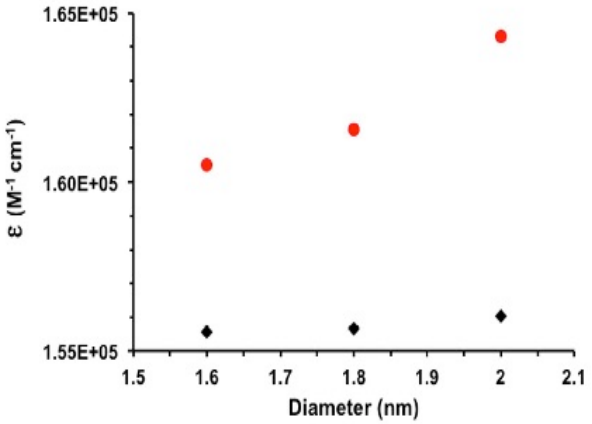

Figure 4.10. Comparison of molar extinction coefficient of DDA passivated CdSe NCs (black diamond) and after exchange with HPDTC (red dots) vs original diameter.

Nevertheless, on the basis of our various experimental approaches and the literature,[275, 278] we have verified our hypothesis that the large decrease in E_{og} in our molecule-like NC is due to the delocalization of the excitonic hole into the X-PDTC ligand monolayer through interfacial electronic states. After critically considering all of the factors described in the literature, which focuses only on excitonic hole delocalization, we suggest that in the ultrasmall size regime both excitonic holes and electrons could undergo the delocalization process with ligand HOMOs and LUMOs, respectively, due to the molecule-like, large band gap of ultrasmall CdSe NCs. However, such a prediction requires theoretical verification, which is currently underway.

4.4.7 Effect of Level of Conjugation on Exciton Confinement

In an effort to gain a deeper understanding of the exciton confinement effects, we expanded our ligands of interest. This next section reports a comprehensive study demonstrating that irrespective of the nanocrystal-ligand energy level alignment before binding to the surface, as determined through our experimental results as well as DFT calculations (see Table 4.3 and Figure 4.24 in appendix). Our results confirm that surface ligand structural parameters (level of conjugation, binding mode, and binding head group) substantially influence the overal delocalization processes and modulate the band-gap of semiconductor nanocrystals. Our studies show the following: (1) The extent of π-conjugation (π–delocalization energy) within the surface ligand, as exemplified by the series pyrene (Py), anthracene (Anth), naphthalene (Naph), and phenyl (Ph), is the dominant factor in causing the largest delocalization of the hole wave function and the highest reduction of the band-gap in our $(CdSe)_{34}$ semiconductor cluster molecules (NCs). (2) The details of surface ligand binding such as attachment mode [monodentate L-type (-

NH_2) *versus* bidentate chelating, dithiocarbamate (-NH-CS_2^-) and carboxylate (-COO^-)], and surface binding head group identity (-SH, -SeH, and –TeH) significantly influence the wave function delocalization. The structural diversity of the various ligands used in this present study is shown in Figure 4.1. Among all the ligand types we studied, our ground-state absorption measurements showed the largest and an unprecedented ~650 meV reduction of band-gap of $(CdSe)_{34}$ NCs upon post-synthetic ligand exchange of oleylamine (OLA) passivation for Py-DTC (**see** Figure 4.1), which was a consequence of delocalization of excitonic hole wave functions. Furthermore, we were able to restore the original band-gap of $(CdSe)_{34}$ NCs by removing Py-DTC from their surface through treatment with triethylphosphine gold(I) chloride (Et_3PAuCl). Although very recently Buhro and coworkers,[304] and our group[4] reported reversible shifts of optical band-gaps of semiconductor nanocrystals upon treatment with Cd(carboxylate)$_2$ ligands, to the best of our knowledge here is the first example where reversible band-gap modulation is demonstrated for semiconductor nanocrystals functionalized with a series of DTC-type ligands.[305-307]

Since the theoretical crystal structure of the $(CdSe)_{34}$ NC is known[5, 6] and it has a homogeneous surface atom composition (28 Cd and 28 Se), these NCs form an ideal model system to achieve a principled understanding of the effects of surface ligand attachment onto many types of solid surfaces through determination of the mechanisms underlying electronic interactions between these NCs and their surface passivating ligands.[308, 309] Moreover, the surface ligand interaction has the potential to dramatically alter NC electronic structure and dictate NC function more than ligand interactions with larger nanocrystals because smaller NCs have a larger surface-to-volume ratio that results

in a large number of atoms becoming available to interaction with the ligands. Our prediction is supported by dramatic changes in the optical band-gap of $(CdSe)_{34}$ NCs upon functionalization of their surface with para-substituted Ph-NH-$CS_2^-NH_4^+$ and Cd(carboxylate)$_2$ ligands[4, 228] as compared to larger CdSe nanocrystals under similar experimental conditions.[305, 306, 310] Moreover, DFT calculations demonstrate that the $(CdSe)_{34}$ NC possesses a stoichiometric ($Cd_{28}Se_{28}$) composition on its surface. In this context, neutral L-type or anionic X-type ligands will interact electrostatically with surface Cd sites to maintain overall charge neutrality of the $(CdSe)_{34}$ NC core. Therefore, we would expect to be able to strip off these ligands through treatment with metal complexes where the interaction is stronger in comparison to the original Cd-ligand bon, and thus achieve *reversible band-gap modulation* that has not been reported in the literature for X-type exciton delocalizing ligands. Because $(CdSe)_{34}$ NCs are thermodynamically very stable,[5, 6, 311, 312] no apparent change in their crystallographic structure is expected to take place during such post-synthetic ligand treatment, as we recently demonstrated for Cd(carboxylate)$_2$ treatment of OLA-passivated $(CdSe)_{34}$ NCs.[4] Finally, the ultra-small size of our NCs will help maintaining their colloidal stability in organic solvents upon functionalization with bulky and hydrophobic Py- and Naph-DTCs. In this article, our investigation of surface passivating ligand-controlled hole wave function delocalization is based on the *hypotheses* listed below:

1) *Ligands bearing the largest aromatic π-conjugation (Figure 1a-d) will result in the highest hole wave function delocalization and the largest band gap reduction in $(CdSe)_{34}$ NCs.*

2) *Ligands containing a soft-base, bidentate chelating head group (Figure 1e and f) will have the stronger interaction with surface Cd^{2+} (soft acid) sites and will result in an increase in interfacial orbital mixing and facile delocalization of hole wave functions of $(CdSe)_{34}$ NCs.*
3) *Ligands containing late row chalcogenide binding head groups (Figure 1h-j) will create a strong NC-ligand interaction and will induce larger exciton wave function delocalization of $(CdSe)_{34}$ NCs.*

4.4.8 Post Synthetic Surface Modification of OLA-passivated $(CdSe)_{34}$ NCs with Conjugated DTC-Containing Ligands

We selected DTC as the binding head group because bidentate chelating head groups have a thermodynamically favorable complex formation free energy and are expected to display strong electronic interaction with $(CdSe)_{34}$ NC, as previously reported for large CdSe nanocrystals.[313] To investigate our first hypothesis, we selected Py-, Anth-, Naph-, and Ph-DTC ligands because of their variable extent of π-conjugation. We have previously demonstrated efficient hole wave function delocalization for Ph-DTC-passivated $(CdSe)_{34}$ NCs where the observed ~510 meV reduction in the band-gap will be used as a reference to examine hypothesis 1.[228] We followed nearly identical post-synthetic surface modification procedures for the various conjugated DTC-containing ligands as was reported earlier by our group and is also provided in the Materials and Methods section. Figure 4.11A illustrates steady-state UV-vis absorption spectra implying the extent of hole delocalization where 650, 620, and 545 meV red-shifts of the lowest energy absorption peak of OLA-passivated $(CdSe)_{34}$ NCs were observed for Py-, Anth-, and Naph-DTC, respectively. Table 4.4 (in appendix) summaries the position of

the lowest energy absorption peak (λ) and reduction of confinement energy (ΔE) of OLA-passivated $(CdSe)_{34}$ NCs before and after functionalization with conjugated DTC-containing ligands. We believe that the observed decrease in $(CdSe)_{34}$ NC band-gap results from lowering the confinement energy of the NC-bound hole resulting in delocalization of its wave function into the ligand monolayer through interfacial orbitals, which are formed from the interaction between ligand and NC. Figure 4.11B shows changes in the confinement energy of OLA-passivated $(CdSe)_{34}$ NCs upon functionalization with different DTC-containing ligands.

As reported in literature for large CdSe nanocrystals[305, 306] and according to the frontier MO theory,[314] interactions of DTC-containing ligands with a nanocrystal will result in formation of interfacial hybrid orbitals. Such orbitals are expected to reduce the confinement energy of the excitons and facilitate the wave function delocalization with the highest delocalization causing the highest reduction of band-gap. Previously, it was also mentioned that the magnitude of wave function delocalization depends on the energy level alignment between HOMOs of the nanocrystal/NC and ligands prior to bond formation.[306] Here, better energetic alignment will increase interfacial orbital mixing between these two entities[315] creating stable interfacial orbitals, and thus the hole wave function from the NC HOMO can delocalize into the hybrid MO and extend the wave function into the conjugated π-system (Figure 4.11C). We determined the HOMO energies *versus* vacuum (see Table S1) of the ligands using DFT calculations using the

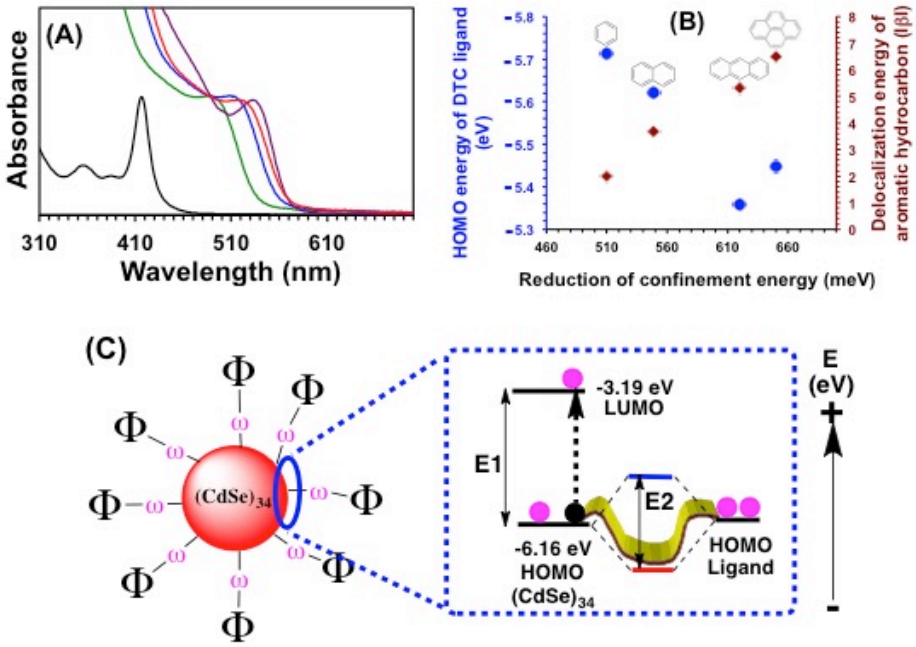

Figure 4.11 . (A) Room temperature steady-state UV-visible absorption spectra (in CH_2Cl_2) of $(CdSe)_{34}$ NCs passivated with various p-conjugated DTC type [-NH-CS_2^-] ligands: Ph-DTC (green line), Naph-DTC (blue line), Anth-DTC (red line), and Py-DTC (purple line). The spectrum of Py-DTC-passivated $(CdSe)_{34}$ NCs was adopted from our published article.[38] The initial OLA-passivated NC spectrum is shown as a black line. (B) Association of reduction in confinement energy of OLA-passivated $(CdSe)_{34}$ NCs with the HOMO (blue dots) and delocalization energy (b) (red diamonds) of various aromatic hydrocarbon-containing, DTC-binding ligands that were prepared via exchange reactions. The delocalization energy values of aromatic hydrocarbons were adopted from the literature[43] where IbI = 0.69 eV. (C) Schematic of the various ligand-passivated NCs. The solid blue ellipsoid highlights the electronic interaction at the NC-ligand interface. The area inside the ellipsoid represents the bond that is manipulated by varying the chemical structure of ω as shown in Figure 4.1 to maximize the electronic interaction of ligand with surface Cd sites. The figure in the blue dotted box represents the molecular orbital diagram of an OLA-passivated $(CdSe)_{34}$ NC after its interaction with a ligand. Using electrochemistry we determined the HOMO and LUMO energies of a OLA-passivated $(CdSe)_{34}$ NC at -6.16 and -3.19 eV, respectively with energy gap of E_1.[10] In the excited state, photoexcitation of the NC creates a hole (black dots) in the HOMO, thus the NC can act as a p-acceptor. According to MO theory,[44] this half-filled HOMO can interact with the filled HOMO of the surface passivating ligand (p-donor) and forming hybrid bonding (red line) and antibonding (blue line) orbitals with energy gap of E_2. The hybrid bonding orbital facilitate the hole wave function (yellow curve band) delocalization from the NC to ligand monolayer, thus red-shifting the lowest energy absorption peak because of reduction of the size of the confinement box.[10] The image is not to scale.

basis set 6-311+G** and the B3LYP functional under their optimized geometries in the gas phase. By comparing energy level alignment between HOMOs of the ligands and the $(CdSe)_{34}$ NC [HOMO energy: -6.16 eV)],[4] Ph-DTC should display the highest reduction of band-gap. However, we observed Py-DTC shows the largest decrease. Therefore, we argue that π–delocalization energy, which follows the highest to lowest order of Ph- <Naph- <Anth- <Py-DTC in the ligand is the more influential factor rather than energy level alignment. We should also mention that not only energy level matching but also the coupling constant between the orbitals of the NC and DTC ligands control the overall electronic interaction and formation of hybrid MOs,[314] which facilitate wave function delocalization. In the present investigation, we only considered energy level alignment to explain the changes in the optical band-gap, because to deconvolute complex electronic interactions between the NC and ligand requires extensive and sophisticated computational calculations[307, 316] that are beyond our expertise.

Verifying the effect of the π–delocalization energy, we found that the bidentate chelating moiety of DTC alone is not sufficient to induce a strong NC-ligand interaction and hole wave function delocalization. To examine this we used aliphatic carbon chain-bearing n-dodecyldithiocarbamate (n-DDTC) to passivate the $(CdSe)_{34}$ NC surface. UV-vis analysis showed negligible changes in confinement energy (~ 8 meV) (Figure 4.12 and Table 4.4), and thus extended exciton delocalization was impossible because of lack of π-conjugation. Furthermore, the DFT-calculated HOMO energy sequence, Ph-DTC < Naph-DTC < n-DDTC < Py-DTC < Anth-DTC, places the aliphatic-containing ligand in-between members of the aromatic sequence. This placement further decouples energy level matching between the ligand HOMO and the NC HOMO as crucial to reducing

confinement energy, with the most influential factor again being the π–delocalization energy that allows efficient delocalization of hole wave functions. Taken together, our selection of surface ligand structural parameters unequivocally demonstrates that the greatest π-conjugation (the largest π–delocalization energy) in the ligand backbone is necessary for the highest delocalization of hole wave functions and the largest reduction of band gap of $(CdSe)_{34}$ NCs that together validate our hypothesis 1.

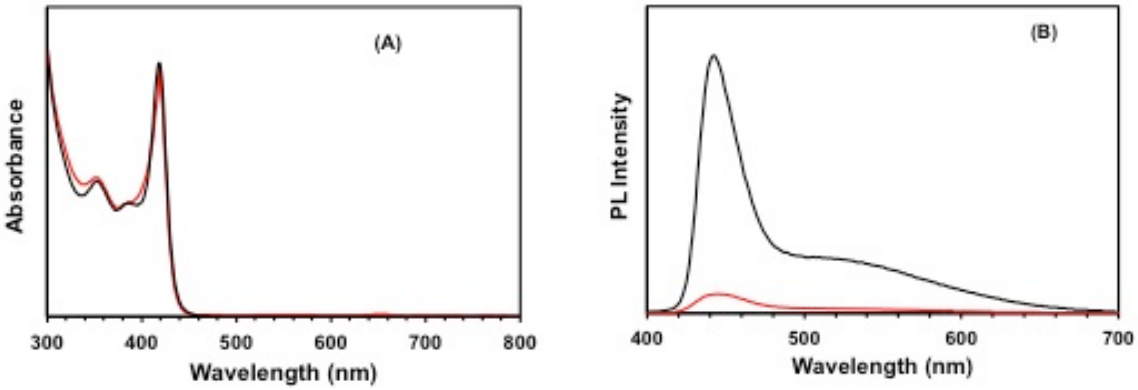

Figure 4.12 Room temperature steady-state UV-visible absorption (A) and PL spectra (B) in CH_2Cl_2 of (black) OLA- and (red) n-DDTC-passivated $(CdSe)_{34}$ NCs. The PL spectra were collected using 350 nm excitation energy

Alternatively, one could argue that possible changes in the three following parameters could potentially explain alteration in the band-gap of our NCs: (i) change in the crystallographic structure,[304] (ii) variation in the number of surface passivating ligands, and (iii) alteration in the core size and/or composition. We performed powder X-ray diffraction analysis of OLA- and Py-DTC-passivating $(CdSe)_{34}$ NCs in which no noticeable changes in the (100), (002), and (101) reflections of their wurtize crystal structure were observed (see Figure 4.13A).[317] This result suggests that the measured red-shifts in the lowest energy absorption peak of OLA-passivated $(CdSe)_{34}$ NCs after Py-DTC treatment did not arise from changes in crystallographic structure.

To quantify the number of ligands attached to the NCs surface, we conducted ^{1}H NMR analysis (see Figure 4.13B). The NCs surface was passivated with both OLA and hole delocalizing ligands where Py-DTC, Anth-DTC, and Naph-DTC were ~60 and ~68, ~68 percent of total surface ligands, respectively. Thus, these treated NCs contained mixed surface passivation. These data are in agreement with our previous report showing that Ph-DTC treatment caused an ~73 percent exchange of original aliphatic amine ligands.

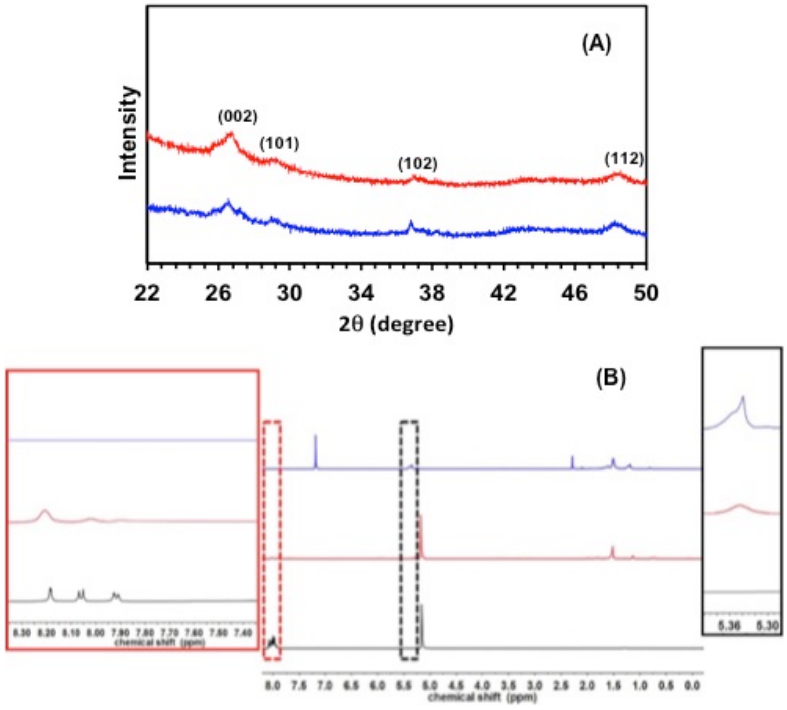

Figure 4.13 (A) XRD patterns of purified (red) OLA- and (blue) mixed Py-/OLA-passivated $(CdSe)_{34}$ NCs. Appearance of broad peaks with low intensity is because of the ultrasmall size of the NCs. (B) . ^{1}H NMR spectra of pure Py-DTC/$^{+}NH_4$ (bottom, black line), purified OLA-passivated $(CdSe)_{34}$ NCs (top, blue line), and mixed Py-/OLA-passivated $(CdSe)_{34}$ NCs (middle, red line). The black and red dotted boxes are expanded in the solid boxes are show vinyl (-CH=CH-) and

This result is significant and suggested that even though the density (number of ligands/nm^2) of Py-DTC on the $(CdSe)_{34}$ NCs surface was the lowest, it caused the highest hole wave function delocalization (see Table 4.5 in Chapter 4 appendix).

Based on the NMR analysis, we propose that the negatively charged -NH-CS_2^- binding motif (1) carries ammonium ions (an L-type bound ion-pair) to counter balance the negative charge (2) electrostatically interacts with the surface Cd sites with a dative (coordinate covalent) type bond (Figure 4.14A)[310] rather than acting as an X-type ligand involving chelating and bridging interactions with Cd sites (see Figure 4.15). This particular electronic interaction preserves the overall charge neutrality of the $(CdSe)_{34}$ core. Previously from FTIR analysis we confirmed that OLA-passivated $(CdSe)_{34}$ NCs do not contain carboxylate type ligands as an impurity on their surface.[4] As illustrated in Figure 4.16, FTIR analysis of mixed ligand-passivated $(CdSe)_{34}$ NCs displays both the N-H bending mode of OLA at 1490 cm^{-1} and the asymmetric S-C-S and C-N stretches of Py-DTC at 1024 and 1235 cm^{-1}, respectively. Importantly, no detectable shift in the position of the S-C-S stretch suggests a weak, monodentate-type interaction between the DTC binding motif and surface Cd sites.[318, 319] Our proposed coordination chemistry characterizing the ligand interaction with NCs is different than for previously reported surface DTC-type ligand exchange on Cd-rich semiconductor nanocrystals, where Cd-bound, chelating X-type carboxylate ligands were replaced with X-type DTC-containing ligands forming new Cd-DTC bonds.[305-307]

Another possible explanation for band-gap modulation of NCs upon DTC-type ligand exchange is permanent changes in the inorganic core size and composition. A recent investigation of Ph-DTC exchange with Cd-rich CdSe nanocrystals has suggested that during the exchange reaction, the DTC binding head-group detaches from the Ph ring through decomposition[320] and then sulfur reacts with surface Cd to form CdS that is then deposited onto the CdSe core. This deposition forms CdSe/CdS core-shell type

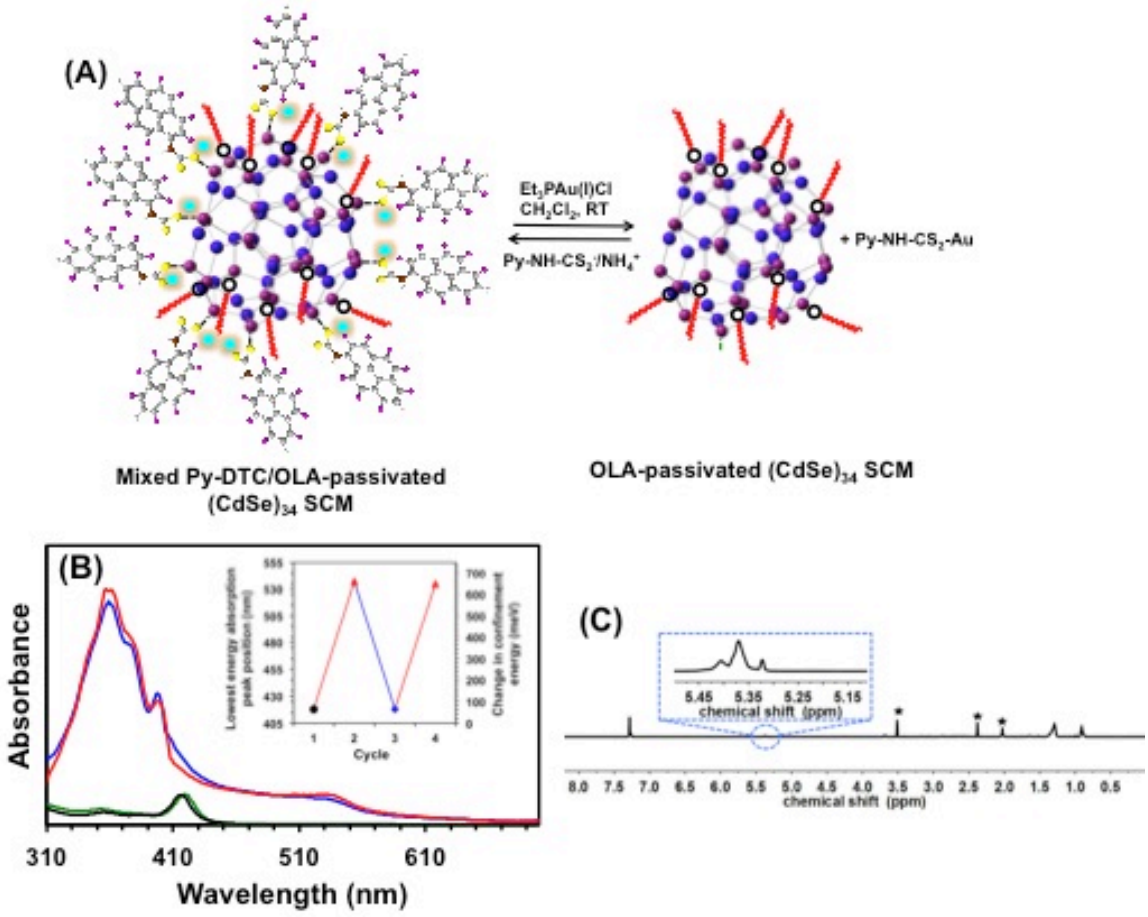

Figure 4.14 (A) Schematic diagram represents reversible ligand exchange of a mixed ligand-passivated NC with Et_3PAuCl. The negatively charged -NH-CS_2^- head group electrostatically interacts with surface Cd site similar to a dative type bond. Purple and blue spheres represent Cd and Se atoms, respectively, of $(CdSe)_{34}$ NC. Yellow and green spheres are S and N of -NH-CS_2. Pink/light blue dots represent ammonium ion. (B) Steady-state absorption spectra of purified OLA-passivated $(CdSe)_{34}$ NCs after synthesis (black line), after Py-DTC treatment (mixed Py-DTC-/OLA-$(CdSe)_{34}$ NCs) (green line), after Et_3PAuCl treatment (partially OLA-passivated NCs) (red line), and after Py-DTC re-treatment (mixed Py-DTC-/OLA-$(CdSe)_{34}$ NCs) (blue line). The inset shows reversibility of the lowest energy absorption peak position of OLA-passivated $(CdSe)_{34}$ NCs (black dot), after repeatedly attaching Py-DTC (red triangles) and removing Py-DTC by Et_3PAuCl treatment (blue diamond). The details of the ligand treatment and removal are provided in the Materials and Method section. (C) ^1H NMR spectrum of Et_3PAuCl-treated and purified OLA-passivated $(CdSe)_{34}$ NCs. The expanded vinyl (-CH=CH-) resonance of OLA is shown in the dotted blue box. The asterisks represent signal from residual solvent. The spectrum was collected in $CDCl_3$ at a 15 s relaxation delay time.

nanocrystals[321] where electron wave function delocalization induces a red-shift in the lowest energy absorption peak. However, such a scenario is very unlikely in our present investigation because $(CdSe)_{34}$ NC possesses a stoichiometric core (1:1 between Cd-to-Se) and thus formation of a CdS layer would require removal of Se from the core to maintain overall charge neutrality. Under this situation the original $(CdSe)_{34}$ core size (1.6 nm in diameter)[4] would decrease resulting in a blue-shift of the lowest energy absorption peak, which is opposite to what we have observed. Perhaps one could argue for formation of a $Cd_{34}Se_{34-x}S_x$ alloy NC during the exchange process, but because of the resulting higher quantum confinement allow NC would display a larger band-gap than the original $(CdSe)_{34}$ NC.[322, 323] Moreover, our ^1H NMR (Figure 4.13B) and

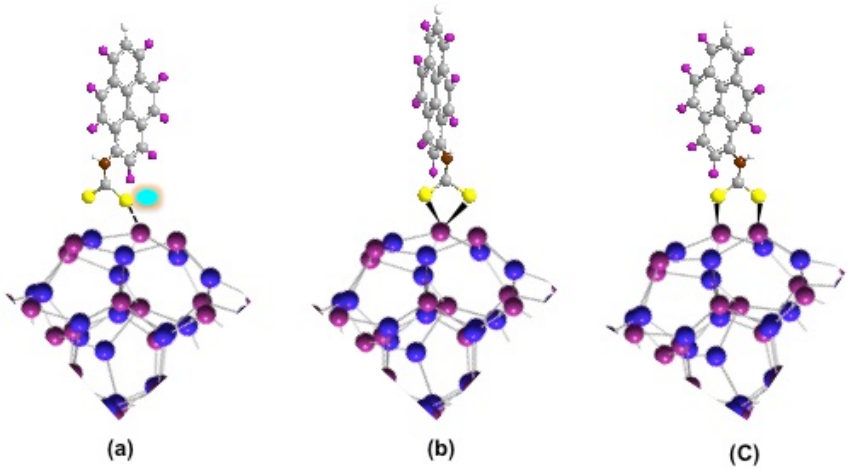

Figure 4.15 Proposed mode of binding of Py-DTC ligand to surface Cd sites of a $(CdSe)_{34}$ NC. Purple and blue spheres represent Cd and Se atoms, respectively. Dative ion-pair (A), chelating (B), and bidentate bridging (C) interactions. The pink/light blue dot represents ammonium ion and the sulfur from -NH-CS_2 is shown as yellow spheres.

FTIR (Figure 4.16) analyses unequivocally demonstrated the presence of Py-DTC ligand on the surface of $(CdSe)_{34}$ NC without any decomposition. Finally "Ostwald ripening," which occurs at temperatures >150 ^oC and requirs addition of Cd and Se precursors,[305]

may be another possible explanation for band-gap modulation where some population of $(CdSe)_{34}$ NCs dissolves to produce monomers that add onto original $(CdSe)_{34}$ NCs to form larger CdSe nanocrystals via slow growth. However, magic-sized $(CdSe)_{34}$ NCs are thermodynamically very stable[6, 316] and unlikely grow into larger nanocrystals during the ligand exchange reaction. Transmission electron microscopy analysis of our Py-DTC-passivating CdSe nanocrystals showed no change in size maintaining ~1.6 nm average diameter (see Figure 4.17). Our mixed Py-DTC/OLA-passivated $(CdSe)_{34}$ NCs displayed their lowest energy absorption maxima at 537 nm (Figure 4.11A) and CdSe nanocrystals displaying their absorption peak at this wavelength would possess a diameter of ~2.8 nm.[305, 324]

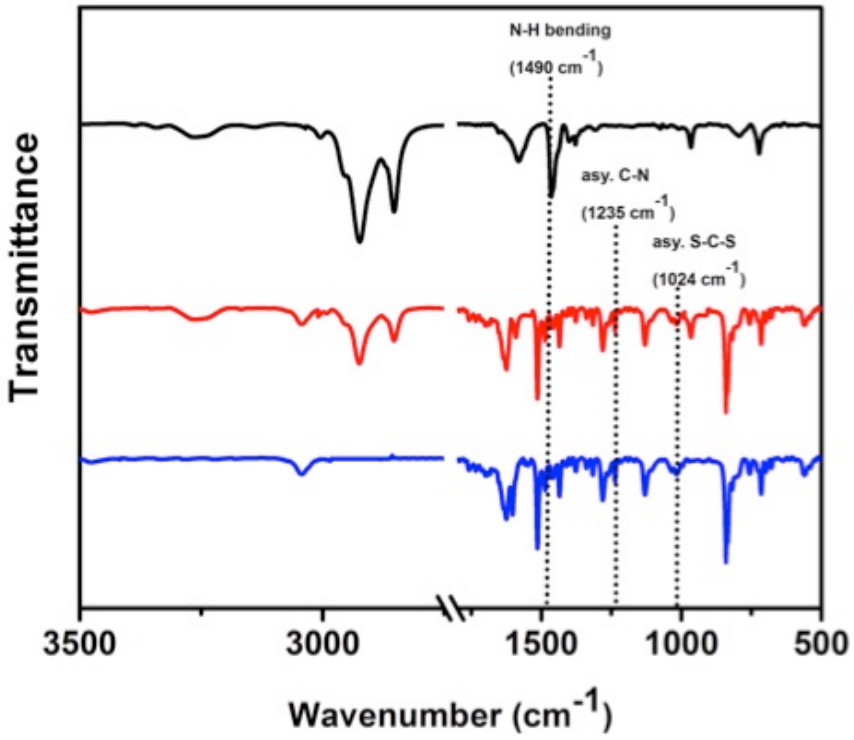

Figure 4.16 FTIR spectra of pure Py-DTC/$^{+}NH_4$ (bottom, blue line), purified OLA-passivated $(CdSe)_{34}$ NC (top, black line), and mixed Py-/OLA-passivated $(CdSe)_{34}$ NCs (middle, red line). The dotted lines represent various vibrational stretches

Our spectroscopy and microscopy characterizations strengthen hypothesis 1 that the red-shifts in the optical band-gap of OLA-passivated $(CdSe)_{34}$ NCs upon treatment with conjugated DTC-containing ligands are due to delocalization of hole wave function and not because of change in crystallographic structure, variation in the number of surface passivating ligands, or alteration in the core size and/or composition. A more definitive proof of our hypothesis would stem from demonstration of restoration of the original band-gap of $(CdSe)_{34}$ NCs by programmable removal of Py-DTC from their

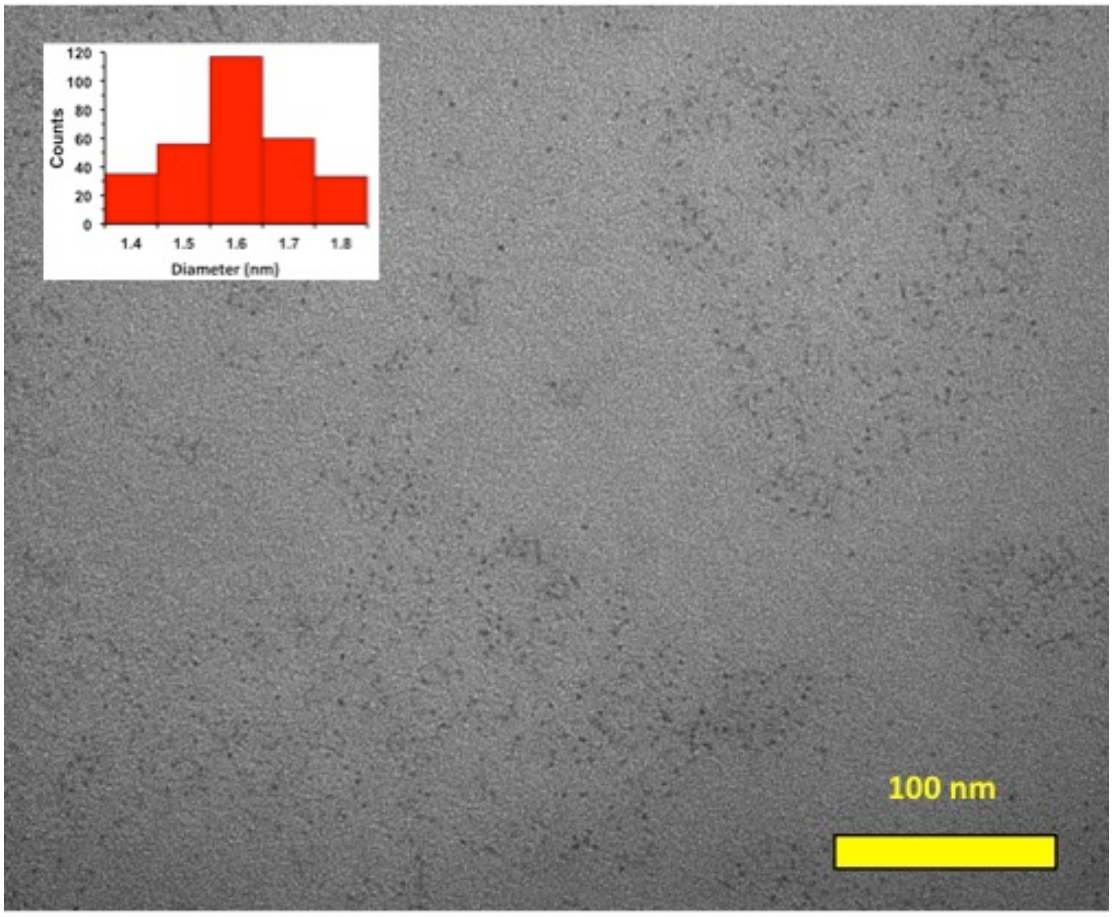

Figure 4.17. TEM image and the corresponding histogram of mixed Py-/OLA-passivated $(CdSe)_{34}$ NCs. The singly OLA-passivated $(CdSe)_{34}$ NCs were also ~1.6 nm in diameter.

surface as similar to an *ion-metathesis* reaction. To the best of our knowledge such band-gap modulation has not yet been reported for DTC-containing ligand-passivated semiconductor nanocrystals. As described above, the interaction between the DTC binding group and surface Cd is weak, and thus we expect that a metal ion such as Au(I) would remove Py-DTC from the $(CdSe)_{34}$ NC surface because of the nearly two fold higher Au-S bond dissociation energy than that of Cd-S.[325] As shown in Figure 4.14A, we used organically soluble Et_3PAuCl to explore this possibility of Py-DTC removal. Figure 4.14B shows UV-vis absorption spectra of mixed Py-DTC/OLA-passivated $(CdSe)_{34}$ NCs before and after treatment with Et_3PAuCl, and then after re-treatment with Py-DTC. The broadening of the absorption peak after removal of Py-DTC could result from some aggregation of NCs because of the inadequate surface passivation. The shape of the absorption peak was nearly restored after OLA treatment with shape similar to OLA-passivated $(CdSe)_{34}$ NCs (see Figure 4.18).

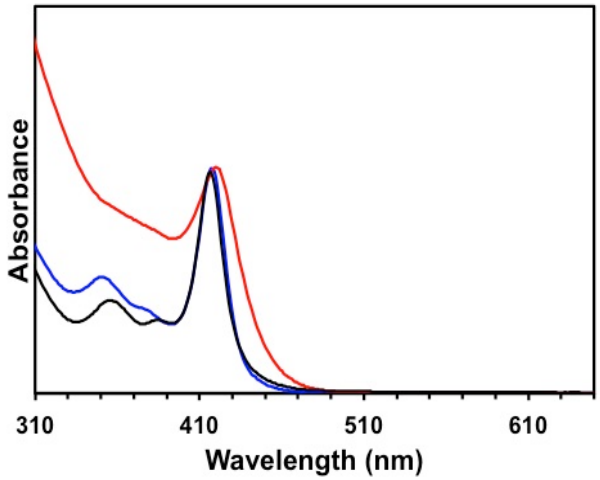

Figure 4.18 Room temperature steady-state $(CdSe)_{34}$ NC UV-visible absorption spectra of initial OLA-passivation (black curve), after Et_3PAuCl treatment forming mixed Py-/OLA-passivation (red curve), and after treatment with OLA (blue curve). The removal of Py-DTC from the surface of $(CdSe)_{34}$ NCs through Et_3PAuCl treatment produced partially OLA-passivated NCs.

We also performed surface structure characterization of mixed Py-DTC-/OLA-passivated $(CdSe)_{34}$ NCs after Et_3PAuCl treatment using NMR and energy dispersive X-ray (EDX) spectroscopy. As shown in Figure 4.14C, no proton signals in the aromatic region (7.9-8.3 ppm) were observed in the ^1H NMR spectrum, suggesting removal of all Py-DTC from the surface of NCs. More importantly, aliphatic proton resonances associated with Et_3P were not detected. This result was in agreement with the EDX analysis where the P peak at ~2.0 keV did not appear (Figure 4.19). However, we observed a weak Cl signal at ~2.6 keV that suggests the chloride ions from Et_3PAuCl may have adsorbed onto the surface of $(CdSe)_{34}$ NC.[326] Taken together, our unique structural characteristics of $(CdSe)_{34}$ NC allow reversible modulation of hole wave function and confinement energy in which the π-delocalization energy profoundly influences the magnitude of band-gap variation as stated in hypothesis 1.

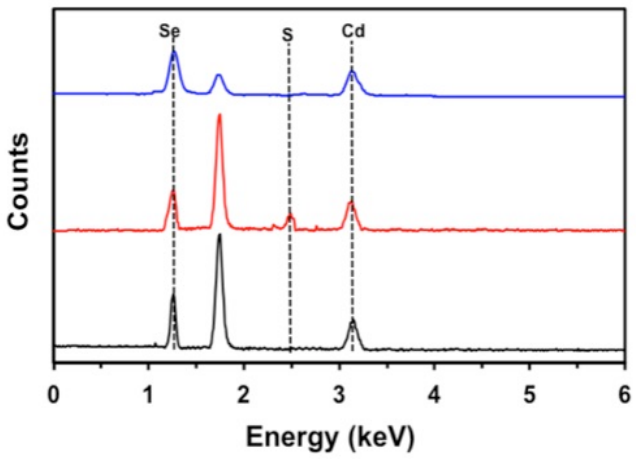

Figure 4.19 Energy dispersive spectroscopic (EDS) profile of purified initial OLA-passivated $(CdSe)_{34}$ NCs (bottom, black line), mixed Py-/OLA-passivated $(CdSe)_{34}$ NCs (middle, red line), and after Et_3PAuCl treatment (top, blue line). The inset shows the expanded spectrum after Et_3PAuCl treatment in which the EDX peak associated with Cl at 2.6 keV was observed

4.4.9 Effects of Ligand Mode of Binding on Band-Gap Modulation of $(CdSe)_{34}$ NCs

Our observed red-shift of 650 meV in the UV-vis absorption spectra of mixed Py-DTC/OLA-passivated $(CdSe)_{34}$ NCs was the motivation to explore how the ligand mode of binding influences the overall photophysical properties. DTC is a soft base and according to the HSAB principle, it should demonstrate strong interaction with the soft acid Cd^{2+}. On the other hand, carboxylate ($-COO^-$) and amine ($-NH_2$) are hard bases and thus their interaction with Cd^{2+} is expected to be weaker. Moreover, a recent study[308] shows that the L-type neutral donor ($-NH_2$) interacts more weakly with CdSe nanocrystals than adsorbed ion pairs (e.g., DTC:$-NH-CS_2^-/NH_4^+$ and $-COO^-/Bu_4N^+$). According to hypothesis 2, the stronger the interaction (coupling strength) between the NC and its ligands, the better the interfacial orbital mixing between them and the higher the delocalization. Figure 4.20 illustrates UV-vis absorption spectra and change in the confinement energy for Py containing ligands with -DTC, $-COO^-/Bu_4N^+$, and $-NH_2$ binding head groups. As expected, mixed Py-COO^-/OLA-passivated $(CdSe)_{34}$ NCs

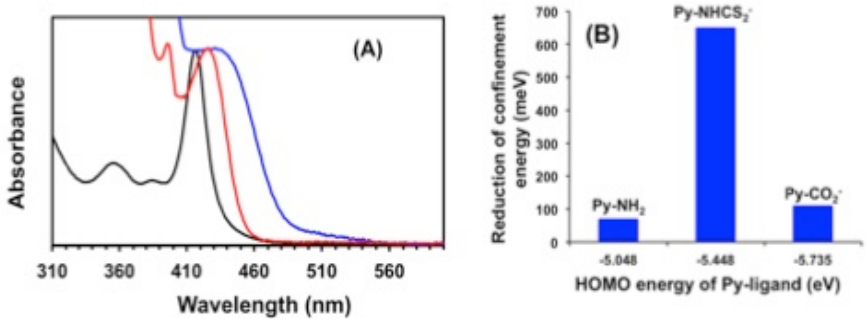

Figure 4.20 A) Room temperature steady-state UV-visible absorption spectra (in CH_2Cl_2) of $(CdSe)_{34}$ NCs passivated with Py-containing ligands with two different head groups: $-NH_2$ (red line) and $-COO^-$ (blue line). The initial OLA-passivated NC spectrum is shown in black. (B) Plot of reduction of confinement energy of OLA-passivated $(CdSe)_{34}$ NCs with respect to the HOMO energy of Py-containing ligands with three different binding head groups that were prepared via ligand exchange reaction.

showed a more than 9-fold smaller change in the confinement energy than Py-DTC/OLA-passivated NCs, although both of them have chelating bidentate binding ability with Cd^{2+}. Table 4.4 summaries the position of the lowest energy excitonic peak (λ) and reduction of confinement energy (ΔE) of OLA-passivated $(CdSe)_{34}$ NCs both before and after functionalization with Py containing various binding head groups. ^{1}H NMR analysis confirmed that the surface population of the Py- DTC and Py-COO^- are almost the same (Table 4.5)

Moreover, the distances between the Py moiety and surface Cd sites through COO^- and DTC linkages are 4.299 and 5.641 Å, respectively (determined from ChemDraw Professional 15.1, Figure 4.21). Therefore, the larger change in the confinement energy of Py-DTC/OLA-passivated $(CdSe)_{34}$ NCs cannot be explained by a longer DTC to Cd separating distance. Mixed Py-NH_2/OLA-passivated $(CdSe)_{34}$ NCs displayed the smallest absorption peak red shift of 70 meV. This result is in agreement

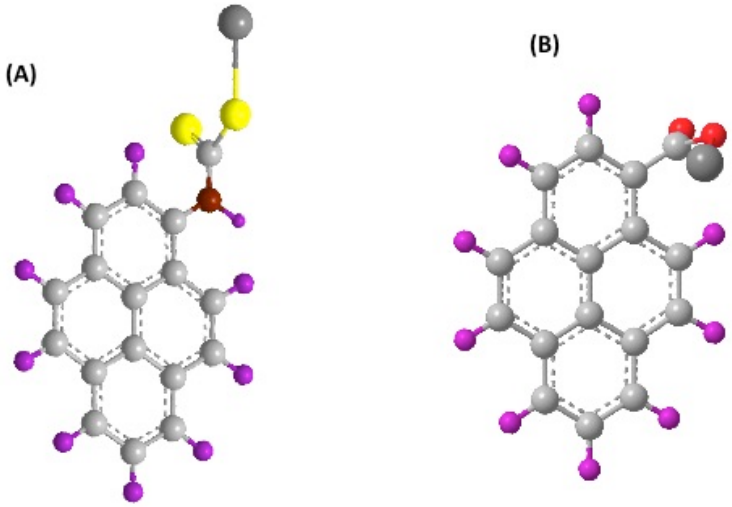

Figure 4.21 ChemDraw images of Cd binding to Py-DTC (A) and Py-COO^- (B). Yellow and dark red spheres are S and N of -NH-CS_2, respectively, and red spheres are oxygen.

with a recent study[308] showing the L-type neutral donor (-NH_2) more weakly interacting with CdSe nanocrystals than the adsorbed ion pairs (e.g., -NH-CS_2^-/NH_4^+ and -COO^- /Bu_4N^+). Nevertheless, our investigation has shown that not only the π-delocalization energy is important for effective delocalization of hole wave functions but ligand mode of binding is also critical.

4.4.10 Effects of Ligand Binding Head Group on Confinement Energy of $(CdSe)_{34}$ NCs

Based on the HSAB principle, Cd-binding ligands containing the hard –NH_2 binding head group favor replacement with soft groups such as chalcogenides. The strength of interaction between the NC and ligand will influence NC interfacial orbital mixing and confinement energy, and will control hole wave function delocalization. We selected the head group series Ph-EH (E = -S, -Se, and -Te) to validate our hypothesis 3. Figure 6A shows UV-vis absorption spectra of three different chalocogenide ligand-passivated $(CdSe)_{34}$ NCs where the reduction in DE is as follows: Ph-SH (136 meV) < Ph-SeH (200 meV) < Ph-TeH (211 meV). Table S2 summaries the corresponding l position. EDX analysis confirmed the formation of mixed Ph-E-/OLA-passivated NCs (Figure 6B). The number of ligand attached to the surface of $(CdSe)_{34}$ NCs was determined from ^{1}H NMR analysis (data not shown). Importantly, the largest shift we observed is 6.5 fold greater than the previously reported value by Brutchey and coworkers for the same ligand system using 4.0 nm diameter CdSe nanocrystals.[27] By considering the energy level alignment between HOMOs of $(CdSe)_{34}$ NC and Ph-E ligands the order should be Ph-TeH < Ph-SH ≈ Ph-SeH (see Table S2). However, we observed a completely different order as shown above. Therefore, the magnitude of decrease in the confinement energy of $(CdSe)_{34}$ NCs upon treatment with Ph-E followed

the HSAB principle. We believe that the energy level alignment between the NC and ligand HOMOs is not close enough for the relaxation of quantum confinement but the strength of the interaction, which is be guided by the HSAB principle, plays a vital role.

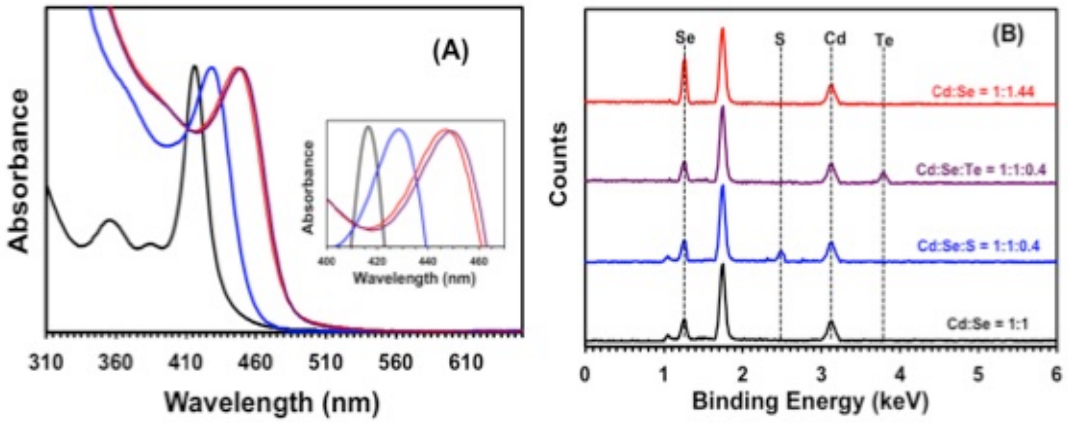

Figure 4.22 Room temperature steady-state absorption spectra (in CH_2Cl_2) of NCs with various surface passivation: Singly $(OLA)_{19}$-passivated $(CdSe)_{34}$ NCs (black line), and mixed $(Ph\text{-}SH)_{14}$-/$(OLA)_5$- (blue line), $(Ph\text{-}SeH)_{15}$-/$(OLA)_4$- (red line), and $(Ph\text{-}TeH)_{15}$-/$(OLA)_4$-passivated (purple line) $(CdSe)_{34}$ NCs. Number of OLA per $(CdSe)_{34}$ NC was reported in the literature.[3, 4] The inset shows expanded region of the lowest energy excitonic transition. (B) EDX profile of various ligand-passivated $(CdSe)_{34}$ NCs. The spectra are color matched to those in (A). The appearance of S and Te originates from the Ph-SH and Ph-TeH ligands while the Ph-SeH ligand treatment increases the Se content in the sample.

4.4.11 Steady-State and Time-Resolved Photoluminescence (PL) Properties of Conjugated DTC-Containing Ligand-Passivated $(CdSe)_{34}$ NCs

We examined the hole wave function delocalization of $(CdSe)_{34}$ NC into the ligand monolayer by characterizing the samples with steady-state PL spectroscopy. The PL spectra of conjugated ligands containing the DTC binding head group exhibited almost 95% quenching of PL peak intensity (Figure 4.23A), which is consistent with the literature reports on DTC-containing ligands.[27, 305, 307] It is known that the attachment of

thiols through Cd-thiolate (Cd-S-) covalent linkage creates hole-trapping sites in Cd-chalcogenide nanocrystals[327, 328] that result in non-radiative recombination of excitons and quenching of PL intensity. Although in our system no covalent Cd-S linkage was formed, the delocalization of the hole wave function still reduced the maximum

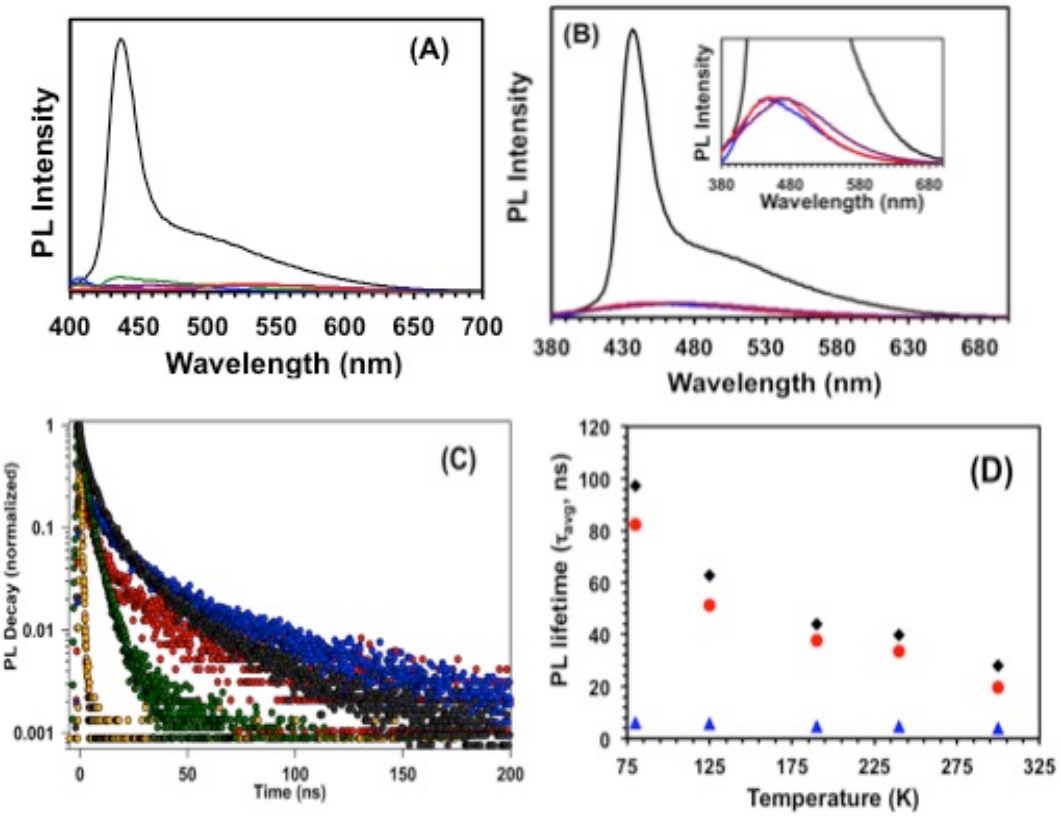

Figure 4.23 Room temperature steady-state PL spectra (in CH_2Cl_2) of various p-conjugated DTC type ligand-passivated $(CdSe)_{34}$ NCs: Ph-DTC (green line), Naph-DTC (blue line), Anth-DTC (red line), and Py-DTC (purple line). (B) Room temperature steady-state PL spectra of only OLA-passivated (black line), and mixed Ph-SH-/OLA- (blue line), Ph-SeH-/OLA- (red line), and Ph-TeH-/OLA-passivated (purple line) $(CdSe)_{34}$ NCs in CH_2Cl_2. The PL spectra were collected at 350 nm excitation energy. The inset shows an expanded region of the mixed Ph-EH-/OLA-passivated $(CdSe)_{34}$ NCs. PL spectrum of original OLA-passivated NCs is shown by a black line in both panel (A) and (B). (C) Typical time-resolved PL traces measured at 300 K for different ligand-passivated $(CdSe)_{34}$ NCs: mixed Py-DTC-/OLA- (blue dots), mixed Naph-DTC-/OLA- (red dots), and mixed Ph-SH-/OLA-passivated (green dots) NCs, and the original OLA-passivated NCs (black dots). All spectra were normalized to 1.0. The instrument response function (IRF, yellow dots) of this system was measured as 0.4 ns. (D) Temperature dependence of t_{avg} for Py-DTC-/OLA- (black diamonds), Naph-DTC-/OLA- (red dots), and Ph-SH-/OLA-passivated (blue triangles) NCs.

probability of radiative recombination of exciton wave functions. We were unable to quantify the reduction of confinement energy from the PL measurements because of the overlapping optical peak position of conjugated DTC ligands and $(CdSe)_{34}$ NCs. As shown in Figure 4.23B, strong PL quenching for Ph-EH ligands was also observed. Importantly, we were able to calculate the reduction of confinement energy from the PL peak position for mixed Ph-EH-/OLA-passivated $(CdSe)_{34}$ NCs (Figure 4.23B, inset). These data nicely corroborate our UV-vis absorption measurements and support the hole wave function delocalization mechanism.

In order to examine the mechanism of hole wave function delocalization, we characterize three different samples by temperature-dependent (85-300 K), time-resolved PL spectroscopy. At 300 K mixed Py-DTC-/OLA-, Naph-DTC-/OLA- and Ph-SH-/OLA-passivated $(CdSe)_{34}$ NCs displayed τ_{avg} values of 27.9, 19.6, 3.9 ns, respectively, whereas singly OLA-passivated NCs showed τ_{avg} of ~22 ns (**see** Figure 4.23C and Table 4.6). The shortening of τ_{avg} after either Naph-DTC or Ph-SH ligand passivation could be from a combined effect involving trap state- and hole delocalization-mediated recombination of excitons in which the presence of surface traps reduces τ_{avg} but the delocalization process increases the $\tau_{avg.}$[4, 240, 329-331] The slight increase in τ_{avg} for Py-DTC-/OLA-passivated $(CdSe)_{34}$ NCs is an indication of relative weaker overlap between electron and hole wave functions, as a consequence of hole wave function delocalization, in comparison to singly OLA-passivated NCs. We believe for Py-DTC-/OLA-passivated $(CdSe)_{34}$ NCs, hole wave function delocalization is the dominant factor rather than trap-state mediated excitonic recombination. However, quantifying the precise contribution for each quantity is difficult under our experimental conditions. Interestingly, the τ_{avg} values determined

for our three above-mentioned ligand-passivated NCs are much higher than the previous report by La Croix et al.[307] and Brutchey and coworkers[27] where the authors suggested a hole transfer mechanism rather than the excited state hole delocalization process. Moreover, in these reports a significant reduction in τ_{avg} was observed after attachment of hole delocalizing ligands. However, according to the literature report as mentioned above, exciton wave function delocalization is expected to increase the τ_{avg} unless a trap-state mediated excitonic recombination takes place.

Our low temperature time-resolved PL measurement show three important excited state dynamic characteristics: Firstly, the fast relaxation component (τ_1) is present both at room temperature and at 80 K for all three above-mentioned hole delocalizing ligands (see Table 4.6). Moreover, τ_1 values determined for all three ligands at five different temperatures are all the same within experimental error. Therefore, in our system phonon-assisted relaxation can be eliminated because under such circumstances, τ_1 should not be observed at 80 K.[27] The biexponential decay observed with τ_1 can be described as decay of bright excitons before reaching thermal equilibrium between bright and dark emitting states.[332] Secondly, as illustrated in Figure 4.23D, mixed Ph-SH-/OLA-passivated $(CdSe)_{34}$ NCs showed nearly identical decay values for the slow component (τ_2) at different temperatures. It has been determined experimentally that the τ_{avg} of semiconductor nanomaterials is temperature independent up to room temperature because exciton localization takes place as a consequence of the presence of trap states.[333, 334] This concept is in agreement with our findings in that we believe trap-state mediated PL properties are more dominant than delocalization processes in Ph-SH-/OLA-passivated $(CdSe)_{34}$ NCs. Thirdly, both Py-DTC-/OLA- and Naph-DTC-/OLA-passivated

$(CdSe)_{34}$ NCs displayed strong temperature-dependent dynamics in which τ_2 and τ_{avg} increased with decreasing temperature. These long-lived, biexponential excited state time constants indicate the presence of a highly delocalized spatial distribution of excitonic wave functions around the NCs and that the effects of carrier trapping are negligible.[335] We did not investigate the excited state dynamics at temperatures <80 K because in ultrasmall NCs, the delocalization process can be masked by bright-dark splitting, which increases as size decreases.[336] Taken together, this first ligand-controlled, temperature-dependent study indicates that the exciton delocalization process in ultrasmall NCs strongly influences their excited state dynamics.

4.5 Conclusion

Herein we report control over the optoelectronic properties of $(CdSe)_{34}$ NCs through a post-synthetic surface ligand exchange with various chalcogenol-based ligands. We began the investigation considering X-PDTC ligands with varying levels of electron donating and withdrawing para-substitutions. It was determined that as the electron withdrawing nature of the substitution increases, better alignment exists between the HOMO of the surface passivating ligand and the HOMO of the CdSe NC. This allows for a greater extent of delocalization of the excitonic hole wave function. These results lead us to investigate other characteristics of the ligand such as level of conjugation, binding mode and binding head group.

Furthermore, we have shown that the excitonic confinement energy of $(CdSe)_{34}$ NCs can be reversibly manipulated – up to a 650 meV shift in the lowest energy excitonic peak – by post synthetic ligand exchange through controlling delocalization of NC hole wave functions through interfacial electronic states. We determined that the

delocalization of hole wave function is predominantly controlled by a combination of extend π-conjugation (highest shift for Py) and binding head group (highest shift for DTC) of surface passivating ligands rather than by energetic alignment between the HOMOs of NC and ligand. Thus, strength of the electronic interaction between NCs and their surface passivating ligands is governed by coordination chemistry and the HSAB principle. Moreover, our steady-state and time-resolved PL studies confirm that hole wave function delocalization weakens electron-hole recombination ability resulting in a relative increase in PL lifetime as compared to the original OLA-passivated $(CdSe)_{34}$ NCs before ligand exchange. Furthermore, our temperature-dependent PL characterization suggest carrier trapping and/or phonon-mediated relaxation does not play a role in determining τ_{avg} but a strong influence by hole wave function delocalization was observed, which provides the first study of hole delocalizing ligand-passivated semiconductor nanocrystals in general.

This interfacial electronic interaction produces strongly coupled NC-ligand hybrid molecules, which have tremendous potential in providing a wealth of information on the physicochemical, photophysical, and electrochemical properties at the molecular level that can be used to maximize charge transfer and transport efficiencies. Despite their potential for providing valuable molecular level information, current ligand-coated CdSe NCs display band-gaps >2.90 eV[5, 6, 317] in the blue region of the solar spectrum. This size gap makes them unsuitable for effective solar-based energy production, which requires visible to near infrared band-gaps. Based on this current work, we predict that an extension of band-gap range for ultrasmall CdSe NCs can be achieved through the appropriate selection of surface ligand chemistry without compromising their core

diameters or compositions, thus enhancing their potential application as photocatalysts. In addition, Py is known to undergo π-stacking by itself or with graphene and carbon nanotubes, and thus there can be p-orbitals overlap and an increase in carrier diffusion length, resulting in facilitation of charge transport for photodetector application.[337]

Using transient absorption (TA) spectroscopy, we were the first to report ultrafast hole transfer of $(CdSe)_{34}$ NCs that were functionalized with the hole delocalizing ligand, Ph-DTC.[338] A recent report by Lian et al.[339] supports our original finding that the existence of exciton delocalization in semiconductor nanocrystals facilitates the extraction of charge carriers. Our current work presenting a comprehensive study on selection of the best hole wave function delocalizing ligand should further enhance TA studies investigating hole transfer from nanocrystals to their ligand monolayer. Moreover, we recently reported the electron wave function delocalization ability of $Cd(carboxylate)_2$ ligands.[4] Taken together, functionalization of $(CdSe)_{34}$ NCs with dual hole and electron delocalization ligands should provide a rational approach for efficient extraction of both types of charge carriers and is a logical step for future time-resolved excited-state PL and TA spectroscopy studies.

4.6 Appendix

Table 4.1. Shift in the lowest-energy (band-edge) absorption of 1.6 nm DDA-passivated CdSe NCs upon the ligand exchange reaction with X-PDTC ligands

Ligand	λ (nm)	Λ E_{og} (nm)	ΛE_{og} (meV)	δR (nm)
DDA(	418			
$(CH_3)_2$-PDTC	456	38	250	0.19
CH_3O-PDTC	464	46	300	0.23
CH_3-PDTC	473	55	344	0.26
F-PDTC	492	73	447	0.34
H-PDTC	504	88	510	0.39
Br-PDTC	510	92	540	0.43
CF_3-PDTC	517	99	569	0.47
CF_3O-PDTC	525	107	610	0.52

Table 4.2. Comparison of change in optical band gap (ΔEog) and apparent increase in the excitonic radius (ΔR) of three different sizes of CdSe NC-passivated with four different ligands

CdSe NCs size (nm)	Passivating ligand	λ (nm)	$\Delta\lambda_{og}$ (nm)	ΔE_{og} (meV)	ΔR(nm)
1.6	DDA	418	-	-	
	OCH_3-PDTC	464	46 (1.53)	300 (8.82)	0.23
	H-PDTC	504	86 (1.00)	510 (4.90)	0.39
	OCF_3-PDTC	510	94 (2.00)	540 (9.53)	0.47
1.8	DDA	440	-	-	
	OCH_3-PDTC	469	29 (0.58)	164 (2.66)	0.15
	H-PDTC	508	68 (0.82)	370 (1.40)	0.31
	OCF_3-PDTC	518	78 (0.94)	420 (1.72)	0.37
2.0	DDA	460	-	-	
	OCH_3-PDTC	480	19 (1.15)	101 (5.40)	0.09
	H-PDTC	517	56 (1.15)	288 (4.90)	0.27
	OCF_3-PDTC	525	65 (0.58)	329 (2.59)	0.32

Table 4.3 HOMO and LUMO energies of the various ligands listed in Figure 1. All energies are given relative to vacuum.

ligand type	HOMO energy (eV)	LUMO energy (eV)
Anth-DTC/NH_4^+	-5.359	-2.022
Py-DTC/NH_4^+	-5.448	-1.884
Naph-DTC/NH_4^+	-5.621	-1.505
Ph-DTC/NH_4^+	-5.713	-1.141
Py-$CO_2^-Bu_4N^+$	-5.735	-2.200
Py-NH_2	-5.048	-1.566
Ph-SH	-6.315	-0.673
Ph-SeH	-6.238	-0.911
Ph-TeH	-5.963	-1.106
n-DDTC/NH_4^+	-5.548	-0.620

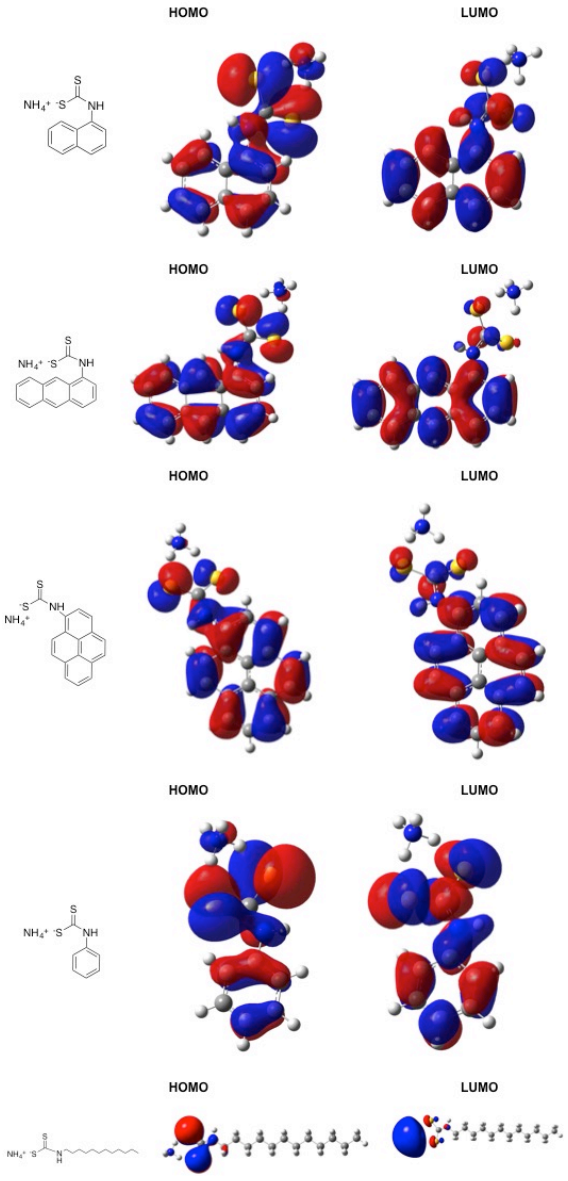

Table 4.4 The lowest energy excitonic peak position (l) and reduction oin confinement energy (DE) of OLA-passivated $(CdSe)_{34}$ NCs before and after treatment with various hole delocalizing ligands. DE was calculated from l values relative to the transition energy of OLA-passivated NCs. HOMO energies are

ligand type	λ (nm)	ΔE (meV)	HOMO energy (eV)
OLA	418		
n-DDTC/NH_4^+	420	08	-5.548
Anth-DTC/NH_4^+	528	620	-5.359
Py-DTC/NH_4^+	537	650	-5.448
Naph-DTC/NH_4^+	513	545	-5.621
Ph-DTC/NH_4^+	504	510	-5.713
Py-$CO_2^-Bu_4N^+$	433	110	-5.735
Py-NH_2	427	70	-5.048
Ph-SH	436	136	-6.315
Ph-SeH	448	199	-6.238
Ph-TeH	450	211	-5.963

Table 4.5 Comparison of reduction of confinement energy (DE) and number and percentage of surface-bound hole delocalizing ligands determined from the ^1H NMR analysis.

ligand type	ΔE (meV)	Average number of ligands[a]	Percentage exchange (%)	Number of ligand per square nm[b]
OLA	-	18	-	2.24
Py-DTC/NH_4^+	650	11	62	1.37
Anth-DTC/NH_4^+	630	13	68	1.62
Naph-DTC/NH_4^+	545	13	68	1.62
Ph-DTC/NH_4^+	510	15	73	1.74
Py-$CO_2^-Bu_4N^+$	110	11	60	1.37

Table 4.6 Time constant and PL decay of various ligand-passivated $(CdSe)_{34}$ NCs at various temperatures. A biexponential fit (Eq. 1 below)[3] was used to determine the average lifetime (Eq. 2 below). The instrument response function (IRF) of this system was measured as 0.4 ns.

Surface passivating Ligand type	Temperature (K)	Biexponential decay values	Average PL lifetime (τ_{avg}, ns)
Mixed Py-DTC/OLA	300	A_1 =0.729, τ_1= 5.06 ns A_2 = 0.271, τ_2= 36.47 ns	27.93
	250	A_1 = 0.675, τ_1= 5.79 ns A_2 = 0.325, τ_2= 49.46 ns	40.91
	200	A_1 = 0.771, τ_1= 4.74 ns A_2 = 0.229, τ_2= 55.19 ns	43.89
	120	A_1 = 0.904, τ_1= 5.78 ns A_2 = 0.096, τ_2= 95.31 ns	62.75
	80	A_1 = 0.915, τ_1= 6.08 ns A_2 = 0.085, τ_2= 140.03 ns	97.32
Mixed Naph-DTC/OLA	300	A_1 = 0.822, τ_1= 3.31 ns A_2 = 0.178, τ_2= 28.32 ns	19.57
	250	A_1 = 0.846, τ_1= 3.44 ns A_2 = 0.154, τ_2= 46.85 ns	34.38
	200	A_1 = 0.846, τ_1= 5.06 ns A_2 = 0.154, τ_2= 49.46 ns	37.70
	120	A_1 = 0.737, τ_1= 5.10 ns A_2 = 0.264, τ_2= 61.88 ns	51.24
	80	A_1 = 0.782, τ_1= 4.17 ns A_2 = 0.218, τ_2= 94.65 ns	82.31
Mixed Ph-SH/OLA	300	A_1 = 0.811, τ_1= 2.97 ns A_2 = 0.189, τ_2= 5.99 ns	3.94
	250	A_1 = 0.863, τ_1= 3.28 ns A_2 = 0.137, τ_2= 8.62 ns	4.85
	200	A_1 = 0.762, τ_1= 2.24 ns A_2 = 0.238, τ_2= 7.09 ns	4.65
	120	A_1 = 0.734, τ_1= 2.81 ns A_2 = 0.266, τ_2= 8.60 ns	5.86
	80	A_1 = 0.716, τ_1= 2.78 ns A_2 = 0.284, τ_2= 8.64 ns	6.01
Only OLA	300	A_1 =0.704, τ_1= 6.55 ns A_2 = 0.296, τ_2= 30.11 ns	22.09

4.7 References

1. Dolai, S., A. Dass, and R. Sardar, *Photophysical and Redox Properties of Molecule-like CdSe NCs.* Langmuir, 2013. **29**: p. 6187.
2. Alivisatos, A.P., *Semiconductor Clusters, Nanocrystals, and Quantum Dots.* Science, 1996. **271**: p. 933.
3. El-Sayed, M.A., *Small Is Different: Shape-, Size-, and Composition-Dependent Properties of Some Colloidal Semiconductor Nanocrystals.* Acc. Chem. Res., 2004. **37**: p. 326.
4. Smith, A.M. and S. Nie, *Semiconductor Nanocrystals: Structure, Properties, and Band Gap Engineering.* Acc. Chem. Res., 2009. **43**: p. 190.
5. Talapin, D.V., et al., *Prospects of Colloidal Nanocrystals for Electronic and Optoelectronic Applications.* Chem. Rev., 2009. **110**: p. 389.
6. Coe, S., et al., *Electroluminescence from single monolayers of nanocrystals in molecular organic devices.* Nature, 2002. **420**: p. 800.
7. Colvin, V.L., M.C. Schlamp, and A.P. Alivisatos, *Light-emitting diodes made from cadmium selenide nanocrystals and a semiconducting polymer.* Nature, 1994. **370**: p. 354.
8. Gur, I., et al., *Air-Stable All-Inorganic Nanocrystal Solar Cells Processed from Solution.* Science, 2005. **310**: p. 462.
9. Huynh, W.U., J.J. Dittmer, and A.P. Alivisatos, *Hybrid Nanorod-Polymer Solar Cells.* Science, 2002. **295**: p. 2425.
10. Kamat, P.V., et al., *Beyond Photovoltaics: Semiconductor Nanoarchitectures for Liquid-Junction Solar Cells.* Chem. Rev., 2010. **110**: p. 6664.
11. Lee, J.S., et al., *Band-like transport, high electron mobility and high photoconductivity in all-inorganic nanocrystal arrays.* Nat. Nanotechnol., 2011. **6**: p. 348.
12. Ochsenbein, S.T., et al., *Charge-controlled magnetism in colloidal doped semiconductor nanocrystals.* Nat. Nanotechnol., 2009. **4**: p. 681.
13. Kambhampati, P., *Unraveling the Structure and Dynamics of Excitons in Semiconductor Quantum Dots.* Acc. Chem. Res., 2010. **44**: p. 1.
14. Klimov, V.I., et al., *Optical Gain and Stimulated Emission in Nanocrystal Quantum Dots.* Science, 2000. **290**: p. 314.
15. Kovalenko, M.V., M. Scheele, and D.V. Talapin, *Colloidal Nanocrystals with Molecular Metal Chalcogenide Surface Ligands.* Science, 2009. **324**: p. 1417.
16. Wang, C., M. Shim, and P. Guyot-Sionnest, *Electrochromic Nanocrystal Quantum Dots.* Science, 2001. **291**: p. 2390.
17. Elward, J.M. and A. Chakraborty, *Effect of Dot Size on Exciton Binding Energy and Electron–Hole Recombination Probability in CdSe Quantum Dots.* J. Chem. Theory Comput., 2013. **9**: p. 4351.
18. Kilina, S., et al., *Surface Ligands Increase Photoexcitation Relaxation Rates in CdSe Quantum Dots.* ACS Nano, 2012. **6**: p. 6515.
19. Brus, L.E., *Electron--electron and electron-hole interactions in small semiconductor crystallites: The size dependence of the lowest excited electronic state.* J. Chem. Phys., 1984. **80**: p. 4403.

20. Bayer, M., et al., *Coupling and Entangling of Quantum States in Quantum Dot Molecules.* Science, 2001. **291**: p. 451.
21. Krenner, H.J., et al., *Optically Probing Spin and Charge Interactions in a Tunable Artificial Molecule.* Phys. Rev. Lett., 2006. **97**: p. 076403.
22. Oosterkamp, T.H., et al., *Microwave spectroscopy of a quantum-dot molecule.* Nature, 1998. **395**: p. 873.
23. Banin, U., et al., *Identification of atomic-like electronic states in indium arsenide nanocrystal quantum dots.* Nature, 1999. **400**: p. 542.
24. Brus, L., *Electronic wave functions in semiconductor clusters: experiment and theory.* J. Phys. Chem., 1986. **90**: p. 2555.
25. Steigerwald, M.L. and L.E. Brus, *Semiconductor crystallites: a class of large molecules.* Acc. Chem. Res., 1990. **23**: p. 183.
26. Amelia, M., et al., *Structural and Size Effects on the Spectroscopic and Redox Properties of CdSe Nanocrystals in Solution: The Role of Defect States.* ChemPhysChem, 2011. **12**: p. 2280.
27. Inamdar, S.N., P.P. Ingole, and S.K. Haram, *Determination of Band Structure Parameters and the Quasi-Particle Gap of CdSe Quantum Dots by Cyclic Voltammetry.* ChemPhysChem, 2008. **9**: p. 2574.
28. Kucur, E., et al., *Determination of quantum confinement in CdSe nanocrystals by cyclic voltammetry.* J. Chem. Phys., 2003. **119**: p. 2333.
29. Long, R., N.J. English, and O.V. Prezhdo, *Defects Are Needed for Fast Photo-Induced Electron Transfer from a Nanocrystal to a Molecule: Time-Domain Ab Initio Analysis.* J. Am. Chem. Soc., 2013. **135**: p. 18892.
30. Yang, Y., W. Rodríguez-Córdoba, and T. Lian, *Ultrafast Charge Separation and Recombination Dynamics in Lead Sulfide Quantum Dot–Methylene Blue Complexes Probed by Electron and Hole Intraband Transitions.* J. Am. Chem. Soc., 2011. **133**: p. 9246.
31. Crisp, R.W., et al., *Coherent Exciton Delocalization in Strongly Coupled Quantum Dot Arrays.* Nano Lett., 2013. **13**: p. 4862.
32. Fafarman, A.T., et al., *Thiocyanate-Capped Nanocrystal Colloids: Vibrational Reporter of Surface Chemistry and Solution-Based Route to Enhanced Coupling in Nanocrystal Solids.* J. Am. Chem. Soc., 2011. **133**: p. 15753.
33. Koole, R., et al., *Electronic Coupling and Exciton Energy Transfer in CdTe Quantum-Dot Molecules.* J. Am. Chem. Soc., 2006. **128**: p. 10436.
34. Micic, O.I., S.P. Ahrenkiel, and A.J. Nozik, *Synthesis of extremely small InP quantum dots and electronic coupling in their disordered solid films.* Appl. Phys. Lett., 2001. **78**: p. 4022.
35. Frederick, M.T. and E.A. Weiss, *Relaxation of Exciton Confinement in CdSe Quantum Dots by Modification with a Conjugated Dithiocarbamate Ligand.* ACS Nano, 2010. **4**: p. 3195.
36. Buckley, J.J., et al., *Chalcogenol Ligand Toolbox for CdSe Nanocrystals and Their Influence on Exciton Relaxation Pathways.* ACS Nano, 2014. **8**: p. 2512.
37. Liang, Y., J.E. Thorne, and B.A. Parkinson, *Controlling the Electronic Coupling between CdSe Quantum Dots and Thiol Capping Ligands via pH and Ligand Selection.* Langmuir, 2012. **28**: p. 11072.

38. Frederick, M.T., et al., *A Molecule to Detect and Perturb the Confinement of Charge Carriers in Quantum Dots.* Nano Lett., 2011. **11**: p. 5455.
39. Frederick, M.T., et al., *Control of Exciton Confinement in Quantum Dot-Organic Complexes through Energetic Alignment of Interfacial Orbitals.* Nano Lett., 2012. **13**: p. 287.
40. Koole, R., et al., *Differences in Cross-Link Chemistry between Rigid and Flexible Dithiol Molecules Revealed by Optical Studies of CdTe Quantum Dots.* J. Phys. Chem. C, 2007. **111**: p. 11208.
41. Dolai, S., et al., *Isolation of Bright Blue Light-Emitting CdSe Nanocrystals with 6.5 kDa Core in Gram Scale: High Photoluminescence Efficiency Controlled by Surface Ligand Chemistry.* Chem. Mater., 2014. **26**: p. 1278.
42. Wessels, J.M., et al., *Optical and Electrical Properties of Three-Dimensional Interlinked Gold Nanoparticle Assemblies.* J. Am. Chem. Soc., 2004. **126**: p. 3349.
43. Bryant, G.W. and W. Jaskolski, *Electronic structure of quantum-dot molecules and solids.* Physica E, 2002. **13**: p. 293.
44. Evans, C.M., M.E. Evans, and T.D. Krauss, *Mysteries of TOPSe Revealed: Insights into Quantum Dot Nucleation.* J. Am. Chem. Soc., 2010. **132**: p. 10973.
45. Newton, J.C., et al., *Low-Temperature Synthesis of Magic-Sized CdSe NCs: Influence of Ligands on NC Growth and Photophysical Properties.* J. Phys. Chem. C, 2012. **116**: p. 4380.
46. Wang, F., et al., *Spectroscopic Identification of Tri-n-octylphosphine Oxide (TOPO) Impurities and Elucidation of Their Roles in Cadmium Selenide Quantum-Wire Growth.* J. Am. Chem. Soc., 2009. **131**: p. 4983.
47. Del Ben, M., et al., *Density Functional Study on the Morphology and Photoabsorption of CdSe NCs.* J. Phys. Chem. C, 2011. **115**: p. 16782.
48. Kasuya, A., et al., *Ultra-stable nanoparticles of CdSe revealed from mass spectrometry.* Nat. Mater., 2004. **3**: p. 99.
49. Wang, Y., et al., *The Magic-Size NC (CdSe)34 as a Low-Temperature Nucleant for Cadmium Selenide Nanocrystals; Room-Temperature Growth of Crystalline Quantum Platelets.* Chem. Mater., 2014. **26**: p. 2233.
50. Jasieniak, J. and P. Mulvaney, *From Cd-Rich to Se-Rich-the Manipulation of CdSe Nanocrystal Surface Stoichiometry.* J. Am. Chem. Soc., 2007. **129**: p. 2841.
51. Li, R., Z. Luo, and F. Papadimitrakopoulos, *Redox-Assisted Asymmetric Ostwald Ripening of CdSe Dots to Rods.* J. Am. Chem. Soc., 2006. **128**: p. 6280.
52. Algar, W.R. and U.J. Krull, *Luminescence and Stability of Aqueous Thioalkyl Acid Capped CdSe/ZnS Quantum Dots Correlated to Ligand Ionization.* ChemPhysChem, 2007. **8**: p. 561.
53. Leatherdale, C.A. and M.G. Bawendi, *Observation of solvatochromism in CdSe colloidal quantum dots.* Phys. Rev. B, 2001. **63**: p. 165315.
54. Thackeray, J.W., et al., *Interaction of diethyldithiocarbamate with n-type cadmium sulfide and cadmium selenide: efficient photoelectrochemical oxidation to the disulfide and flat-band potential of the semiconductor as a function of adsorbate concentration.* J. Am. Chem. Soc., 1986. **108**: p. 3570.
55. Wang, L.W. and A. Zunger, *Pseudopotential calculations of nanoscale CdSe quantum dots.* Phys. Rev. B, 1996. **53**: p. 9579.

56. Jasieniak, J., M. Califano, and S.E. Watkins, *Size-Dependent Valence and Conduction Band-Edge Energies of Semiconductor Nanocrystals.* ACS Nano, 2011. **5**: p. 5888.
57. Querner, C., et al., *Size and ligand effects on the electrochemical and spectroelectrochemical responses of CdSe nanocrystals.* Phys. Chem. Chem. Phys., 2005. **7**: p. 3204.
58. Herron, N., et al., *Crystal Structure and Optical Properties of Cd32S14(SC6H5)36. DMF4, a Cluster with a 15 Angstrom CdS Core.* Science, 1993. **259**: p. 1426.
59. Vossmeyer, T., et al., *A "Double-Diamond Superlattice" Built Up of Cd17S4(SCH2CH2OH)26 Clusters.* Science, 1995. **267**: p. 1476.
60. Boev, V.I., et al., *Dipole–dipole interaction effect on the optical response of quantum dot ensembles.* Phys. B, 2003. **338**: p. 347.
61. Kaushik, A.P., B. Lukose, and P. Clancy, *The Role of Shape on Electronic Structure and Charge Transport in Faceted PbSe Nanocrystals.* ACS Nano, 2014. **8**: p. 2302.
62. Kilina, S., S. Ivanov, and S. Tretiak, *Effect of Surface Ligands on Optical and Electronic Spectra of Semiconductor NCs.* J. Am. Chem. Soc., 2009. **131**: p. 7717.
63. Puzder, A., et al., *The Effect of Organic Ligand Binding on the Growth of CdSe Nanoparticles Probed by Ab Initio Calculations.* Nano Lett., 2004. **4**: p. 2361.
64. Wang, Y., et al., *The Magic-Size NC (CdSe)34 as a Low-Temperature Nucleant for Cadmium Selenide Nanocrystals; Room-Temperature Growth of Crystalline Quantum Platelets.* Chemistry of Materials, 2014. **26**(7): p. 2233-2243.
65. Buckley, J.J., et al., *Chalcogenol Ligand Toolbox for CdSe Nanocrystals and Their Influence on Exciton Relaxation Pathways.* ACS nano, 2014. **8**(3): p. 2512-2521.
64. Wang, Y., et al., *The Magic-Size NC (CdSe)34 as a Low-Temperature Nucleant for Cadmium Selenide Nanocrystals; Room-Temperature Growth of Crystalline Quantum Platelets.* Chem. Mater., 2014. **26**: p. 2233.
65. Munro, A.M., et al., *Phenyldithiocarbamate Ligands Decompose During Nanocrystal Ligand Exchange.* The Journal of Physical Chemistry C , 2016
66. Scheele, M., et al., *PbS nanoparticles capped with tetrathiafulvalenetetracarboxylate: utilizing energy level alignment for efficient carrier transport.* ACS nano, 2014. **8**(3): p. 2532-2540.
67. Lawrence, K.N., et al., *Dual Role of Electron-Accepting Metal-Carboxylate Ligands: Reversible Expansion of Exciton Delocalization and Passivation and Nonradiative Trap-States of Molecule-Like CdSe Nanocrystals*. Journal of the American Chemical Society, 2016. **138**[39]. P. 12318-12325
68. Hoffmann, R., *A chemical and theoretical way to look at bonding on surfaces.* Reviews of Modern Physics, 1988. **60**[3]: p.601
69. La Croix, A.D., et al., *Design of a hole trapping ligand.* Nano Letters, 2017.
70. de Mello Donegá, C., M. Bode, and A. Meijerink, *Size-and temperature-dependence of exciton lifetimes in CdSe quantum dots.* Physical Review B, 2006. **74**(8): p. 085320

71. Mokari, T. and U. Banin, *Synthesis and properties of CdSe/ZnS core/shell nanorods.* Chemistry of materials, 2003. **15**(20): p. 3955-3960.
72. Jin, S., et al., *Enhanced Rate of Radiative Decay in CdSe Quantum Dots upon Adsorption of an Exciton-Delocalizing Ligand.* Nano letters, 2014. **14**(9): p. 5323-5328.

CHAPTER 5. DIRECT SYNTHESIS OF WHITE-LIGHT EMITTING ULTRASMALL PEROVSKITE NANOCRYSTALS

5.1 Synopsis

Organic-inorganic hybrid perovskites, direct band-gap semiconductors have shown tremendous promise for optoelectronic device fabrication. We report the first colloidal synthetic approach to prepare ultrasmall (~1.5 nm diameter), white light emitting, organic-inorganic hybrid perovskite NCs. The nearly pure white-light emitting ultrasmall NCs were obtained by selectively manipulating the surface chemistry (passivating ligands and surface trap-states) and controlled substitution of halide ions. The NCs displayed a combination of band-edge and broadband photoluminescence properties, covering a major part of the visible region of the solar spectrum with unprecedentedly large quantum yields of ~12% and photoluminescence lifetime of ~20 ns. The intrinsic white light emission of perovskite NCs makes them ideal and low cost hybrid nanomaterials for solid-state lighting applications

5.2 Introduction

The ever-increasing global demand for energy drives the need to discover highly efficient materials capable of saving energy in solid-state lighting (SSL) applications, such as light-emitting diodes (LEDs).[1,2] In this context, pure white-light emitting materials, and their subsequent uses in LED fabrication, will be a most effective way to reduce global power consumption. Currently, white-light LEDs are prepared by: (i) mixing single wavelength emitting organic phosphors,{3} and (ii) constructing multi-layer films composed of blue, green, and red color

emitting semiconductor quantum dots (QDs).[4,5] However, the self-absorption process between different organic phosphors reduces device efficiency, a similar device characteristic that has also been observed for QD-based LEDs. Ultrasmall semiconductor NCs (e.g., CdSe) display white-light, they require expensive, complicated and high temperature synthetic methods.[6-8] Recently, white-light emitting bulk organic-inorganic perovskites were synthesized,[9,10] which would not only expand SSL research but also facilitate inexpensive LED fabrication.

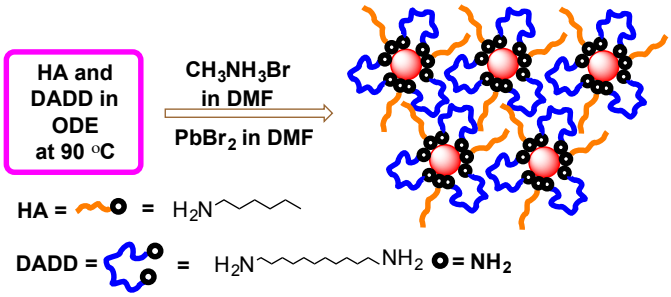

Figure 5.1 Schematic presentation of the synthesis of white-light emitting organolead bromide perovskite nanocrystals.

In this study, we report the first colloidal synthetic method to prepare white-light emitting, ultrasmall (~1.5 nm diameter) methylammonium lead bromide ($CH_3NH_3PbBr_3$) perovskite NCs.. These PNCs display a combination of band-edge and broadband photoluminescence (PL) with a quantum yield (QY) of ~5% and PL lifetime of ~7 ns. We hypothesize that the broad emission properties originate from the presence of surface-related mid-gap trap-states. Furthermore, we showed selective manipulation of band-gap and trap-states via the preparation of mixed halide ($CH_3NH_3PbCl_xBr_{3-x}$) NCs through controlled anion exchange reactions enhanced both QY and PL lifetime at least two-fold. We believe these ultrasmall NCs will provide fundamentally important information at the

molecular level because they bridge the gap between molecule-and-NCs,[11] and will be a promising candidate for white light phosphors for SSL application.[12]

5.3 Methods and Materials

5.3.1 Materials

Lead (II) bromide ($PbBr_2$, 99.999%), methylamine solution (CH_3NH_2 2.0 M in THF), hydrobromic acid (HBr, 48%), 1-octadecene (ODE, 90%), hexylamine (HA 99%), 1,12-diaminododecane (DADD, 99%), acetone (99.5%, ACS reagent), N,N-dimethylformamide (DMF) were purchased from Sigma-Aldrich. Hydrochloric acid (HCl, 37%) was purchased from Fisher Scientific. ODE was kept under high vacuum overnight and transferred to the glovebox under N_2 atmosphere prior to use. Polyurethane beads were purchased from Fluka. All solvents were purged with N_2 for 30 min prior to use. Bulk methylammonium lead bromide ($MAPbBr_3$) single crystals were grown according to the literature procedure[2] for X-ray diffraction analysis.

5.3.2 Synthesis of Methylammonium Bromide (CH_3NH_3Br)

CH_3NH_3Br was synthesized according to the literature procedure.[147] Briefly, an equivalent amount of HBr was added drop-wise to a solution of methylamine in ethanol (20 mL) at 0°C. The reaction mixture was stirred for 3 hr and then solvent was removed by rotary evaporation and the solid was dissolved in a minimum amount of ethanol and recrystallized by adding ether. The solid was then dried under vacuum producing a snow-white crystalline material that was inside a N_2 filled glove box for further use. CH_3NH_3Br was synthesized under identical mole ratio of the reagents and similar experimental procedure.

5.3.3 Synthesis and Purification of White-Light Emitting $CH_3NH_3PbBr_3$ NCs.

Under optimized reaction condition, 2 mL of ODE was placed in a 25 mL 1-neck round bottom flask and stirred at 90° C for 45 min and then 0.067 mmol DADD and 0.03mmol HA were added simultaneously and stirred for an additional 30 min. Separately, 0.032 mmol of CH_3NH_3Br and 0.1 mmol of $PbBr_2$ were dissolved in 100 μL and 200 μL of DMF, respectively. The CH_3NH_3Br was added to the round bottom flask first and allowed to react for 30 sec and then the $PbBr_2$ solution was added. The reaction was allowed to run for 3 min and then the entire solution was quenched by adding 10 mL of acetone resulting in the formation of a white solid. The solid was centrifuged at 5000 rpm for 5 minutes, dissolved in toluene and centrifuged at 7000 rpm for 2 min. The colorless supernatant was collected and dried using a rotavap before being stored in the glove box for further characterization.

5.3.4 Chloride Substitution.

In a typical substitution, ~4 mg of the purified CH_3NH_3PbBr3 NCs were dissolved in 5 mL of toluene and allowed to stir for 15 min at room temperature inside the glove box. Then, 0.05 mmol of solid CH_3NH_3Cl was added and the solution was stirred for 1 hr. The insoluble materials (CH_3NH_3Cl and CH_3NH_3Br are insoluble in toluene) were removed via centrifugation at 5000 RPM for 2 minutes and the solution was collected. White solid was obtained by drop wise additional of acetone. The solid then collected via centrifugation and dried under N_2 flow.

5.3.5 UV-vis Absorbance Characterization.

Absorption spectra were collected with a Varian Cary 50 Scan UV-visible spectrophotometer using a 1 cm quartz cuvette over the range of 300-800 nm. All spectra were collected in toluene, which was used as a background for these measurements.

5.3.6 Ground State Photoluminescence, Excited State Lifetime, and Absolute Quantum Yield Measurements

The photoluminescence (PL) emission spectra were acquired using a Cary Eclipse fluorescence spectrophotometer from Varian Instruments using a 1 cm quartz cuvette. The lifetime measurements were recorded using a time-correlated single photon counting (TCSPC) experimental set up. The data acquisition card (DAQ) was from Edinburgh Instrument (TCC900). The laser was a 405 nm pulsed laser from PICOQUANT (LDH-D-C-405M. CW-80MHz) with pulse width < 100 ps. The detector was a photomultiplier tube (PMT) from the HAMAMATSU (HT422-40). The following stretched-exponential equation was used to determine the excited state lifetime.[13]

$$\langle t \rangle = \tau_{av} = \frac{\int_0^\infty g(t) t dt}{\int_0^\infty g(t) dt} = \frac{1}{\Gamma_{str} \beta} \bar{\Gamma}\left(\frac{1}{\beta}\right),$$

5.3.7 ^{1}H NMR Characterization.

The ^{1}H NMR spectra were obtained with a Bruker AVANCE III 500 instrument at 500 mHz frequency. Typically, ~10-15 mg of purified sample was dissolved on 0.6 mL of chloroform-d at room temperature. Minimum of 1024 scans were collected with a 30° pulse angle, 3 sec acquisition, and 3 sec of relaxation. All data were plotted via TOPSPIN 2.1 software.

5.3.8 Transmission Electron Microscopy (TEM) Characterization.

For TEM analysis, samples were prepared inside a glove box by placing 10 μL of dissolved perovskite NCs (NCs) in toluene onto a carbon-coated copper grid (Electron Microscopy Science). The sample was allowed to sit for 30 seconds and any excess solution was removed by wicking with a Kimwipe to avoid aggregation. Images were obtained using a JEOL-3200FS-JEM instrument at 200 kV beam energy. The size of the PNCs was determined using ImageJ software.

5.3.9 Energy Dispersive X-ray (EDS) Analysis.

EDS analysis was performed using a Hitachi S-4700 field emission scanning electron microscope. The measurements were conducted at a pressure of $<5 \times 10^{-9}$ Torr. For EDS analysis, the PNCs were drop-casted on a piranha-cleaned silicon wafer inside a N_2 filled glove box, and the solution was allowed to evaporate at room temperature. (*Warning*: piranha solution is highly reactive and must be handled with extreme caution. It reacts violently with organic materials and may not be stored in tightly closed vessels). Before use, piranha-cleaned wafers were washed with copious amounts of Nanopure water and ethanol, and then dried in a vacuum oven at 120° C overnight.

5.3.10 Powder X-ray Diffraction (XRD) Analysis.

XRD analysis was conducted using a Bruker D8 Discover X-Ray Diffractometer. An IμS microfocus X-ray source was used, and the operating voltage and current were 50 kV and 1000 mA, respectively. A thin film of PNCs was prepared on a piranha cleaned glass coverslip by drop-casting the toluene solution of dissolved PNCs inside the glove box.

5.4 Results and Discussion

5.4.1 Characterization of $CH_3NH_3PbBr_3$ NCs

As illustrated in Figure 5.2A, purified $CH_3NH_3PbBr_3$ NCs in toluene display a sharp absorption peak at 402 nm. The NCs exhibited a combination of band-edge (emission maxima at 403 nm) and broadband (emission maxima at 512 nm) PL emission that are markedly different than both organic-inorganic hybrid[14,15,16] and inorganic[17,18,19.20] perovskite NCs, which display sharp band-edge emission features. The PLE spectrum (Figure 5.2B) of the NCs was identical in shape to that of the absorption spectrum. Therefore, our white-light NCs have their lowest energy transition at 402 nm. The $CH_3NH_3PbBr_3$ NCs display short emission lifetimes ($t_{band\text{-}edge}$: ~3 ns and $t_{broadband}$: 7 ns), see Figure 5.2C. As shown in Figure 5.2D, low resolution transmission electron microscopy (TEM) analysis of the purified NCs showed the presence of ultrasmall NCs (see Figure 5.2E) with a narrow size distribution. An average diameter of 1.5 nm (see Fig. 5.2E) was determined from the high-resolution TEM analysis (Figure 5.3A). The diameter of the NCs corresponds to only ~2 unit cells. Therefore, it was extremely difficult to capture TEM images showing lattice spacing. Exposure (5 min) of the electron beam did not damage the NCs. The NCs CIE chromaticity coordinates were (0.304, 0.351) (Figure 5.3B), which fall within the white light region of pure white light CIE coordinates of (0.333, 0.333) as perceived by the naked eye.

The sharp absorption feature indicates narrow size distribution of synthesized $CH_3NH_3PbBr_3$ NCs that resemble ultrasmall CdSe NCs (<2.0 nm in diameter).[2-24] A narrow size distribution would result in a sharp band-edge PL peak rather than a combination of band-edge and broadband peaks. The broad PL feature and short PL lifetimes suggest the presence of surface related trap sites in the NCs, not their size distribution. Our organic-inorganic hybrid NCs are coated with primary amines, which are known to be weak s-donating, L-type ligands[25] and their interaction with Pb^{2+} in NCs would lead to formation of antibonding orbitals below the conduction band of NCs.[26] The newly formed orbitals serve as electron trapping mid-gap states if not fully

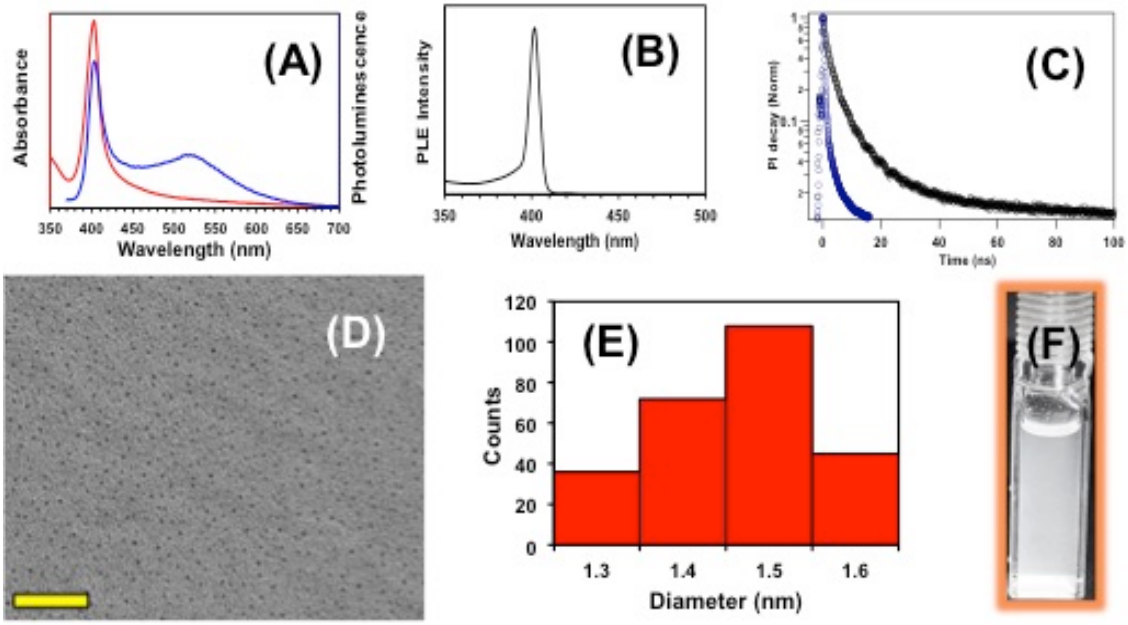

Figure 5.2 (A) UV-visible absorption (red) and PL (blue) spectra of $CH_3NH_3PbBr_{3.8}$ NCs at room temperature in toluene. The excitation wavelength was 350 nm. (B) PLE spectrum of $CH_3NH_3PbBr_{3.0}$ NCs at room temperature in toluene. (C) PL decay traces (blue: band-edge at 409 nm; black: broad-edge at 515 nm) of the NCs excited at 405 nm. (D) TEM image of the NCs with 50 nm scale bar. (E) Histogram shows PNCs with an average 1.5 nm in diameter. (F) White-light emitting PNCs under illumination of UV light.

passivated, resulting in broad emission in the PL spectra. Moreover, the broad-band emission dominates because the relative number of atoms on the surface of the NCs increases as their size decreases.[26] In this context, ultrasmall CdSe NCs are known to display a combination of band-edge and broadband PL emission due to large surface to volume ratio and the presence of mid-gap trap states.[27-31] Therefore, the PL spectrum of our 1.5 nm diameter $CH_3NH_3PbBr_3$ NCs nicely corroborate results from ultrasmall CdSe NCs. We calculated PL quantum yield for the NCs and found it to be 5%, which is at least 10-fold higher than the first generation, white-light emitting organic-lead halide bulk perovskites.[14] However, quantum yield of our NCs is much lower than conventional 3.3-7.0 nm diameter $CH_3NH_3PbBr_3$ quantum dots (QDs) (50-70%).[29, 30] It is known that the larger QDs display higher quantum yield than ultrasmall NCs because of relatively fewer surface defects in the crystal structure of the QDs, which allows the majority of the exciton recombination to take place radiatively.

It is important to mention that our $CH_3NH_3PbBr_3$ NCs displayed approximately 90 and 120 nm blue-shifts of band-gap in comparison to $CH_3NH_3PbBr_3$ QDs (3.3 nm diameter)[29] and bulk[2] perovskite, respectively. Considering the relatively small exciton Bohr radius (~2.0 nm) of $CH_3NH_3PbBr_3$ (weak quantum confinement),[31] the observed blue shifts of NCs were large and significant. Recent effective mass approximation (EMA) calculations by our group[359] and others[34-36] demonstrated that a simple spherical quantum well-based EMA calculation is not applicable to ultrasmall NCs. A possible explanation is the potential delocalization of exciton wave functions in the strong confinement regime altering the confinement.

The energy dispersive spectroscopy (EDS) characterization (Figure 5.3C) showed bromide rich NCs with Pb/Br atomic ratio of 3.8. The powder X-ray diffraction (XRD) analysis (Figure 5.3D red line) demonstrated broad peaks in comparison to the bulk perovskites (black line), two-dimensional (2D) materials,[33] and large anisotropically-shaped organolead halide perovskite nanostructures.[34] We should differentiate between our <2.0 nm diameter NCs and 2D $CH_3NH_3PbBr_3$ material in terms of the Pb:Br ratio. It was reported that in 2D single-layered $CH_3NH_3PbBr_3$ perovskites, the Pb:Br ratio is 1:4 using a formula of $[PbBr_4]$12, 33] The XRD pattern of our $CH_3NH_3PbBr_3$ NCs is similar to a literature report of small $CH_3NH_3PbBr_3$ nanocrystals.[29] Our ultrasmall NCs exhibited cubic structure (Figure 5.3D) and thus consist of octahedral unit cells of $[PbBr_6]^{4-}$. Therefore, excess bromide ions should reside at the surface of the $CH_3NH_3PbBr_3$ NCs. Our experimental data are in agreement with the literature suggesting an ~4.0 Pb/Br ratio for <2.0 nm diameter

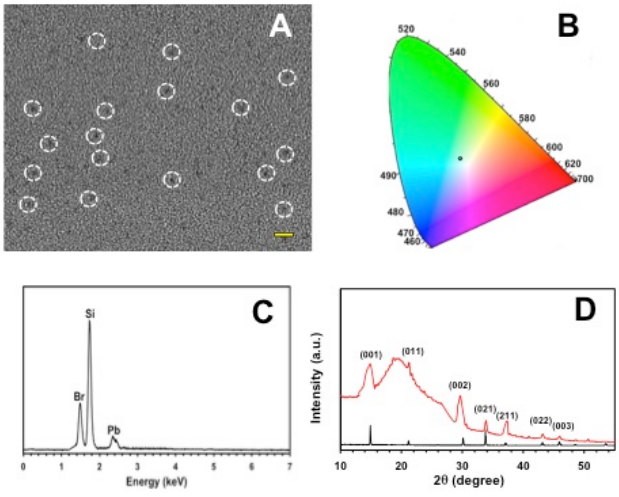

Figure 5.3. (A) High resolution TEM image of $CH_3NH_3PbBr_{3.8}$ NCs, (B) The CIE coordinates of ultrasmall $MAPbBr_{3.8}$ PNCs were found to be (0.304, 0.351), (C) A representative EDS spectrum of the ultrasmall $MAPbBr_{3.8}$ NCs, (D) –X-ray diffraction (XRD) analysis of the bulk perovskite (black) and ultrasmall NCs (red).

NCs.[29] Therefore, because of higher bromide content in the structure of ultrasmall NCs than traditional $CH_3NH_3PbBr_3$ perovskite, we refer to them as $CH_3NH_3PbBr_{3.8}$ for the rest of this communication. Appearance of the broad peak at 1.52 ppm associated with the NH_2 resonance of amine in the ^1H NMR analysis confirmed the presence of a primary amine (hexylamine (HA) and/or diaminododecane (DADD)) at the surface of the NCs (Figure 5.4). Moreover, the a and b protons that were adjacent to $–NH_2$ appearing at 2.72 and 1.6 ppm, respectively, were also broad and resembled surface attached ligands.

5.4.2 Role of HDA and DADD in WLE Synthesis

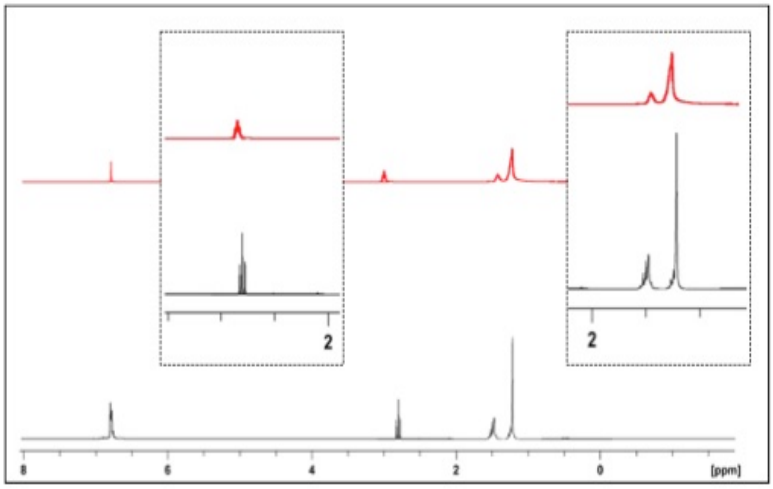

Figure 5.4 NMR characterization of ultrasmall $CH_3NH_3PbBr_{3.8}$ NCs. The black line is the 1H NMR spectrum of the pure DADD ligand and the red line is the purified ultrasmall $CH_3NH_3PbBr3.8$ NCs.

Although absorption spectra and white light emission under photoexcitation of our ultrasmall $CH_3NH_3PbBr_3$ NCs are similar to the literature reports of bulk 2D perovskite,[9,10] atomically thin 2D perovskite,[33] and quasi-2D layered organic-$PbBr_3$ perovskite materials,[35] the physical, emission, and structural properties of our NCs are

markedly different than those 2D materials. (1) Our ultrasmall $CH_3NH_3PbBr_3$ NCs are fully soluble in non-polar organic solvents such as toluene and chloroform (Figure 5.2F), but 2D perovskite materials are not. Therefore, their optical characterizations of bulk and atomically thin 2D materials were conducted in solid-state[9, 10, 33] as oppose to our colloidal-state analysis. (2) 2D organic-$PbBr_3$ perovskite display either sharp band-edge[33, 36] or broadband [9,10] PL properties, but our ultrasmall $CH_3NH_3PbBr_{3.8}$ NCs display a combination of band-edge and broadband emission. (3) In addition, the diffraction peaks in our ultrasmall $CH_3NH_3PbBr_{3.8}$ NCs were dramatically broadened as compared to any-type of 2D perovskites.[33, 36] The XRD patterns of our NCs are similar to the literature report of ~3.3 nm diameter $CH_3NH_3PbBr_3$ NCs,[29] which display relatively sharper XRD peaks than our $CH_3NH_3PbBr_{3.8}$ NCs, suggesting an even smaller size than the literature report of 3.3 nm diameter $CH_3NH_3PbBr_3$ NCs. Finally, synthesis of bulk or atomically thin, 2D layered organic-$PbBr_3$ perovskite requires short chain diamines as surface passivating ligands. [33, 9, 10] In this context, we have found that the presence of

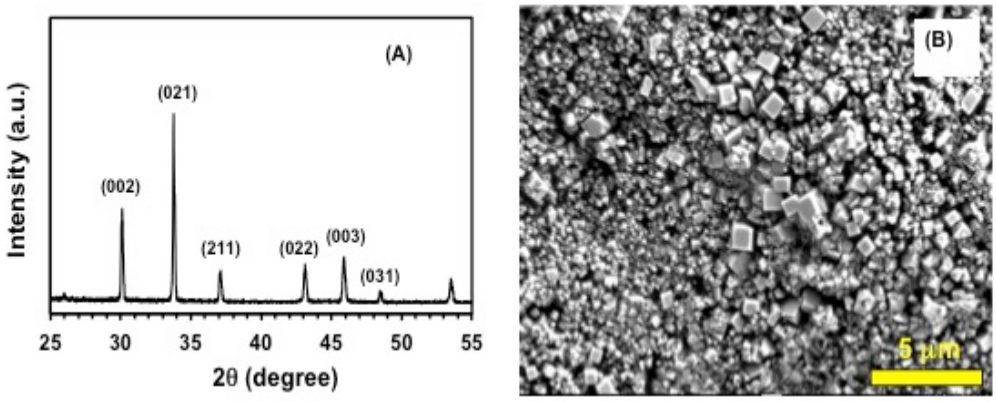

Figure 5.5 XRD spectrum (A) and SEM (B) image of the perovskite materials prepared in the absence DADD

both medium chain length monoamine (HA) and long chain length diamine (DADD) in the reaction mixture is essential to obtain white-light emitting $CH_3NH_3PbBr_{3.8}$ NCs. In this context, synthesis of NCs in the absence of DADD while keeping other conditions identical resulted in insoluble bulk $CH_3NH_3PbBr_3$ perovskite (Figure 5.5). Furthermore, absence of HA produced white-light emitting $CH_3NH_3PbBr_3$ NCs but QY was found to be <0.6% (see Figure 5.6 for optical and XRD characterization). Therefore, the presence of HA and DADD onto the surface of $CH_3NH_3PbBr_3$ NCs is a prerequisite to keep them in their ultrasmall size regime and maintain the surface related trap-states, resulting in white-light emission.

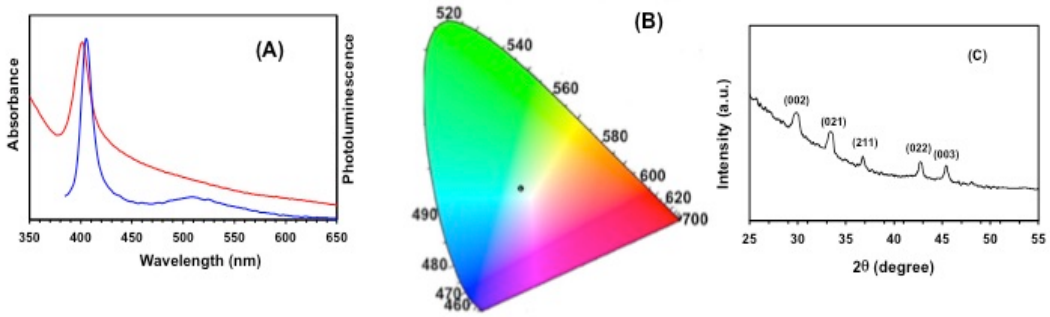

Figure 5.6 Characterization of $CH_3NH_3PbBr_{3.8}$ NCs synthesized in the absence of HA. (A) The absorption (402 nm) and emission (403, 512 nm) spectra of the PNCs in toluene. (B) CIE coordinates (0.338, 0.387) of the $CH_3NH_3PbBr_{3.8}$ NCs. (C) The XRD pattern still matches that of cubic phase perovskite, while the broad peaks represent ultrasmall size NCs.

5.4.3 Proof of Trap State Emission

As shown in Figure 5.2A, $CH_3NH_3PbBr_{3.8}$ NCs display a combination of band-edge and broadband PL properties. It is mentioned in the literature that the broad PL emission of 2D perovskite materials generally occurred from self-trapping of excitons or electrons/holes.[10, 37, 38] This electronic process is different than our proposed mechanism, which involves radiative recombination of excitons at mid-gap trap-states

giving our broad PL peak. To unravel the exact mechanism, we performed power dependent excitation PL studies (see Figure 5.7A). Importantly, the broad PL emission peak became saturated as the power was increased (Figure 5.7B). Thus, the experimental data do not support the self-trapping of excitons because if this would occur the PL intensity would follow a linear relationship with excitation power.[37, 38] Considering that the trap-state concentration in $CH_3NH_3PbBr_{3.8}$ NCs is finite and slow to relax, trap-state PL would be expected to saturate at high excitation power, as shown for GaN.[39] Therefore, our results strongly support trap-state-related emission. Importantly and as expected, the band-edge PL peak demonstrated a linear dependence with excitation power. Taken together, our experimental data suggest that the PL properties we observed (Figure 5.2A) appear solely from the ultrasmall $CH_3NH_3PbBr_{3.8}$ NCs but not from a mixture of three-dimension (3D) and 2D structures. Furthermore, our optical data are in agreement with our XRD pattern that indicates ultrasmall NCs of 3D crystal phase.

5.4.4 Tuning Optical Properties Through Anion Exchange

Based on the results described above, we propose that our white-light emission originates from contributions of sharp emission in the blue region and broad emission in the green region and thus is a combined effect from the large band-gap and presence of mid-gap trap states. In other words, by systematic manipulation of spectral features we should be able to control the NCs CIE chromaticity coordinates as well as brighten the white-light emission. Therefore, we would expect to be able to enhance these photophysical properties of $CH_3NH_3PbBr_{3.8}$ NCs by increasing exciton binding energy and/or reducing trap states. To achieve this, we performed anion exchange

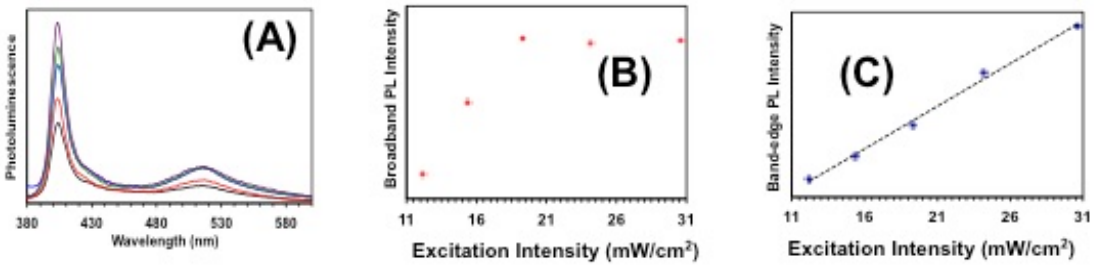

Figure 5.7 (A) PL spectra of $CH_3NH_3PbBr_{3.8}$ NCs at different excitation power density (mW/cm^2): black (11.2), red (15.4), blue (19.3), green (24.2), and purple (30.6). Dependence of broadband (B) and band-edge (C, R^2 =

reactions of purified, ultrasmall $CH_3NH_3PbBr_{3.8}$ NCs with methylammonium chloride (CH_3NH_3Cl). The EDS analysis (Figure 5.8A) confirmed the formation of mixed halide, $CH_3NH_3PbCl_{1.3}Br_{2.5}$ NCs, which displayed cubic crystal structure (Figure 5.8B).). A slight shift of the (022) plane to a higher diffraction angle in $CH_3NH_3PbCl_{1.3}Br_{2.5}$ NCs in comparison to the original $CH_3NH_3PbBr_{3.8}$ NCs suggests exchange of bromide ions by chloride ions. Thus, we hypothesize that the majority of the surface bromide ions, along with some octahedral unit cells of $[PbBr_6]^{4-}$ bromide ions, were exchanged with chloride ions (Figure 5.8C) TEM analysis confirmed no detectable change in the size of NCs due to chloride exchange (Figure 5.9A). However, due to their extremely small size, it would be difficult to accurately measure so slight a variation in the core diameter of NCs.

5.4.5 Characterization of $CH_3NH_3PbCl_{1.5}Br_{2.5}$ NCs

Absorption measurement of our $CH_3NH_3PbCl_{1.3}Br_{2.5}$ NCs showed an ~6 nm blue shift in the band-gap (Figure 5.9C), which is in agreement with the EDS analysis described above and the literature that chloride substitution of both bulk organic-$PbBr_3$ perovskites[40] and $CH_3NH_3PbBr_3$ NCs[41, 42] increases the band-gap because of the

stabilization of their valence band with more electronegative chloride as compared to bromide.[43] Small blue-shift is also in agreement with the suggestion that fewer octahedral unit cells of $[PbBr_6]^{4-}$ bromide ions were exchanged with chloride ions. Thus, the cubic crystal structure of the NCs is dominated by the bromide ions. In the PL characterization (Figure 5.9D), we observed changes in the position and shape of the broad-band emission in mixed halide perovskite NCs that could suggest an influence of chloride in the excited states, which are involved in the emission properties.[44] Moreover, increase in the band-gap increases the exciton binding energy[45] that results in an enhancement of the possibility of more efficient recombination of the excitons.[26] We observed a QY up to 12% of $CH_3NH_3PbCl_{1.3}Br_{2.5}$ and radiative lifetimes ($t_{band\text{-}edge}$: ~5

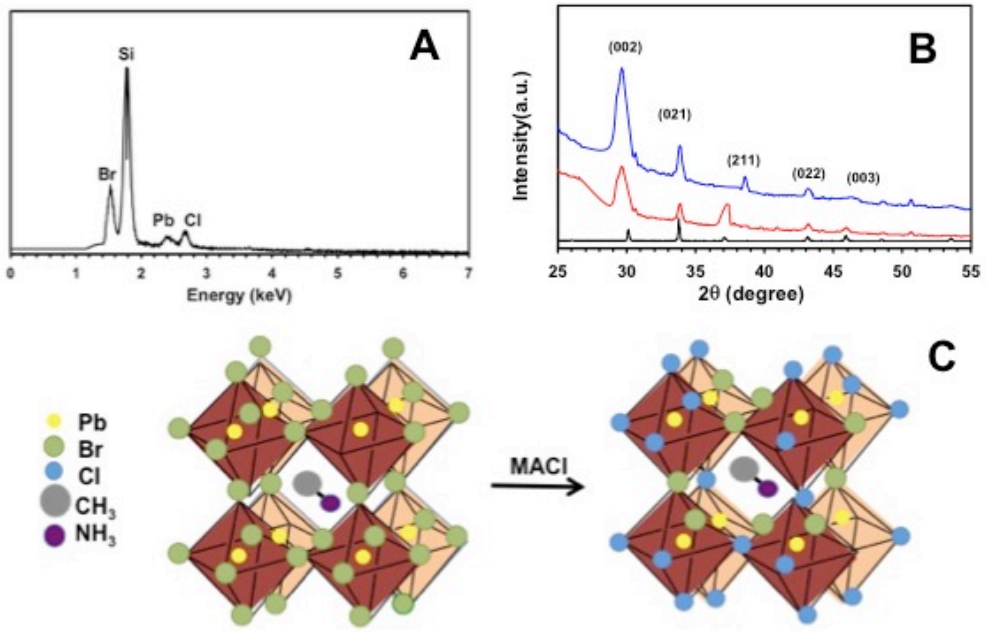

Figure 5.8 (A) Representative EDS spectrum of the ultrasmall $CH_3NH_3PbCl1.3Br2.5$ NCs, (B) The XRD pattern of the $CH_3NH_3PbBr3.8$ NCs (red), $CH_3NH_3PbCl1.3Br2.5$ NCs (blue), and bulk $CH_3NH_3PbBr_3$ perovskite., and (C) schematic depiction of halide substitution.

ns and $t_{broadband}$: 19 ns) see Figure 5.10. The broadband emission lifetime is more than two fold higher than $CH_3NH_3PbBr_{3.8}$ NCs. Moreover, we observed nearly homogeneous emission (determined from the PL lifetime) of our $CH_3NH_3PbCl_{1.3}Br_{2.5}$ NCs (data not shown). Importantly, the PLQY of our $CH_3NH_3PbCl_{1.3}Br_{2.5}$ NCs is higher than the white-light emitting bulk organic-lead halide perovskites (PL-QY = 9%).[10] The CIE chromaticity coordinates (Figure 5.9E) of $CH_3NH_3PbCl_{1.3}Br_{2.5}$ are (0.332, 0.341) which are very close to the CIE coordinates of pure white-light. Perhaps as recently demonstrated for $CsPbBr_3$ NCs,[44, 46] control halide exchange and preparation of

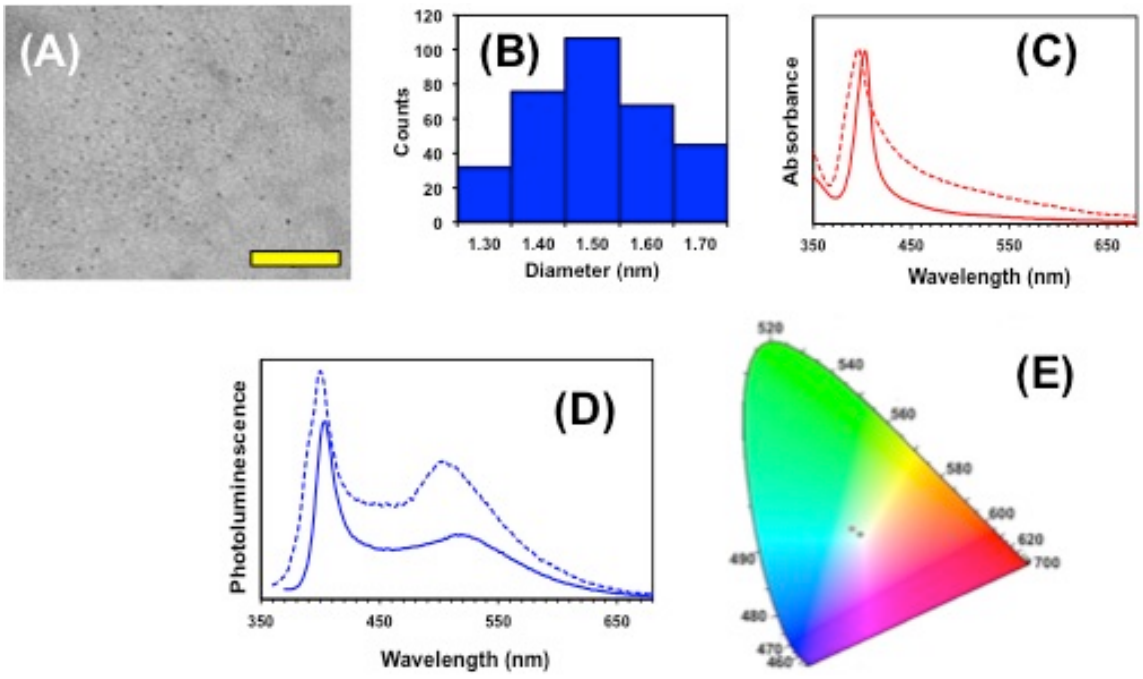

Figure 5.9 Fig. 4 (A) TEM image of the $CH_3NH_3PbCl1_{.3}Br_{2.5}$ NCs. The scale bar is 50 nm. (B) Histogram for PNCs shown in panel A. (C) UV-vis spectra of CH_3NH_3 $PbBr_{3.8}$ (solid line) and $CH_3NH_3PbCl_{1.3}Br_{2.5}$ (dotted line) PNCs. (D) PL spectra of $MAPbBr_{3.8}$ (solid line) and MA $CH_3NH_3PbCl_{1.3}Br_{2.5}$ (dotted line) NCs at 350 nm excitation. (E) CIE coordinates of $CH_3NH_3PbBr_{3.8}$ (red) and $CH_3NH_3PbCl_{1.3}Br_{2.5}$ (black) NCs.

white-light emitting inorganic perovskite NCs are feasible if one were able to synthesize them in their ultrasmall size regime. We should mention that prolonged chloride

exchange of $CH_3NH_3PbBr_{3.8}$ NCs resulted in insoluble white materials, thus demonstrating the importance of controlling the structural modification of NCs to obtain desired photophysical properties.

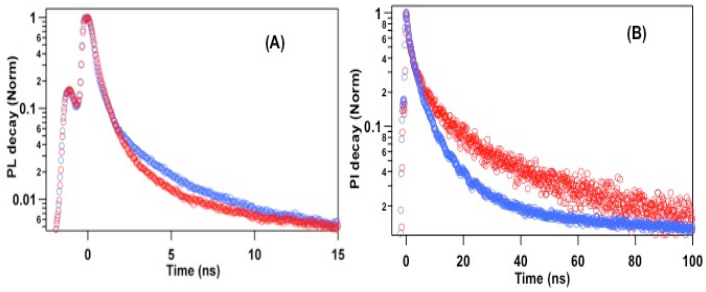

Figure 5.10 PL decay traces of band-edge collected at 409 nm (A) and broadband peaks collected at 515 nm (B) of $MAPbBr_{3.8}$ (blue) and $MAPbCl_{1.3}Br_{2.5}$ (red) PNCs. Stretched exponential fit of TCSPC spectra were used to determine the time constants.

5.4.6 Excitation Dependence of Emission Properties and LED Fabrication

Our structural and spectroscopic characterizations suggest that the bromide at the surface of the $CH_3NH_3PbBr_{3.8}$ NCs were exchanged with chloride. Because of the higher electronegativity of chloride than bromide, surface exchange reduces the surface related radiative mid-gap trap states[45] and increases the QY and radiative lifetimes as observed previously for CdSe[47] and CdTe NCs,[46] respectively. In order to further investigate the trap state-related emission, we studied the excitation wavelength dependent PL properties. Figure 5.11A demonstrates the broadband emission intensity as a function of excitation wavelength of $CH_3NH_3PbBr_{3.8}$ and $CH_3NH_3PbCl_{1.3}Br_{2.5}$ NCs. The nonlinearity in the relationship along with change in the broadband emission peak in $CH_3NH_3PbBr_{3.8}$ NCs suggest the presence of variable defect sites,[48] which were not observed for $CH_3NH_3PbCl_{1.3}Br_{2.5}$ NCs as a consequence of the reduction of nonradiative surface mid-

gap trap states. We also observed the change in the broadband peak shape between these two NCs (Figure 3.11B), suggesting the presence of different trap sites. Another important observation we made is the increase in $t_{broadband}$ of $CH_3NH_3PbCl_{1.3}Br_{2.5}$ over that of $CH_3NH_3PbBr_{3.8}$ NCs. However, one should expect the opposite effect in lifetime after chloride substitution because of the increase in confinement energy that would result in higher exciton binding energy and efficient recombination of excitons. It is reported that the kinetic energy of excitons increases as the confinement energy increases.[46, 47] Under such circumstance, the excitonic wave functions could easily fill the organic-inorganic hybrid core of $CH_3NH_3PbCl_{1.3}Br_{2.5}$ more completely than $CH_3NH_3PbBr_{3.8}$ NCs, and thus be prone to delocalize into the ligand monolayer. The delocalization of exciton wave functions increases the PL lifetime and PL-QY, as recently reported for ultrasmall CdSe NCs.[48] Nevertheless, further investigation is required to fully delineate the origin of the white-light emission of these ultrasmall organic-inorganic NCs. The unique photophysical properties of these NCs have tremendous potential for SSL applications, as we demonstrated with a proof-of-concept white-light source fabrication using a thin coating of $CH_3NH_3PbCl_{1.3}Br_{2.5}$ NCs in polyurethane (Figure 5.11C).

Recently, it was reported that perovskite QDs display excellent PL-QY,[17, 29, 24, 49, 50] high carrier mobilities, and larger diffusion lengths,[51] which are crucial electronic properties for photovoltaic applications. These electronic properties arise

because of excellent passivation of the QDs surface and reduction of the nonradiative trap states. However, the very narrow band-edge emission characteristic of QDs makes it

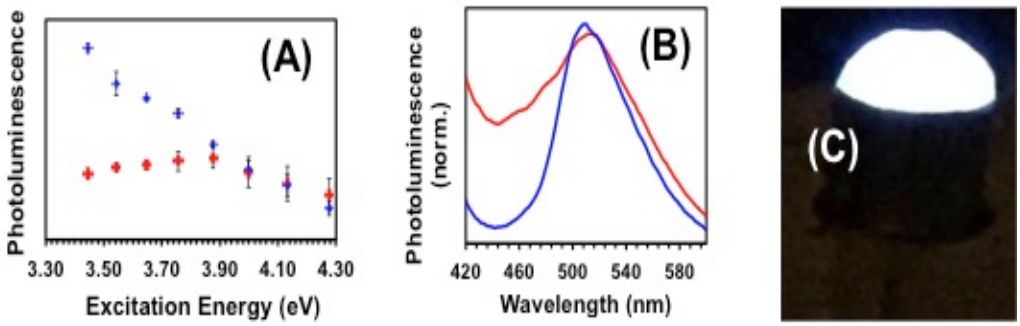

Figure 5.11 (A) Excitation wavelength dependent broadband PL intensity of $CH_3NH_3PbBr_{3.8}$ (red) and $CH_3NH_3PbCl_{1.3}Br_{2.5}$ (blue) NCs. (B) Comparison of broadband PL peak of $CH_3NH_3PbBr_{3.8}$ (red) and $CH_3NH_3PbCl_{1.3}Br_{2.5}$ (blue) NCs at 350 nm excitation. (C) A 5 mm commercial UV LED (360 nm) coated with $CH_3NH_3PbCl_{1.3}Br_{2.5}$ NCs in polyurethane

difficult to produce white light emission and fabricate LEDs for SSL applications. In this present study, we utilized surface-related trap states (defect sites) to generate a complimentary broadband emission in NCs. The combined band-edge and broadband emissions of our NCs cover most of the visible region of the solar spectrum, which in turn results in white-light emission. Taken together, manipulation of the appropriate amount of radiative trap states in NCs will enhance their optoelectronic properties and facilitate their applications in white light emitting LED fabrication.

5.5 Conclusion

In summary, we have developed the first hybrid perovskite NC synthetic method that is capable of producing nearly pure white light, thus enhancing the possibility to use these NCs as single source materials for SSL applications. Our NCs would provide three

important beneficial features in LED fabrication in comparison to traditionally used phosphors (organic and/or inorganic) or mixtures of different light-emitting QDs: (1) Mixing of multiple single light-emitting phosphors is commonly performed to cover the entire visible region of the solar spectrum. This mixing process reduces the device efficiency because the different phosphors decompose at different rates. (2) Inorganic phosphors require metal ion doping in order to achieve white-light emission.[52, 53] (3) White-light emitting multi-layer films can be prepared by mixing various color-emitting QDs but the devices suffer significant deficiency due to the self-absorption process that arises from different sized NCs. Our organic-inorganic hybrid NCs obviate all these drawbacks. Moreover, these NCs have the potential to provide fundamentally new optical and electronic properties at the molecule-nanocrystal interface that could be utilized to maximize charge transport efficiency in optoelectronic devices.

5.6 References

1. The Promise of Solid State Lighting for General Illumination; Optoelectronics Industry Development Association: Washington, D. 2001.
2. Using Light-Emitting Diodes, 2010. http://www1.eere.energy.gov/buildings/ssl/sslbasics_ledbacics.html; **accessed Nov 2010.**
3. Tang, C., et al., *Recent Progress in Polymer White Light-Emitting Materials and Devices.* Macromol. Chem. Phys., 2013. **214**(3): p. 314-342.
4. Coe, S., et al., *Electroluminescence from single monolayers of nanocrystals in molecular organic devices.* Nature, 2002. **420**(6917): p. 800-803.
5. Colvin, V.L., M.C. Schlamp, and A.P. Alivisatos, *Light-emitting diodes made from cadmium selenide nanocrystals and a semiconducting polymer.* Nature, 1994. **370**(6488): p. 354-357.
6. Yu, K., *CdSe Magic-Sized Nuclei, Magic-Sized NCs and Regular Nanocrystals: Monomer Effects on Nucleation and Growth.* Adv. Mater., 2012. **24**(8): p. 1123-1132.
7. Harrell, S.M., J.R. McBride, and S.J. Rosenthal, *Synthesis of Ultrasmall and Magic-Sized CdSe Nanocrystals.* Chem. Mater., 2013. **25**(8): p. 1199-1210.
8. Kim, B.H., et al., *Synthesis, Characterization, and Application of Ultrasmall Nanoparticles.* Chem. Mater., 2013. **26**(1): p. 59-71.
9. Dohner, E.R., E.T. Hoke, and H.I. Karunadasa, *Self-Assembly of Broadband White-Light Emitters.* J. Am. Chem. Soc., 2014. **136**(5): p. 1718-1721.
10. Dohner, E.R., et al., *Intrinsic White-Light Emission from Layered Hybrid Perovskites.* J. Am. Chem. Soc., 2014. **136**(38): p. 13154-13157.
11. Cossairt, B.M. and J.S. Owen, *CdSe Clusters: At the Interface of Small Molecules and Quantum Dots.* Chem. Mater., 2011. **23**(12): p. 3114-3119.
12. Shi, D., et al., *Low trap-state density and long carrier diffusion in organolead trihalide perovskite single crystals.* Science 2015. **347**(6221): p. 519-522.
13. Tan, Z.-K., et al., *Bright light-emitting diodes based on organometal halide perovskite.* Nat. Nano., 2014. **9**(9): p. 687-692.
14. van Driel, A.F., et al., *Statistical analysis of time-resolved emission from ensembles of semiconductor quantum dots: Interpretation of exponential decay models.* Phys. Rev. B, 2007. **75**(3): p. 035329.
15. Zhang, F., et al., *Brightly Luminescent and Color-Tunable Colloidal CH3NH3PbX3 (X = Br, I, Cl) Quantum Dots: Potential Alternatives for Display Technology.* ACS Nano, 2015. **9**(4): p. 4533-4542.
16. Zhu, F., et al., *Shape Evolution and Single Particle Luminescence of Organometal Halide Perovskite Nanocrystals.* ACS Nano, 2015. **9**(3): p. 2948-2959.
17. Schmidt, L.C., et al., *Nontemplate Synthesis of CH3NH3PbBr3 Perovskite Nanoparticles.* J. Am. Chem. Soc., 2014. **136**(3): p. 850-853.
18. Zhang, D., et al., *Solution-Phase Synthesis of Cesium Lead Halide Perovskite Nanowires.* J. Am. Chem. Soc., 2015. **137**: p. 9230-9233.

19. Akkerman, Q.A., et al., *Tuning the Optical Properties of Cesium Lead Halide Perovskite Nanocrystals by Anion Exchange Reactions.* J. Am. Chem. Soc., 2015. **137**(32): p. 10276-10281.
20. Protesescu, L., et al., *Nanocrystals of Cesium Lead Halide Perovskites (CsPbX3, X = Cl, Br, and I): Novel Optoelectronic Materials Showing Bright Emission with Wide Color Gamut.* Nano Lett., 2015. **15**(6): p. 3692-3696.
21. Swarnkar, A., et al., *Colloidal CsPbBr3 Perovskite Nanocrystals: Luminescence beyond Traditional Quantum Dots.* Angew. Chem. Inter. Ed., 2015. **54**(51): p. 15424-15428.
22. Dolai, S., et al., *Mechanistic Study of the Formation of Bright White Light-Emitting Ultrasmall CdSe Nanocrystals: Role of Phosphine Free Selenium Precursors.* Chem. Mater., 2015. **27**(3): p. 1057-1070.
23. Dolai, S., et al., *Isolation of Bright Blue Light-Emitting CdSe Nanocrystals with 6.5 kDa Core in Gram Scale: High Photoluminescence Efficiency Controlled by Surface Ligand Chemistry.* Chem. Mater., 2014. **26**(2): p. 1278-1285.
24. Wang, Y., et al., *The Magic-Size NC (CdSe)34 as a Low-Temperature Nucleant for Cadmium Selenide Nanocrystals; Room-Temperature Growth of Crystalline Quantum Platelets.* Chem. Mater., 2014. **26**(7): p. 2233-2243.
25. Bowers, M.J., J.R. McBride, and S.J. Rosenthal, *White-Light Emission from Magic-Sized Cadmium Selenide Nanocrystals.* J. Am. Chem. Soc., 2005. **127**(44): p. 15378-15379.
26. Lawrence, K.N., et al., *Solvent-like ligand-coated ultrasmall cadmium selenide nanocrystals: strong electronic coupling in a self-organized assembly.* Nanoscale, 2015. **7**(27): p. 11667-11677.
27. Anderson, N.C., et al., *Ligand Exchange and the Stoichiometry of Metal Chalcogenide Nanocrystals: Spectroscopic Observation of Facile Metal-Carboxylate Displacement and Binding.* J. Am. Chem. Soc., 2013. **135**(49): p. 18536-18548.
28. Knowles, K.E., et al., *Chemical Control of the Photoluminescence of CdSe Quantum Dot-Organic Complexes with a Series of Para-Substituted Aniline Ligands.* J. Am. Chem. Soc., 2009. **132**(3): p. 1041-1050.
29. Landes, C.F., M. Braun, and M.A. El-Sayed, *On the Nanoparticle to Molecular Size Transition: Fluorescence Quenching Studies.* J. Phys. Chem. B, 2001. **105**(43): p. 10554-10558.
30. Rosson, T.E., et al., *Bright White Light Emission from Ultrasmall Cadmium Selenide Nanocrystals.* J. Am. Chem. Soc., 2012. **134**(19): p. 8006-8009.
31. Kasuya, A., et al., *Ultra-stable nanoparticles of CdSe revealed from mass spectrometry.* Nat. Mater., 2004. **3**(2): p. 99-102.
32. Gonzalez-Carrero, S., R.E. Galian, and J. Perez-Prieto, *Maximizing the emissive properties of CH3NH3PbBr3 perovskite nanoparticles.* J. Mater. Chem. A, 2015. **3**(17): p. 9187-9193.
33. Tanaka, K., et al., *Comparative study on the excitons in lead-halide-based perovskite-type crystals CH3NH3PbBr3 CH3NH3PbI3.* Solid State Commun., 2003. **127**(9–10): p. 619-623.

34. Teunis, M.B., et al., *Mesoscale Growth and Assembly of Bright Luminescent Organolead Halide Perovskite Quantum Wires.* Chem. Mater., 2016. **10.1021/acs.chemmater.6b01793**.
35. Sichert, J.A., et al., *Quantum Size Effect in Organometal Halide Perovskite Nanoplatelets.* Nano Lett., 2015. **15**(10): p. 6521-6527.
36. Dou, L., et al., *Atomically thin two-dimensional organic-inorganic hybrid perovskites.* Science, 2015. **349**(6255): p. 1518-1521.
37. Vybornyi, O., S. Yakunin, and M.V. Kovalenko, *Polar-solvent-free colloidal synthesis of highly luminescent alkylammonium lead halide perovskite nanocrystals.* Nanoscale, 2016. **8**(12): p. 6278-6283.
38. Yuan, Z., et al., *Highly luminescent nanoscale quasi-2D layered lead bromide perovskites with tunable emissions.* Chem. Commun., 2016. **52**(20): p. 3887-3890.
39. Yuan, Z., et al., *A facile one-pot synthesis of deep blue luminescent lead bromide perovskite microdisks.* Chem. Commun., 2015. **51**(91): p. 16385-16388.
40. Yangui, A., et al., *Optical Investigation of Broadband White-Light Emission in Self-Assembled Organic–Inorganic Perovskite (C6H11NH3)2PbBr4.* J. Phys. Chem. C, 2015. **119**(41): p. 23638-23647.
41. Hu, T., et al., *Mechanism for Broadband White-Light Emission from Two-Dimensional (110) Hybrid Perovskites.* J. Phys. Chem. Lett., 2016. **7**(12): p. 2258-2263.
42. Reshchikov, M.A. and H. Morkoç, *Luminescence properties of defects in GaN.* J. Appl. Phys., 2005. **97**(6): p. 061301.
43. Pellet, N., et al., *Transforming Hybrid Organic Inorganic Perovskites by Rapid Halide Exchange.* Chem. Mater., 2015. **27**(6): p. 2181-2188.
44. Pathak, S., et al., *Perovskite Crystals for Tunable White Light Emission.* Chem. Mater., 2015. **27**(23): p. 8066-8075.
45. Jang, D.M., et al., *Reversible Halide Exchange Reaction of Organometal Trihalide Perovskite Colloidal Nanocrystals for Full-Range Band Gap Tuning.* Nano Lett., 2015. **15**(8): p. 5191-5199.
46. Umebayashi, T., et al., *Electronic structures of lead iodide based low-dimensional crystals.* Phys. Rev. B, 2003. **67**(15): p. 155405.
47. Brus, L.E., *Electron--electron and electron-hole interactions in small semiconductor crystallites: The size dependence of the lowest excited electronic state.* J. Chem. Phys., 1984. **80**(9): p. 4403-4409.
48. Nedelcu, G., et al., *Fast Anion-Exchange in Highly Luminescent Nanocrystals of Cesium Lead Halide Perovskites (CsPbX3, X = Cl, Br, I).* Nano Lett., 2015. **15**(8): p. 5635-5640.
49. Schreuder, M.A., et al., *Control of Surface State Emission via Phosphonic Acid Modulation in Ultrasmall CdSe Nanocrystals: The Role of Ligand Electronegativity.* J. Phys. Chem. C, 2009. **113**(19): p. 8169-8176.
50. Califano, M., *Origins of Photoluminescence Decay Kinetics in CdTe Colloidal Quantum Dots.* ACS Nano, 2015. **9**(3): p. 2960-2967.
51. Hoy, J., et al., *Excitation Energy Dependence of the Photoluminescence Quantum Yields of Core and Core/Shell Quantum Dots.* J. Phys. Chem. Lett., 2013. **4**(12): p. 2053-2060.

52. Frederick, M.T., et al., *A Molecule to Detect and Perturb the Confinement of Charge Carriers in Quantum Dots.* Nano Lett., 2011. **11**(12): p. 5455-5460.
53. Lawrence, K.N., et al., *Dual Role of Electron-Accepting Metal-Carboxylate Ligands: Reversible Expansion of Exciton Delocalization and Passivation of Nonradiative Trap-States in Molecule-Like CdSe Nanocrystals.* J. Am. Chem. Soc., 2016. **DOI: 10.1021/jacs.6b04888**.
54. Gonzalez-Carrero, S., et al., *Blue-luminescent organic lead bromide perovskites: highly dispersible and photostable materials.* J. Mater. Chem. A, 2015. **3**(26): p. 14039-14045.
55. Vikash Kumar, R., et al., *Excellent green but less impressive blue luminescence from CsPbBr 3 perovskite nanocubes and nanoplatelets.* Nanotechnology, 2016. **27**(32): p. 325708.
56. Yettapu, G.R., et al., *Terahertz Conductivity within Colloidal CsPbBr3 Perovskite Nanocrystals: Remarkably High Carrier Mobilities and Large Diffusion Lengths.* Nano Lett., 2016. **16**(8): p. 4838-4848.
57. Ki, W. and J. Li, *A Semiconductor Bulk Material That Emits Direct White Light.* J. Am. Chem. Soc., 2008. **130**(26): p. 8114-8115.
58. Sun, C.-Y., et al., *Efficient and tunable white-light emission of metal–organic frameworks by iridium-complex encapsulation.* Nat. Commun., 2013. **4**: p. 1-7.

CONCLUSION

The purpose of this dissertation is to examine how unique aspects of surface chemistry control shape evolution and optoelectronic properties in direct band gap (metal chalcogenide and perovskite) NCs. Through this work we were able to investigate the following; (1) the growth and formation of structurally well-defined perovskite NCs, (2) the development of a facile gram scale synthesis of II-IV metal chalcogenide anisotropic NCs; (3) the effect of surface ligand chemistry on optoelectronic properties of semiconductor NCs; and (4) the tailoring of surface chemistry to produce white-light emission of perovskite NCs.

Chapter 1 introduces the literature background of direct band gap semiconductors and the expansion of their applications due to their unique optoelectronic properties. These properties can be controlled by shape as well as the interactions between the NC and surface passivating ligand leading to exciton delocalization. Finally, through passivation or composition, the surface chemistry can also influence the emission of direct band gap semiconductor NCs. We begin Chapter 2 by studying the shape evolution of well-defined methyl ammonium lead bromide ($CH_3NH_3PbBr_3$) anisotropic NCs. A programmable synthesis of anisotropic $CH_3NH_3PbBr_3$ NCs (including wires, platelets, cubes, and large sheets) was developed and the importance of surface ligand, solvent system, and reaction temperature to produce each of these structures was determined. The QWs, having one of the highest reported QY of any nanostructure in the literature to date, require the presence of a long chain acid and octyl ammonium ions on the surface to not only direct 1D growth but also to promote bundle formation. The QPLs require a system containing a chlorinated solvent to drive the desired 2D growth, as

well a long chain amine to promote the assembly into platelet stacks. Finally, the 3D growth of the QCs wee determined to be a mainly kinetic-controlled process.

In Chapter 3, we continue our investigation of shape evolution but turn to II-IV metal chalcogenide NCs. Here we developed a versatile, low temperature, and gram scale synthesis of QWs, QPLs, and QRs. This investigation lead to a better understanding of the mesoscale assembly growth mechanism and how surface passivating ligand, precursor concentration, and temperature contribute to control shape evolution. The 1D growth of the QWs were found to occur in the presence of a long chain amine, while the QPLs required a long and short chain amine and higher temperatures to generate 2D growth. Finally, the temperature and precursor ratios were found to be crucial for the successful synthesis of QRs. Time dependent optical characterization and ex-situ growth confirmed that $(CdSe)_{13}$ and $(CdSe)_{19}$ NCs are the precursors of these anisotropic shapes.

Next in Chapter 4, we examine how the post-synthetic ligand exchange of the native amine ligands with various chalcogenol ligands controls the optoelectronic properties of $(CdSe)_{34}$ NCs. These ultrasmall NCs make an ideal system to investigate the effect of surface chemistry on these properties due to their large surface to volume ratios allowing for even a minute change in the surface chemistry to have immense results. We began the investigation with a class of well-known PDTC ligands with various para substitutions. As the para functional group became more electron withdrawing, a larger extent of hole delocalization was observed. These results initiated a closer examination of other characteristic of the ligand (level of conjugation, binding mode, and binding head group) to determine how these parameters impact the

delocalization of the wave function. The largest extent of delocalization, and subsequent reduction of the gap (of 650 meV), was observed upon exchange with Py-DTC. Through control experiments to investigate the extent of delocalization with other DTC ligands containing different levels of conjugation and pyrene ligands with various binding head groups, both the level of conjugation and bidentate binding mode were found to be crucial to achieve greater delocalization.

Finally in Chapter 5, we developed the synthesis of ultrasmall $CH_3NH_3PbBr_3$ perovskite NCs and tailored their white-light emission by tuning the surface composition and trap states. It was found that by replacing surface bromide ions with chloride ions, the CIE coordinates and emission color could be tuned to match that of nearly pure white-light. These mixed halide NCs displayed large quantum yields of ~12% and radiative lifetime of ~20 ns and as a proof of concept were used to fabricate an LED device.

Overall this dissertation provides valuable information on how unique aspects of surface chemistry control both shape evolution and optoelectronic properties of direct band gap semiconductor NCs. The knowledge gained may help to further promote and optimize the development and application of semiconductor-based solid-state devices.

PUBLICATIONS

1. **Teunis, M.B.,** Liyanage, T., Dolai, S.K., Muhoberac, B.B., Sardar, R.S., and Agarwal, M. *Unraveling the Mechanism Underlying Surface Ligand Passivation of Colloidal Semiconductor Nanocrystals: A Route for Preparing Novel Hybrid Nanomaterials*.Adv. Mater. 2017, Submitted.

2. **Teunis, M.B**., Johnson, M.A., Muhaberac, B.B., Seifert, S., and Sardar, R.S. *Programmable Colloidal Approach to Hierarchical Structures of Methylammonium Lead Bromide Perovskite Nanocrystals with Bright Photoluminescent Properties*. Chem. Mater. 2017, Submitted

3. **Teunis, M.B**., Lawrence, K.N., Dutta, P., Siegel, A.P., and Sardar, R.S. *Pure White-Light Emitting Ultrasmall Organic-Inorganic Hybrid Perovskite NCs*. Nanoscale. 2016, 8, 17433-17439

4. Lawrence, K.N., Dutta, P., Nagaraju, M., **Teunis, M.B**., Muhaberac, B.B., and Sardar, R.S. *Dual Role of Electron-Accepting Metal-Carboxylate Ligands: Reversible Expansion of Exciton Delocalization and Passivation of Nonradiative Trap-States in Molecule-Like CdSe Nanocrystals*. J. Am. Chem. Soc. 2016, 28 (4), 1107-1120

5. **Teunis, M.B**., Jana, A., Dutta, P., Johnson, M.A., Mandal, M., Muhoberac, B.B., and Sardar, R.S. *Mesoscale Growth and Assembly of Bright Luminescent Organolead Halide Perovskite Quantum Wires.* Chem. Mater. 2016, 28 (14), 5043–5054.

6. Jana, A., Lawrence, K.N., **Teunis, M.B**., Mandal, M., Kumbhar, A., and Sardar, R.S. *Investigating the Control by Quantum Confinement and Surface Ligand Coating of Photocatalytc Efficiency in Chalcopyryrte Copper Indium Diselenide Nanocrystals*. Chem. Mater. 2016, 28 (4), 1107–1120.

7. Xie,Y., **Teunis, M.B**., Prandit,B., Sardar, R.S., and Liu, J. *Molecule-like CdSe NCs Passivated with Strongly Interacting Ligands: Energy Level Alignment and Photoinduced Ultrafast Charge Transfer Processes*. J. Phys. Chem. C. 2015, 119 (5), 2813–2821.

8. **Teunis, M.B**., Dolai, S.K., and Sardar, R.S. *Effects of Surface-Passivating Ligands and Ultrasmall CdSe Nanocrystal Size on the Delocalization of Exciton Confinement*. Langmuir. 2014, 30 (26), 7851-7858.